OCS Study
MMS 2009-060

Modeling Waves and Currents Produced by Hurricanes Katrina, Rita, and Wilma

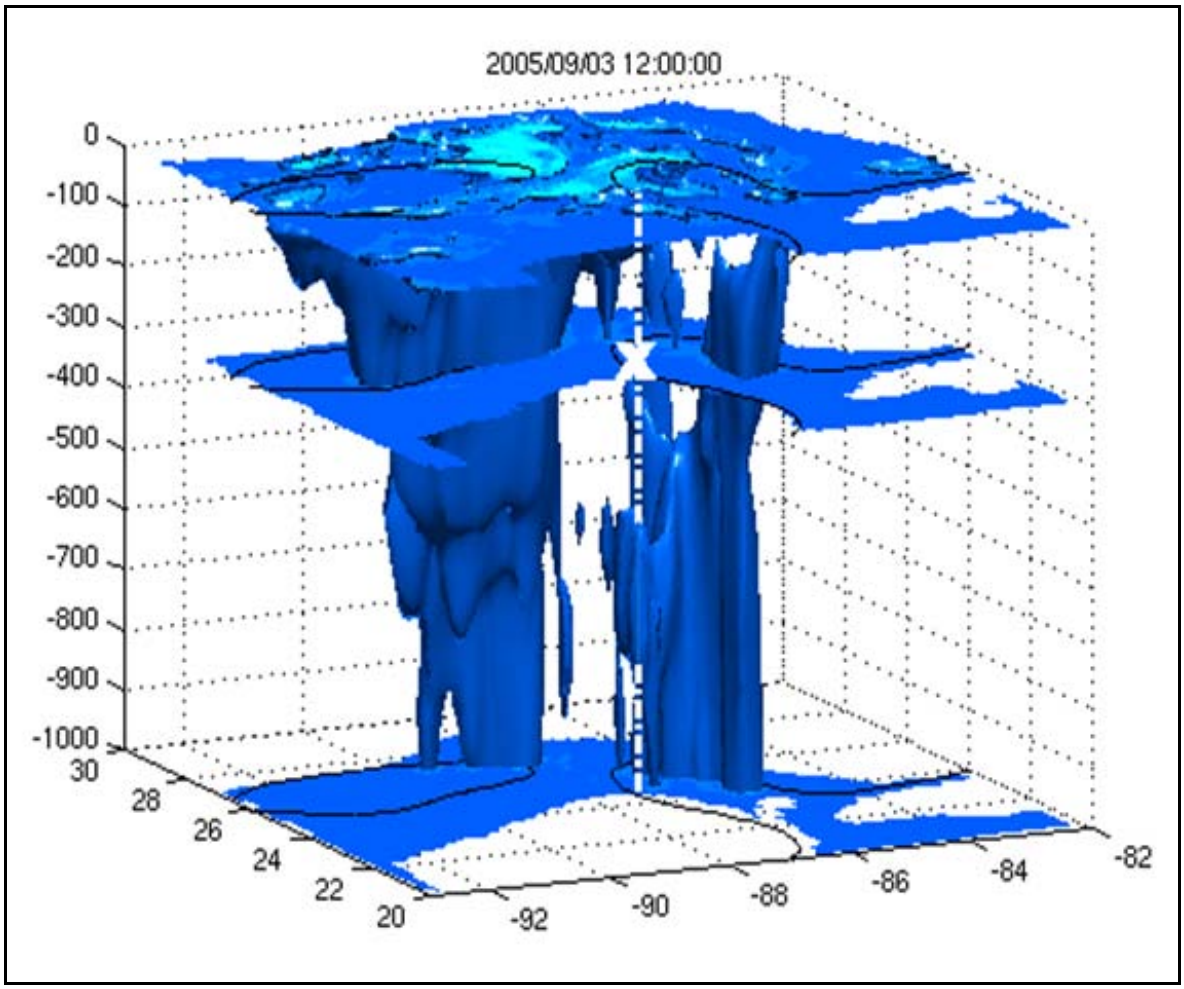

MMS
U.S. Department of the Interior
Minerals Management Service
Gulf of Mexico OCS Region

OCS Study
MMS 2009-060

Modeling Waves and Currents Produced by Hurricanes Katrina, Rita, and Wilma

Authors

Lie-Yauw Oey
Dong-Ping Wang

Prepared under MMS Contract
1435-01-06-CT-39731
by
Princeton University
Program in Atmospheric and Oceanic Sciences
Sayre Hall
Princeton, NJ 08544

Published by

U.S. Department of the Interior
Minerals Management Service
Gulf of Mexico OCS Region

New Orleans
November 2009

DISCLAIMER

This report was prepared under contract between the Minerals Management Service (MMS) and Princeton University. This report has been technically reviewed by the MMS and approved for publication. Approval does not signify that the contents necessarily reflect the views and policies of the Service, nor does mention of the trade names or commercial products constitute endorsement of recommendation for use. It is, however, exempt from review and compliance with the MMS editorial standards.

REPORT AVAILABILITY

This report is available only in compact disc format from the Minerals Management Service, Gulf of Mexico OCS Region, at a charge of $15.00, by referencing OCS Study MMS 2009-060. The report may be downloaded from the MMS website through the Environmental Studies Program Information System (ESPIS). You will be able to obtain this report also from the National Technical Information Service in the near future. Here are the addresses. You may also inspect copies at selected Federal Depository Libraries.

Minerals Management Service
Gulf of Mexico OCS Region
Public Information Office (MS 5034)
1201 Elmwood Park Boulevard
New Orleans, Louisiana 70123-2394
Telephone requests may be placed at
(504) 736-2519, 1-800-200-GULF, or
Rush Orders: 1-800-553-6847
Fax: (504) 736-2620

U.S. Department of Commerce
National Technical Information Service
5285 Port Royal Road
Springfield, Virginia 22161
Phone: (703) 605-6040
Fax: (703) 605-6900
Email: bookstore@ntis.gov

CITATION

Suggested citation:

Oey, L.-Y. and D.-P. Wang. 2009. Modeling waves and currents produced by Hurricanes Katrina, Rita, and Wilma. U.S. Dept. of the Interior, Minerals Management Service, Herndon, Virginia. OCS Study MMS 2009-060. xviii + 135 pp.

ABOUT THE COVER

A three-dimensional surface of inertial energy = 0.03 m^2s^{-2} on September 3, 2005, at 12:00 GMT after Hurricane Katrina, obtained from the model showing the deep penetration of intense energies to deep layers due to the presence of the warm-core ring and Loop Current. The location of LSU mooring where extensive model-observational analyses have been conducted (see text) is shown as vertical dashed line.

ACKNOWLEDGMENTS

Sponsor Acknowledgments: The study was sponsored by the Minerals Management Service/DOI, under Contract #1435-01-06-CT-39731. The Contract Officer Technical Representative was Dr. Carole Current and period of study was from Jun, 2006 through Jun, 2008. We are also grateful to the NOAA/Geophysical Fluid Dynamics Laboratory for the permission to use their supercomputing facilities.

Other Acknowledgments: We benefited from discussions with Carole Current, Alexis Lugo-Fernandez, Walter Johnson, and Ron Lai. Special thanks also to Dr. Carole Current for her encouragements throughout the course of this project. Contributions by co-authors (listed in each chapter) are acknowledged; in particular those from George Mellor on the development of the coupled wave-current model. Xiaohua Lin's contributions in coding and analyzing the model and observations are also acknowledged.

TABLE OF CONTENTS

Page

FIGURES

TABLES

ACRONYMS AND DEFINITIONS OF COMMONLY-USED VARIABLES

Acronym	**Meaning**
ADCP	Acoustic Doppler Current Profiler
AOML	Atlantic Oceanographic and Meteorological Laboratory
AVISO	Archiving, Validation and Interpretation of Satellite Oceanographic data
AVISOM	AVISO SSHA + the (present) model 10-year mean SSH
BEnF	Bred Ensemble Forecast
ConA	Control analysis; sometimes referred to as hindcast or nowcast in the literature and is often used as initial field for forecasting
ConF	Control Forecast, meaning the "conventional" (single) forecast
EnB	Ensemble breeding
EnMB	Ensemble mean breeding
EnMF	Ensemble mean forecast
GCM	General Circulation Model
GODAE	Global Ocean Data Assimilation Experiment
HRD	Hurricane Research Division
NCEP	National Centers for Environmental Prediction
NOAA	National Oceanic and Atmospheric Administration
OBS	Observation(s)
OHC	Ocean Heat Content
POM	Princeton Ocean Model
RMS	Root Mean Square
SSH	Sea Surface Height
SSHA	Sea Surface Height Anomaly
SST	Sea Surface Temperature

Variable	**Meaning**
$\varepsilon_m(kN)$	The perturbation of the m^{th} member of a breeding cycle, k = 0,1,…K; the last one for k = K is used (with the corresponding control analysis) to initialize the ensemble forecasts—see $T_m(kN)$ definition below
$\delta\eta$	Sea surface height anomaly or SSHA
$\delta\eta_o$	Observed sea surface height anomaly from satellite
$\delta\eta^f(n)$	The unperturbed (i.e., conventional) forecast SSHA (i.e., ConF) at time "n"
$\delta\eta^f{}_m(n)$	The perturbed m^{th}-member forecast SSHA at time "n"
$A_m(n)$	Spatial average of the m^{th}-member bred vector at time "n"
BV	Bred vector = the difference between perturbed and unperturbed forecasts
CC	Complex correlation between two vectors, also called vector correlation
GR_k	Bred-vector growth rate for the k^{th}-cycle
K	Total number of breeding cycles; this work has used K = 8 and 10
M	Total number of ensemble members; this work uses M = 20
N	Number of days per breeding cycle; this work uses N = 7
T	Potential temperature; also used more generally to denote a state vector
$T_m(kN)$	The m^{th} ensemble member of the perturbed analysis of "T" at the start of a breeding cycle, i.e., $T_m(kN) = T^a(kN) + \varepsilon_m(kN)$, k = 0,1,…K-1. For k = K, $T_m(KN)$ is used to initialize the ensemble forecasts

T^a	The “T” obtained from a control analysis or ConA
$T^f(n)$	The unperturbed (i.e., conventional) forecast (i.e., ConF) at time “n”
$T^f_m(n)$	The m^{th}-member of the perturbed forecast at time “n”

SUMMARY

The 2005 Atlantic hurricane season, with three Category-5 hurricanes within a time span of two months (Katrina, Rita and Wilma, August to October) in the Caribbean Sea and the Gulf of Mexico, underscored an important fact: as populations boom in coastal regions and as the earth embraces a warmer climate with higher sea-surface temperatures (SST) over the tropical oceans, the next decade may see increasingly more intense storms that pose greater risks than ever before (Emanuel, 2005a). In particular, the strong currents and waves produced by Hurricanes Katrina (August 23-30, 2005) and Rita (September 18-26) caused considerable human sufferings and property losses, as well as damage to gas and oil facilities in the northern Gulf of Mexico continental shelf and slope. The Minerals Management Service (MMS) wishes to assess the impacts of these waves and currents, hence our research. Assessments of wave and current responses to intense hurricanes are important especially in view of forecast threats of increasingly more powerful storms due to the warming climate. We have conducted such an assessment study using a combination of numerical modeling and observational data analyses. The goal is to provide the MMS with our best estimates of the strengths as well as spatial and temporal distributions of currents and waves during Katrina and Rita in the northern Gulf of Mexico. It was further suggested during the Kick-Off-Meeting that a study of the effects of Hurricane Wilma could provide additional insights, and this too has been conducted. In addition to providing practical assessments, we also focus on basic understanding of the physics of the ocean response to these intense hurricanes, and to a more limited extent, the physics of air-sea interaction as well.

Our research has resulted in six papers. This report begins with a Prologue, which is then followed by seven chapters comprising primarily of the six papers. Some chapters have been extended to reflect additional materials that were omitted from the published papers. The chapters are arranged starting with the models' foundation of deriving the best estimate of the background field prior to each storm (the Loop Current and eddies), to discussing the storms' surface responses, then sub-surface responses, then finally to storm-Loop interaction problem.

Specific objectives as requested by MMS are

1. conduct a realistic simulation of responses of currents and waves to Hurricanes Katrina and Rita throughout the entire water column in the northern Gulf of Mexico;
2. determine the length of time for which substantial ocean response to these hurricanes persisted, and
3. determine the area or areas of greatest wave height and current speed.

We have achieved all these goals. We have analyzed extensively both observations and model results, and have gained an improved understanding of the physics of ocean response due to intense hurricanes, as well as the complex interactions of these responses with meso-scale eddies (warm rings and Loop Current) in the Gulf of Mexico. For Hurricane Wilma, we witnessed once-in-a-lifetime coincidence of a slowly-moving powerful storm which stalled over a powerful ocean current—the Loop Current, in the vicinity of a channel (Yucatan) through which a large amount of warm water flows. The interaction was significant and scientifically intriguing and can have profound implications for hurricane predictions. For Katrina and Rita, we simulated not only the detailed surface wave and current fields, but also the penetration of

storm-generated inertial energy into the deep portions of the ring and the Loop Current. We determined that deep penetrations of (storm-induced) inertial energy occur preferentially within these warm oceanic structures that have significant anticyclonic vorticity. In the case of Katrina, we found a curious phenomenon of subsurface inertial energy trapped over a frontal cyclone at the base of the Loop Current. This was further confirmed by the MMS mooring at (87^{o}W, 25.5^{o}N) deployed by the LSU scientists. To the best of our knowledge, this was the first time that such a phenomenon has been discovered. These deep penetrations and trapping of inertial energy occur days (up to ~10) after the storms have passed, and can have important implications to the overall circulation in the Gulf because by virtue of their high frequencies (i.e., inertial), they contribute to deep mixing. Given that the Gulf is almost completely closed below about 1000 m, the phenomena provide a means by which mass may be exchanged between the upper and lower layers; this in turn will affect the circulation and heat (salt) budget of the Gulf.

On a more practical level, we have also delineated regions of strong waves and currents that accounted for the severe damage to a giant oil platform as well as the uprooting of an NDBC buoy during Katrina. These regions predominantly occurred to the right of the storms. This is not new of course, but we did identify the very intense inertial currents (up to 3 m/s) and extraordinarily high waves (20 m) that ensued.

The above also points to the importance of an accurate analysis field for the Loop Current and warm rings prior to the storm. This we accomplished through a combination of satellite data assimilation and ensemble breeding that provide the improved error covariances. We show that the technique substantially improves the analysis fields.

Finally, advances on the numerical model have been made. The most significant is the completion of a fully coupled wave-current model – the first we believe in the literature. Details of this model are not included in this report, but the relevant paper is in press (Mellor et al., 2008).

PROLOGUE

The 2005 Atlantic hurricane season, with three Category 5 hurricanes within a time span of two months (Katrina, Rita and Wilma, August to October; see Figure P.1 and Table P.1; source: http://www.nhc.noaa.gov/pastall.shtml), in the Caribbean Sea and the Gulf of Mexico underscored an important fact: as populations boom in coastal regions, and as the earth embraces a warmer climate with higher sea-surface temperatures (SST) over the tropical oceans, the next decade may see increasingly more intense storms that pose greater risks than ever before (Emanuel, 2005a). An impact study of the strong currents and waves produced by these storms is therefore timely as well as urgently necessary. This is so in particular in view of increased offshore oil and gas activities in the northern Gulf in recent years. We have conducted such an impact-assessment study using a combination of numerical modeling and observational data analyses. The goal is to provide the Minerals Management Service (MMS) with our best estimates of the strengths as well as spatial and temporal distributions of currents and waves during Katrina and Rita in the northern Gulf of Mexico. Additionally, a study of the effects of Hurricane Wilma has also been conducted.

This project also allows us to explore scientific questions that are relevant to MMS's overall goal of not only obtaining the best estimates of the circulation in the Gulf, but also of understanding it and the forcing associated with it. Through understanding, we improve the analysis skills which in turn strengthen the MMS' capability to conduct impact assessments. Given that the Gulf's circulation is dominated by the Loop Current and the omnipresence of eddies, we study extensively the interaction of powerful hurricanes with dynamically equally powerful oceanic storms.

We begin (Chapter 1) therefore with a careful study of how best we can represent the ocean state (Loop Current and eddies) in the Gulf. We then (Chapter 2) simulated and analyzed extensively the currents and waves induced by Hurricanes Katrina, then Rita (Chapter 3). Here maps of waves and currents are given. We then examine in great details (Chapters 4 and 5) how storm-induced near-inertial energy at the surface can penetrate deep (500 m ~ 1,000 m) in "chimneys" at preferred locations dictated by the Loop Current and rings, and moreover how subsurface cyclones may play an important role in trapping the energy and therefore possibly also in deep mixing. Finally, in Chapters 6 and 7, we show the importance of hurricane-Loop interaction by analyzing in great details the Hurricane Wilma case, and a new index for measuring the potential importance of the ocean heat capacity on hurricane strength is proposed. Our research also included the development of a new wave model that is now fully coupled with the ocean-current model, and a test of this new model for the Katrina case has also been conducted. This last research resulted in a paper by Mellor et al. (in press), which is available from http://www.aos.princeton.edu/WWWPUBLIC/PROFS/ (click "Publications").

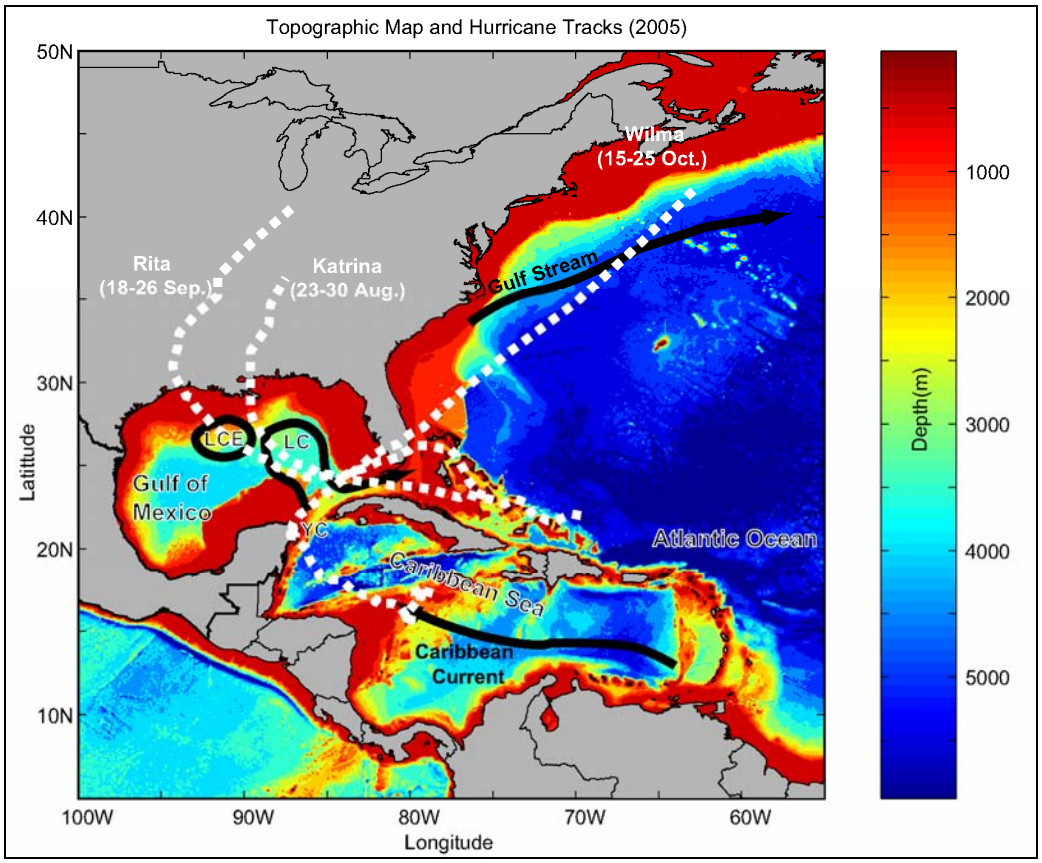

Figure P.1. Topographic map of the western North Atlantic (excluding the Pacific Ocean in the south-west corner, this is the area covered by our ocean forecast model, PROFS, see text for details). The major ocean currents are indicated by heavy black arrows. The tracks of the three strongest hurricanes in 2005 are indicated in dashed white lines; all three reached a Category 5 status during their lifespan (Katrina and Rita in the Gulf of Mexico and Wilma in the Caribbean Sea). Acronyms are LC: Loop Current, LCE: Loop Current eddy, and YC: Yucatan Channel. Though schematic, the LC and LCE positions depicted here are closed to the actual ones during Katrina and Rita.

Table P.1.

Ten Most Intense Atlantic Hurricanes
(as measured by central pressure).

(Four of these (in bold-red), Ivan, Katrina, Rita and Wilma, occurred in recent years. This may foretell a trend of ever more powerful storms related to increased tropical ocean SST due to a warming climate (Emanuel, 2005a).)

Rank	Hurricane	Season	Minimum Pressure
1	**Wilma**	2005	882 mbar (hPa)
2	Gilbert	1988	888 mbar (hPa)
3	"Labor Day"	1935	892 mbar (hPa)
4	**Rita**	2005	897 mbar (hPa)
5	Allen	1980	899 mbar (hPa)
6	**Katrina**	2005	902 mbar (hPa)
7	Camille	1969	905 mbar (hPa)
	Mitch	1998	905 mbar (hPa)
9	**Ivan**	2004	910 mbar (hPa)
10	Janet	1955	914 mbar (hPa)

CHAPTER 1. OCEAN STATE ESTIMATION—LOOP CURRENT AND EDDIES[1]

Synopsis

Satellite data assimilation with bred-ensemble schemes is used to estimate the state of the Loop Current and eddies in the Gulf of Mexico prior to the arrivals of hurricanes. A case-example for Hurricane Katrina is demonstrated here.

Summary of the Main Results

As will be seen in subsequent chapters, an accurate knowledge of the location and strength of the Loop Current and eddies are necessary to accurately hindcast the ocean currents and waves impacted by hurricanes. This chapter describes our efforts to derive such an accurate analysis field. The idea is intimately tied to deriving the best initial fields for forecasting. Below is a summery of our findings.

Ocean forecasting with a General Circulation Model (GCM) commonly begins from an initial analysis obtained by data assimilation. Instead of a single initial state, bred-ensemble forecasts (BEnF; Toth and Kalnay, 1993, 1997) begin from an ensemble of initial states obtained by using the GCM to breed fast-growing modes into the analysis. Here we apply the technique to forecast the locations and strengths of the Loop Current and rings from July through September 2005. Model results are compared against satellite observations, surface drifter trajectories, and moored currents. It is found that BEnF gives closer agreements with observations than the conventional single forecast. The bred-vectors (perturbed minus unperturbed state-vectors) have growth rates ≈ 0.04~0.08 day^{-1} and spatial (cyclone-anticyclone) scales ≈ 200~300 km suggestive of baroclinic instability mode in the Loop Current and rings. As in atmospheric applications, initializations with these growing vectors contribute to the more accurate ensemble mean forecast

1.1. INTRODUCTION

The Loop Current is the dominant feature of the circulation in the eastern Gulf of Mexico and the formation region of the Florida Current-Gulf Stream system (Figures 1.1 and 1.2). It originates at the Yucatan Channel through which approximately 23~27 Sv (1 Sv = 10^6 m^3 s^{-1}) transport passes with a large minimum-maximum range of 14~36 Sv (Johns et al. 2002; Sheinbaum et al. 2002). Peak speeds of 1.5 to 1.8 m s^{-1} have been observed near the surface in the Loop Current (e.g., Nowlin, 1972; Forristal et al. 1992; see Oey et al. 2005a for other references). The Loop Current feeds the Florida Current which transports significant amounts of heat poleward. The Loop episodically sheds warm-core rings (e.g., Cochrane, 1972; Vukovich, 1995) at intervals of approximately 3 to 18 months (Sturges and Leben, 2000; Leben, 2005). These rings have diameters ≈ 200~300 km, vertical extent ≈ 1000 m, and swirl speeds ≈ 1.8~2 m s^{-1}; they generally translate westward at 2~5 km day^{-1} and have lifetimes of months to approximately a year (Nowlin, 1972; Elliott, 1982; Vukovich and Crissman, 1986; Cooper et al. 1990; Forristal et al. 1992). The Loop Current and its rings are powerful oceanic features that

[1] This chapter is based on Yin and Oey, 2007.

affect, either directly or indirectly through their smaller-scale subsidiaries, just about every aspect of oceanography of the Gulf (Oey et al. 2005a).

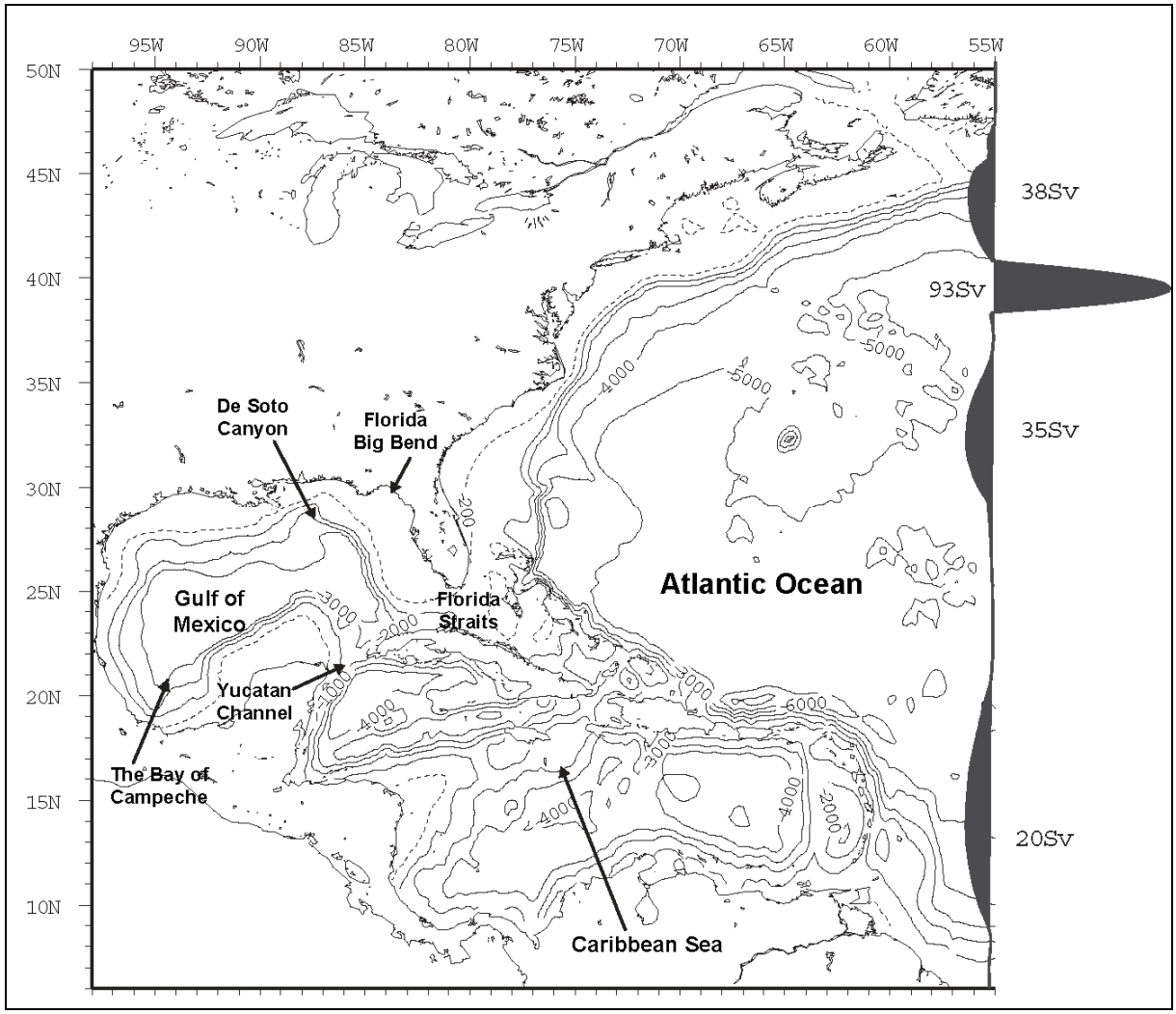

Figure 1.1. A locator map of the study region: the Gulf of Mexico and surrounding ocean regions. The domain shown is also the model domain. Time-independent inflow and outflow that account for the large-scale transports (Svedrup + thermohaline) are specified across the open boundary at 55°W as a function of latitude (as indicated with silhouette profiles). Contours show isobaths in meters.

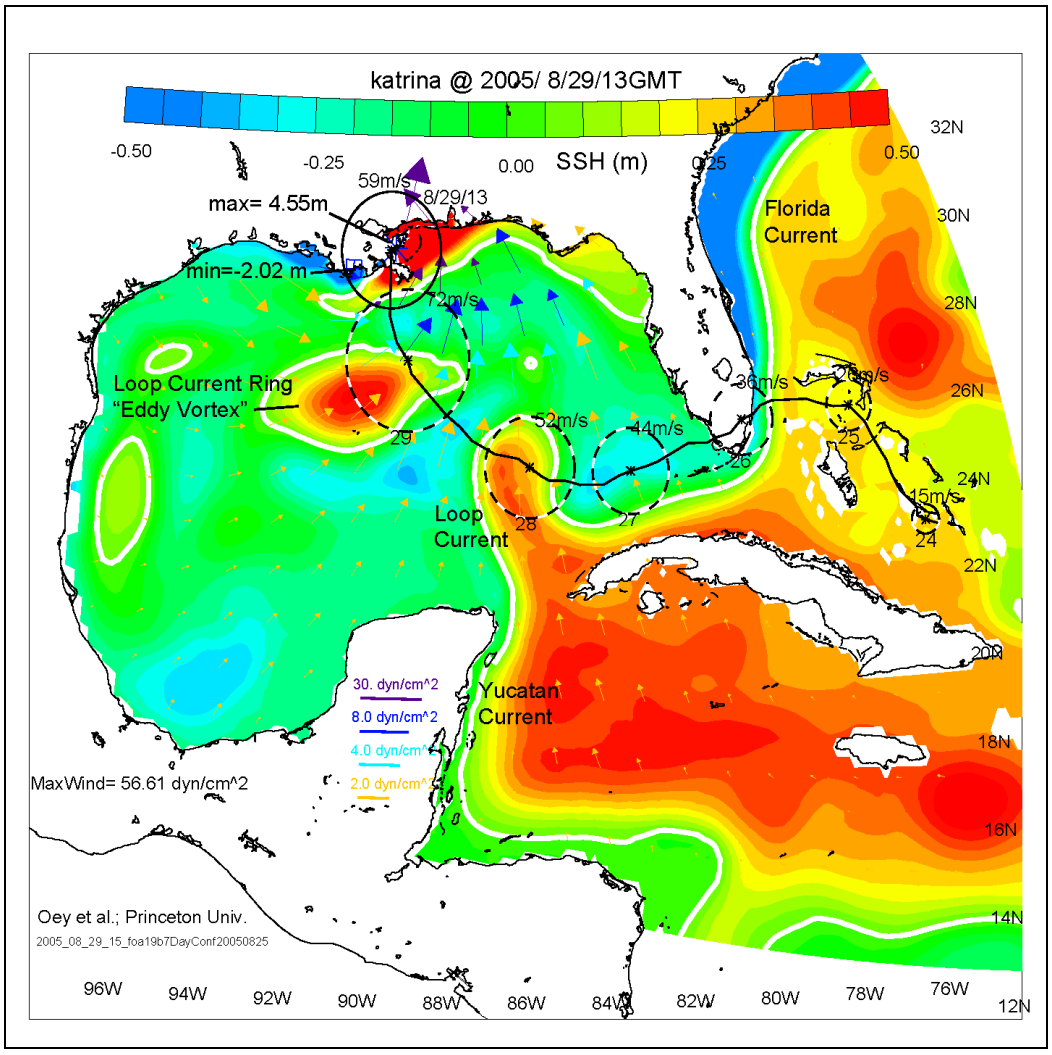

Figure 1.2. An illustrative figure of the Loop Current and its associated ring during the study period. Shown here in color is the forecast (ConF) sea-surface height (SSH; white contour is SSH = 0) on August 29 at 13:00 GMT just after Hurricane Katrina made landfall (solid circle) at New Orleans. Note the high SHH (red; max ≈ 4.6m) near New Orleans. The storm's path is shown as solid black line and its intensities are shown proportional to the size of circles (dashed) plotted at daily intervals beginning at August 24. Colored vectors indicate wind stresses with the indicated scales.

In addition to producing strong ocean currents, the Loop and rings possess, by virtue of their deep thermoclines, large values of the Ocean Heat Content (OHC; Leipper and Volgenau, 1972):

$$OHC = \rho_o C_p \int_{Z_{26}}^{\eta} (T - 26) dz \,, \qquad \mathrm{T} \geq 26°\mathrm{C},$$

where Z_{26} (>0) is depth of the 26 °C isotherm, η = sea-surface height (SSH) , ρ_o density of sea water and C_p the specific heat of water. Sea surface temperatures (SST's) in excess of 26°C are necessary for tropical cyclogenesis (Palmen, 1948; DeMaria and Kaplan, 1994). Regions where OHC > 60~90 kJ/cm^2 have been empirically found to be conducive to storm intensification, and OHC has been used as one of several parameters in hurricane prediction schemes (DeMaria et al.

2005). Typical values of OHC in summer through autumn easily exceed 60 kJ/cm^2 within the Loop and rings (e.g., Oey et al. 2006, 2007). Scharroo et al. (2005) suggest that the large heat contents of the Loop and a ring (which is named "Eddy Vortex") during Hurricane Katrina (August 23-30, 2005) may have resulted in the rapid intensification of the storm (Figure 1.2).

It is therefore of scientific and practical values to accurately forecast (and hindcast) the locations, paths and strengths of the Loop Current and rings. (In this work, by forecast we mean forward model integration without data assimilation.) Oey et al. (2005b) compared fourteen 4-week forecasts of Loop Current and rings' frontal positions against observations for the period August 1999 through September 2000. Each forecast was initialized from a data-assimilative analysis field which in this work will be referred to as the control analysis (ConA). Their model (which was based on the Princeton Ocean Model or POM, see below) correctly predicted the separation of a powerful ring from the Loop Current three weeks in advance. The mean frontal position errors ≈ 25 km while the root-mean-square (RMS) errors ≈ 50 km over the four-week forecast horizon. The authors suggested that the largest contributor to the forecast errors was error in the initial ConA field.

Oey et al. (2005b) utilized the methodology commonly used in ocean forecasting: one first initializes the model from a ConA field, and then integrates the model forward. This type of forecast will be referred to as the control forecast (ConF). In this work, instead of a single forecast initialized from one analysis field, we conduct an ensemble of forecasts with initial fields obtained using the breeding method (Toth and Kalnay, 1997). An eight-week forecast horizon is chosen, from end of July through the middle of September 2005. This period coincides with the passage of Hurricane Katrina—August 23-30, 2005. As depicted in Figure 1.2, there was a large sea-level (maximum $\eta = 4.5$ m) setup along the Mississippi-Alabama coast when Katrina made land-fall at the northern Gulf Coast. The storm breached the levees that protected New Orleans from Lake Pontchartrain, and most of the city was subsequently flooded, causing considerable human suffering and property losses. Although accurate wind field for Katrina is included in our forecast, short-time ocean currents and waves produced by the hurricane will not be our main focus here. This work concentrates instead on estimating the positions and strengths of the Loop Current and ring(s). The goal is to compare the skills of the conventional forecast (i.e., ConF) versus bred-ensemble forecast (i.e., BEnF) through direct comparison with observations.

We describe the model, forcing and assimilation method in Chapter 1.2. Breeding and ensemble forecasting are described in Chapter 1.3, where we also discuss bred vectors (perturbed minus unperturbed state-vectors). In Chapter 1.4 we compare our results against (a) sea-surface height anomaly (SSHA) from satellite, (b) trajectories of a NOAA/AOML hurricane drifter (http://www.aoml.noaa.gov/phod/dataphod/), and (c) Acoustic Doppler Current Profiler (ADCP) measurements. Chapter 1.5 concludes the chapter.

1.2. THE MODEL, WIND FORCING, CONTROL ANALYSIS AND FORECAST

The Model

Our circulation model for the Caribbean Sea and the Gulf of Mexico is based on the Princeton Ocean Model (Mellor, 2004), and has been tested for process studies as well as in realistic simulations (Oey and Lee, 2002; Ezer et al. 2003; Wang et al. 2003; Fan et al. 2004; Oey and Zhang, 2004; Oey, 2004; and Oey et al. 2003a and b, 2004, 2005a and b, 2006, 2007). A brief description is given below.

The model domain includes the northwestern Atlantic Ocean west of 55°W as shown in Figure 1.1. At 55°W, estimates of inflow and outflow transports are specified in combination with radiation conditions. The baroclinic velocities are specified using the radiation conditions. Climatological temperature and salinity are specified during inflow and advected out using one-sided differencing at outflow. Details of open boundary conditions are in Oey and Chen (1992). The model is forced by wind to be detailed below, as well as by monthly discharges from 34 rivers along the northern Gulf Coast according to the method given in Oey (1995; 1996). The model horizontal grid-size is variable; it is approximately 10 km in the Loop Current and northwestern Caribbean Sea, and about 5 km in the northeastern Gulf of Mexico. There are 25 terrain-following (the so-called sigma-coordinate) layers with 10 of them in the top 250 m for local water depth ≈ 2500 m. The Mellor and Yamada's (1982) turbulence closure scheme modified by Craig and Banner (1994) to effect wave-enhanced turbulence near the surface is used. To account for mixing in stable stratification (e.g., internal waves; MacKinnon and Gregg, 2003), Mellor's (2001) modification of a Richardson-number-dependent dissipation is used. In this work, surface heat and evaporative fluxes are set to zero so that the SST variations are due to model's internal dynamics; in the case of forcing by a hurricane, Price (1981) found that surface cooling by these fluxes is small compared to cooling by mixing.

The Wind

We combine the analyzed winds from the Hurricane Research Division (HRD; http://www.aoml.noaa.gov/hrd/) with the National Centers for Environmental Prediction's (NCEP) global wind analysis (the Global Forecast System winds; Caplan et al. 1997). The HRD data is given in a 1000 km × 1000 km (dimensions are approximate) moving "box" centered about the hurricane's track. Storm centers are first linearly interpolated to hourly locations. Consecutive HRD maps are then overlapped at the hourly locations and linearly interpolated. The hourly maps are then merged with NCEP wind using a weight that retains the HRD data within a circle of radius = 0.8 × side of the box (i.e., ≈ 400 km), and that smoothly (using a tanh function) merges the HRD and NCEP winds beyond that radius. Animations of both the HRD and HRD/NCEP merged winds are posted on our web site: http://www.aos.princeton.edu/WWWPUBLIC/PROFS/. Figure 1.3 shows the merged winds for Katrina (August 24-29, 2005).

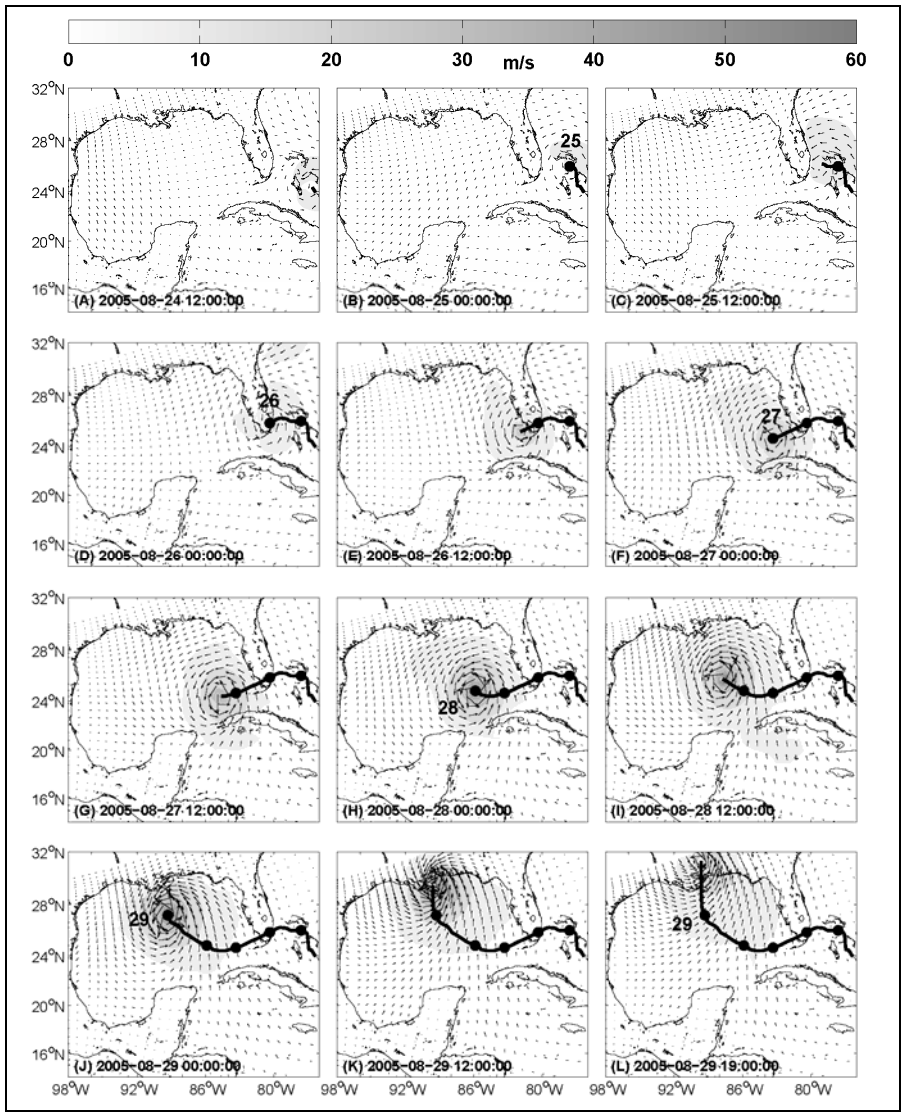

Figure 1.3. Twelve hourly plots of HRD/NCEP winds showing the path of Hurricane Katrina from (A) August 24 at 12:00 GMT through (K) August 29 at 12:00 GMT, 2005. The last panel (L) is for August 29 at 19:00 GMT. Dots indicate daily locations of the storm's eye.

To calculate wind stresses, we use a bulk formula with a high wind-speed limited drag coefficient that fits data for low-to-moderate winds (Large and Pond, 1981) and data for high wind speeds (Powell et al. 2003), as given in Oey et al. (2006):

$$
\begin{aligned}
C_d \times 10^3 &= 1.2, && |\mathbf{u_a}| \le 11 \text{ m s}^{-1};\\
&= 0.49 + 0.065\,|\mathbf{u_a}|, && 11 < |\mathbf{u_a}| \le 19 \text{ m s}^{-1};\\
&= 1.364 + 0.0234\,|\mathbf{u_a}| - 0.00023158\,|\mathbf{u_a}|^2, && 19 < |\mathbf{u_a}| \le 100 \text{ m s}^{-1} \quad (1)
\end{aligned}
$$

where $|\mathbf{u_a}|$ is the wind speed.[2] According to this formula, C_d is constant at low winds, is linearly increasing for moderate winds, reaches a broad maximum for hurricane-force winds, $|\mathbf{u_a}| \approx$ 30~50 m s^{-1}, and then decreases slightly for extreme winds. Donelan et al. (2004) suggest that the C_d-leveling at high wind may be caused by flow separation from steep waves. Moon et al. (2004) found that C_d decreases for younger waves that predominate in hurricane-forced wave fields. Bye and Jenkins (2006) attribute the broad C_d-maximum to the effect of spray, which flattens the sea surface by transferring energy to longer wavelengths.

Data Assimilation and Control Analysis (ConA)

We assimilate satellite SSHA ($\delta\eta_o$, from AVISO, www.aviso.oceanobs.com; Ducet et al. 2000) and SST (from the United States GODAE, www.usgodae.org) to derive ConA to initialize the model forecast. Satellite data are assimilated into the model following the methodology given in Mellor and Ezer (1991) and Ezer and Mellor (1994). In this method, SSHA is projected into the subsurface temperature field using pre-computed correlation factors derived from a long-time (≈ 10 years) prognostic integration that has yielded a statistical equilibrium eddy field. Thus the resulting temperature anomaly (δT) is (<.> is time-averaging, and T is the potential temperature):

$$\delta T(x,y,z,t) = F_T(x,y,z)\, \delta\eta_o(x,y,t), \tag{2}$$

where the correlation factor is ($\delta\eta$ = model SSHA)

$$F_T = <\delta T\, \delta\eta>/<\delta\eta^2>, \tag{3a}$$

and the corresponding correlation coefficient is

$$C_T = <\delta T\, \delta\eta>/(<\delta T^2><\delta\eta^2>)^{1/2}. \tag{3b}$$

Ezer and Mellor (1994) assimilate along-track $\delta\eta_o$ data assuming a linear-saturation error growth model for the first-guess error. Our experience has been that if AVISO $\delta\eta_o$ maps are assimilated the following simplified formula (see Wang et al. 2003) suffices:

$$T^a = T + (2\, R_A C_T^2/(1 + 2\, R_A C_T^2 - C_T^2))\, (T_O - T) \tag{4}$$

where T is the model (first-guess) temperature, T^a denotes the analysis temperature, R_A is the ratio of the assimilated time step Δt_A to the de-correlation time scale Δt_E of the model eddy field, and T_O is the 'observed' temperature inferred from (2),

$$T_O = <T> + F_T\, \delta\eta_o. \tag{5}$$

Instead of using the model mean for <T> in (5), our past experience has been that setting $<T> = T_C$, the observed temperature climatology, helps to control long-term (~ 10 years) drift in the model. For the present application, the differences are small. Formula (4) assumes that the

[2] In Oey et al. (2006), the coefficient for $|\boldsymbol{u_a}|^2$ was erroneously rounded off to *0.0002*.

AVISO map errors are small compared to the model errors, and that $\Delta t_A << \Delta t_E$. We follow Ezer and Mellor (1994) and set Δt_A = 1 day. The Δt_E is estimated from the above-mentioned 10-year prognostic model run and is ≈ 30 days in regions of the Gulf of Mexico dominated by the Loop Current and rings. This may be compared with the value of 20 days used by Ezer and Mellor's (1994) for the Gulf Stream which therefore appears to have shorter meander and eddy evolution time scales. The Δt_E is also proportional to the time scale of the model error growth, and the 30-day value is consistent with Oey et al.'s (2005b) findings of predictability time scales of about one month for the Loop Current and its associated rings. As pointed out by Ezer and Mellor (1994), the assimilation (4) is such that $T^a \approx T_O$ in regions where the correlation is high ($C_T^2 \approx 1$), but $T^a \approx T$ where the correlation is low. A similar assimilation of SST is also carried out after (4) with C_T and F_T replaced by the corresponding functions that use δ(SST) in place of $\delta\eta$ in (3). The SSHA and SST assimilations complement each other: SSHA assimilation is most effective over deep waters (for isobath > 500 m) while SST assimilation influences waters on shallow shelves. For more details see Wang et al. (2003), Fan et al. (2004), and Oey et al. (2005b).

Using the assimilation procedure above, we produce daily ConA fields from May/26 through Nov/17, 2005.

Control (Unperturbed) Forecasts (ConF)

We define ConF to be a model run that is free from any data assimilation and that is initialized from a ConA field. Two 8-week forecasts, July 21-September 15 and July 28-September 22, 2005 are conducted to cover different periods for comparison with observations (below). The two runs give similar results during their overlapped period. These initial dates are about one month prior to the date when Katrina made landfall in the northeastern Gulf of Mexico on August 29, 2005. The same forecast periods are used for the ensemble forecast experiments, described next.

1.3. THE BREEDING METHOD AND BRED-ENSEMBLE FORECAST (BENF)

Toth and Kalnay (1993, 1997; see also Chapter 6 of Kalnay, 2003) develop the breeding method and describe its application to atmospheric ensemble forecasting. We outline their ideas modified for the present oceanic application; readers should consult their works for details. Leith (1974) showed that in a perfect model environment averaging the ensemble forecasts yields a mean forecast superior (in the sense of smaller RMS error) to the control forecast, provided that the ensemble perturbations are representative of the span of possible errors in the initial analysis (ConA). The ConA contains, in addition to the random observational errors, growing errors associated with the instabilities of the evolving flow. This is because for the first guess the analysis repeatedly uses the model forecast ("T" in equation 4), which after some time diverges from the analysis (an approximation of the true state) (Lorenz, 1963; 1965; 1993). In other words, forecast errors are dominated by the fastest growing ones due to flow instability (Lorenz, 1965). These dominant errors are called "singular modes" in modern terminology (Kalnay, 2003, Chapter 6). At each analysis cycle, the errors are reduced in size because of new observations, but are not eliminated. These dynamically developed errors are therefore present at the next analysis cycle ready to amplify again, i.e., they represent the uncertainty in ConA. The breeding method mimics the analysis cycle and generates perturbations along the initial error pattern as in the following descriptions.

Let the daily analysis at time "n" (the n^{th} day) of the state vector "T" (e.g., T = the grid-point temperatures) be $T^a(n)$, n = 0, 1, 2, … K×N, where n = 0 is some (reference) past time, K is an integer that denotes the total number of breeding cycles (see below), and N is the number of days per cycle; thus the time t = K×N days will be the forecast start time. The goal is to generate an ensemble of perturbed state vectors $T_m(n=K\times N)$, m = 1, 2, … M, that contain the aforementioned fast growing modes, and that are then used as initial conditions for ensemble forecasts. Here, M = total number of ensemble members used, superscripts "a" and "f" (see below) denote analysis and forecast respectively, and the subscript "m" indicates a perturbed variable as well as the m^{th} member of the ensemble; also, time dependence only is indicated inside the parentheses following a variable, the spatial dependence is omitted. The method consists of the following steps (Figure 1.4):

(a) At time t = 0 (= n), add a small arbitrary perturbation $\varepsilon_m(0)$ to $T^a(0)$: $T_m(0) = T^a(0) + \varepsilon_m(0)$, m = 1, 2, … M, to form M perturbed analyses. Then integrate the model forward without data assimilation (i.e., forecast) for N days using the perturbed and unperturbed analyses, $T_m(0)$ and $T^a(0)$ respectively (k = 1 in Figure 1.4). Denote the resulting M perturbed forecasts by $T^f_m(N)$, m = 1, 2, … M, and the single unperturbed forecast as $T^f(N)$. Note that $T^f(N)$ is just ConF at time "N;"

(b) Subtract the unperturbed forecast $T^f(N)$ from each of the M perturbed forecasts $T^f_m(N)$, to obtain M perturbation vectors at time N: $\varepsilon_m(N) = c_m(N)(T^f_m(N) - T^f(N))$, where for each m the $c_m(N)$ is a factor that scales the RMS of $\varepsilon_m(N)$ over the phase space to equal the initial RMS of $\varepsilon_m(0)$ (this initial RMS will be set to be the same constant for all M members). Here, by phase space we mean the grid points where the initial perturbations in step (a) are introduced. Form the new perturbed analysis vectors at time N: $T_m(N) = T^a(N) + \varepsilon_m(N)$, m = 1, 2, … M;

(c) Integrate the model forward (without data assimilation) to the next N days from n = N through n = 2N using the perturbed and control analyses at time N obtained from step (b), $T_m(N)$ and $T^a(N)$ respectively (in Figure 1.4, increase k by 1, i.e., k becomes 2, and loop back). The resulting M perturbed forecasts are $T^f_m(2N)$, m = 1, 2, … M, and the unperturbed forecast is $T^f(2N)$.

Steps (b) and (c) are repeated to obtain at t = KN days the unperturbed vector $T^f(KN)$, all M members of the perturbed vectors $T^f_m(KN)$, hence the scaled perturbations $\varepsilon_m(KN)$, and finally the control and perturbed analysis vectors $T^a(KN)$ and $T_m(KN)$, respectively (last loop in Figure 1.4, with k = K). Toth and Kalnay (1997) argue that after the breeding cycle the perturbed analysis vectors $T_m(KN)$ are dominated by growing modes each of which is a combination of the fastest-growing singular modes of the nonlinear system; in other words, the ensemble perturbations $\varepsilon_m(KN)$ are contained in the subspace of the probability distribution of the ocean state about our best estimate $T^a(KN)$. The authors show that the breeding method gives ensemble mean that is superior to randomly generated ensemble forecasts. Their results agree with Ehrendorfer and Tribbia (1997) who found that the fastest growing combinations of possible analysis errors give the best results as initial ensemble perturbations for at least the short-range forecasts.

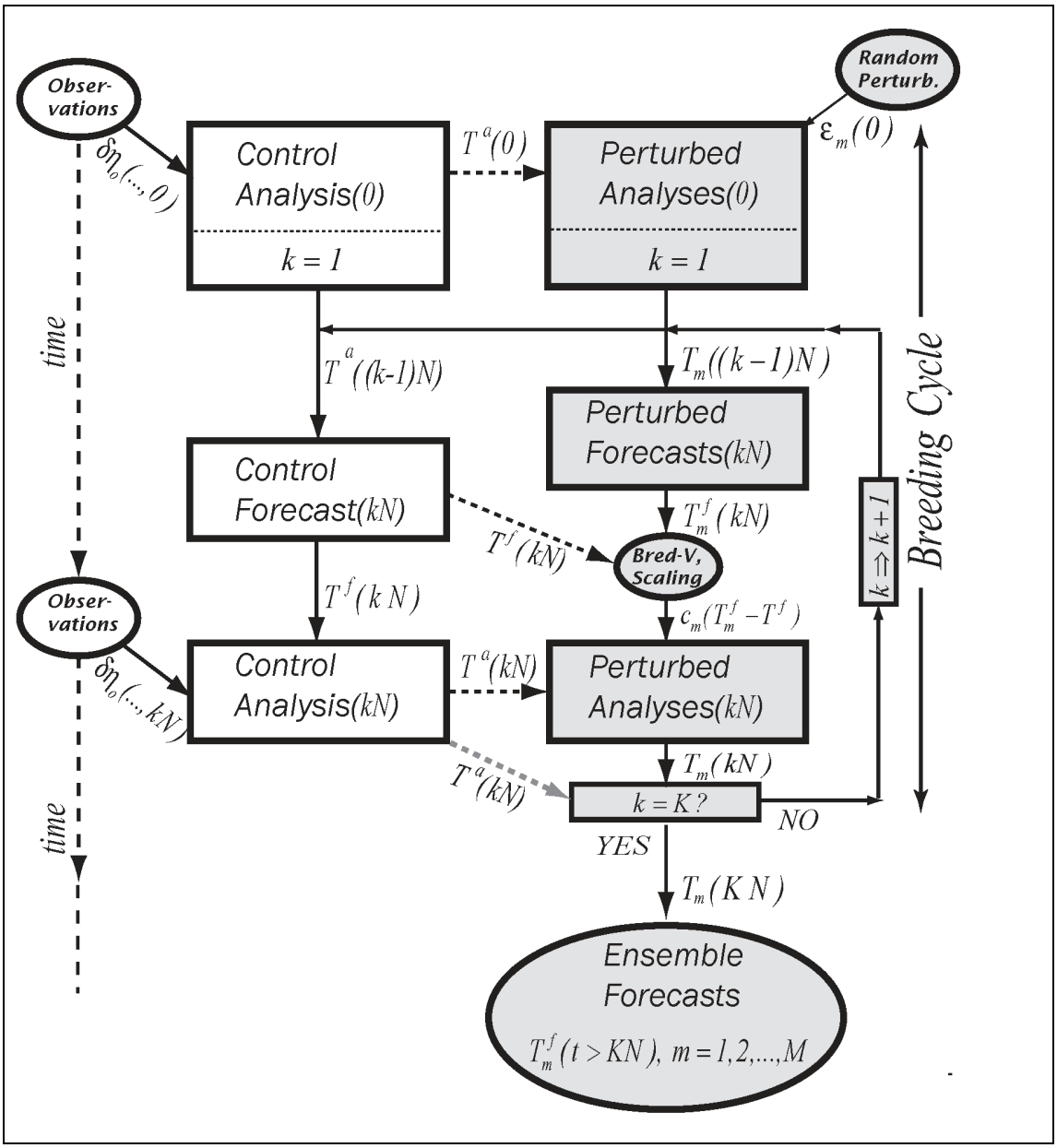

Figure 1.4. A flow chart that describes the breeding cycle and ensemble forecasting. The flow diagram shown on the left-hand side is the conventional analysis-and-forecast cycle. The breeding cycle of ensemble forecasting is indicated by shaded flow boxes and ellipses on the right.

The growing modes can be seen in plots of the bred vectors **BV** = $T^f_m(n)-T^f(n)$, i.e., the difference between perturbed and unperturbed forecasts (Yang et al. 2006). For example, Figure 1.5a shows spatial contours for **BV** member#12, and Figure 1.5b (upper panel) shows temporal evolutions of spatially-averaged amplitudes ("A_m") for different members. In these calculations, N = 7 (7-day breeding cycle) and K = 10 (total of 10 cycles). The growth rate (GR_k) for the k^{th}-cycle in the lower panel of Figure 1.5b is defined as $GR_k = \ln(A_m(kN)/A_m((k-1)N))/N$, k = 1, 2, …, K. The **BV** in Figure 1.5a is near the peak-growth of the breeding cycle (i.e., k = 7, Figure 1.5b); other members show similar patterns of cyclones and anticyclones (c.f. Yang et al. 2006).

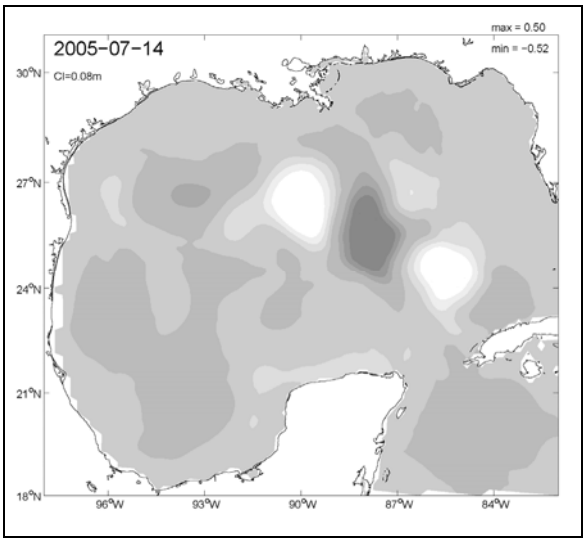

Figure 1.5a. Example of a bred vector (member#12) in terms of sea-surface height at July 14, 2005 near the peak of its growth (see next figure). Darkest shade $\geq$ +0.4 m and lightest shade $\leq$ –0.4 m.

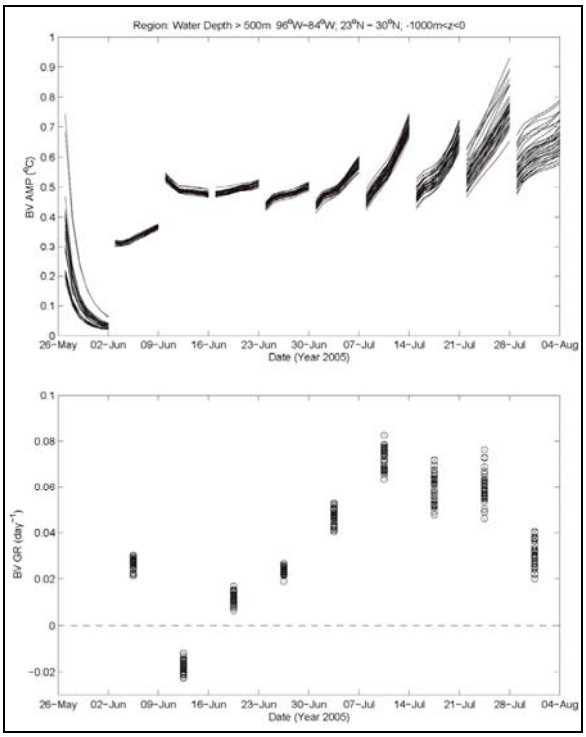

Figure 1.5b. Bred vector amplitudes in terms of temperature averaged over the indicated region (upper panel) and the corresponding growth rate (lower panel) for 10 breeding cycles each of 7 days.

The initial patterns in step (a) above consist of random fields (specified; see below) which decay during the first cycle (Figure 1.5b). Following each breeding cycle, the cyclonic-anticyclonic patterns of Figure 1.5a grow, and they mature after the 6~7th cycle shown. The organized structures have large amplitudes in the vicinity of the Loop Current and rings; they have wavelengths of approximately 200~300 km and $GR_k \approx 0.04$~0.08 day^{-1}. The wavelengths and growth rates strongly indicate that they are baroclinic instability mode of the system.

Bred-Ensemble Forecast

Based on an examination of the bred vectors (e.g., Figure 1.5), we choose N = 7 (7-day breeding cycle), K = 8 (total of 8 cycles), and M = 20 (20 ensemble members). The bred vectors achieve near-maximum growths in about 8 breeding cycles (Figure 1.5b) and the time scales are consistent with typical estimates for baroclinically unstable waves in the ocean, about 10 days or less (Wang, 1993). We have also tested M = 10, 30 and 50, and found little differences in the ensemble means when M ≈ 20 or greater. Since our analysis scheme (see above section for ConA) calculates $T^a(n)$ by assimilating $\delta\eta_o$ from satellite, we follow Miyazawa et al. (2005; who also use a similar scheme based on Mellor and Ezer, 1991) and replace in steps (a)-(c) above the $T^f_m(n)$ by $F_T\delta\eta^f_m(n)$, and the $T^f(n)$ by $F_T\delta\eta^f(n)$, where F_T is given by (3a) and $\delta\eta^f_m(n)$ and $\delta\eta^f(n)$ are respectively the perturbed and unperturbed forecast SSHA's at the nth day. However, $T^f_m(n)$ and $T^f(n)$ are available at each n, and future work may test the option of directly using them. For the RMS of $\varepsilon_m(0)$, it should be large enough to excite linear instability, but not too large that the perturbations lead to solutions that are saturated with finite-amplitude waves, since that would defeat our objective of breeding the growing modes. Kalnay (2006, personal communication) recommended a value ≈< 10% of the magnitude of the state-vector, and we use RMS($\varepsilon_m(0)$) = 0.07 m (|SSHA| ≈ 1 m). As in Miyazawa et al. (2005), we also specify the initial random perturbation (i.e., $\varepsilon_m(0)$) using Evensen's (1994) pseudo random field with a horizontal correlation scale of 0.7^o. Toth and Kalnay's (1993) experience and the **BV** plots shown in Figure 1.5 suggest however that the particular details of $\varepsilon_m(0)$ is not crucial. Also, when computing the bred vector in step "b" above, Miyazawa et al. (2005) appear to have used "the assimilation run," i.e., the SSHA that corresponds to $T^a(n)$ derived from ConA, in place of the $\delta\eta^f(n)$ we use. The difference should be small since bred vectors strongly project onto the growing modes of the analysis (Toth and Kalnay, 1997).

As in the ConF experiments, two 8-week ensemble forecasts, July 21-September 15 and July 28-September 22, 2005 are conducted to cover different periods for comparison with observations (below). The two ensemble forecasts give similar results during their overlapped period. The bred-ensemble forecast is called BEnF, the corresponding ensemble breeding is EnB (i.e., steps "a" through "c" above) and the ensemble mean forecast and breeding are EnMF and EnMB, respectively.

1.4. COMPARISONS WITH OBSERVATIONS

One way for assessing the "goodness" of a forecast is to conduct twin experiments (examples are given in Anderson et al. 1996). In such an assessment, the results from a control run are treated as "observations" which are then used to assimilate into and compared against a different run (initialized differently, say). The advantage is that we then have at our disposal "observations" of every modeled variable in the entire (model) space-time domain. The drawback is that the "observations" and model are not independent of each other. The method is

therefore well-suited for testing assimilation schemes but may not produce reliable measures of forecast skills. Another way is to compare the model (e.g., forecast) against an analysis that is the most complete, thereby treating the latter as "observations." A recent example of this approach is Miyazawa et al. (2005). However, it is clear that this way of assessment lessens but does not entirely eliminate the problem of model and observation inter-dependency. The third way is to use observations to assess the analysis or forecast (Wang et al. 2003; Kamachi et al. 2004; Oey et al. 2005a, 2006, 2007; Oke et al. 2004; Paduan and Shulman, 2005). Clearly, comparisons against observations are the ultimate way one should judge if a forecast is any good. In this section, we compare both analyses and forecasts against observations: (a) satellite SSHA; (b) NOAA drifter trajectories; and (c) ADCP measurements over the northeastern slope of the Gulf of Mexico. Figure 1.6 shows the ADCP locations.

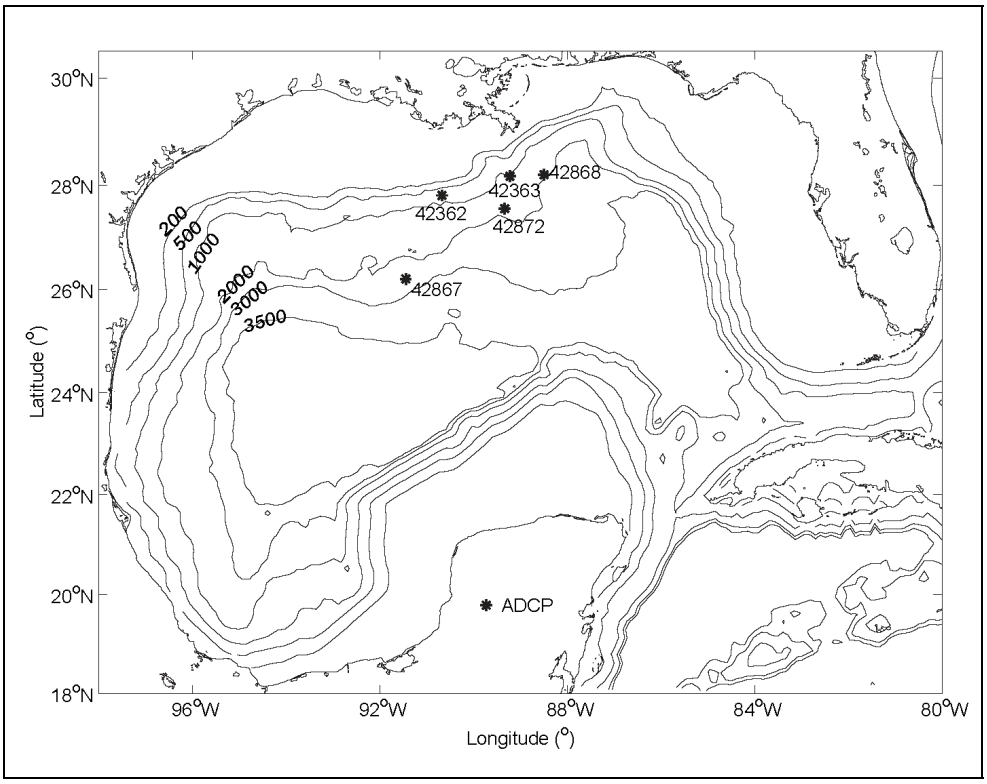

Figure 1.6. ADCP stations where model results are compared against observed currents. Contours are isobaths in meters.

Comparison Against Satellite SSH

When comparing the model results against satellite SSH, one should be mindful that the latter is not the "truth." In addition to uncertainty in the mean, satellite maps are based on objective analyses with presumed spatial and temporal scales (Ducet et al. 2000). In some cases, the model can provide more accurate information pertaining to the small and fast scales of the real ocean (Wang et al. 2003; Oey et al. 2007). Nevertheless, satellite data are suited for studying larger-scale eddies and Loop Current which are the focus of this work (e.g., Leben, 2005).

Figure 1.7 shows daily-averaged SSH plotted every week from July 07 through September 22, 2005. The background color is ConA. The SSH = 0 lines are plotted for satellite (i.e., AVISO + ten-year model mean, henceforth AVISOM; black), ConF (blue), ensemble mean (red) and ensemble members (white); the contour lines give in each case the corresponding estimates of the frontal positions of the Loop Current and rings. The track of a surface drifter is shown in green beginning at July 21. In this case, the breeding ends and hence forecasts start on July 28, 2005; the last four weeks of the 8-week breeding (Figures 7A-D) and the entire 8-week forecast (Figure 1.7E-L) are shown. The ConA can be seen to be similar to AVISOM, though the former shows a warm ring that is nearly or already detached throughout the period shown in Figure 1.7, whereas the Loop Current in AVISOM maps appear to be on the verge of shedding a ring (e.g., Figure 1.7F,G), but did not do so until September 15~22 (Figure 1.7K,L). On the other hand, the ensemble mean agrees well with AVISOM throughout the breeding period (EnMB; through July 28, Figure 1.7A-D), and also for the first five weeks of the forecast (EnMF; July 28-September 01, Figure 1.7E-I). After September 01, the Loop current rapidly extends westward in an elongated shape (Figure 1.7I-J). Thereafter a warm ring is shed (Figure 1.7K-L), and both ConF and EnMF fail to reproduce AVISOM or the ConA. When interpreting satellite SSH, there is some uncertainty with regard to the mean. We have therefore checked the AVISOM maps against (1) SSH maps using the original AVISO mean estimated from a seven-year altimetric mean SSH, (2) the University of Colorado's (UOC) maps (http://argo.colorado.edu/~realtime/gsfcgom-real-time_ssh/) and (3) the NOAA/AOML maps (http://www.aoml.noaa.gov/phod/dataphod/work/trinanes/INTERFACE/index) using different model means. These various maps yield similar results. Most of the differences occur during the first 8~9 weeks (July 07~September 01) shown in Figure 1.7. During that period, the NOAA/AOML and AVISO maps show a Loop Current-ring system that is either disconnected or barely connected – features that are in between AVISOM and the ConA maps of Figure 1.7, whereas in UOC maps the Loop-ring system is more smoothly connected.

During and a few days after the passage of a hurricane, the ocean surface undergoes rapid temporal and spatial changes that cannot be accurately depicted by maps such as the AVISOM (Oey et al. 2007). Nonetheless, AVISO (or other similar products) provides a yardstick to check forecast results before and (days) after the hurricane. Figure 1.7 suggests that the EnMF (red) is visually better than the ConF (blue). A more quantitative assessment is shown in Figure 1.8 which plots the correlations between various modeled and AVISO SSHA's (upper panel) over the region north of 23^{o}N and west of 84^{o}W, and where the water depths ≥ 500 m. The corresponding RMS differences ("errors"; lower panel) are also shown. The figure shows that ConA for the entire period, EnMB for the first 8 weeks and EnMF during the first 4~5 weeks of the forecast period all have relatively high correlations and small RMS errors. The ConA-AVISO correlation is approximately 0.9 during the first 6 weeks, and decreases to about 0.74 at the 9th~11th weeks before increasing again to approximately 0.85 at the end of the forecast period, a max-min range of about 0.16. At the beginning date of the forecast, July 28, the EnMB has a slightly higher correlation (about 0.05) and a lower RMS error (about 0.02 m) than the ConA. But these differences are small and statistically insignificant. Lin et al. (2006) analyzed the 1999-2000 satellite data and found that the ConA-AVISO correlation can fluctuate from low's of about 0.67 to high's of 0.9 within a 1~3-month period when the Loop Current and rings undergo rapid changes: as for example when a ring separates from the Loop Current, or when the Loop Current retracts or expands (e.g., Oey et al. 2003a and b). The standard deviation for the

period 1999-2000 is 0.18. Their results are consistent with the variation of ConA-AVISO correlation shown in Figure 1.8.

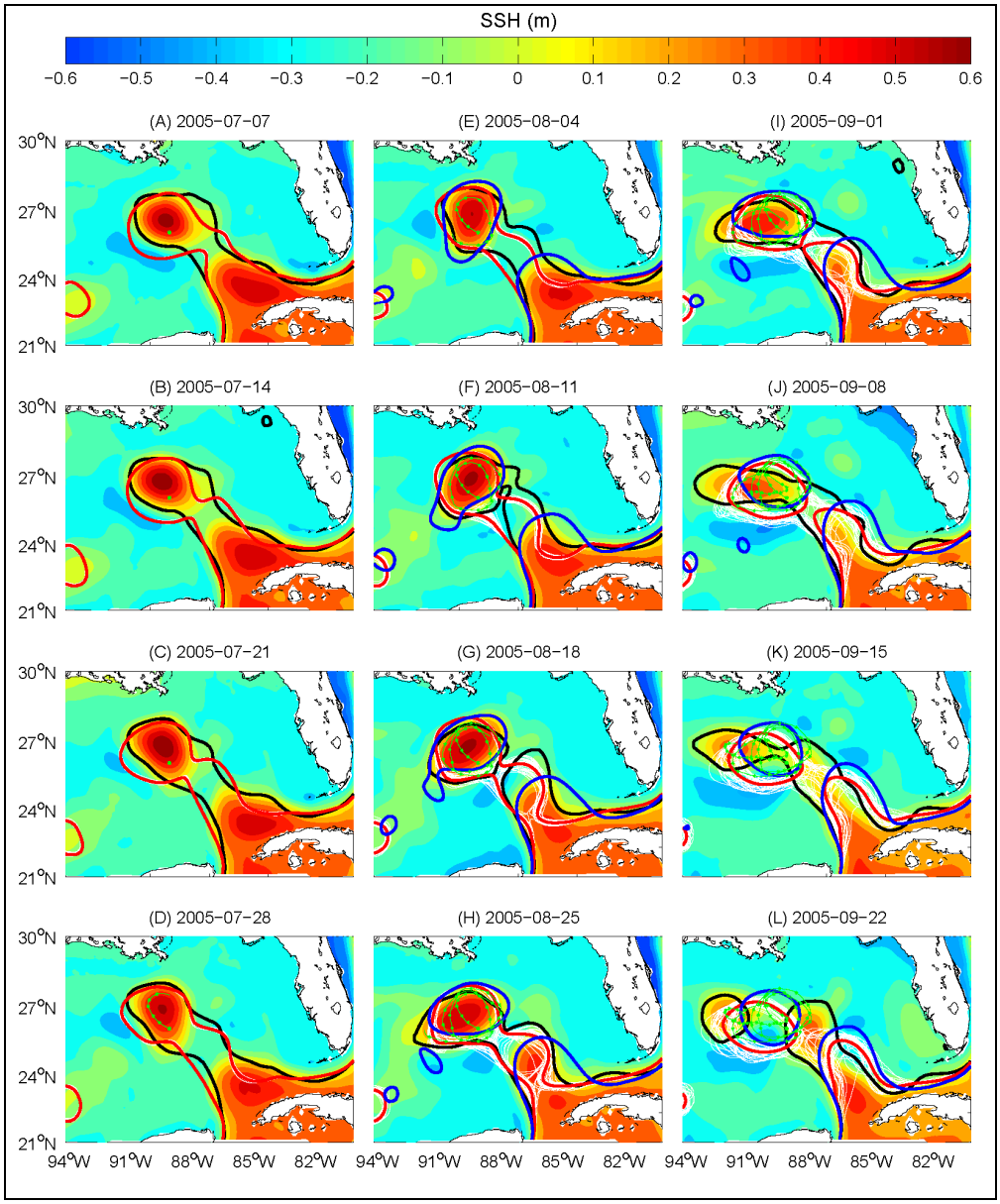

Figure 1.7. Daily-averaged SSH's shown weekly during the last 4 weeks of breeding (A-D) and 8 weeks of forecast (E-L). Background color is ConA. Lines are SSH=0 contours of: black: AVISOM; red: EnMB's (A-D) and EnMF's (E-L); white: EnB members (A-D) or BEnF members (E-L); and blue: ConF. Green line is drifter trajectory marked daily, shown from July 21.

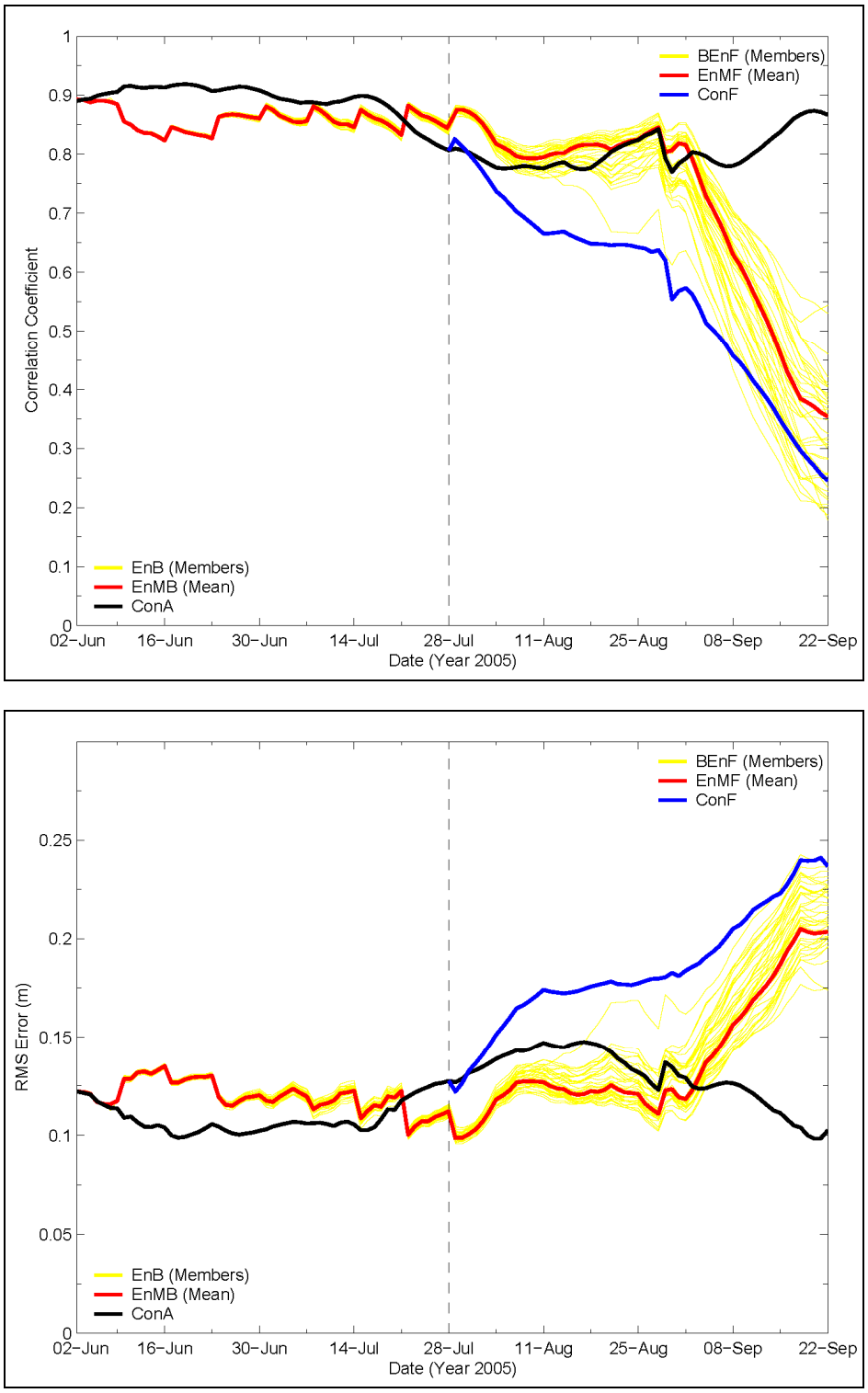

Figure 1.8. Upper panel: correlation between AVISOM and various model SSHA's as indicated for the region north of 23°N, west of 84°W and in water with depths > 500 m; lower panel: the corresponding root mean squared SSHA error. Vertical dashed line indicates the initial date of forecasts.

Fluctuations in ConA-AVISO correlation (and in the corresponding RMS error) reflect the fact that both the satellite SSHA maps and model have errors which are most pronounced during periods of large changes in the Loop Current and rings; this is indeed the case during the present study period (see Figure 1.7). The above-mentioned differences between EnMB and ConA at the initial forecast date (July 28), or indeed the differences between EnMB, ConA and EnMF during the first 12~13 weeks of the study period in Figure 1.8, are therefore statistically insignificant when compared with the variability of the errors inherent in the satellite SSHA maps and model. It is therefore significant that EnMF provides a good forecast through the time when Katrina arrived (August 25). In comparison, the quality of ConF deteriorates after only 1~2 weeks of forecast (July 28~August 11, Figure 1.8). The EnMF (and BEnF members) deteriorates after Katrina, in the final 2~3 weeks of forecast. It will be an interesting future research to study if the rapid decline in the forecast quality in these final weeks is related to the intense disturbances caused by the hurricane.

To ascertain that the above findings (that EnMF gives superior forecasts to the ConF) hold for different periods, we conducted ten additional forecast experiments, i.e., ten different samples of initial ocean states. The forecast start-dates of seven of these are successively weekly-shifted from that shown in Figure 1.8; they produce similar results as Figure 1.8 (not shown). The three others are more interesting as the start-dates: November 1, 2005, March 18, 2006, and August 25, 2006, are more widely separated, by 3~4 months. The corresponding correlations and RMS errors are shown in Figure 1.9. The EnMF can be seen to consistently outperform ConF even for the worse breeding case of Figure 1.9E and F. These findings are consistent with Leith's (1974) theoretical analysis, mentioned previously. Figures 8 and 9 show that useful forecasts of mesoscale eddies may be obtained for up to 4~6 weeks.

Comparison Against NOAA Drifter

We compare paths of modeled drifters with the trajectory of the NOAA drifter shown in Figure 1.7 for an eight-week period from July 21 through September 15, as follows (c.f. Fan et al. 2004). For each of the eight 7-day periods, a (model) drifter is released at the "day-0" position of the observed drifter, and is tracked for 7 days using Awaji et al.'s (1980) method. This gives eight sample trajectories and the corresponding deviation distances (i.e., errors) which are then averaged. Figure 1.10 plots averaged deviations for ConA, EnMF, AVISOM and ConF, and Figure 1.11 the trajectories. All four cases are similar in the first 2~3 release days, with errors for ConA and AVISOM slightly less than EnMF or ConF. At day-7, ConA produces the least error (as can be expected) while EnMF gives an improved forecast than ConF (and AVISOM). These improvements can be seen in Figure 1.11 – the EnMF (red with markers) trajectories generally follow the observed (magenta with markers) trajectories from the week-1 forecast (Figure 1.11A) through the period of Katrina (Figure 1.11F); the EnMF trajectories deviate from the observed during the 7^{th}~8^{th} weeks of the forecast (Figure 1.11G-H). In contrast, the ConF trajectories begin to deviate from the observed in the 4^{th} week (Figure 1.11D).

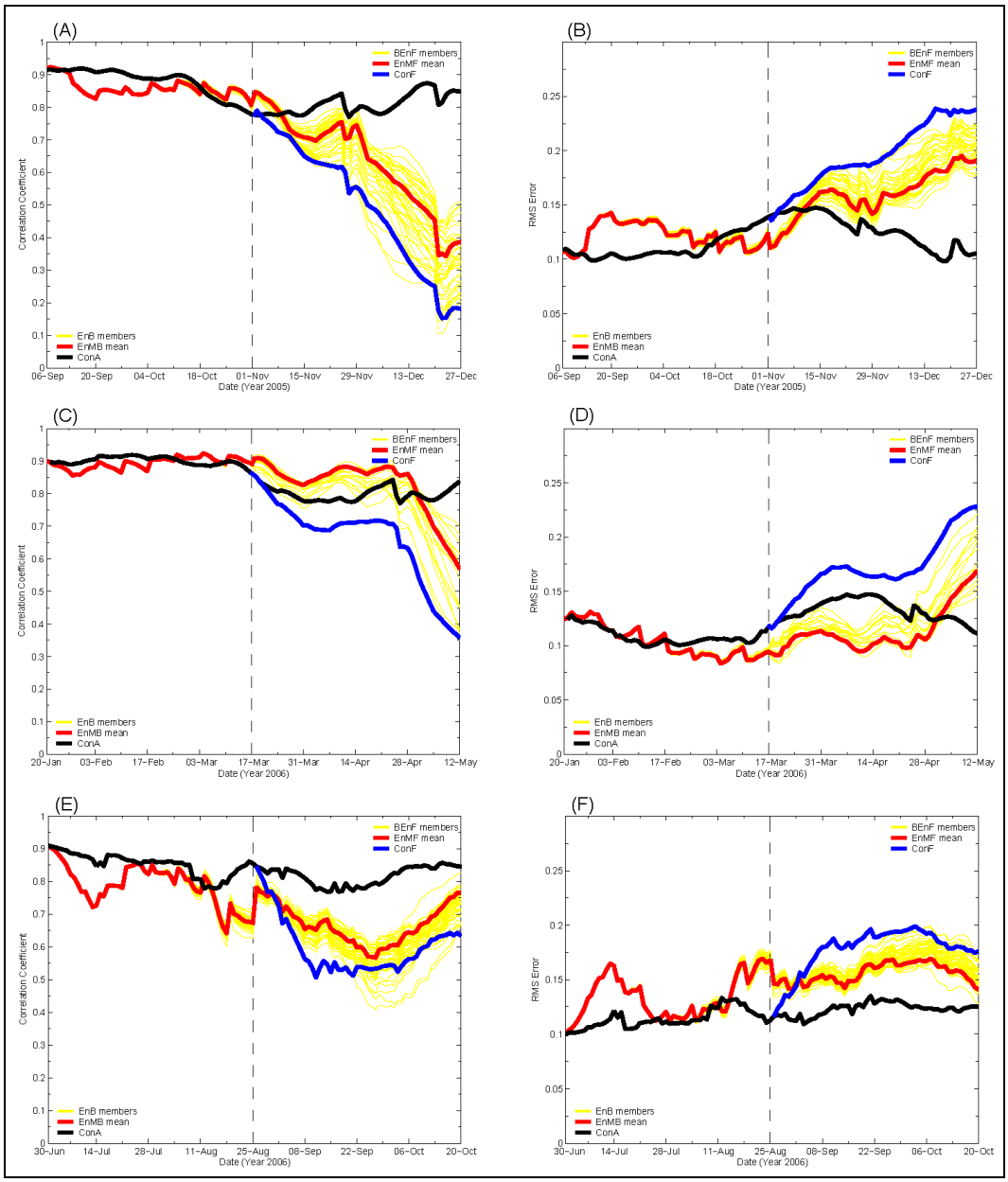

Figure 1.9. Correlation between AVISOM and model SSHA's (left panels A, C and E) and the corresponding root mean squared SSHA (right panels B, D and F), as in Figure 1.8, for three different forecast start dates: November 1, 2005 (A & B), March 17, 2006 (C & D), and August 25, 2006 (E & F).

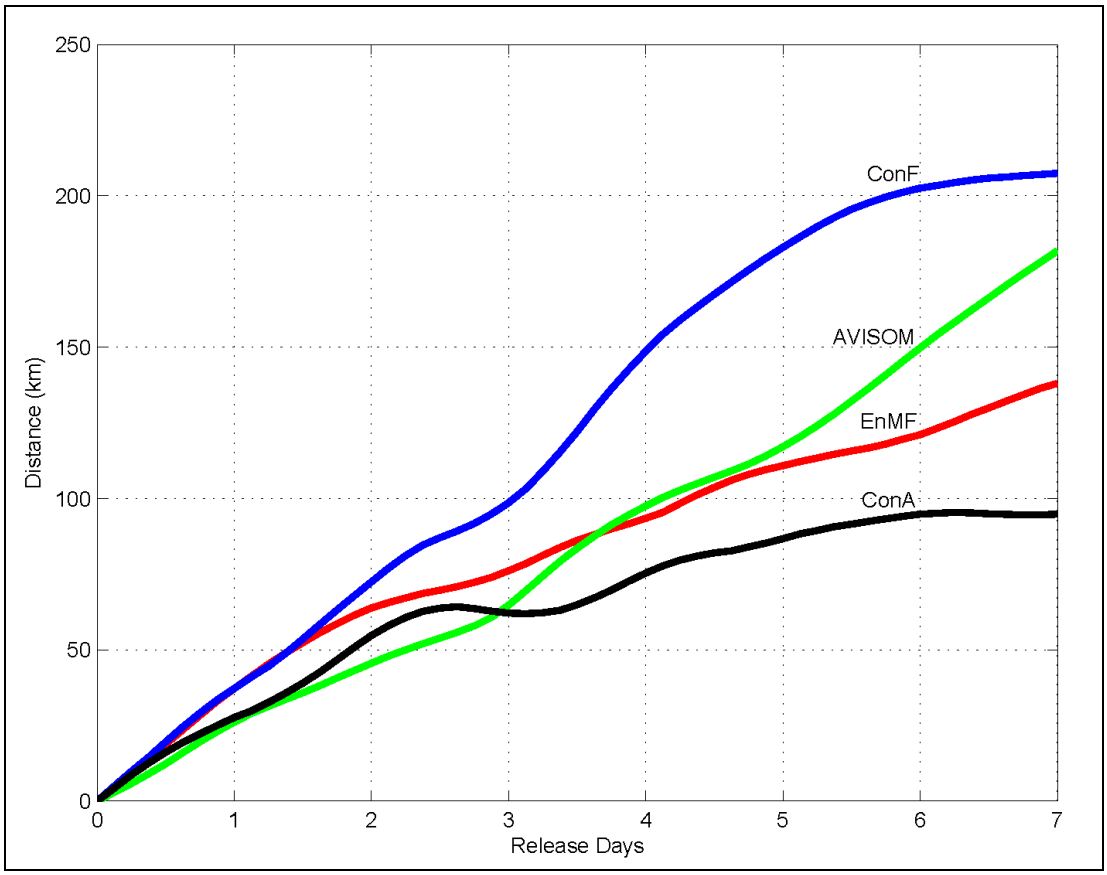

Figure 1.10. Averaged deviations of the indicated model drifter trajectories from the observed trajectory as distances in km, plotted as a function of drifter release days. The averaging is over the eight 7-day periods (or ensembles) from July 21 through September 15, 2005.

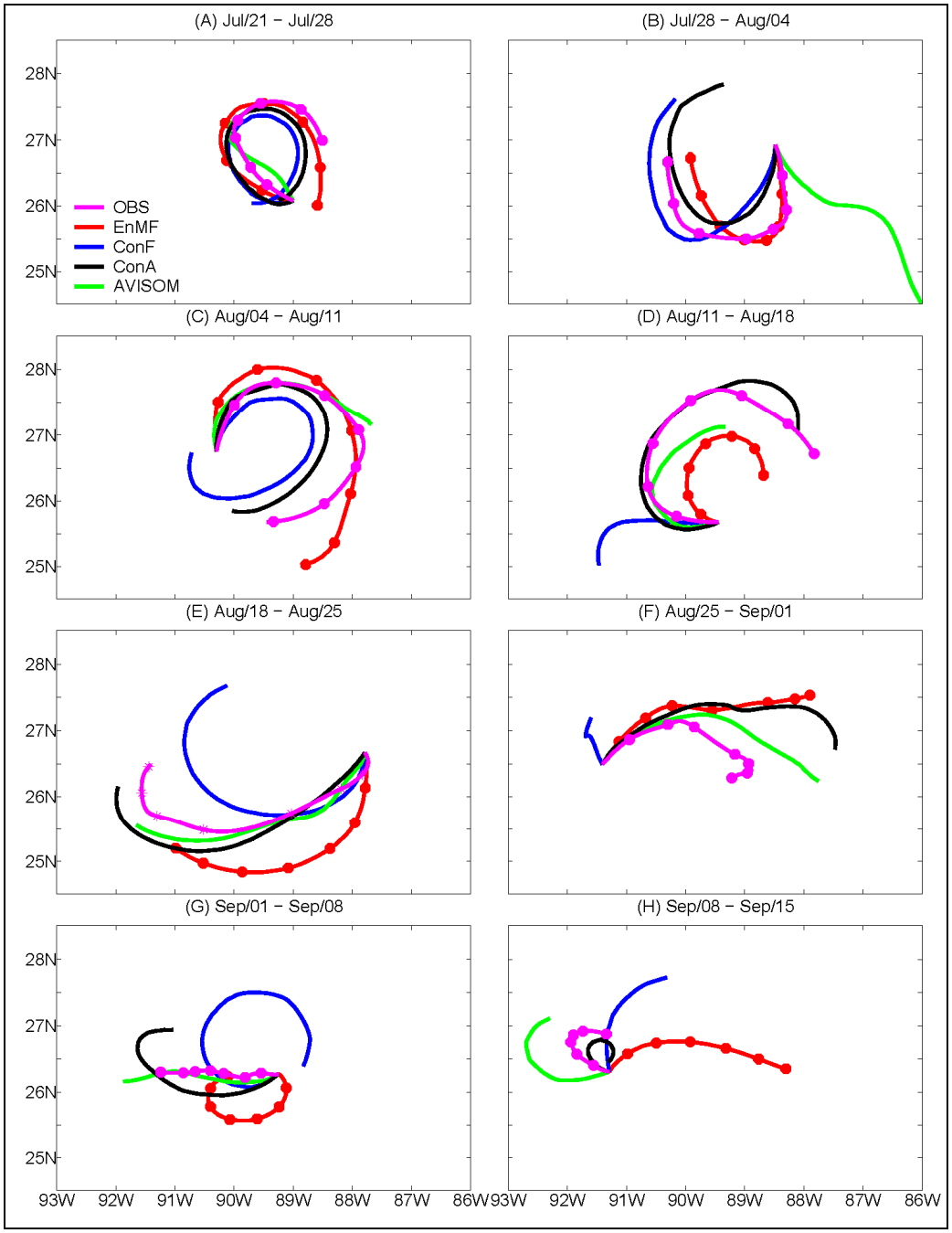

Figure 1.11. Modeled and observed drifter trajectories for each of the eight release periods from July 21 through September 15, 2005. Markers on "OBS" and "EnMF" indicate the daily positions.

Comparison Against ADCP Observations

Five ADCP time series over the northern Gulf of Mexico were available during the forecast period July 21-September 15, 2005 (Figure 1.6 shows the ADCP locations). These ADCP's were operated by the oil industry; through an arrangement with MMS and NOAA the data were

made publicly available at the NDBC site http://www.ndbc.noaa.gov/. All five ADCP's returned velocity data through August 27, 2005 just before Katrina arrived at the northern Gulf, from approximately −75 m through −1000 m at depth intervals of about 30 m. Three ADCP's (42868, 872 and 867) intermittently returned data after the storm (see Figure 1.12 below). The data were processed for obviously bad values (either discarded or linearly interpolated from neighboring good values if the gap is not too large), and daily-averaged. The modeled velocities were also daily averaged and interpolated onto the observation locations. Figure 1.12 compares the observed and forecast (EnMF and ConF) speeds as a function of time and depth.

Because of their locations, the ADCP's measured currents around the western, northwestern and northern rims of the Loop-ring system (c.f. Figure 1.7). In the upper 400 m, directions are predominantly northward, northeastward and eastward. Figure 1.12 shows observed speeds $>\approx 1$ m/s at the three northeastern stations "868," "363" and "872" (Figure 1.12a-c) closest to the Loop-ring system. At the first two stations, speeds reached a maximum around August 11, after which date the Loop-ring system began to move west-southwestward away from the moorings; at "872" currents remained strong through August 27. At the northwestern station "362" (Figure 1.12d), currents were moderately strong (0.5~0.6 m/s) at the beginning, July 21~August 04, but diminished thereafter as the Loop-ring system drifted southward. At the southwestern station "867" (Figure 1.12e), speeds did not become strong until later, around August 11~18, and also in September. The forecasts, the EnMF in particular, reproduce these gross observed features. The error plots in the lower two panels of Figure 1.12a-e show that the EnMF generally gives a more accurate depiction of the observed speeds than the ConF. The forecast vertical shears are weaker than those observed, however (e.g., stations "868" and "363," Figure 1.12a and b).

Additional measures of the forecast skill are given in Figure 1.13. In Figure 1.13a we show the complex correlations (CC's) computed in time as a function of depth, and in Figure 1.13b the complex correlations were computed in the vertical as a function of time (Kundu, 1976; see Appendix 1.1). Correlation amplitude $|CC| \approx 1$ and phase $\theta_{CC} \approx 0$ would indicate that the modeled and observed currents match closely in time (Figure 1.13a; temporal CC) or in the vertical (Figure 1.13b; vertical CC). The temporal CC's for EnMF are clearly improved over those for ConF at all stations except "872" where both show comparable values. The CC's (for EnMF) are high $>\approx 0.8$ near the surface $z >\approx -200$ m at all stations except "867" where $|CC| \approx 0.5$ and $|\theta_{CC}| \approx < 15^o$ for $z >\approx -400$ m. In particular, at station "362," $|CC| \approx 0.9$ and $|\theta_{CC}| \approx < 15^o$ throughout the water column. As plots for the individual EnF members in Figure 1.13 show, there is greater uncertainty (spread) in the forecast results deeper in the water column. The improvement in EnMF over ConF is less clear for vertical CC's (Figure 1.13b). This is because both forecasts are in general less correlated with observations at deeper levels (c.f. Figure 1.13a). Figure 1.13b shows that both forecasts have comparable CC-values. One can identify periods when $|CC| >\approx 0.7$ and $|\theta_{CC}| \approx < 25^o$ at stations "868" and "363" prior to August 18, station "872" between August 11~27 and also September 3~6, station "362" prior to August 4 and station "867" from August 14~25 and also around September 15. Forecast uncertainty in general increases with time at all stations except for the southwestern-most station "867," where the model appears to show a more consistent prediction (less spread) as the approach of the Loop-ring system at later forecast dates (August 14~25 and also around September 15).

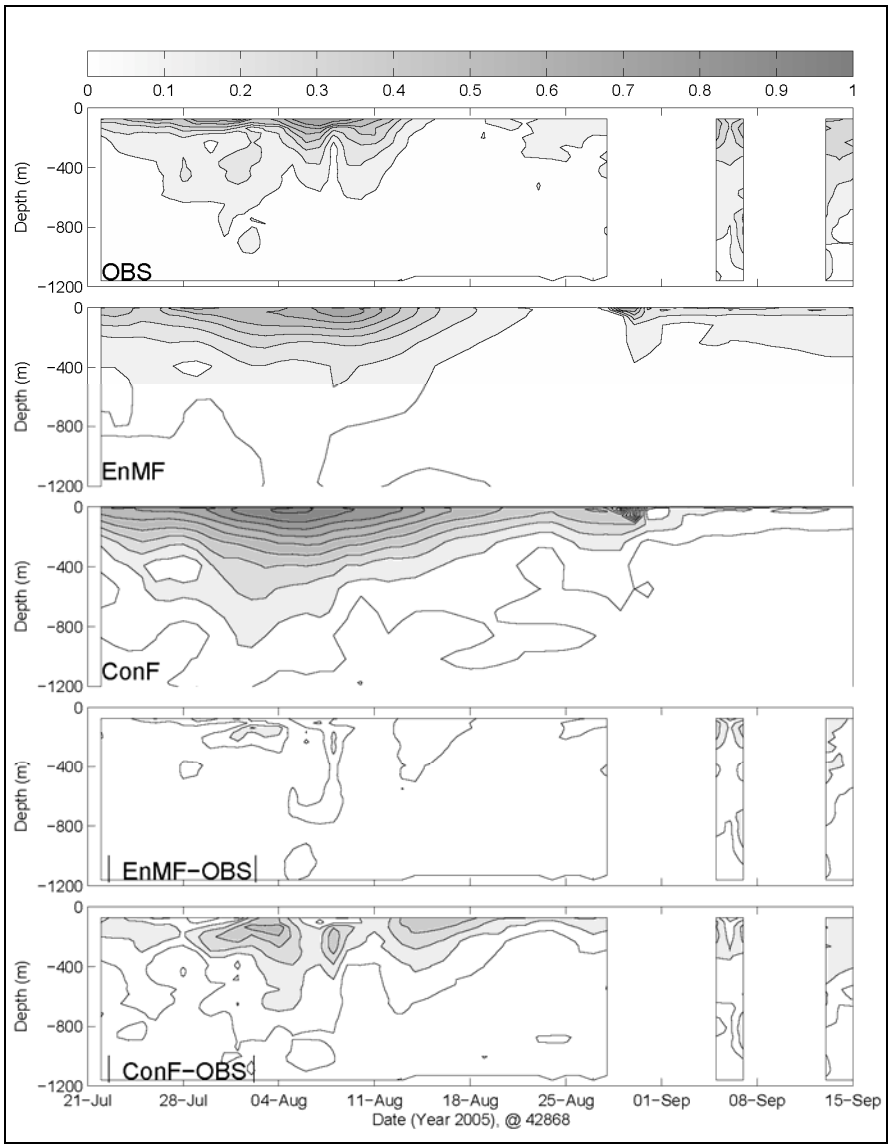

Figure 1.12a. Comparisons between modeled and observed speeds (m/s) at ADCP station 42868 for the period July 21 through September 15, 2005. From top to bottom panels: observation, EnMF, ConF, |EnMF-Obs| and |ConF-Obs|. See Figure 1.6 for ADCP locations.

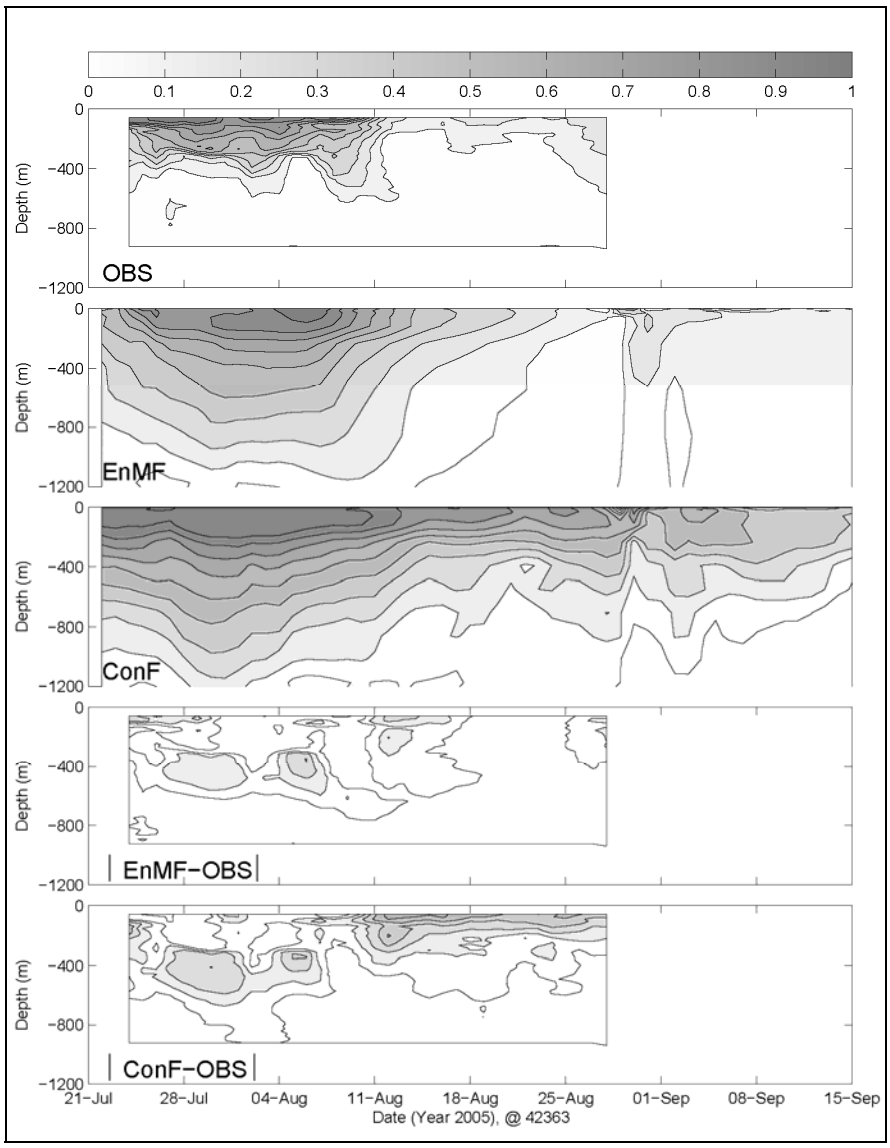

Figure 1.12b. Comparisons between modeled and observed speeds (m/s) at ADCP station 42363 for the period July 21 through September 15, 2005. From top to bottom panels: observation, EnMF, ConF, |EnMF-Obs| and |ConF-Obs|. See Figure 1.6 for ADCP locations..

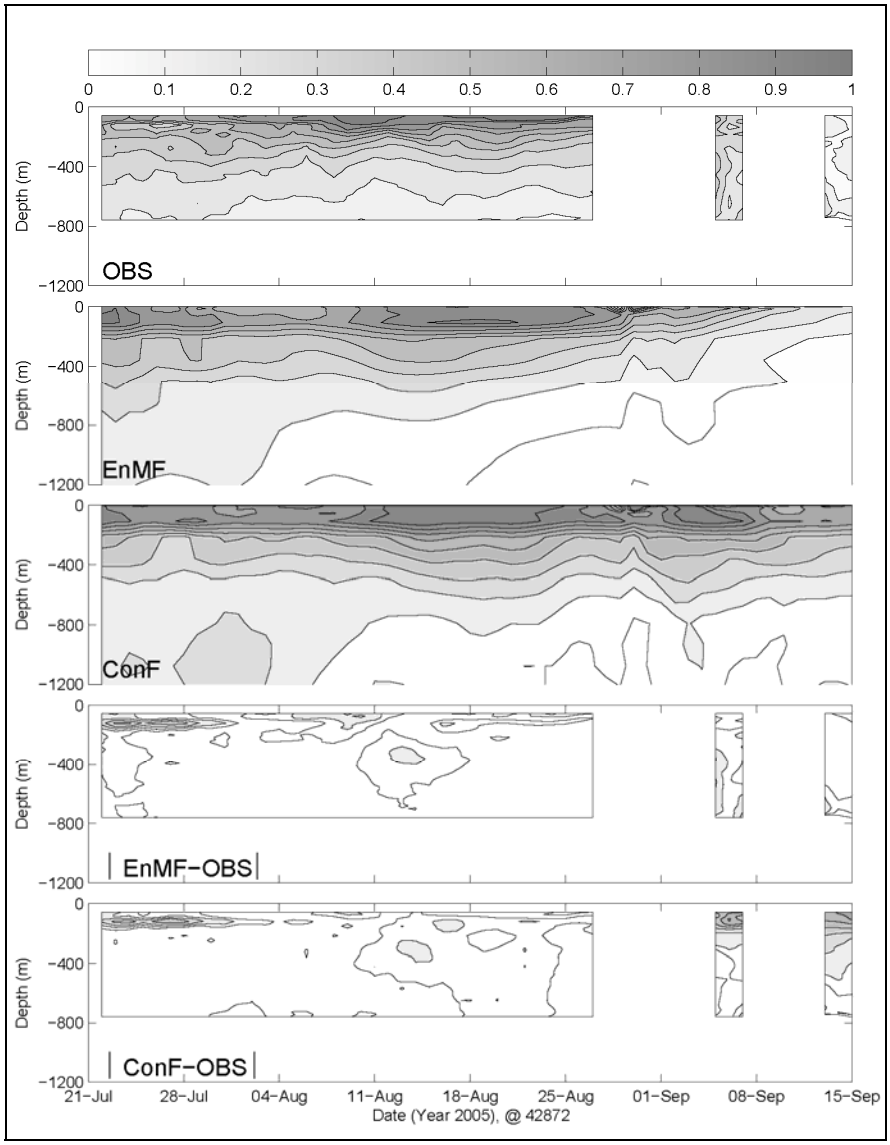

Figure 1.12c. Comparisons between modeled and observed speeds (m/s) at ADCP station 42872 for the period July 21 through September 15, 2005. From top to bottom panels: observation, EnMF, ConF, |EnMF-Obs| and |ConF-Obs|. See Figure 1.6 for ADCP locations.

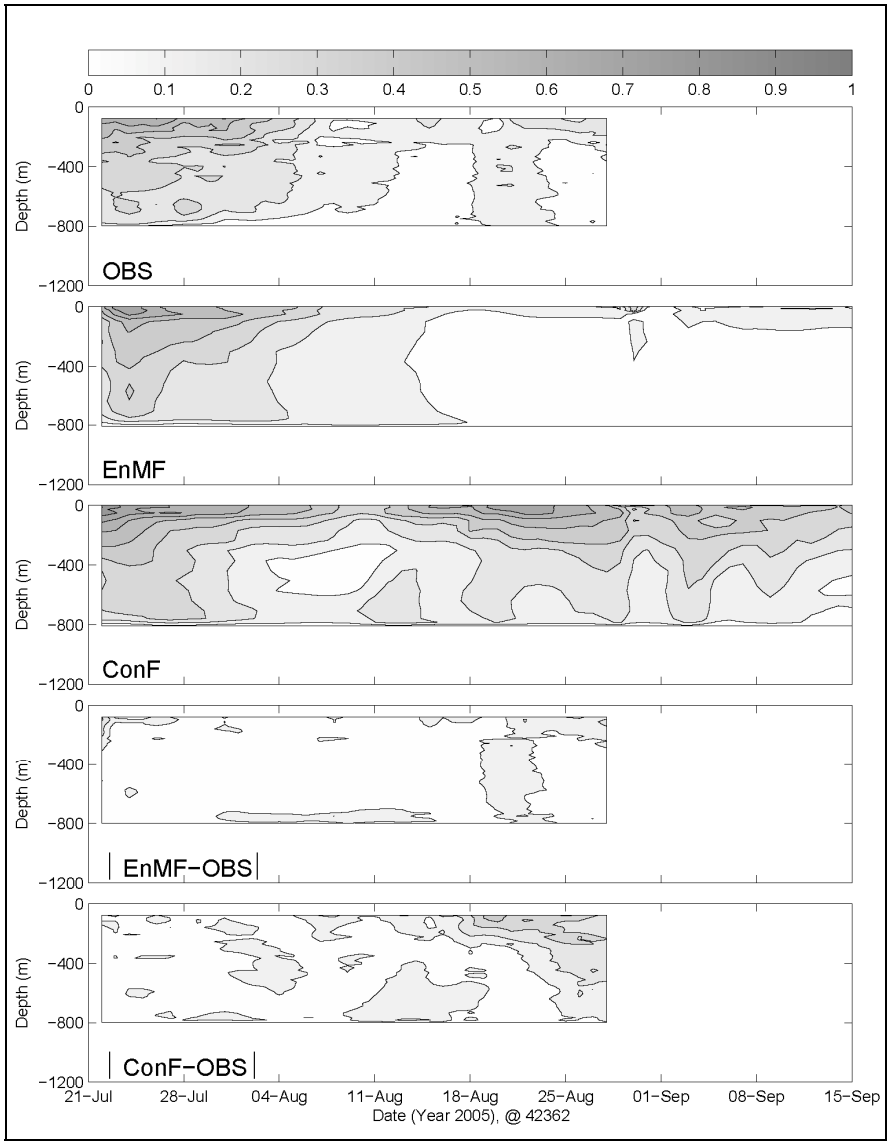

Figure 1.12d. Comparisons between modeled and observed speeds (m/s) at ADCP station 42362 for the period July 21 through September 15, 2005. From top to bottom panels: observation, EnMF, ConF, |EnMF-Obs| and |ConF-Obs|. See Figure 1.6 for ADCP locations.

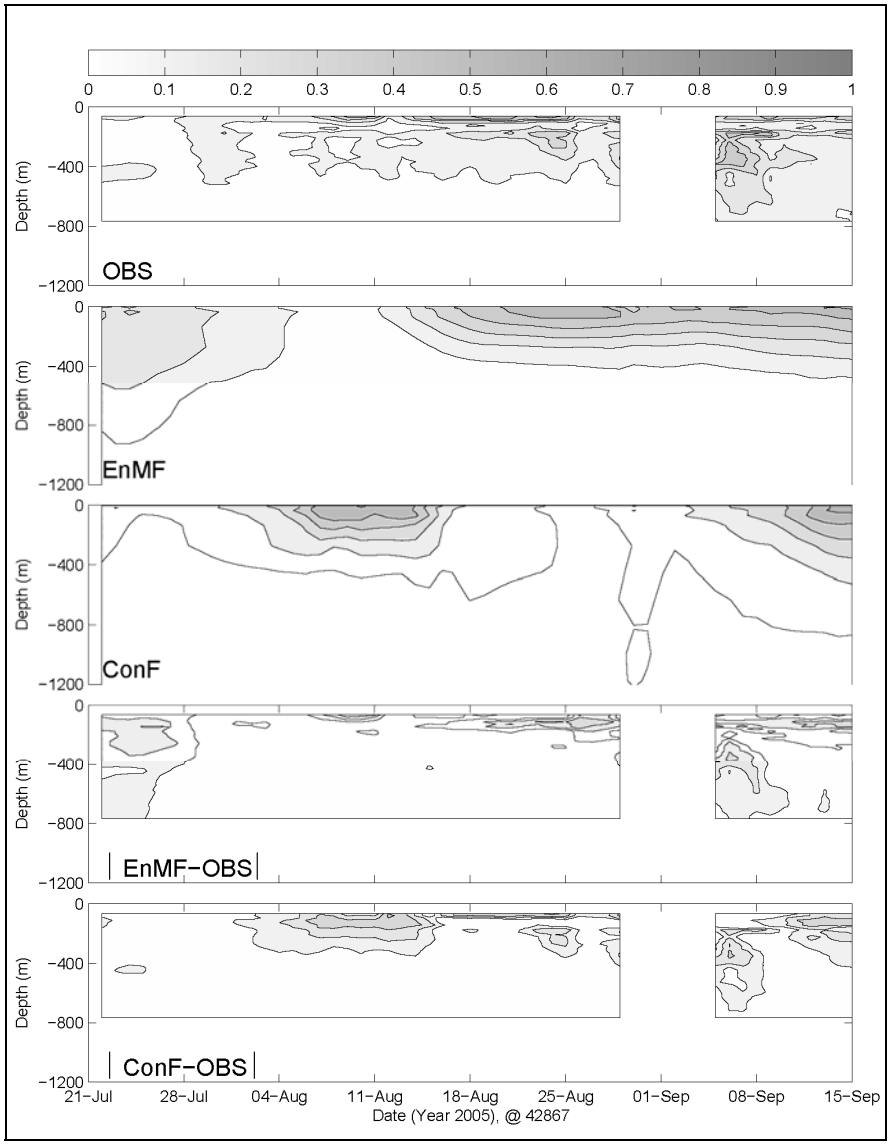

Figure 1.12e. Comparisons between modeled and observed speeds (m/s) at ADCP station 42867 for the period July 21 through September 15, 2005. From top to bottom panels: observation, EnMF, ConF, |EnMF-Obs| and |ConF-Obs|. See Figure 1.6 for ADCP locations.

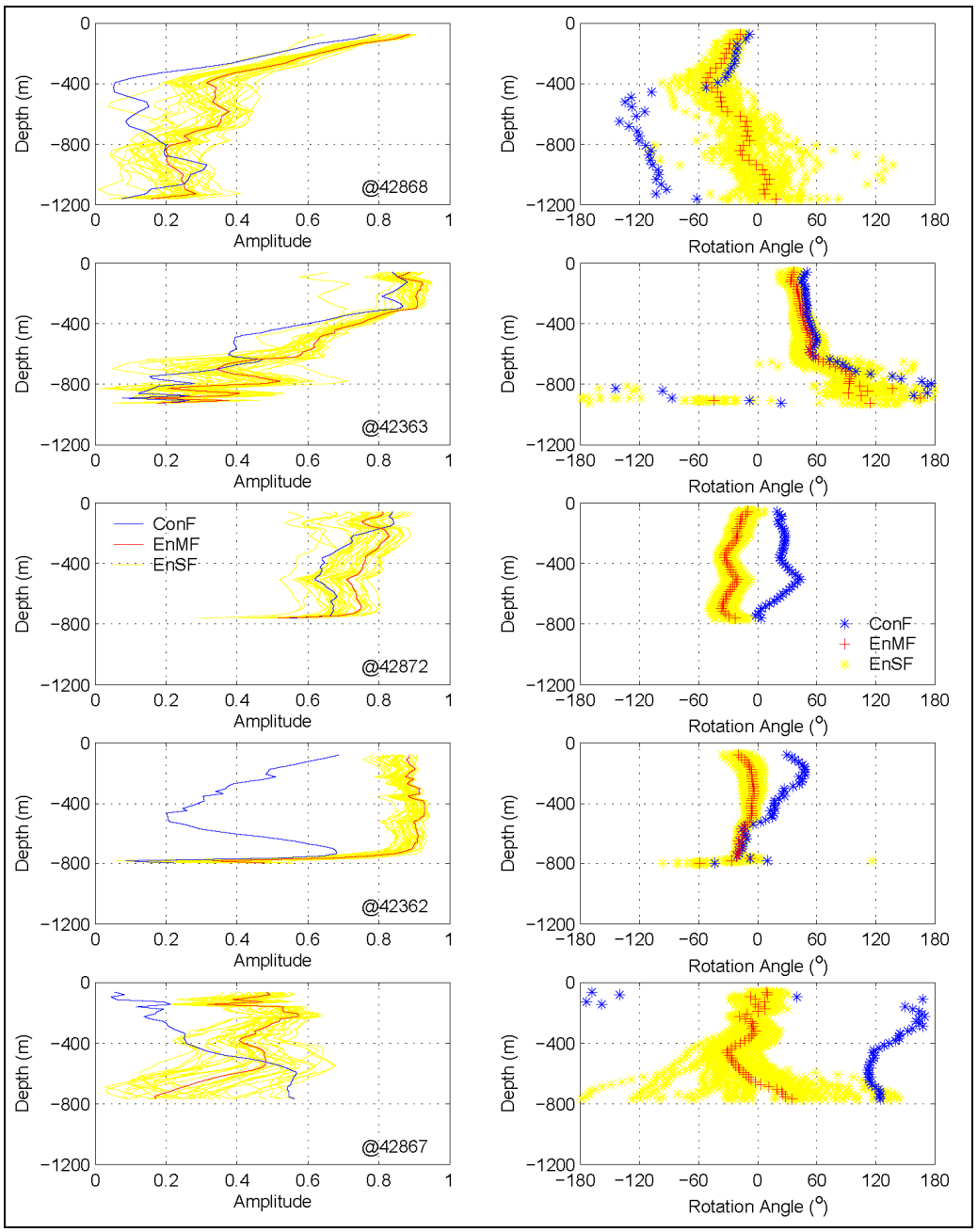

Figure 1.13a. Vector correlations of currents at the five ADCP stations with EnMF (red) and also with ConF (blue). Left column is the amplitude and right column is rotation angle (positive means model is rotated anticlockwise from observation). At each station, the correlations are computed over the time period from July 21 through September 15, 2005, then plotted as a function of depth.

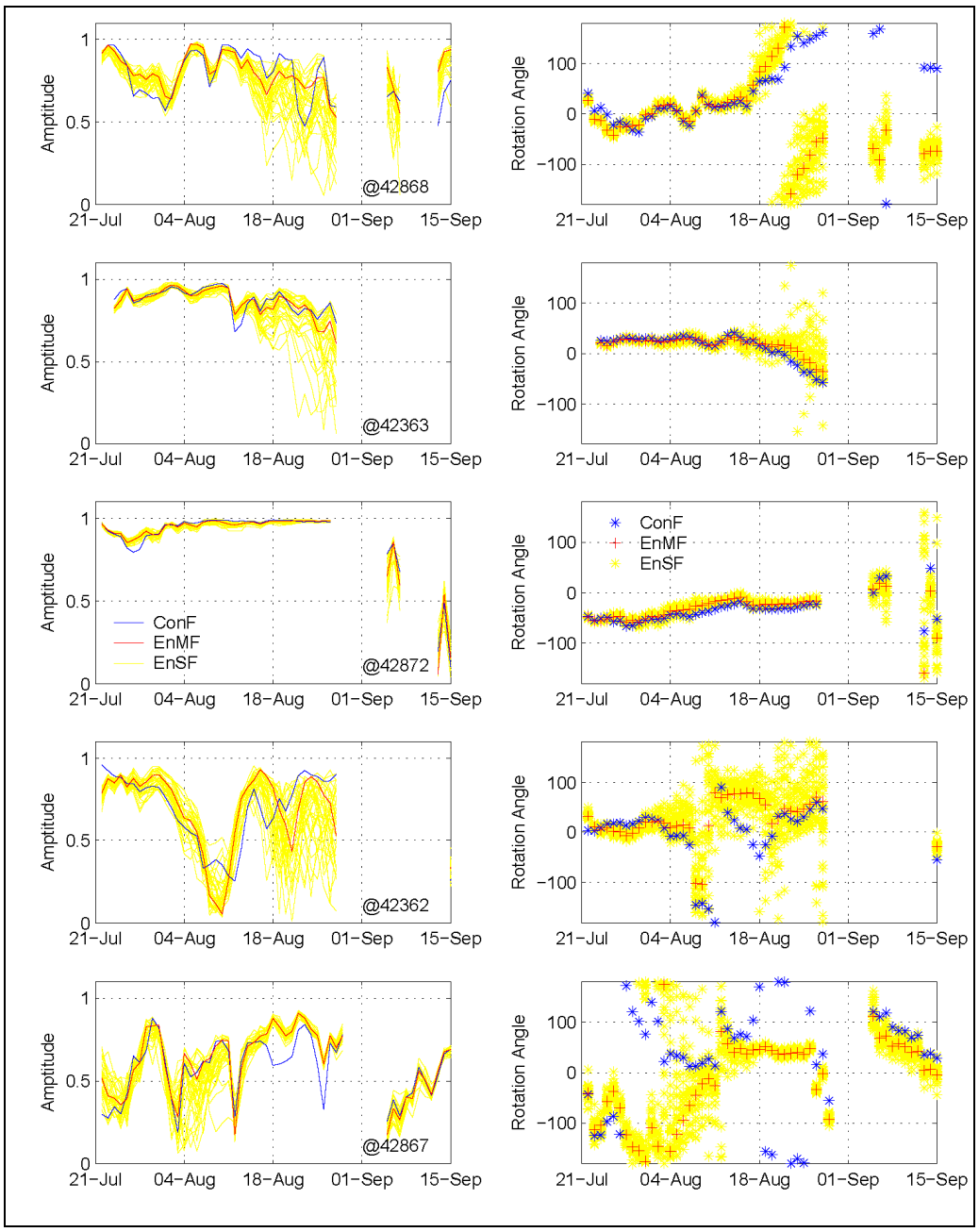

Figure 1.13b. Vector correlations of currents at the five ADCP stations with EnMF (red) and also with ConF (blue). Left column is the amplitude and right column is rotation angle (positive means model is rotated anticlockwise from observation). At each station, the vector correlations are computed over the water column (–100 m > ≈ z > ≈ –1000 m), then plotted as a function of time from July 21 through September 15, 2005.

1.5. CONCLUSIONS

This work uses the bred-ensemble forecast (BEnF) technique (Toth and Kalnay, 1993, 1997) to estimate the locations and strengths of the Loop Current and ring in Jul-September 2005, a period during which Hurricane Katrina (August 24-30) passed over the eastern and northeastern Gulf of Mexico. We show that breeding (after 7~8 cycles) produces growing modes (bred vectors) which have patterns and growth rates akin to baroclinic unstable modes in the Gulf of Mexico, with largest amplitudes in the vicinity of the Loop Current and ring. The bred vectors represent the uncertainty in our analysis (initial state). Previous atmospheric experiences indicate that the use of these bred vectors as perturbations in ensemble forecasting can improve the forecast.

To assess model skills, results from the control analysis (ConA), control forecast (ConF), and ensemble mean forecast (EnMF) are compared against observations consisting of satellite, drifter and ADCP data. The EnMF is found to be statistically indistinguishable from ConA for the first 4~5 weeks of the forecast. This is a rather surprising result though it needs to be confirmed in future studies with a large sample of forecast cases and with different models. We show that EnMF consistently produces superior forecasts to the ConF, in that the EnMF results are "closer" to the observations. Ensemble forecasting is also useful in that by examining the forecast-spread (of the Loop Current frontal positions for example) of the ensemble members, one can estimate the reliability of the forecast (it is a questionable forecast if there is too much spread; c.f. Figures 7E-H with 7I-L; also Figure 1.13a, stations 42872 and 867), as well as the forecast probability (for cases in which members are clustered in 2 or 3 distinct groups).

The implications of our results for future work follow. Firstly, the EnMF provides a viable way to more accurately estimate ocean responses to hurricanes. This is because these responses are rapid and locally intense, and data assimilation using smoothed satellite SSHA maps in ConA can produce false results (c.f. Oey et al. 2006, 2007); good BEnF during the first 4~5 weeks before the storm can provide a better alternative. Secondly, for the same reason, EnMF should provide a more accurate ocean field (which is input to wave models such as the WaveWatch-3 model or the Simulating WAves Nearshore—SWAN model) for estimating surface waves. Thirdly, the EnMF provides an alternative means by which one can more accurately estimate the locations and strengths of oceanic warm features (Loop Current and rings), which in turn may aid in hurricane predictions (DeMaria et al. 2005). Finally, bred vectors may be used to provide time-dependent error covariance to improve analyses.

CHAPTER 2. HINDCAST OF WAVES AND CURRENTS IN HURRICANE KATRINA[3]

Synopsis

Using the ocean-state analyses of Loop Current and eddies discussed in Chapter 1 as initial fields, the current and wave models are run in forecast modes using accurate high-resolution winds to assess the sea and wave states and their impacts upon the northern Gulf of Mexico during Hurricanes Katrina.

Summary of the Main Results

Hurricane Katrina caused extensive damage to offshore oil and gas production facilities. In this study, the state-of-the-art ocean circulation (Princeton Ocean Model) and surface wave (Wave Watch III) models, together with high-resolution analyzed winds from NOAA Hurricane Research Division, are used to simulate the current and wave conditions during Katrina. The model simulation shows large (maximum significant wave height ≈ 24 m) surface waves and strong (≈ 2.5 m/s) wind-driven and inertial currents superposed on the Loop Current and Loop Current Eddy. The simulated wave fields are verified with surface buoy and satellite altimetry observations; the agreement generally is better than 0.5 m and the correlation coefficient is above 0.95. Also, while the observed 55 ft significant wave heights on National Data Buoy Center (NDBC) buoy 42040 surpassed the previous record in the Gulf of Mexico, circumstantial evidence suggests that waves as large as 70 ft might have occurred in the storm path. Comparison with the operational analysis suggests that the current NCEP model system tends to underestimate spatial extent of the serious wave impact.

Methods described herein for Hurricane Katrina lay the groundwork for similar simulations and analyses for Hurricane Rita to be discussed in Chapter 3.

A Brief History of Hurricane Katrina (descriptions courtesy of NCEP)

Tropical Storm Katrina was upgraded to a hurricane status two hours before it made landfall at south Florida on August 25 at 22:30:00 GMT. Katrina weakened over land to a tropical storm, but it regained hurricane status at August 26 at 06:00:00 GMT about one hour after entering the Gulf of Mexico. Rapid intensification occurred during the first 24 hours due in part to the storm's movement over the warm Loop Current. On August 27, the storm was upgraded to Category 3 intensity. On August 28 at 12:00:00 GMT Katrina strengthening to a Category 5 storm and reached its peak at 17:00:00 GMT with maximum sustained winds of 175 mph (280 km/h) and a central pressure of 902 mbar (hPa). Katrina made landfall at 11:00:00 GMT on August 29 as a Category 3 hurricane with sustained winds of 125 mph (200 km/h) with higher gusts, near Buras-Triumph, Louisiana. At landfall, hurricane-force winds extended outward 120 miles (190 km) from the center and the storm's central pressure was 920 mbar (hPa). A few hours later, after weakening slightly, it made landfall for a third time near the Louisiana/Mississippi border with 120 mph (190 km/h) sustained winds, still a Category 3. Record storm surges smashed the entire Mississippi Gulf Coast and into Alabama, peaking at 34 feet in Bay St. Louis, Mississippi and reaching 13 feet (4 m) even as far away as Mobile,

[3] This chapter is based on Wang and Oey, 2008.

Alabama. Storm surge was high in part because of the hurricane's extreme size, and the fact that it weakened only shortly before landfall; waves were even larger as many had been generated while the storm was at Category 5 intensity.

2.1. INTRODUCTION

Hurricane Katrina was the costliest and one of the deadliest storms ever to hit the U.S. coast (Knabb et al. 2005). The storm began as a tropical depression over the southeastern Bahamas on 23 August, and was upgraded to tropical storm Katrina on 24 August. After crossing southern Florida as a Category 1 hurricane, Katrina intensified rapidly over the warm Gulf of Mexico water between 26 and 28 August, and became a Category-5 hurricane by 1200 UTC 28 August with maximum sustained winds of 175 mph. The storm weakened to a Category 3 hurricane before making landfall near the Louisiana-Mississippi border at 1100 UTC 29 August. Figure 2.1 shows the storm track with daily (0000 UTC) positions marked.

Katrina caused extensive damage to offshore oil and gas production facilities; 46 platforms and 4 jack-up rigs were destroyed. Perhaps most remarkably, Katrina inflicted severe damage on the 36,500-ton Royal Dutch Shell's Mars platform located at about 130 miles south of New Orleans in 3,000 ft of water. (The full recovery of Mars production took a year and half and over 1 million man-hours.) Mars was the most prolific oil producing platform in the Gulf of Mexico. Before the storm, it produced 148,000 barrels of oil and condensate per day and 160 million cubic feet of gas. The billion-dollar platform also was designed to withstand “140-mph winds and crashing waves up to 70 ft high simultaneously” (Hays, 2007). Less spectacular but certainly worth noting was the capsizing of National Data Buoy Center (NDBC) data buoy 42003, the first loss of a deepwater buoy in the NDBC 30-year history of operation in the Gulf of Mexico. The record peak significant wave heights of 55 ft at buoy 42040, a shallow-water buoy located at about 100 miles southeast of New Orleans, also surpassed the record set a year ago at the same buoy during Hurricane Ivan (Panchang and Li 2006). The buoy and platform locations are marked in Figure 2.1.

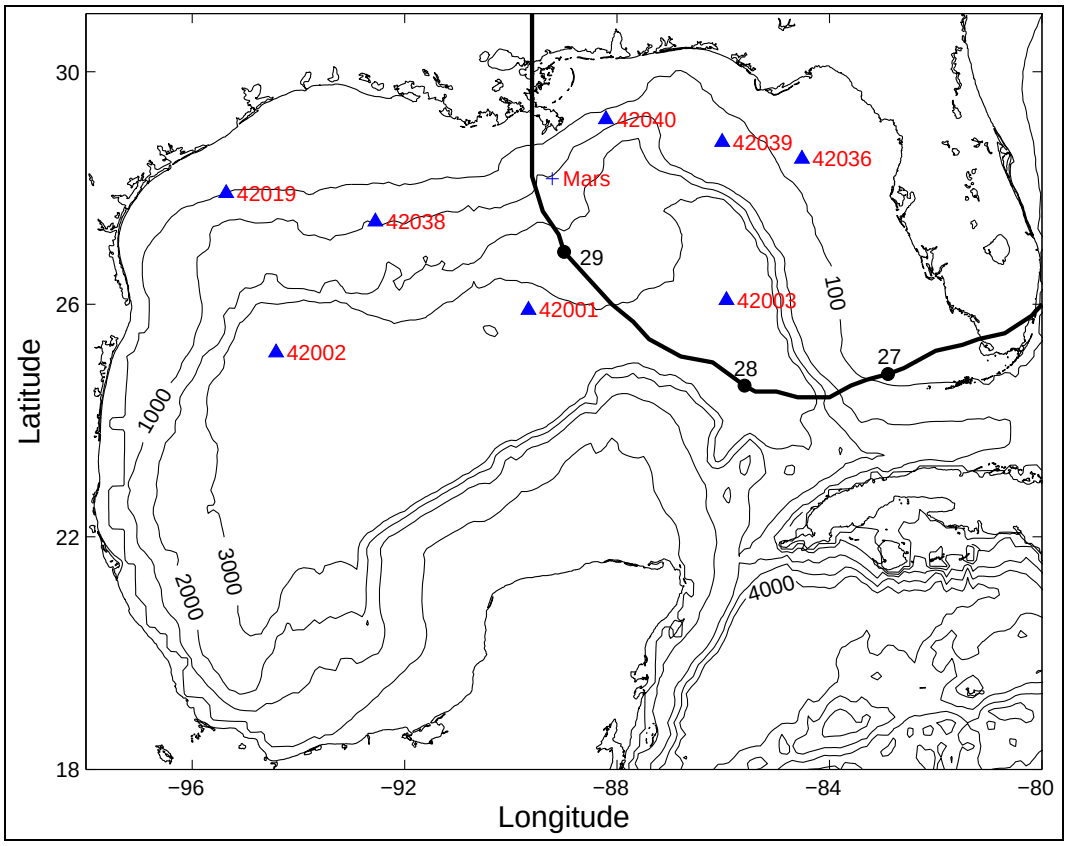

Figure 2.1. Gulf of Mexico bathymetry map with Hurricane Katrina's path. The path (solid line) and 00UTC/date positions (solid circles) are marked. NDBC buoys (triangles) and Mars platform (cross) also are indicated.

As is true in any extreme storm, while large waves and currents were expected, very few direct surface observations were available during Katrina. For assessing of storm damage to offshore facilities, on the other hand, it is essential that the peak wave and current conditions can be accurately estimated. In this study, state-of-the-art ocean circulation and surface wave models driven by wind forcing derived from high-resolution hurricane wind analysis, are used to simulate (hindcast) the ocean states during Katrina. The wave model is validated with buoy and satellite altimetry data. The storm-induced surface currents from the circulation model have not been verified, as at present there is no publicly available information about the surface currents in the path of Katrina.

2.2. MODELS

The Princeton Regional Ocean Forecast System (PROFS) for the Caribbean Sea and the Gulf of Mexico (http://www.aos.princeton.edu/WWWPUBLIC/PROFS/) is used to simulate the Loop Current, Loop Current Eddy and upper ocean wind-driven response. The model is based on the results of Chapter 1. The model continuously assimilates satellite SSHA from AVISO (www.aviso.oceanobs.com) and SST from US-GODAE (www.usgodae.org) through 18 August. Thereafter the model is allowed to run without further injection of satellite data. Surface heat and evaporative fluxes are set to zero. The same model has been used to study the ocean

responses to hurricanes (see previous and later chapters; or Oey et al. 2006, 2007; Yin and Oey 2007).

The National Centers for Environmental Prediction (NCEP) Wave Watch III (WW3) (Tolman 2002) is used to model the surface waves. The WW3 is used in operational forecasts (Alves et al. 2005) as well as in process studies (e.g., Moon et al. 2003; Chu et al. 2004). It is a third generation wave model which treats explicitly the wave-wave interaction and dissipation due to whitecapping and wave-bottom interaction. In this study the model domain is restricted to the Gulf of Mexico from 98^o to 77^{o}W and from 14^o to 32^{o}N. The spatial resolution is 0.1^o× 0.1^o, and the discrete spectrum consists of 36 directions ($\Delta\theta$ =10^o) and 34 frequencies (from 0.042 Hz to 1 Hz with a logarithmic increment). The model incorporates hourly surface currents from PROFS.

The NCEP Global Forecast System (GFS) at present does not adequately resolve the tropical cyclones. In this study, the GFS winds are blended with the NOAA Hurricane Research Division (HRD) high-resolution analyzed winds (http://www.aoml.noaa.gov/hrd/). The HRD wind analysis uses all available surface weather observations (e.g., ships, buoys, coastal platforms, surface aviation reports, reconnaissance aircraft data adjusted to the surface, etc.), and is gridded in a 1000 km × 1000 km moving "box" centered about the hurricane's track. From HRD winds, storm centers are first linearly interpolated to hourly locations, and consecutive HRD maps are then overlapped at the hourly locations and linearly interpolated. The hourly HRD winds are merged with GFS winds using a weight that retains the HRD data within a circle of radius = 0.8 × side of the box (~400 km) and that smoothly transits into the GFS winds beyond that radius. Figure 2.2 shows snapshots of GFS+HRD on 0600 UTC 28 August and 0600 UTC 29 August.

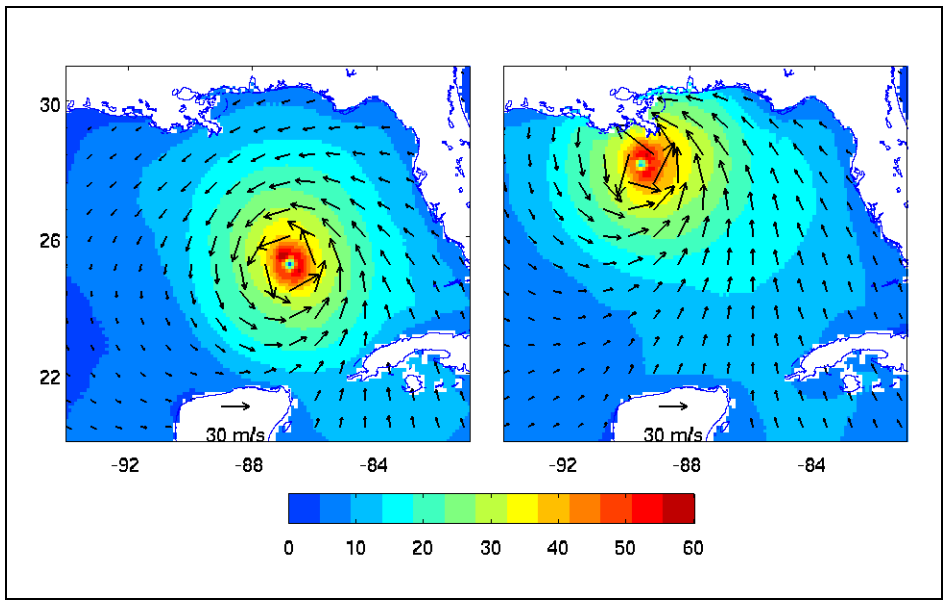

Figure 2.2. Hurricane Katrina wind vectors (in m/s) on (left) 0600 UTC 28 August and (right) 0600 UTC 29 August from the blended HRD+GFS analysis.

Following Oey et al. (2006), the wind stress in PROFS is calculated from the wind using a bulk formula:

$$\begin{aligned} C_d \times 10^3 &= 1.2, && |u_a| \le 11 \text{ m/s}; \\ &= 0.49 + 0.065\,|u_a|, && 11 < |u_a| \lesseqgtr 19 \text{ m/s}; \\ &= 1.364 + 0.0234|u_a| - 0.00023158|u_a|^2, && 19 < |u_a| < 100 \text{ m/s}. \end{aligned} \quad (1)$$

where $|u_a|$ is the wind speed. At present the maximum speed of 100 m/s is adequate even for intense hurricanes such as Katrina. The formula incorporates the limited drag coefficient in high wind speeds (Powell et al. 2003). The wave model, on the other hand, uses the wind as input and calculates the wind stress internally based on a wave boundary layer parameterization (Tolman and Chalikov 1996). The wave model starts on 0000 UTC 25 August when Katrina was still a tropical storm near Bahamas. The hourly model results are saved for the subsequent analysis.

2.3. RESULTS

Currents

A fast moving storm such as Katrina excites large inertial currents (Gill 1982). In the northeastern Gulf, the averaged inertial period is about 26 hours. To separate rapidly fluctuating inertial motions from otherwise relatively steady currents, the model surface currents are decomposed into the daily mean currents and harmonic-fitted inertial amplitudes. While filtering of inertial motion using simple average (box filter) is crude, it is adequate in this application as the mean currents are comparable in magnitude with the inertial currents. Figure 2.3 shows daily mean currents for 27-30 August with daily mean sea surface heights superimposed. The most conspicuous flow features are the Loop Current and Loop Current Eddy, marked by anticyclonic circulations around high sea levels (and correspondingly, deep upper layer). On 28 August, Katrina passed over the Loop Current and Loop Current Eddy. Scharroo et al. (2005) suggested that the deep warm layer was partially responsible for the sudden increase of storm intensity. Superposed on the Loop Current and Loop Current Eddy are large (1 to 1.5 m/s) transient wind-driven surface currents. The wind-driven currents are frictionally driven and their pattern generally follows the wind. On 27 August the wind-driven currents were concentrated over the west Florida shelf, and on 28 August they were over the northeast of the Loop Current and on the shelves. On 29 August when Katrina approached the Louisiana and Mississippi coasts, the surface currents had a strong onshore component. The associated large storm surges in Lake Pontchartrain led to the eventual failure of the levee system in New Orleans. (The model predicted maximum surge height was 4.5 m.)

Figure 2.4 shows daily inertial amplitudes. Large inertial currents with amplitudes > 2 m/s are concentrated under the storm. Unlike the wind-driven currents, the inertial amplitudes are much larger on the right of the storm path than on the left. The amplitude asymmetry is the consequence of fast-moving storm. In a stationary storm, the inertial currents, which rotate in a clockwise circle, would be destroyed within few inertial cycles. In a moving storm, however, the wind vectors turn clockwise on the right side of the storm path (relative to a fixed frame) and turn counterclockwise on the left side. Consequently, the inertial amplitudes are amplified on the right side and suppressed on the left side of the storm. The effect is particularly striking when the wind vectors rotate at about the same rate as the inertial motion (Chang and Anthes 1978; Price 1981).

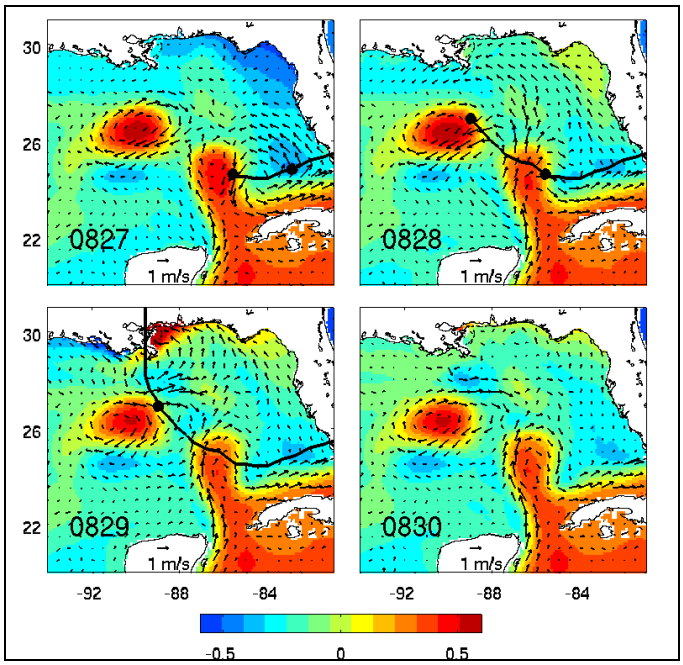

Figure 2.3. Model daily mean surface currents from 27-30 August. The daily mean sea surface heights (in m) are superimposed. (Coastal sea levels near the storm path on 29 August are off the scale.) Solid line is the storm path, and the start and end of the day is marked.

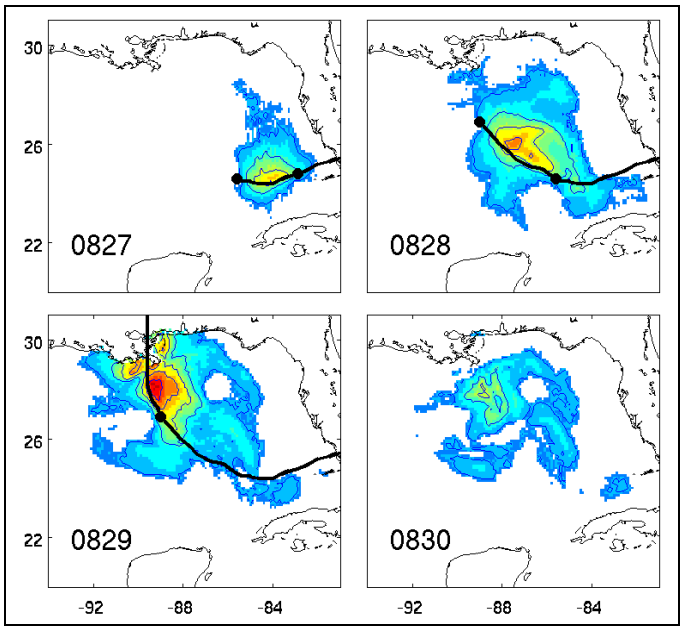

Figure 2.4. Model daily surface inertial amplitudes (in m/s) from 27-30 August. Only the amplitudes > 0.5 m/s are shown. Solid line is the storm path, and the start and end of the day is marked.

The inertial motions tend to persist long after the storm has passed. For example, on 30 August large inertial amplitudes (~ 1 m/s) were still present whereas the wind-driven currents almost completely vanished. We also noted that the inertial currents are considerably smaller (< 0.5 m/s) over the Loop Current, the Loop Current Eddy, and an anticyclonic eddy north of the Loop Current (Figure 2.4). This is consistent with the previous observations (Kunze 1985) and model studies (Wang 1991) that in regions of strong negative (anticyclonic) vorticity surface inertial energy would rapidly escape below the surface mixed layer. Indeed, after Katrina large inertial currents were found below the mixed layer (George Forristall, personal communication).

Waves

Figure 2.5 shows snapshots of significant wave heights and dominant wave periods on 0600 UTC 28 August and 0600 UTC 29 August. (Waves are instantaneous value, not the daily averages.) The wave heights are significantly bigger on the right of the storm path. The wind speed, duration and fetch impact the wave growth. Since the waves travel with the storm on the right side of the storm path but are away from the storm on the left side, the waves grow much bigger on the right side because of the longer fetch. The wave period patterns reveal the directions of wave spreading. The dominant (long-period) swells on 28 August were concentrated in the forward direction of the storm, and on 29 August they were towards the west along the coast.

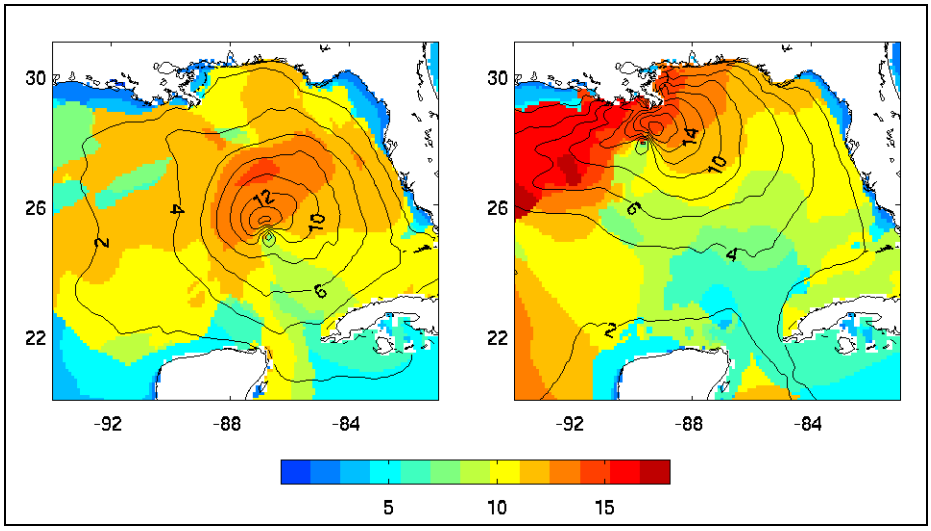

Figure 2.5. Model significant wave heights (in m) and dominant wave periods (in s) for (left) 0600 UTC 28 August and (right) 0600 UTC 29 August.

Figure 2.6 shows swath of maximum wave heights, the maximum values of significant wave heights throughout the hurricane passage. The highest waves are concentrated along the storm path and are biased to the right. The predicted maximum wave heights were over 20 m on 29 August. We note that WW3 is not applicable in the shallow water. When the wave heights are comparable to the water depth, effects such as depth-induced wave breaking and bottom friction become important (Booij et al. 1999). Thus, the predicted >10 m waves along the Louisiana and Mississippi coasts should not be taken literally. Nevertheless, results from regional wave model typically are used to specify forcing at the open (seaward) boundaries for a coastal wave model (e.g., Xu et al. 2007).

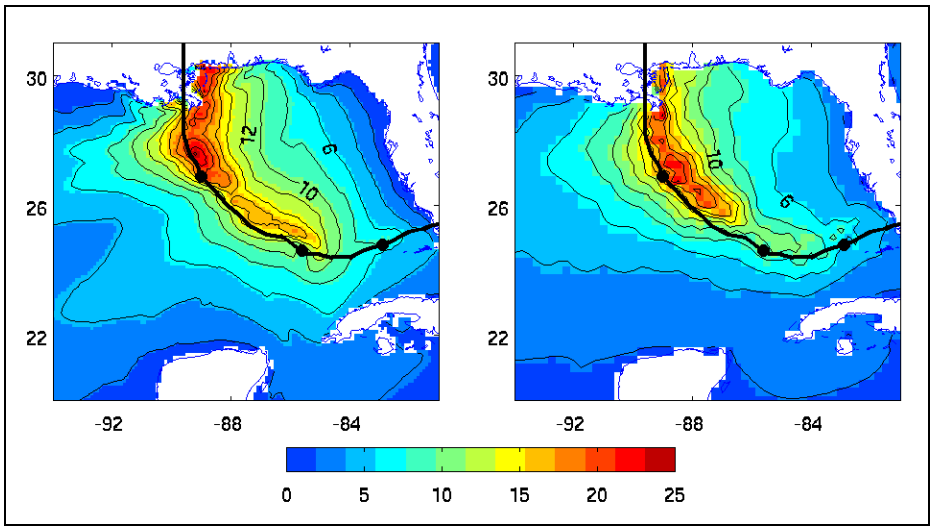

Figure 2.6. Swath of maximum wave heights (in m): (left) this study and (right) NCEP operational model. Solid line is the storm path.

The predicted significant wave heights (Figure 2.7) and dominant wave periods (Figure 2.8) are compared with the NDBC buoy observations (the buoy locations are marked in Figure 2.1). The model predictions are excellent at every buoy whether near the storm path or in the western Gulf. Averaged over the storm period (27-30 August), the mean bias is 0.07 m, mean absolute error is 0.48 m, and correlation coefficient = 0.97. We note that the model slightly underestimates the maximum wave height at 42040 (15.3 m vs. 16.9 m), which can be attributed to the large spatial gradient of maximum wave heights in the buoy vicinity (Figure 2.6) and perhaps uncertainty in the wind field.

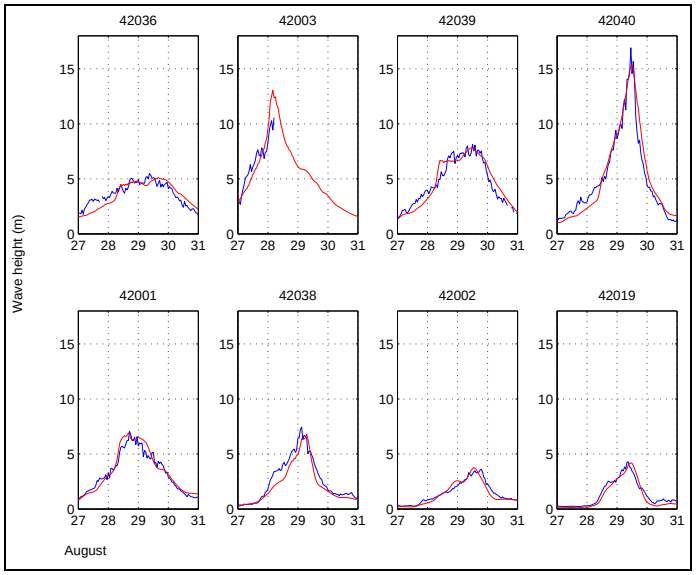

Figure 2.7. Comparison of simulated (red) and observed (blue) significant wave heights at eight NDBC buoys. Buoy locations are marked in Figure 2.1.

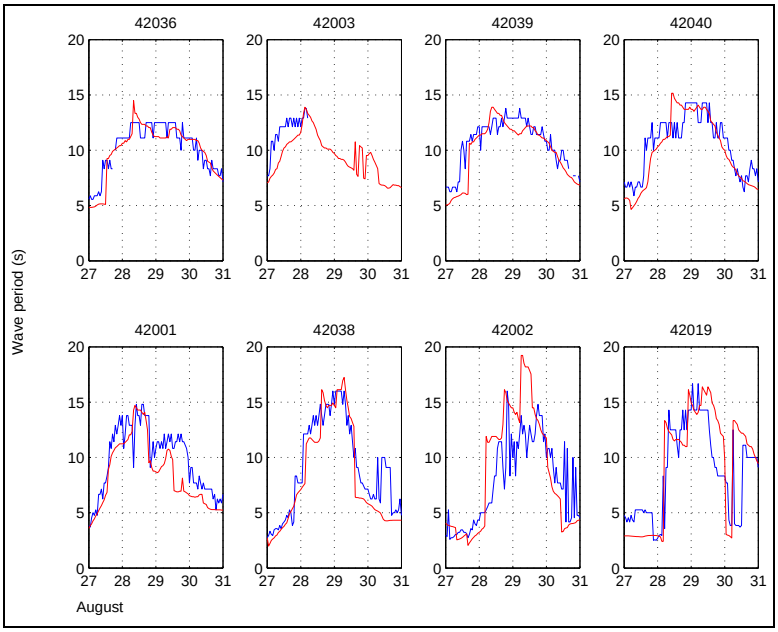

Figure 2.8. Comparison of simulated (red) and observed (blue) dominant wave periods at eight NDBC buoys. Buoy locations are marked in Figure 2.1.

It is interesting to contrast the wave heights between different buoys. Buoys 42003 and 42040 faced about the same maximum winds (not shown), but the waves were much larger at 42040. The difference is due to the longer fetch, as the waves arriving at 42040 experienced an extra day of the storm forcing. Also, the waves at 42003 were about twice as large as those at 42001, reflecting the bias of larger waves on the right of the storm path. In the western Gulf, the swell conditions are nicely reproduced. For example, at 42019, the first arrival of long period (> 10 s) swells at 0500 UTC 28 August is clearly indicated in the sudden rise of the dominant wave periods (Figure 2.8). We also note that the waves only became substantial (> 1 m) after 26 August that the model initiation (starting on 25 August) has no effect on the results.

Satellite altimetry provides a broad spatial coverage of wave fields. Figure 2.9 shows all available satellite tracks (28-30 August) in the eastern Gulf during Katrina and a comparison of significant wave heights between the model and altimetry. The model grids are interpolated to the nearest altimetry track. The agreement is excellent (correlation coefficient $\gamma = 0.96$; mean bias = 0.26 m; mean absolute error = 0.46 m). The linear regression line is

$$H_m = 1.13 \times H_s - 0.09 \qquad (2)$$

where H_m and H_s are respectively modeled and satellite significant wave heights (in m). The >1 slope can be attributed to systematic error in altimetry wave measurements (Tolman 2002). It is also noted that the altimetry is limited to wave heights < 8 m. For larger waves, the altimetry measurements are too scattered to produce meaningful averages and are excluded (AVISO, personal communication).

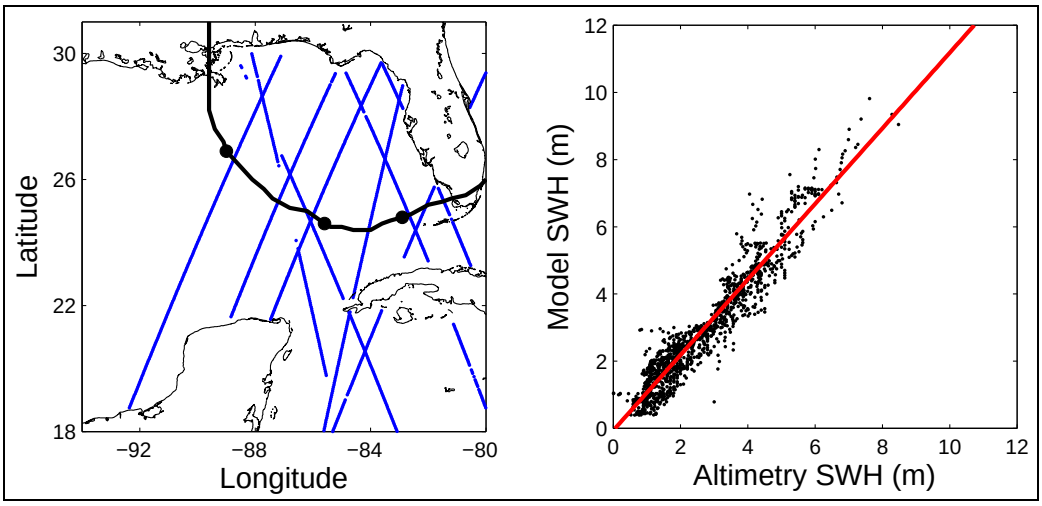

Figure 2.9. (Left) Satellite altimetry tracks during Hurricane Katrina. (Right) Regression of significant wave heights between model and altimetry.

Comparison with NCEP operational wave model

The NCEP North Atlantic Hurricane regional wave model (NAH) is based on the same generic WW3 model. The NAH model domain covers the entire North Atlantic Ocean from 98^o to 30^{o}W and 0^o to 50^o N. The NAH model resolutions (0.25^o × 0.25^o, 24 directions and 25 frequencies) however are much coarser than used in this study. The NAH model also does not incorporate the surface currents. The wind fields in the NAH model are based on the high-resolution hourly winds from the Geophysical Fluid Dynamics Laboratory (GFDL) hurricane model, blended with the GFS winds. The 3-hourly NCEP model analyses are obtained from http://polar.ncep.noaa.gov/waves. In damage assessment the most important parameter is the predicted maximum wave heights. The swath of maximum wave heights from NAH model is included in Figure 2.6 for comparison with our study. The NAH model has coarser resolution, but its general pattern is similar to our study—large waves are concentrated along the storm path and wave heights are biased to the right. The largest wave predicted by the NAH model (22 m) also agrees well with ours (24 m) (considering the difference in spatial resolution). However, in the NAH model the large waves are constrained much closer to the storm path. In other words, the spatial extent impacted by the large waves in the NAH model is considerably less (by about 50%) than in our study. This is perhaps best illustrated in comparison of the model predictions at the two buoys (42003 and 42040) which recorded the largest waves. In both cases, the NAH model underestimates the maximum wave heights substantially by as much as 5 m (Figure 2.10).

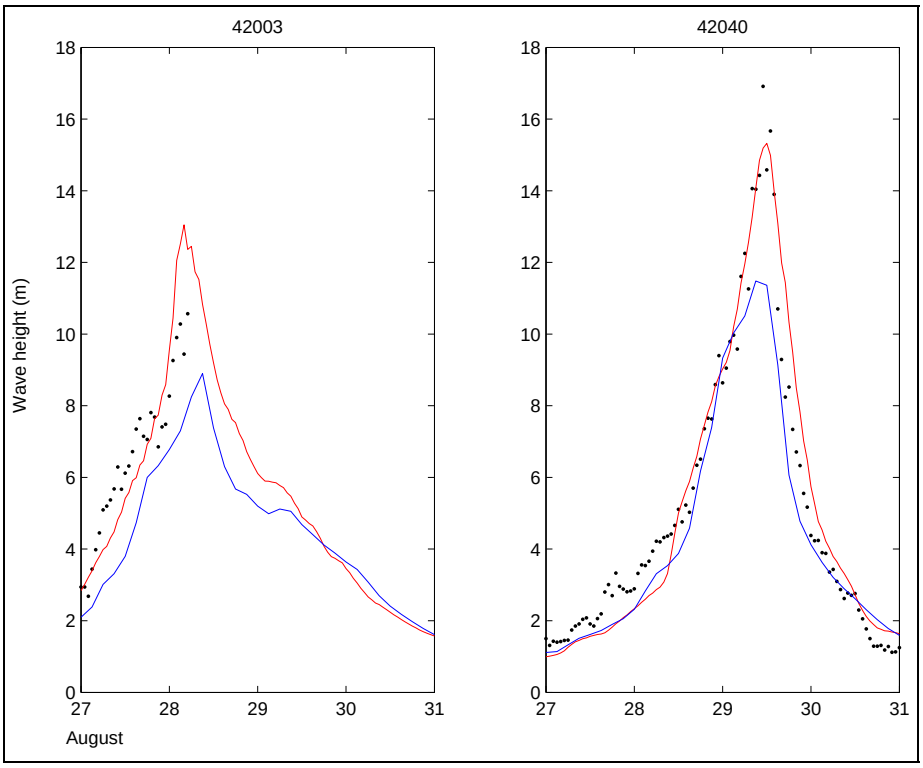

Figure 2.10. Comparison of significant wave heights between this study (red), operational model (blue), and buoy observations (dots) for (left) 42003 and (right) 42040. Buoy 42003 was lost after 0500 UTC 28 August.

2.4. DISCUSSION

Extensive damages on offshore oil and gas production facilities during Hurricane Katrina suggest strong combined wind, wave and current forces. The NDBC buoys, which are few and scattered, are not adequate to map the extreme sea states. In this study, the model simulation (hindcast) provides plausible account for the loss of buoys and platforms. Buoy 42003 was capsized when the predicted wave heights reached 13 m (Figure 2.7), which exceeded the largest waves ever recorded on 42003 (~11 m) (Panchang and Li 2006). The large waves combined with strong winds (> 32 m/s) and currents might be responsible for this first ever loss of deepwater NDBC buoy in the Gulf of Mexico. For the Mars platform, on 0400 UTC 29 August the maximum waves were about 20 m (~66 ft) (Figure 6) and maximum winds were about 57 m/s (~128 mph). (The maximum waves/winds were not at the exact location but in the close vicinity.) We do not know the time the Mars facility was severely damaged, but it is probably no coincidence that the predicted sea states had indeed approached the platform design criterion of simultaneous 70 ft waves and 140 mph winds.

It is well recognized that the drag coefficients used in WW3 are far too large under the hurricane wind condition (Moon et al. 2004). The model success therefore must partly be attributed to careful tuning (Alves et al. 2005). However, since the buoy and altimetry rarely recorded waves > 10 m, the wave model has not actually been 'validated' for very large waves. In this study, evidence strongly suggests that the predicted large waves were 'real'. However, whether WW3 is valid in high wind conditions (when its physics apparently fails) can only be

tested by direct measurement of extreme waves in the path of major (> Category 3) hurricanes. The Gulf of Mexico provides 25 percent of the domestic oil supply and 11 percent of the domestic gas production. Accurate marine forecasts of hurricane sea states are of vital interest to the nation’s economic well being.

CHAPTER 3. HINDCAST OF WAVES AND CURRENTS IN HURRICANE RITA

Synopsis

Similar simulations and analyses as those for Katrina (Chapter 2) are conducted here for Hurricane Rita. Thus the current and wave models are again run in forecast modes using accurate high-resolution winds to assess the sea and wave states and their impacts upon the northern Gulf of Mexico.

Summary of the Main Results

In this chapter, we have found it useful whenever appropriate to compare the responses due to Rita and Katrina. In comparison to Katrina, simulated surface waves (maximum significant wave-height ≈ 22 m instead of 24 m) and storm-driven inertial currents (2.2 m/s instead of 2.5 m/s) produced by Hurricane Rita are a little less. Although at both storms' most intense stages after crossing the Loop Current, Hurricane Rita was actually slightly more intense (Table P.1), it also more rapidly dissipated thereafter probably because the storm passed over a cyclone with cooler SST. Before making landfall, Rita crossed over the same ring Eddy Vortex that was 4 weeks earlier crossed by Katrina. The ring had become weaker and smaller after Katrina, yet it probably sustained the storm's intensity. When the high-resolution winds were used to drive the ocean, as in Chapter 2 for Katrina, the simulated wave fields agreed well with observations from surface buoy and satellite altimeters.

Brief History of Hurricane Rita (descriptions courtesy of NCEP)

Rita became a hurricane with a closed eyewall almost due south of Florida on September 20 at 14:00:00 GMT. Four hours later, Rita had reached Category 2 strength with 100 mph (160 km/h) maximum sustained winds. As Hurricane Rita entered the Gulf of Mexico, it rapidly increased in intensity. On September 21 at 15:00:00 GMT, Rita's maximum sustained winds increased to 140 mph (225 km/h; Category-4). Rita continued to gain strength unabated and became a Category 5 storm with maximum wind speeds of 165 mph (265 km/h) on September 21 at 20:00:00 GMT. On September 22 at 03:00:00 GMT Rita's maximum sustained winds had increased to 175 mph (280 km/h) with an estimated minimum pressure of 897 mbar (hPa). As with Hurricane Katrina, Hurricane Rita's rapid intensification may in part be attributed to its encounter with the Loop Current. As the storm traversed west-northwestward towards Texas/Louisiana, it weakened but remained at Category-4 with maximum sustained wind speeds of 140 mph on September 23 at 12:00:00 GMT just south/southeast of the Louisiana-Texas shelf and slope. The still powerful storm may have been fueled by its encounter with a Loop Current eddy (the "Eddy Vortex"; Figure 3.1b), the same one crossed over by, and probably weakened as a result of, Katrina 4 weeks earlier. Hurricane Rita continued to weaken to a Category-3 hurricane (maximum sustained wind speed ≈ 115 mph) as it made landfall near the border of Texas and Louisiana on September 24 at 12:00:00 GMT.

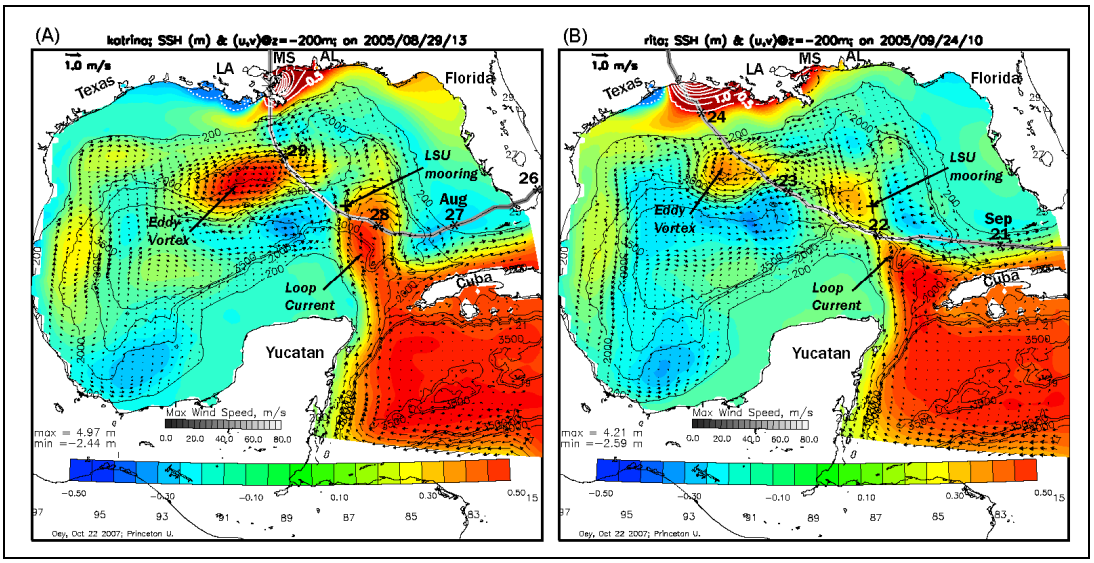

Figure 3.1. Model sea-surface height (color: red ≥ +0.5 m and blue ≤ –0.5 m; also white contours on shelves) and currents (vectors) at z =–200 m shortly after Hurricanes (A) Katrina and (B) Rita made landfalls at the northern Gulf of Mexico coast, on August 29 at 13:00 GMT and September 24 at 10:00 GMT, respectively. The fields are hourly-averaged (i.e., near-instantaneous); note the extreme sea-surface highs along the coast to the right of the storm, and lows farther left. Hurricane tracks are marked daily, with wind speeds indicated in gray scale. The location of mooring at (87°W, 25.5°N) is indicated with a "+" and note its "change" of position relative to the Loop Current for the two storms. Thin contours show isobaths in meters.

3.1. INTRODUCTION

The model simulations and analyses for Hurricane Rita are similar to those for Hurricane Katrina. An analysis field of the Loop Current and eddies is first produced. It is instructive to compare how the ocean state has evolved in the relatively short time-span of less than 1 month from Katrina to Rita, and the change is significant. Figure 3.1 compares the two states in terms of SSH and the (u,v) at z = –200 m, on (a) August 29 at 13:00 GMT and (b) September 24 at 10:00 GMT when the two storms made landfalls at the northern Gulf States (Louisiana and Texas/Louisiana respectively). Being hourly-averaged, these are snapshot maps so that the currents contain a substantial amount of storm-induced energy (inertial in particular; and yes even at z = –200 m). This is clear not only near the northern Gulf Coast, where storm surges, max/min SSH ≈ +4.5 to 5m and –2.5m, are seen, but also over the deeper regions south of the Mississippi delta for Katrina (Figure 3.1a), and also to the right of Rita's track from the Loop Current to the northern portion of the Eddy Vortex in Figure 3.1b. Quite apparent also is the significant change in the Loop and Eddy Vortex, both are weaker during Rita, and in fact the Loop shed a small ring after Rita.[4] Figure 3.1 also shows the location of the LSU mooring where current measurements were available during the 2005 hurricane season. Of interest here is the change in the relative position of the mooring with respect to the state of the Loop during the two

[4] An earlier, experimental version of our model was run in real-time during Rita and predicted correctly the shedding of this ring which was later observationally confirmed.

storms: west of the Loop during Katrina but to the east of the Loop during Rita. We shall see in Chapter 4 that these changes impact the way near-inertial internal energy propagates through the water column. For this chapter (as in Chapter 2 for Katrina), we will focus on the surface response.

3.2. METHODOLOGY

Figure 3.2 shows the eight NDBC stations where we verified the wind data used to drive the model as well as the simulated wave characteristics (below); Rita path is also shown. As for the Katrina case, we use a merged HRD and NCEP (GFS) wind product to drive our wave and current models. Figure 3.3 shows Rita wind vectors on two dates, September 22 at 1200UTC 9 hours after its peak intensity and also September 23 at 1200UTC. Though the storm was more intense on the earlier date, its inner eyewall had been replaced by a larger outer one during the 24 hour period, and the storm expanded in size by about 50% in agreements with the passive microwave images shown in Figure 3.4 (see also descriptions in Knabb et al. 2005).

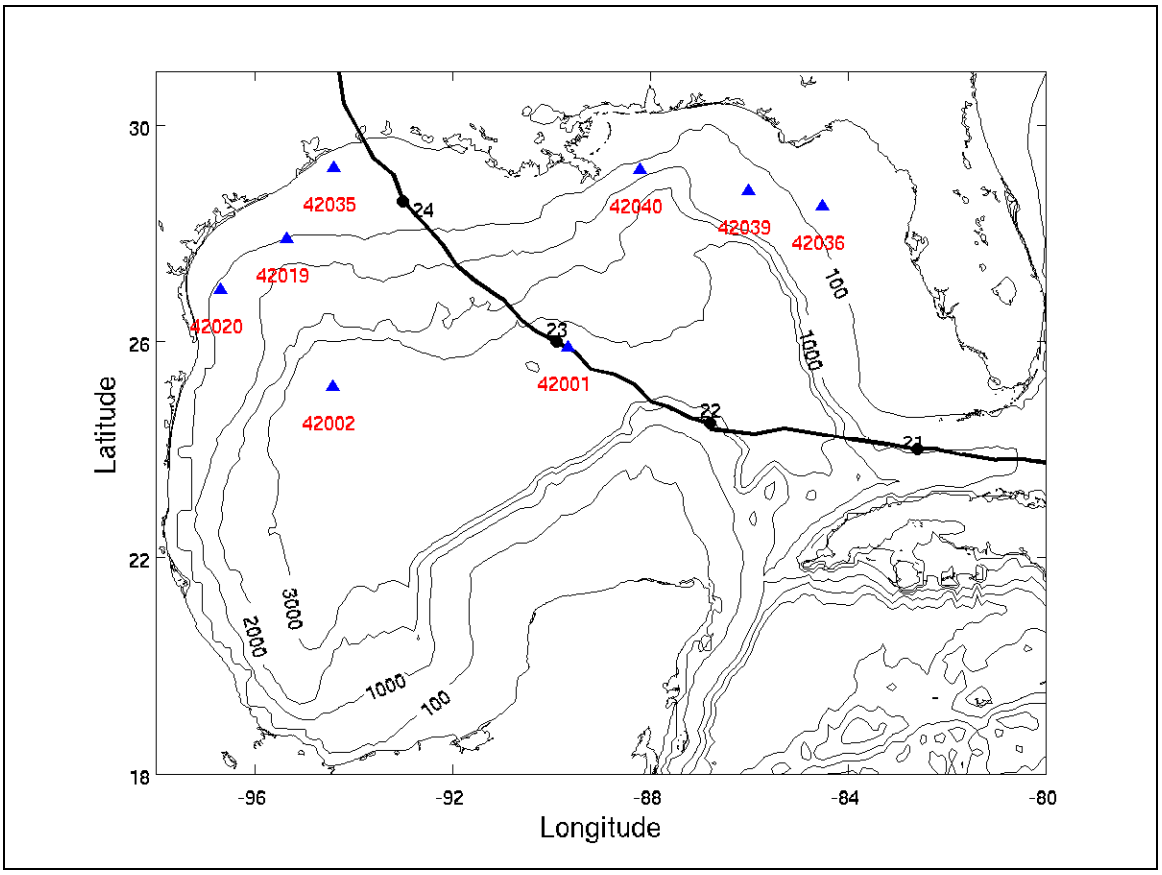

Figure 3.2. Gulf of Mexico bathymetry map with Hurricane Rita's path. The path (solid line) and 00UTC/date positions (solid circles) are marked. NDBC buoys (triangles) are indicated.

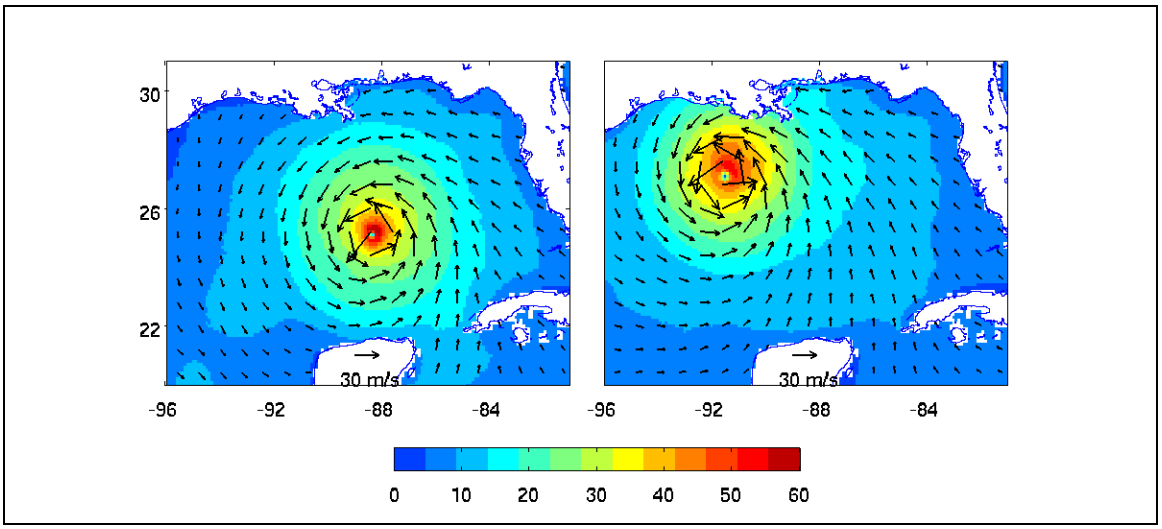

Figure 3.3. Hurricane Rita wind vectors (in m/s) on (left) 1200 UTC 22 September and (right) 12000 UTC 23 September from the blended HRD+GFS analysis.

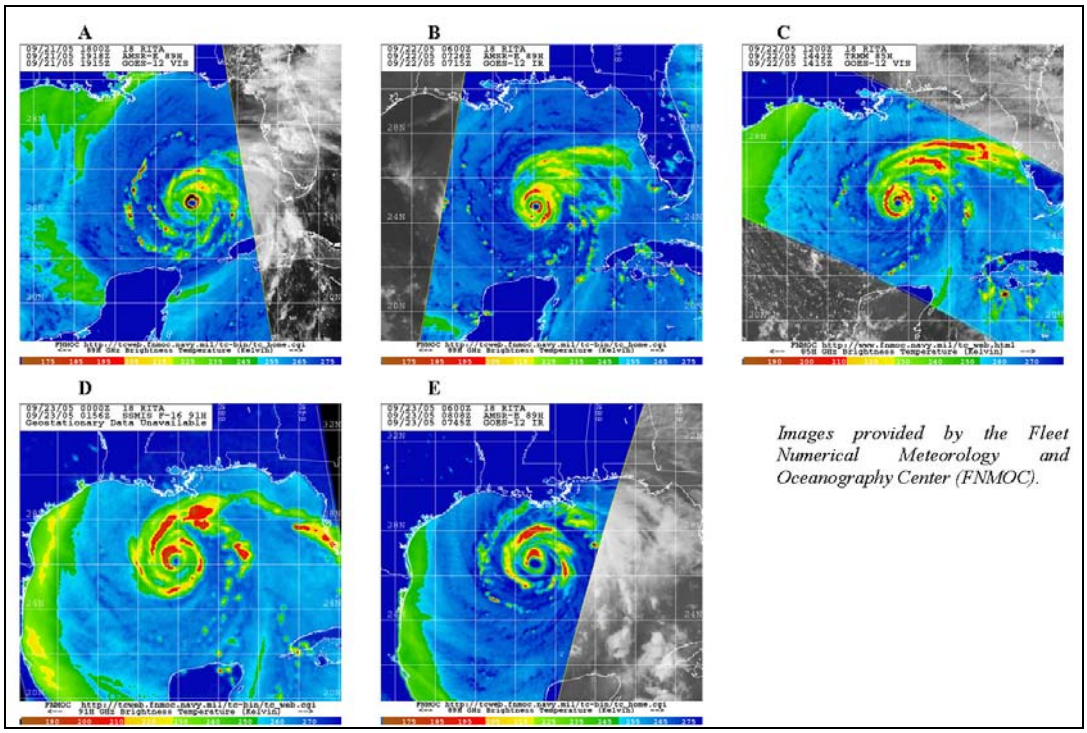

Figure 3.4. Series of 85-91 GHz passive microwave images of Hurricane Rita during 21-23 September 2005, showing the enlargement of the storm's eye after its peak strength (panels C-E). From Knabb et al. (2005).

The ocean state prior to Rita was estimated as in Chapters 2 and 1 by assimilating satellite data. In this case, the assimilative analysis was carried through September 16; thereafter no further data were assimilated and the model was run in the "forecast" mode forced by the merged HRD and NCEP winds for an additional 30 days.

3.3. RESULTS

Figure 3.5 shows the daily-mean SSH (color) and surface (at the first sigma level) currents (vectors) on September 21-24, 2005. Rita's track is shown in black and the two dots indicate the beginning and ending times of the particular date displayed on each panel. This shows clearly the apparent coincidence that when the storm reached its peak intensity on September 22 at 03:00UTC it just passed over the Loop, but that thereafter the storm weakened. Figure 3.6 shows the corresponding inertial amplitudes (m/s). Similar to those for Katrina (Figure 2.4), these are largest to the right of the storm track. However, the intensity for Rita is not only weaker, but also the areas with significant inertial amplitudes (say the yellow-red regions where amplitudes > 1.5 m/s in the Figures 2.4 and 3.6) are more limited. One may compare, for example, the amplitudes when each storm was at its respective peak strength: the panel labeled August 28 in Figure 2.4 for Katrina and September 22 in Figure 3.6 for Rita. This comparison suggests that the more-limited inertial region in the case of Rita is not determined by the strength of the storm alone (since Rita's peak wind was actually slightly stronger). Comparing August 28 with August 29 in Figure 2.4 when Katrina has weakened and September 22 with September 23 in Figure 3.6 when Rita has weakened also suggest similar things. We will see in Chapter 4 that an important determining factor for the accumulation of inertial energy is the background vorticity. In the above examples when the regions of significant inertial amplitudes are more limited (widespread), we will find that they are also regions with predominantly cyclonic (anticyclonic) vorticity.

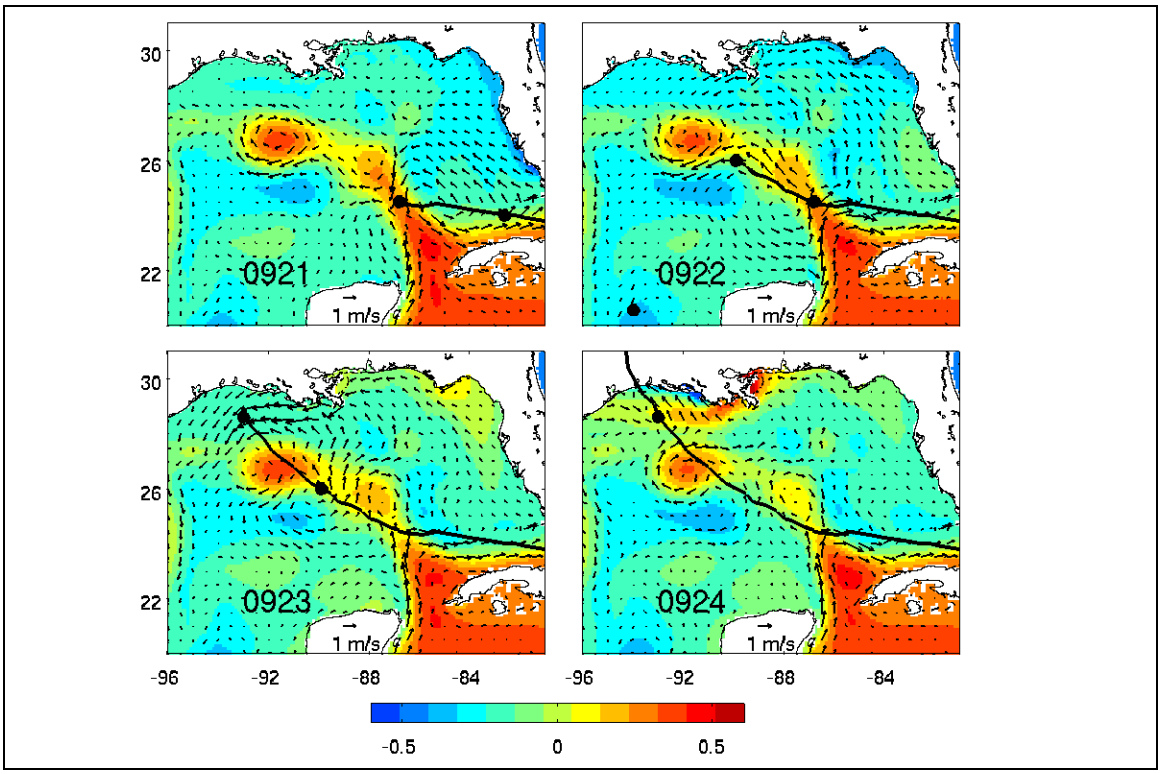

Figure 3.5. Model daily mean surface currents from 21-24 September. The daily mean sea-surface heights (in m) are superimposed. (Coastal sea levels near the storm path on 24 September are off the scale.) Solid line is the storm path, and the start and end of the day are marked.

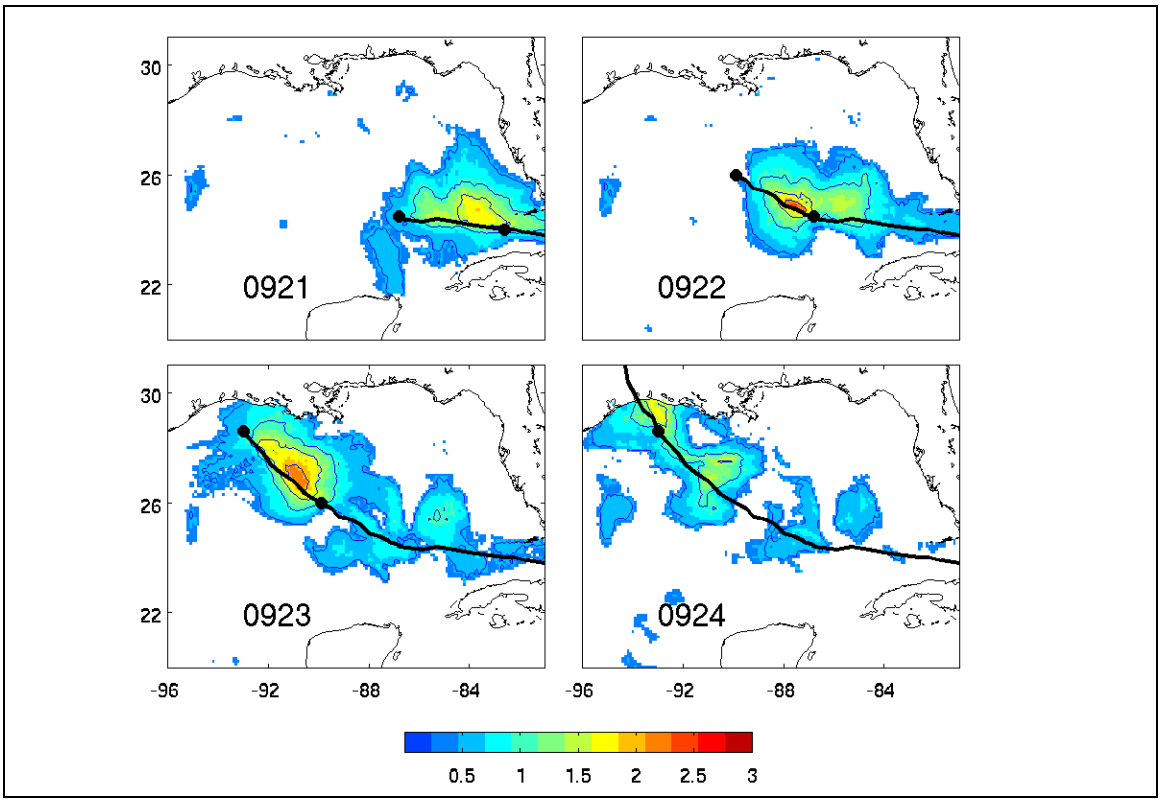

Figure 3.6. Model daily surface inertial amplitudes (in m/s) from 21-24 September. Only the amplitudes > 0.5 m/s are shown. Solid line is the storm path, and the start and end of the day are marked.

Figure 3.7 shows snapshots of significant wave heights and dominant wave periods on 1200 UTC 22 September and 1200 UTC 23 September. (Recall again that waves are instantaneous value, not the daily averages.) These have similar characteristics as those obtained for Katrina (c.f. Figure 2.5): wave heights are larger on the right of the storm path. The wave spreading as revealed by the wave period patterns (colors) show that the dominant (long-period) swells on 22 September were concentrated in the forward direction of the storm, to its west, since Rita was moving west-northwestward. Similarly to the Katrina case, the waves spread westward along the coast when Rita neared the coast on 23 September. Figure 3.8 shows swath of maximum wave heights: the maximum values of significant wave heights throughout the hurricane passage. The highest waves are concentrated along the storm path and are biased to the right. The predicted maximum wave heights were over 20 m on 23 September at approximately 1800 UTC. In comparison to the NCEP calculation (Figure 3.8 right panel), the present wave height is quite a bit higher and is also more widespread.

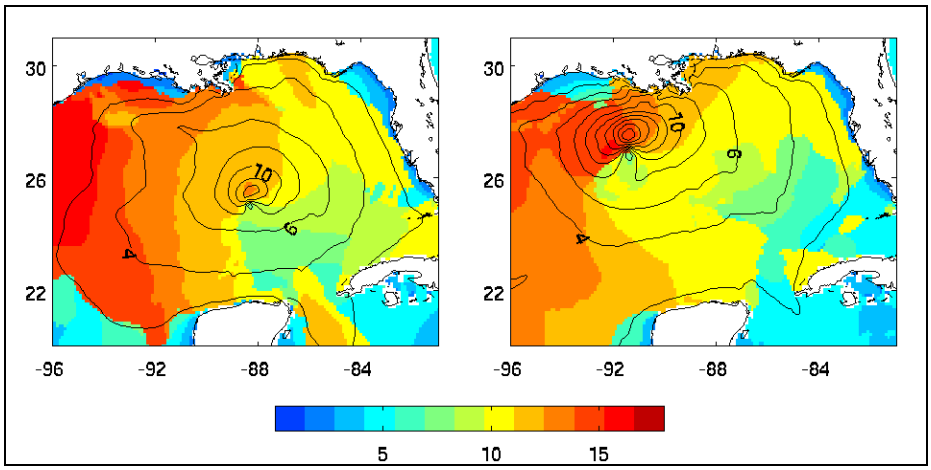

Figure 3.7. Model significant wave heights (in m) and dominant wave periods (in s) for (left) 1200 UTC 22 September and (right) 1200 UTC 23 September.

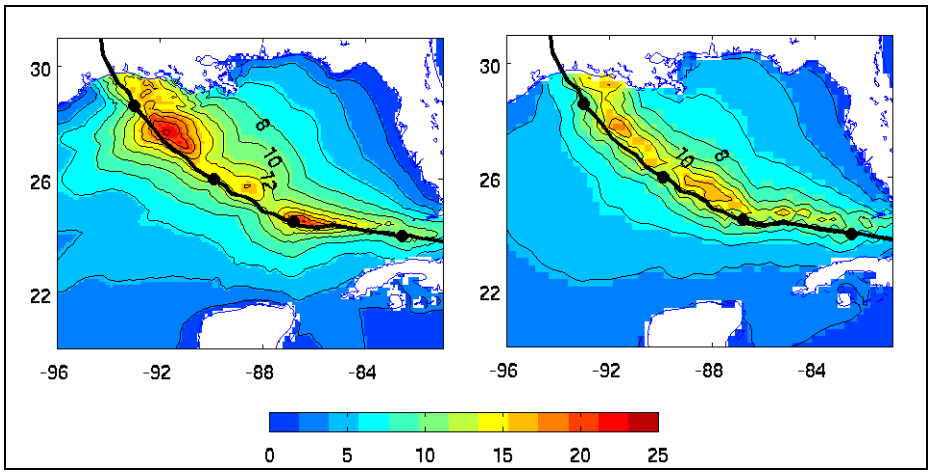

Figure 3.8. Swath of maximum wave heights (in m): (left) this study and (right) NCEP operational model. Solid line is the storm path.

Our calculation does present an improvement over NCEP's. The predicted significant wave heights (Figure 3.9) and dominant wave periods (Figure 3.10) are compared with the NDBC buoy observations (the buoy locations are marked in Figure 3.2). The model predictions are excellent. Discrepancies can again be attributed to uncertainty in the wind field. Figure 3.11 shows all available satellite tracks during Rita (21-24 September) and a comparison of significant wave heights between the model and altimetry. The model grids are interpolated to the nearest altimetry track. As with the buoy comparisons, the agreement is again excellent.

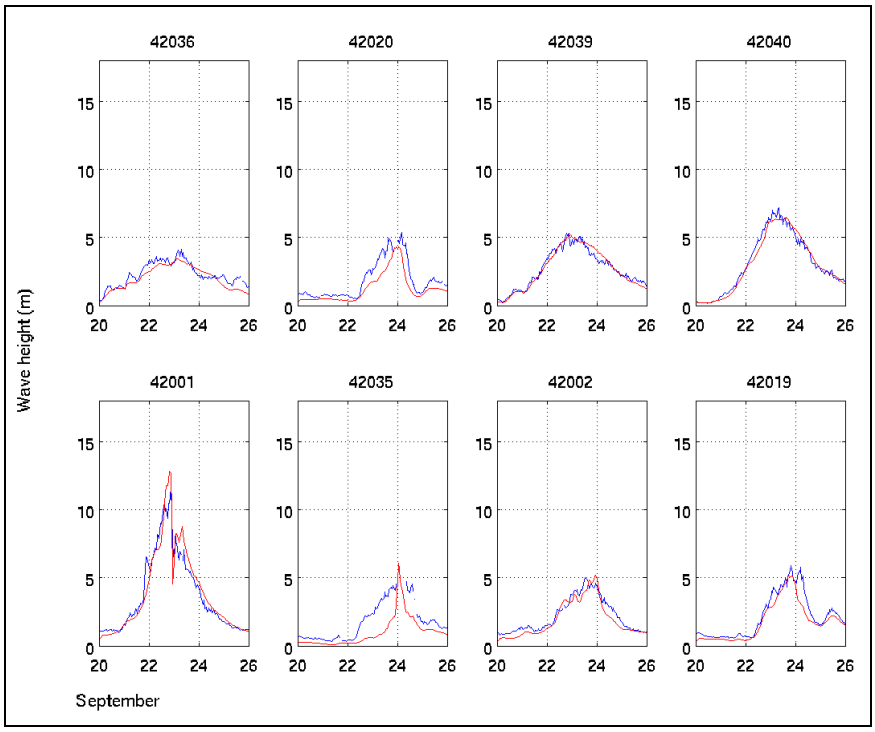

Figure 3.9. Comparison of simulated (red) and observed (blue) significant wave heights at eight NDBC buoys. Buoy locations are marked in Figure 1.

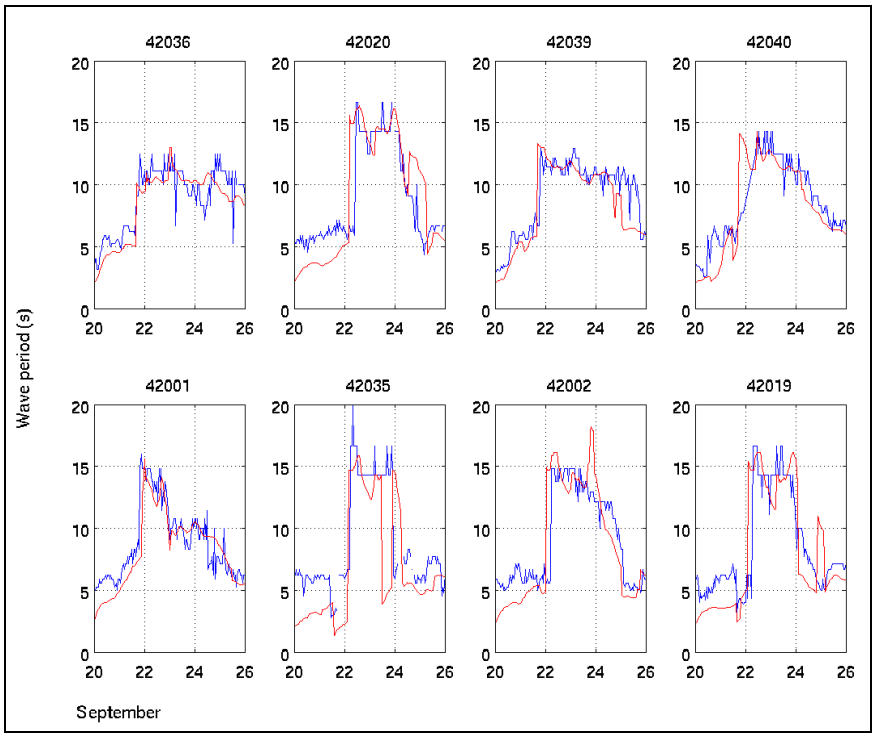

Figure 3.10. Comparison of simulated (red) and observed (blue) dominant wave periods at eight NDBC buoys. Buoy locations are marked in Figure 1.

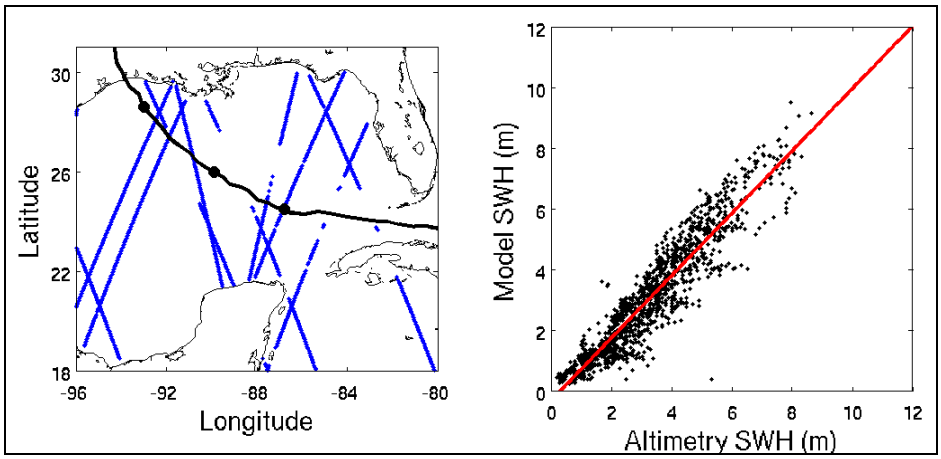

Figure 3.11. (Left) Satellite altimetry tracks during Rita. (Right) Regression of significant wave heights between model and altimetry.

3.4. CONCLUSIONS

Many of the results of ocean wave responses produced by Hurricane Rita are similar to those induced by Hurricane Katrina. It is quite remarkable that the wave model WW3 performed so well, provided of course that the wind forcing used is of high-resolution. The model grid resolution is also important. Comparison with NCEP shows that our model performs quite a bit better, in that it agrees better with observed NDBC wave data.

On the other hand, the storm-induced surface (inertial) current responses are quite different for Hurricanes Rita and Katrina. During Katrina, the Loop and warm ring (Eddy Vortex) were much more well-defined and stronger, while during Rita they were weaker and smaller. These differences resulted in different background (i.e., the slow, non-storm part) vorticity relative to the respective storm track. The upshot is that the inertial response during Rita is less widespread than that during Katrina. We will further explore these different physics by examining in more details the subsurface responses in the next two chapters.

CHAPTER 4. STORM-INDUCED SUBSURFACE RESPONSES: HURRICANE KATRINA[5]

Synopsis

Subsurface trapping of near-inertial energy commonly occurs in a baroclinic anticyclone. We found observational evidence supported by model simulation and ray-tracing that such trapping occurred in an intense frontal cyclone at the base of the Loop Current after the passage of Hurricane Katrina.

Summary of the Main Results

Hurricane Katrina left behind intense upwelling and downwelling cells in its wake; these cells generate near-inertial motions that propagate downward to depths of 500~1000 m beneath Eddy Vortex (a warm ring) and the Loop Current. Observations at the edge of the Loop Current after the storm show near-inertial energy amplified at a depth of approximately 600~700 m below the surface. Intense super-inertial (frequencies > Coriolis) motions arrived 3~5 days after the storm, and these were followed by sub-inertial motions that lasted for 4~5 days. Ray-analysis using the eddy field obtained from a numerical simulation with data assimilation suggests that the amplification was caused by trapping of near-inertial waves in a frontal cyclone at the base of the Loop. Super-inertial motions were triggered outside the Loop and rapidly propagated downward, while sub-inertial energy was triggered inside the Loop and was advected around the Loop before arriving at the mooring site.

4.1. INTRODUCTION

Near-inertial currents or waves (NIW's) are long internal waves with frequencies above the Coriolis frequency f (Gill, 1982), or above an effective Coriolis frequency $f_{eff} = f(1+\varsigma/f)^{1/2} \approx f + \varsigma/2$ for small Rossby number $Ro = \varsigma/f$ in (background) flow with non-zero vorticity ς (Mooers, 1975; Kunze, 1985—henceforth K85). Except for waves with anomalously low frequencies (Mooers, 1975), NIW's have frequencies above f_{eff}. Inertial energy initiated in a region with more negative vorticity than its surroundings would then tend to be trapped, e.g., inside an anticyclonic vortex, resulting in vertical "chimneying" of NIW's to subsurface. Shay et al. (1998) observed strong inertial motions (0.06 m s^{-1}) at a 725 m depth in a warm ring in the western Gulf of Mexico after the passage of Hurricane Gilbert. Kunze (1985) explains that in the case of a baroclinic eddy (e.g., warm rings, or the Loop Current, LC), there can be vertical trapping and mixing in a critical layer (see Kunze et al. 1995, for turbulence measurements in a Gulf Stream warm ring, and for an excellent review with other references).

By the same reasoning, once generated near the surface, NIW's tend to radiate away over a cyclone (defined as a localized region where $\varsigma > 0$); "chimneys" and trapping are less likely. However, background flow and topography of f_{eff} can be quite complex. Thus, NIW's may enter a subsurface mesoscale field and be surrounded by strong positive vorticity beneath and to one side, i.e., in a frontal cyclone, where inertial motions may then linger. Here, we describe such a trapping at a mooring (see location in Figure 4.1) near the LC in the Gulf of Mexico after the passage of Hurricane Katrina. Huang et al.'s (1998) Empirical Mode Decomposition for a non-

[5] This chapter is in part based on Oey et al. 2008.

stationary time-series is used to extract the NIW amplitude and frequency modulations. A numerical model is used to estimate the eddy field which is then used to calculate energy paths by ray-tracing.

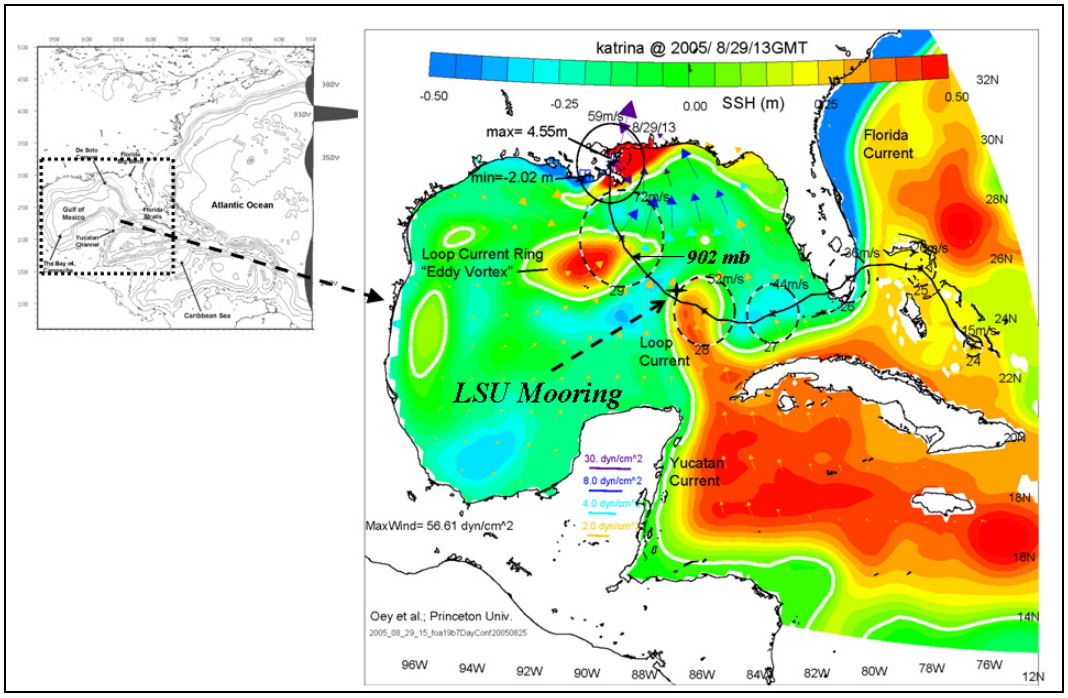

Figure 4.1. Study location and the location of the LSU mooring on a simulated SSH map during Hurricane Katrina on August 29 at 13:00 GMT. Katrina track is also shown together with daily "intensity circles" of radii that are proportional to the storm's maximum wind speed as shown. The small inset on left shows the entire model domain.

4.2. DATA

The LSU (Louisiana State University) mooring consists of two ADCPs, one upward-looking set at 140 m and the other downward-looking set at 3200 m at (87°W, 25.5°N; Figure 4.1) in water of 3356 m where the bottom is relatively flat. The period was May/30-Nov/302005. This paper focuses on NIW's produced by Hurricane Katrina (August 26-30, 2005), when the mooring was located near the northwestern edge of the LC. Additional Aanderra current meters were deployed between the two ADCPs to sample the entire water column. The top ADCP measured near-surface currents up to z = –60 m, while the bottom ADCP sampled near-bottom currents; the bottom-most currents were measured at z = –3340 m. We focus on the upper-level currents, roughly from z ≈ –100 m to about –1500 m below. Data return was excellent. The data is averaged and sampled hourly.

4.3. MODELS

The Circulation Model

The Princeton Ocean Model (henceforth "the model;" http://www.aos.princeton.edu/WWWPUBLIC/htdocs.pom/) is used to provide the background flow for ray-tracing (below).

The model includes LC and rings, assimilated using satellite data up to 7 days prior to a hurricane's entrance into the Gulf; thereafter the model is run for 16 days without further assimilation. The model has been extensively checked against observations (e.g., Yin and Oey 2007; see also http://www.aos.princeton.edu/WWWPUBLIC/PROFS/publications.html). The model horizontal grid Δ is variable from 3 km (northern slope) to 10 km (near the Yucatan Channel). For this work, 51 (instead of 26 in previous work) terrain-following sigma levels are used in the vertical, with twenty-three of them in the upper 1500 m of the water column near the mooring.

In principle, the model can give a detailed description of the complex three-dimensional NIW field (in response to wind forcing) and its interaction with the slower field of the LC and rings. However, the model's resolution is coarse particularly in the vertical in which $\Delta z \approx O(2\pi/k_3) \approx$ O(100 m), where k_3 = vertical component of the wavenumber vector **k**. Thus, the model can only describe qualitatively the structures of the NIW field, and how the up-and-down movements of the isopycnals behind the storm are sources of NIW's (see below). Paths of NIW energy cannot be accurately portrayed by the 3-D model, and we take it more as providing to the ray model (below) the slow background field (which the 3-D model does rather well; see above link or Chapter 1) through which NIW's propagate, rather than as a model that can resolve the details of NIW's.

The Ray-Tracing Model

The ray equations (K85) have reduced physics but these can be computed very accurately to describe NIW propagation. The model assumes small Ro and large geostrophic Richardson number Ri, but includes their effects (to first order) through f_{eff} and vertical (geostrophic) shears $\partial\mathbf{u_h}/\partial z$ ($\mathbf{u_h}$ = (u,v), horizontal velocity). The Eulerian frequency is:

$$\omega \approx f_{eff} + N^2k_h^2/(2f\,k_3^2) + (\partial\mathbf{u}/\partial z\times\mathbf{k}).\mathbf{n_3}/k_3 + \mathbf{k}\bullet\mathbf{u} \qquad (4.1)$$

is the sum of the intrinsic (ω_o) and Doppler-shift (**k•u**) frequencies, and is constant along the ray. Here, **u** = (u,v,w), N^2 = squared buoyancy frequency, $k_h^2 = k_1^2+k_2^2$ is the squared horizontal wavenumber and $\mathbf{n_3}$ is the unit vector in z. The ray equations are:

$$dx_i/dt = \partial\omega/\partial k_i + u_i \qquad (4.2a)$$
$$dk_i/dt = -\partial\omega/\partial x_i, \qquad (4.2b)$$

where i = 1, 2 and 3, x_i the position vector, u_i (=**u**) the flow velocity vector, and k_i (=**k**) the wavenumber vector. The RHS of equation (4.2b) is (minus) the group velocity with components given by:

$$C_{g1} = N^2k_1/(f\,k_3^2) - (\partial u_2/\partial x_3)/k_3 \qquad (4.3a)$$
$$C_{g2} = N^2k_2/(f\,k_3^2) + (\partial u_1/\partial x_3)/k_3 \qquad (4.3b)$$
$$C_{g3} = -N^2k_h^2/(f\,k_3^3) - (\partial\mathbf{u}/\partial x_3\times\mathbf{k}).\mathbf{n_3}/k_3^2 = Cgz1 + (Cgz2 + Cgz3) \qquad (4.3c)$$

In the above equations we have freely mixed the subscript notations (1, 2 and 3) with xyz-notations: thus, $(u_1, u_2, u_3) = (u, v, w)$, $(x_1, x_2, x_3) = (x, y, z)$, $(k_1, k_2, k_3) = (k_x, k_y, k_z)$ etc.

Equations (4.2a and b) constitute six differential equations which are solved using the fourth-order Runge-Kutta scheme with a time step = 0.1 hour. The modeled (u, v) field is used to

estimate the (initial) horizontal wavelengths using a method by Meid et al. (1986; who used ship data). Thus a mean (averaged over 10 days) large-scale velocity field is removed and the residuals which consist of inertial waves over the period of the storm are analyzed. Figure 4.2 shows a typical residual v-field along an approximately zonal line passing through the mooring at z=-410 m. One sees wavelengths of about 40-60 km from this plot. From profiles (similar to that shown in Figure 4.2) at different times and locations, we obtain a range of estimates of $2\pi/k_h$ = 35~70 km. For estimates of the initial vertical wavelength, a similar method is applied to the observed (u, v) at the mooring. (Unfortunately, the mooring resolution below 150m is not sufficiently fine to resolve meaningfully the λ_z.) Figure 4.3 shows an example of residual u (west-to-east; solid) and v (dash) plots for September 02, 2005, five days after Katrina passed over the mooring (we show below that this was when the first group of NIW's arrive at depths below the mooring). The figure shows that u leads v propagating downward, and the plot indicates a $2\pi/k_z = \lambda_z \approx 80$m (the parallel lines show every 8m). This and other similar plots (and also estimates using $\tan^{-1}(u/v)$) yield estimates of vertical wavelengths $2\pi/k_z$ = 70~140 m. Similar values of λ_z are also obtained using the model response though again one needs to be wary of the model limitation because of the relatively coarse vertical resolution used.

Rays are traced using these ranges of the wavelengths and also the wave angles k_2/k_1 (details below). These horizontal and vertical wavelengths are comparable to those estimated by K85 (40 km and 100 m), and by Meid et al. (1986; 32~50 km and 50 m). The $\mathbf{u}$, ς, N^2 and $\partial\mathbf{u_h}/\partial z$ are from the circulation model, averaged over 5 days: August 28-September 01, 2005 (5 days following the storm). The averaging is in accord with the "slowly-varying background" assumption implicit in the ray equations.

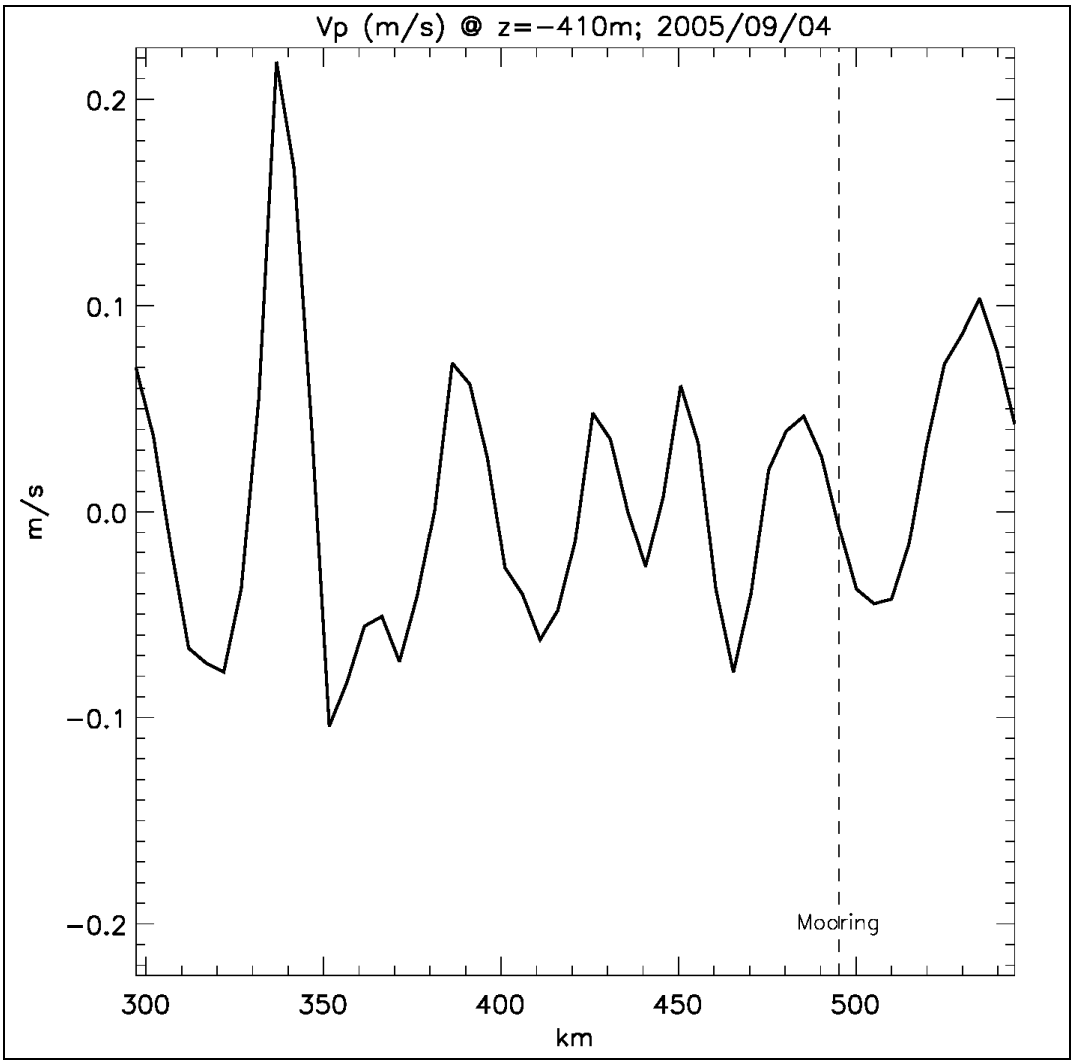

Figure 4.2. Residual y-component modeled velocity v after a mean large-scale field is removed (to reveal the inertial wave) along an approximately zonal line passing through the mooring at z=-410 m, on September 4, 2005 (approximately one week after Hurricane Katrina passed over the mooring).

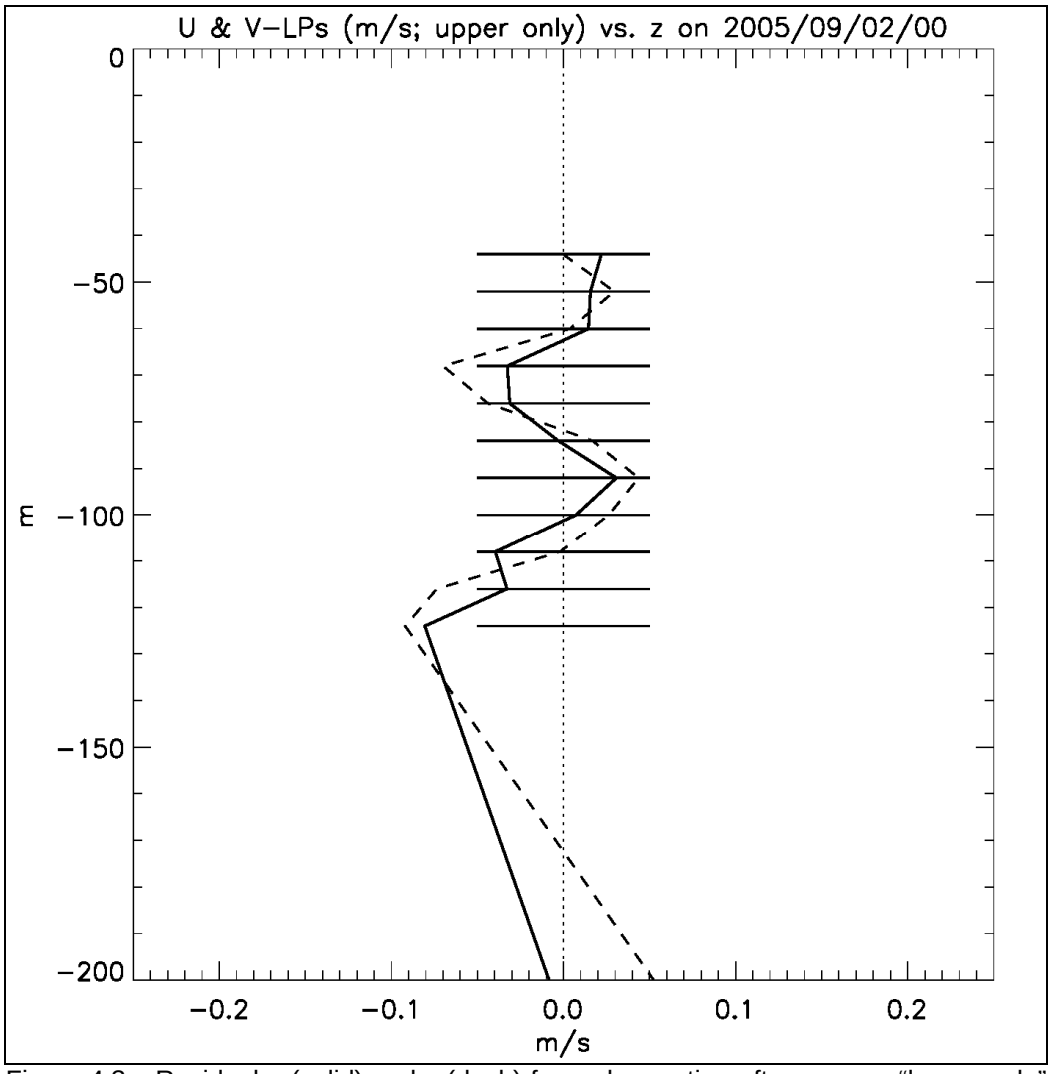

Figure 4.3. Residual u (solid) and v (dash) from observation after a mean "large-scale" vertical profile is removed (to reveal the inertial wave) at the LSU mooring on September 2, 2005.

4.4. RESULTS

Hurricanes produce mixing and flow divergences that alter the upper-ocean heat content (OHC), which in turn affects the storm (Emanuel, 2005b). The mixing is predominantly due to the current shears produced by the hurricane's strong wind stresses (e.g., Price, 1981). Flow divergences(±) result in vertical isopycnal movements with strong upwelling and downwelling cells ($w \approx \pm 10^{-3}$ m/s) which tend to be confined directly under the hurricane eye and in its wake (Price, 1981; Gill, 1982; Greatbatch, 1983). At a progression speed U of approximately 3 m/s, Katrina was a relatively slow-moving hurricane; however, the ratio of its progression speed to the first-mode baroclinic phase speed (which is C ≈ 2.5 m/s in the Gulf (Chelton et al. 1998)) ≈ 1.2. The storm is supercritical and leaves behind a train of lee waves which may be seen as upwelling and downwelling cells along the path (Geisler, 1970; Price, 1981). Figure 4.4 shows the SSH (colors) and currents plotted as Eulerian trajectories, on August 29 at 15:00 GMT;

Katrina track is also shown. Figure 4.5 shows the corresponding vertical velocity w at z = –100 m. The figures show that, while the train of lee waves is not apparent in the total surface elevation (SSH, Figure 4.4), the w-contours of Figure 4.5 show a series of alternating upwelling and downwelling cells aligned with the storm's path. The scales of these cells are approximately 100 km to either side of the track and the along-track wavelength is also about 100 km. Except for special field programs (Price, 1981; Shay et al. 2000), measurements of these cells are very difficult to make, yet the cells make up a large portion of the energetic signals induced by the hurricane; they serve in part as forcing of downward-propagating near-inertial waves that we will discuss below. The intensity of these cells is very strong with maximum and minimum vertical velocities reaching ±100 m/day respectively. We find that these extreme signals show up in sea-surface height anomalies (SSHA) in high-resolution track data from satellite altimeters, which can therefore be used to confirm the model's predicted positions of the cells—low SSHA correspond to upwelling cells etc (Oey et al. 2007). Figure 4.6 shows again the w-contours (similar to Figure 4.5) but for August 28 at 15:00 GMT when ENVISAT along-track data was available; the satellite track is shown as dashed line crossing almost exactly the position of the storm on August 28. The storm track is also shown color-scaled with Katrina's maximum sustained wind speed. The figure shows upwelling (blue; centered near the position of the storm on August 28) and downwelling (red; centered at 24.5^{o}N, about 200 km north of the western tip of Cuba) cells that have just been produced less than two days after Katrina. Figure 4.7 shows the SSHA; this shows a dip of about –60 cm around 24.5^{o} N coincident with the center of the upwelling cell mentioned above. It is encouraging that the location and timing of the upwelling cell behind the storm agree with the low in sea-surface height anomaly (SSHA) recorded by the satellite.

Figure 4.8 (map) shows sea-surface height (SSH) contours indicating the LC and a newly-shed warm ring (the Eddy Vortex), and the colors are depths of NIW-energy ("$(u^2+v^2)/2$" = 0.03 m^2s^{-2}) from the circulation model on September 03 at 12:00 GMT, 6 days after Katrina (c.f. Wang and Oey, 2008); inset on top-right shows the corresponding three-dimensional surface. Energetic inertial chimneys (current amplitude ≈0.24 m/s) penetrate to 1000-m depth to the right of the storm in the LC and warm-core ring. As seen in animation (not shown) and ray-tracing (below), the chimneys are advected anticyclonically around the rim of the LC and ring. Under the LC, penetration is deeper on the eastern side (> 1200 m compared to 800 m in the west). Regions outside the LC and ring are void of these strong inertial chimneys. The region of low SSH or cyclonic vorticity between the LC and the ring will be seen to be where super-inertial waves are produced by the storm.

Katrina winds ($|\mathbf{u_a}|$ > 60 m/s) produced a strong NIW response at the mooring. This consists of clockwise-rotating currents with downward-propagating group velocity through the upper 100~1000m (Figure 4.8; lower panel; Hurricane Rita is included for comparison). In the case of Katrina, the NIW penetrates and amplifies to depths of about z = –640m with amplitudes exceeding 0.3 m/s around September 05. The amplitude attenuates at z = –760m (not shown) to approximately 0.15 m/s, and quite abruptly becomes very small (amplitude <≈ 0.1 m/s) at z = –1005m. The response to Rita is less both in terms of the amplitudes and depths of penetration.

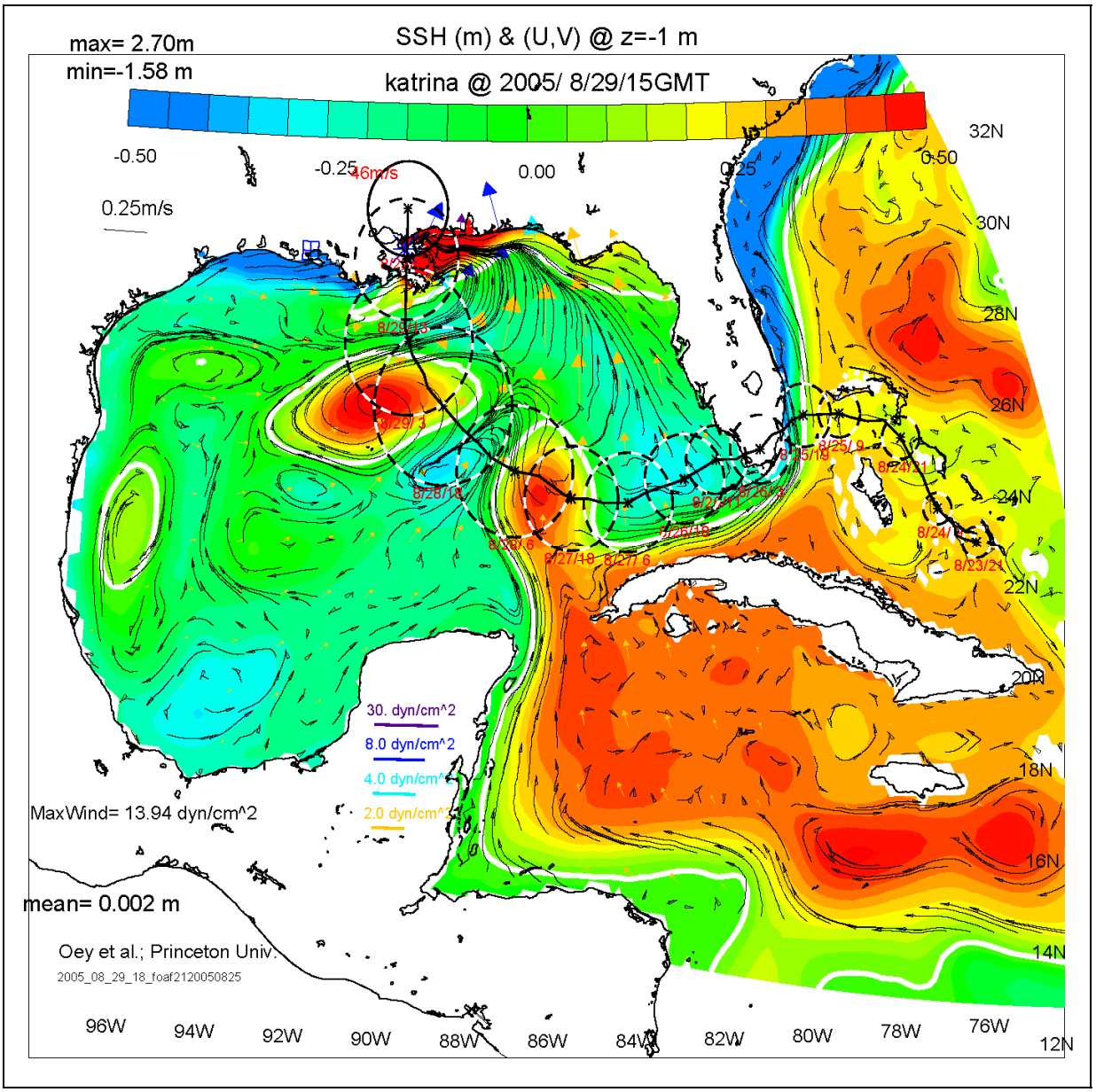

Figure 4.4. Simulated ocean response to Hurricane Katrina. Colors are sea-surface height (SSH; white contour is SSH = 0) on which the surface current trajectories at z=–1m are superimposed, on August 29 at 15:00 GMT just after the storm made landfall at New Orleans. Katrina's path is also shown with intensity circles plotted at 12-hourly interval. Colored vectors indicate wind stresses with the indicated scales.

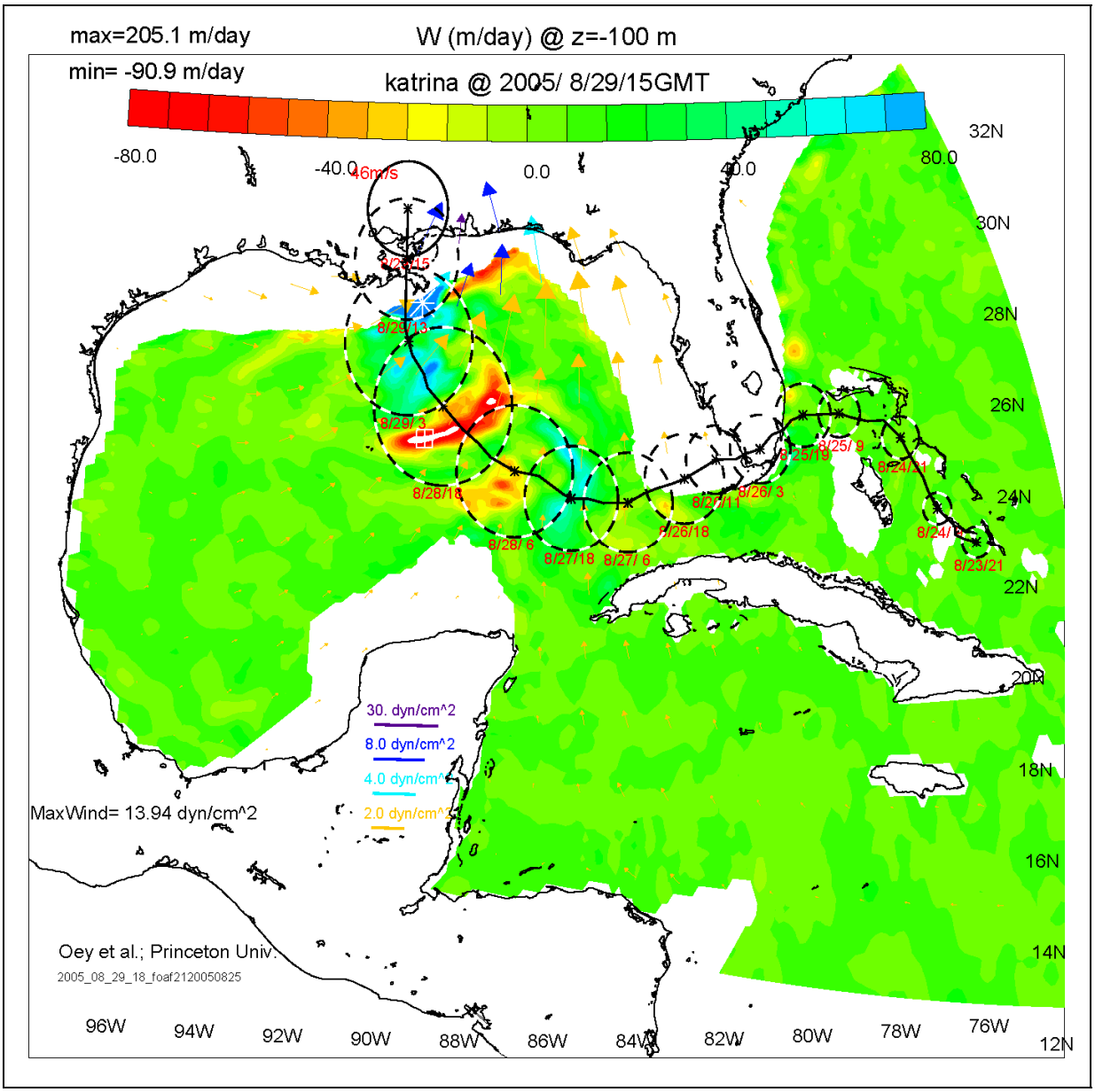

Figure 4.5. Simulated vertical velocity (w) (m/day) during Hurricane Katrina. White asterisk (south of the Mississippi Delta at 28.5°N) denotes maximum w and white square with a cross inside it (south of the Delta at 26°N) denotes minimum w (i.e., downwelling); values are printed on top left corner of the panel.

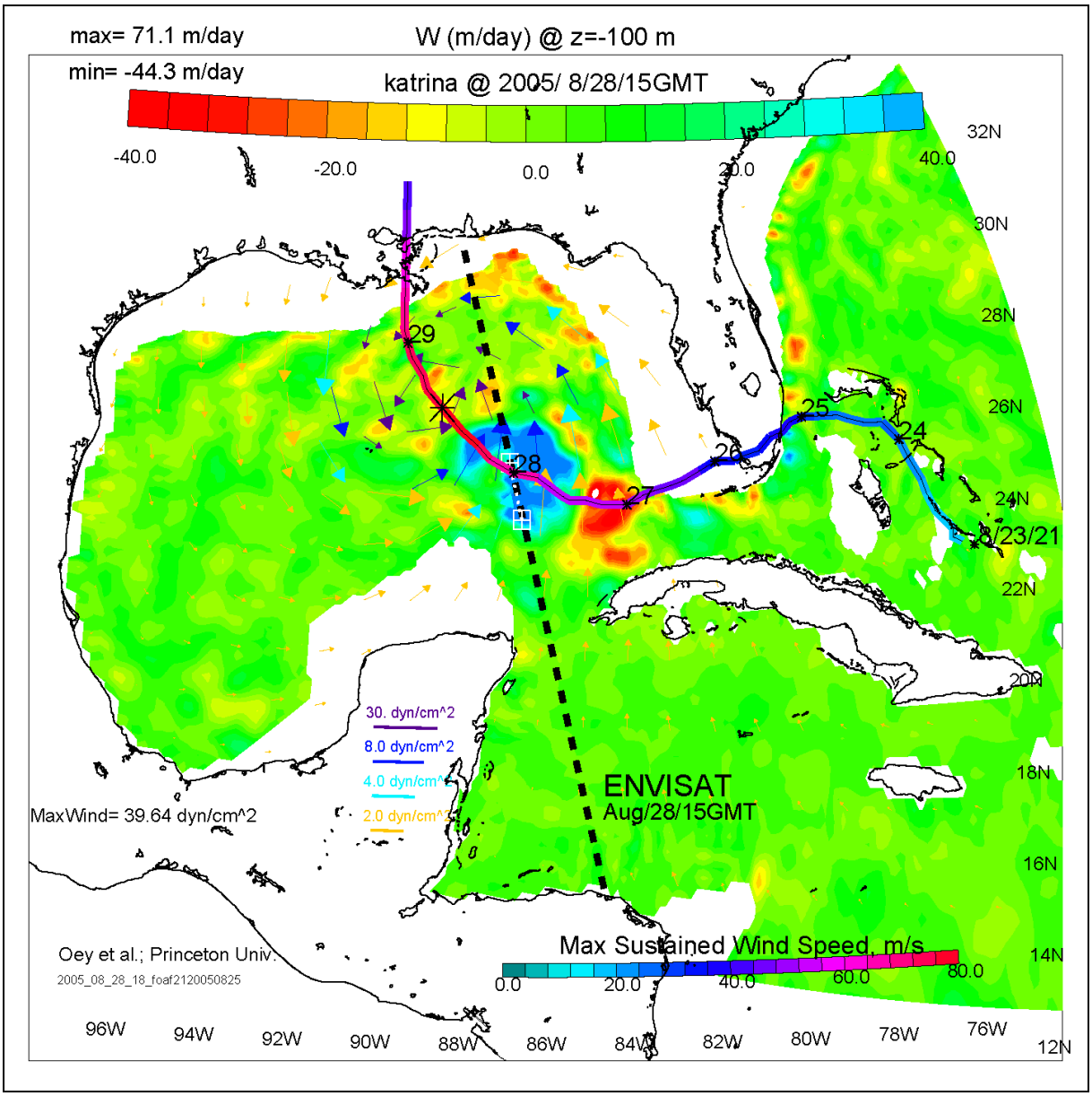

Figure 4.6. Simulated vertical velocity w contours (m/day; blue is upwelling and red downwelling) on August 28 at 15:00 GMT when Hurricane Katrina was at its peak strength. Vectors are wind stresses and colors indicate magnitudes shown. Katrina's path is shown with intensity indicated in color (color-bar at bottom); small asterisks indicate daily positions of the hurricane center, and the large asterisk position at the plotted time. The thick dashed line indicates ENVISAT satellite track, and the two white crossed-squares connected by dots along the satellite track indicate region of low SSHA (< –36 cm) as shown in Figure 4.7.

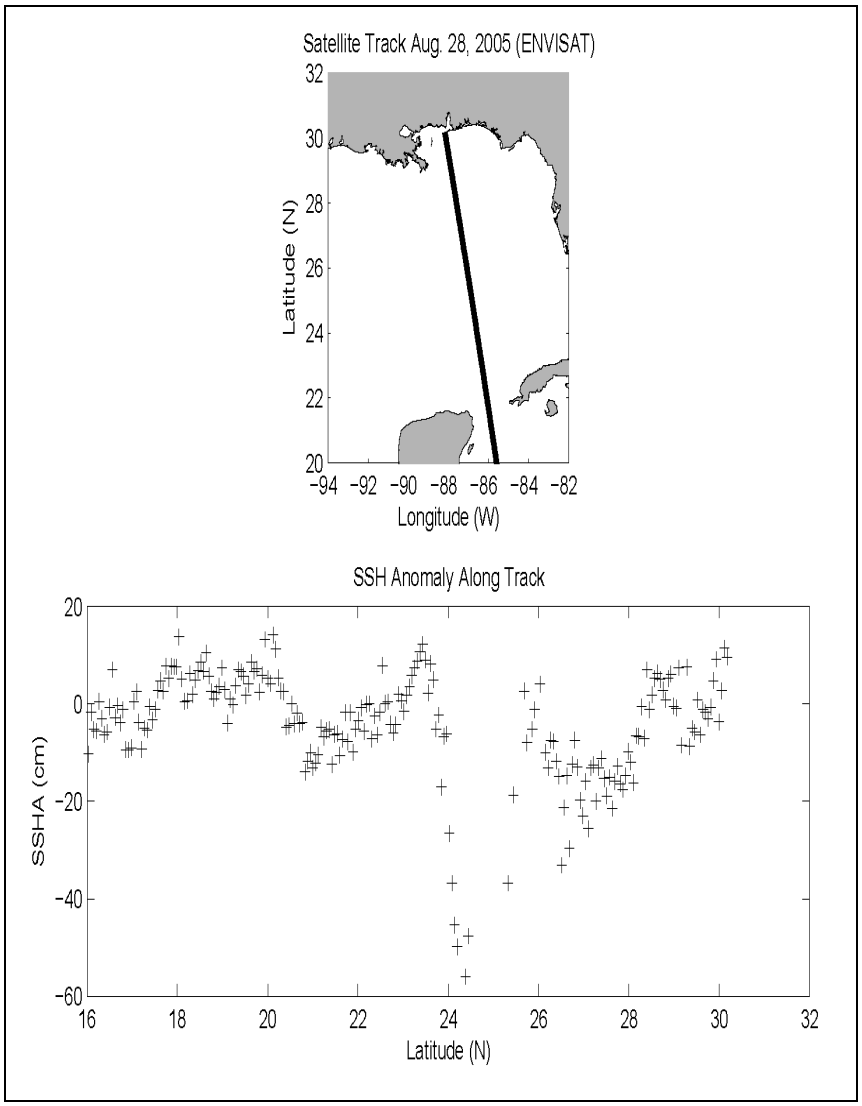

Figure 4.7. ENVISAT satellite sea-surface height anomaly (SSHA; lower panel) on August 28 at 15:00 GMT. Values less than –36 cm are indicated in Figure 4.6. Upper inset shows the ENVISAT track.

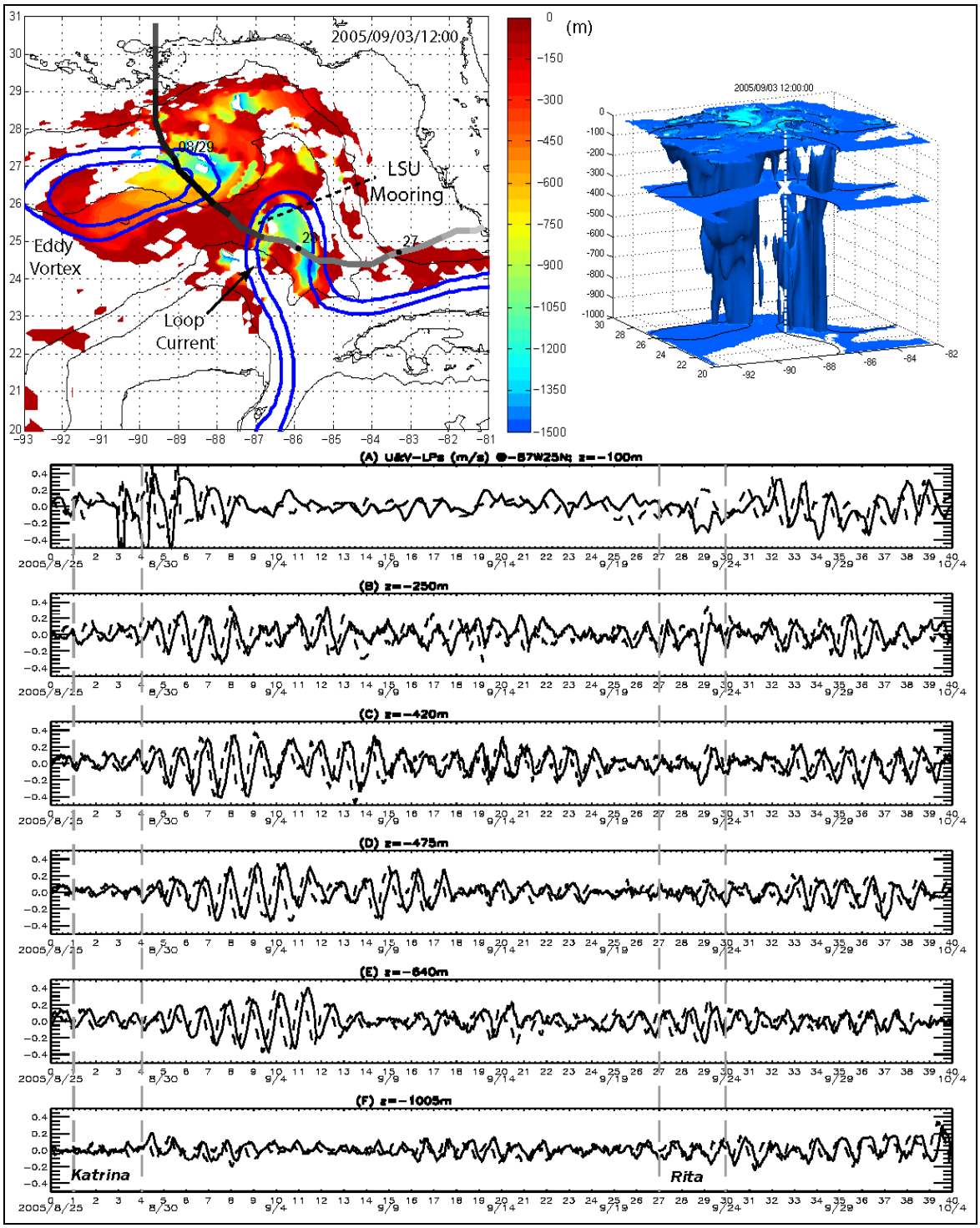

Figure 4.8. Map: study area showing depths (color) of NIW-energy = 0.03 m^2s^{-2} on September 3 at 12:00 GMT, mooring location, Katrina track (dark indicates wind speed > 60 m/s), and the thick contours are SSH = 0, 0.2 m. The top-right inset shows the corresponding 3-D surface of NIW. Time series: observed high-passed u (west-east; solid) and v (dashed) velocities (m/s) at the mooring at the indicated depths, during Hurricanes Katrina (August 26-29) and Rita (September 21-24).

Empirical Mode Decomposition Analysis

We use the Empirical Mode Decomposition to extract the various Intrinsic Mode Functions and then compute their Hilbert spectra (Huang et al. 1998; see also Lai and Huang, 2005 for an oceanographic application of the method). Unlike FFT, Huang et al.'s method can accommodate rapid frequency variations with little spurious harmonics. The time series can be non-stationary as well as non-linear. The method is efficient; for our time series it yields only nine intrinsic modes each of which (after the Hilbert transform) gives frequency and amplitude (hence energy) as a function of time. The first mode is short-period (hours) fluctuations with very small amplitude (rms ~ 10^{-3} m/s), while the ninth is the 'residue' which is (nearly) constant (in time) and has also a very small amplitude (rms ~ 10^{-4} m/s). Modes in between have various amplitude and frequency contents. The second and third modes have near-inertial periods. Their Hilbert spectra for the 6-month period Jun-Nov, 2005 near the surface ($z \approx> -250$ m; not shown) indicate strong NIW-energy variation both in amplitude and frequency, and a tendency for sub-(super-)inertial waves to be produced when the mooring is inside (outside) the LC where $\varsigma < 0$ ($\varsigma > 0$). Figure 4.9a shows the spectra at $z = -640$ m focusing on the response to Katrina. This shows energy E (red indicates high > 3×10^{-2} m^2s^{-2}) as a function of time (August 25-September 14) and ω/f, where $f \approx 6.28\times10^{-5}$ s^{-1} at the mooring location. Black line is the wind power $P_w = \log_{10}((|\mathbf{u_a}|/5)^3)/4$ (plot positive only; i.e., for $|\mathbf{u_a}|>5$ m/s) at NDBC 42003 (25.74° N, 85.73° W) near the mooring, and the peak indicates passage of Katrina. Figure 4.9a shows that the high-E response that arrives first 3~5 days after the storm (on September 1~3) are super-inertial ($\omega/f > 1$); the mooring then recorded sub-inertial ($\omega/f < 1$) waves on September 4~6. Figure 4.9b shows contours of the time-integral Hilbert spectra, $h(\omega; z)$. Data less than 200 m from the bottom were omitted. To make a smooth plot, the $h(\omega; z)$ is calculated for the entire 6-month period, but it is dominated by Katrina. Figure 4.9b shows asymmetric distribution of energy towards $\omega/f < 1$ in the upper 1000 m of the water column. At lower frequencies ($\omega/f <\approx 0.4$) nearer the surface, the asymmetry is because the mooring was located predominantly within the LC during the observation period. At near-inertial frequencies, ($0.8 <\approx \omega/f <\approx 1.2$), the asymmetry indicates bias towards slightly sub-inertial oscillations in a negative background vorticity field $\varsigma/f < 0$. A conspicuous feature is the intensified subsurface NIW energy near $z \approx -500$ m to -700 m.

Ray Analysis

The model indicates that the LC and Eddy Vortex play an important role in horizontally advecting and also vertically confining the NIW into "chimneys" (Figure 4.8). Experiments with initially-level isopycnals (i.e., no LC and rings; not shown) produce very different NIW response confined to the upper 200 m. We now use the model flow field and show by way of ray-tracing how the subsurface intensification of NIW energy (Figure 4.9b) may be explained by stalling (vanishing $\mathbf{u} + \mathbf{C_g}$ ($=(C_{g1}, C_{g2}, C_{g3})$, the group velocity)) of rays at the base of the LC.

Each ray is traced from the mooring at $z = -600$ m, with initial vertical wavelengths $2\pi/k_z$ incrementally looped from 70–140 m, horizontal wavelengths $2\pi/k_h$ from 35–70 km and wave-angles k_2/k_1 from $-\pi$ through π. Rays are excluded if they do not pass above $z = -200$ m and when they do, if no portion of the ray comes within 100 km on either side of Katrina. These limits are reasonable for inertial energy originating from the storm, and result in two (more manageable) groups of rays represented by Rays#1W and 1E respectively in Figure 4.9c. Ray#1W (1E) is super- (sub-) inertial NIW's originating from the west (east) or cyclonic (anticyclonic) side of the LC in the proximity of the storm's track. Other rays that do not pass

through the mooring at z ≈ –600 m are also similarly traced: examples are rays 2, 3 and 4 in Figure 4.9c.

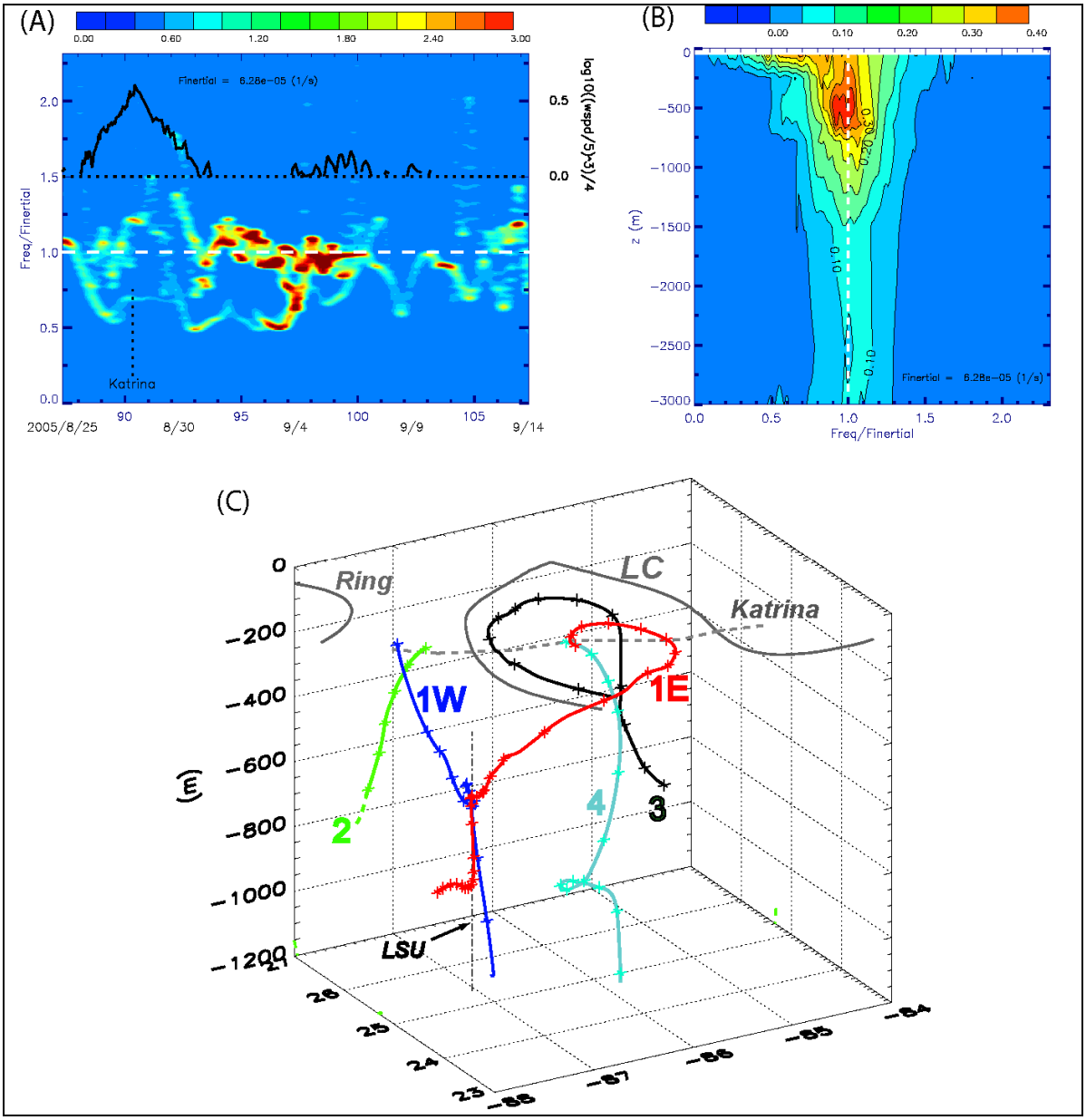

Figure 4.9. (A) Hilbert energy spectra (color; unit: 10^{-2} m^2s^{-2}) of near-inertial currents at z = –640 m as a function of time (days since May 30, 2005, and date are shown) and ω/f. Black line is wind power at NDBC buoy 42003. (B) Time-averaged Hilbert spectra as a function of ω/f and depth. (C) Near-inertial wave rays "1" through "4" marked daily (by '*'). The Loop (LC), ring and Katrina track are shown.

Ray#1W shows that the NIW energy observed at z ≈ –600 m (Figure 4.9b) originates near the surface (z = –100 m) approximately 70 km west and 20 km north of the mooring, i.e., near the Katrina's center on August 28 at 10:00:00 GMT between the LC and Eddy Vortex, in a region of positive ς so that $f_{eff} > f$. The ray propagates towards the base of the LC (z ≈ –600 m of

the mooring); the arrival time, 4~6 days later, approximately agrees with that observed (Figure 1). The ray 'stalls' near z = –600 m (crowding of the daily markers '*', for about 7 days), suggesting an accumulation of energy there. This coincides with the observed intensification of energy near this depth (Figure 4.9b). At first thought, however, the stalling is puzzling because rays originating west of the LC (as ray#1W) propagate into a region of increasingly negative ς in the LC (i.e., a smaller f_{eff} than its initial value) and thus would either penetrate deep (deeper than z ≈ –600 m) or otherwise would be reflected (K85). We explain below what cause the 'stalling.'

Loop Current frontal cyclones are often seen in high-resolution satellite SST's (e.g., http://fermi.jhuapl.edu/avhrr/gm/averages/index.html). These cyclones originate as small perturbations along the highly sheared current on the western side of the LC in the Yucatan Channel and amplify (in the model) through baroclinic instability over the north Campeche Bank as the LC enters the deep water of the Gulf of Mexico; the LSU mooring is located where frontal cyclones often pass (Oey, 2008). During Katrina, the model suggests that a subsurface cyclonic meander sat astride the mooring. Figure 4.10a shows this with ς/f (color) and velocity at z = –600 m where a subsurface cyclone with maximum $\varsigma/f \approx +0.4$ and a diameter of about 70~100 km is seen. From the surface, where $\varsigma/f \approx +0.23$ (not shown), ray#1W first propagates downward (towards the LC) through an environment of weaker and even slightly negative ς before encountering the cyclone where the f_{eff} increases under and east of the ray, the ray's intrinsic frequency ≈ f_{eff}, hence $(k_h/k_3)^2$ (equation 4.1), and its vertical group velocity C_{g3} (equation 4.3c) become small near the cyclone. This behavior is illustrated in Figure 4.11, which plots the terms on the RHS of equation (4.3c) as well as the "w" and "C_{g3}+w" terms along Ray1W (ray originating west of the mooring) as it propagates downward and eastward towards the mooring's depth at z≈–600m. The figure shows that Cgz1 (black line; which remains <0 throughout the ray-trajectory) dominates the "vertical-shear" terms Cgz2 (lighter blue) and Cgz3 (orange). It shows also that, from the surface through z ≈ –350 m, the ray propagates first through a region of downwelling w (green) < 0 before encountering upwelling (for z <≈ –350 m) as it nears the subsurface cyclone. The total "C_{g3}+w" (darker blue) follows closely the dominant term Cgz1 (black line) but with important (and interesting) modification near the stalling depth z ≈ –600 m when "C_{g3}+w" actually becomes slightly positive because of the increased upwelling (w ≈ +30 m/day, green) near the cyclone. Therefore, because of the weakened Cgz1 (< 0) near the cyclone, the upwelling counters the downward C_{g3} and helps to maintain the vertical stalling near the cyclone.

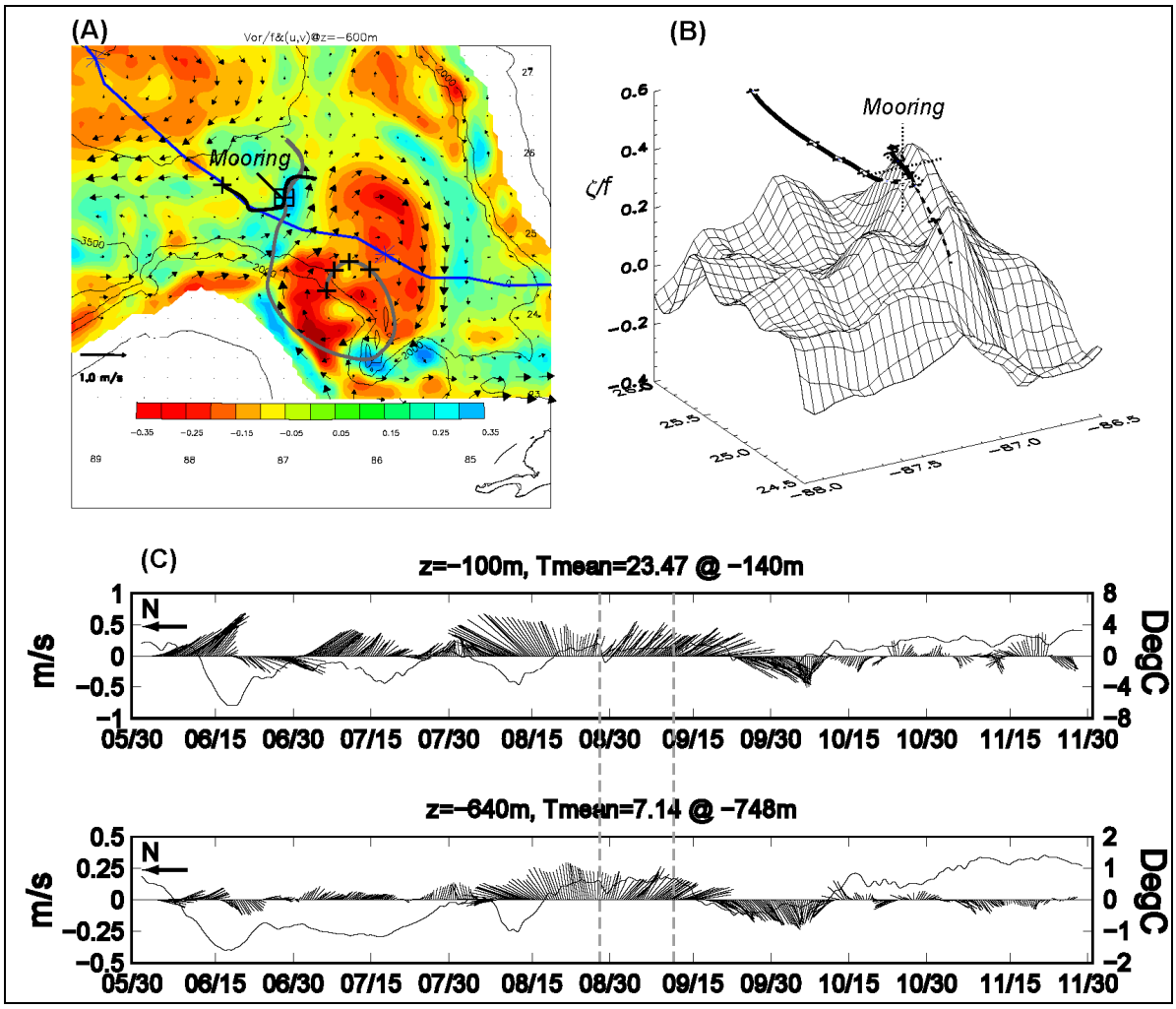

Figure 4.10. (A) Modeled vectors (shown every 4 grid points) and ς/f (colors) at z = –600 m. The mooring location is where super-(black) and sub-(dark grey) inertial NIW rays pass at z = –600 m; shown are rays projected onto the xy-plane. The rays' locations at z = –100 m are marked by "+" which also marks the first 3-daily locations of the sub-inertial ray. Katrina track is shown in blue and the two asterisks on it mark the storm's positions on August 28 and August 29 respectively. (B) The same ς/f plotted as 3-D surface toward which ray#1W propagates. (C) Observed 40-hour low-passed velocity shown as sticks at z = –100 m and z = –640 m with positive y-axis pointing due east, and temperature time-series (solid line) shown as deviation from the mean shown at the indicated depths. The temperatures are taken from the depths nearest to the depths of the ADCP velocity measurements. Period when NIW's are prevalent is bracketed in grey dashed lines.

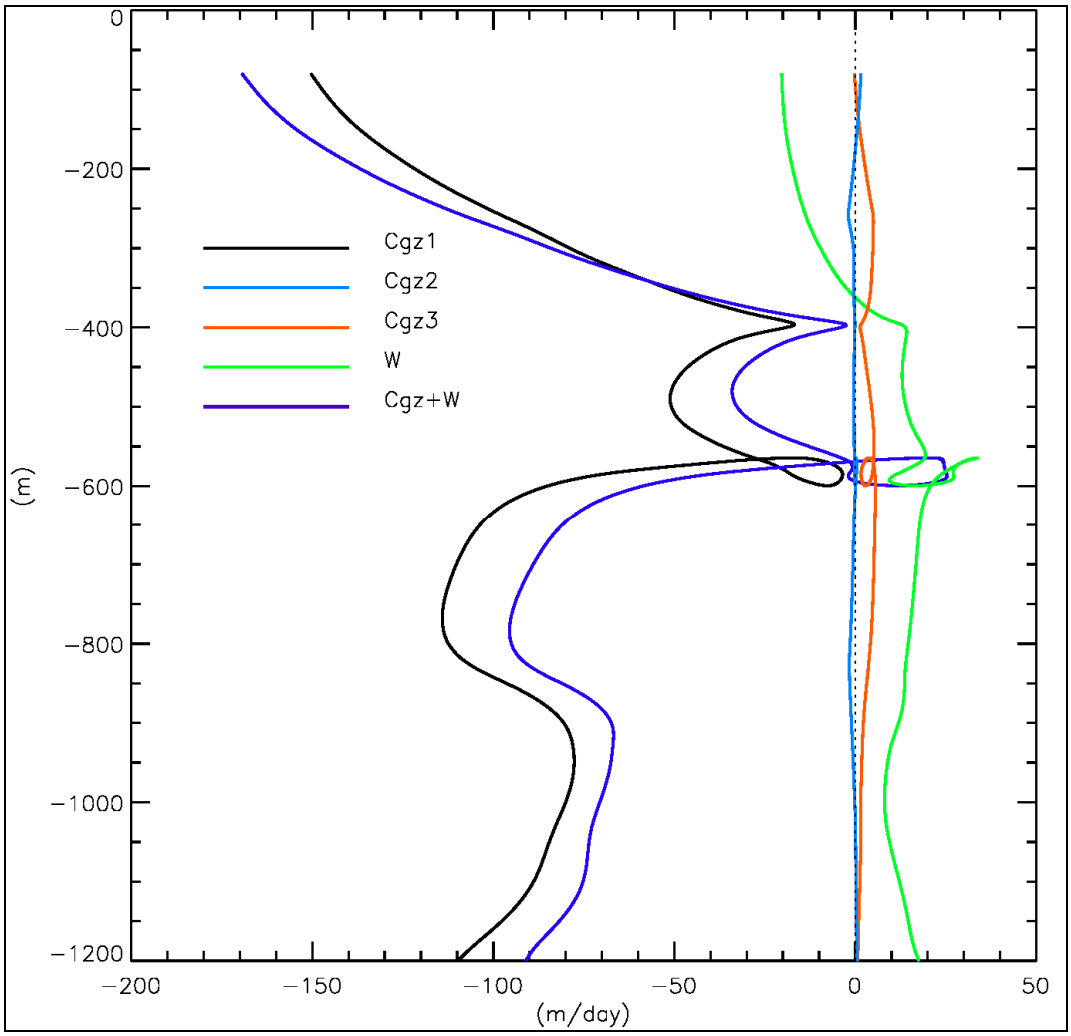

Figure 4.11. Plots of the various terms in the vertical component of the group velocity, as well as of the vertical velocity w, and the total Cgz + w along the ray#1W of Figure 4.9c as discussed in text.

Why is Cgz1 weak near z ≈ –600m? Figure 4.12 plots its two factors, k_h^2/k_z^3 and N (the factor 1/2 is included for plot convenience), again along Ray1W. This shows that N decreases by about 60% from the surface to z ≈ –600m. Thus the N^2/f factor alone weakens Cgz1 by a little more than a factor of 2 (f ≈ constant). There is a much more significant decrease due to k_h^2/k_z^3 and near z ≈ –600m this factor becomes ≈ 0. It is quite easy to understand why k_h^2/k_z^3 decreases drastically near z ≈ –600m (there is another though less dramatic decrease near z ≈ –400m, and the effect on "C_{g3}+w" is notice-able though (with the help also of a quite significant horizontal mean flow at this depth, not shown) the wave is able to "escape", Figure 4.11). To see what factors contribute to a decrease in k_h^2/k_z^3 we examine separately how k_h^2 and k_3^3 (or k_z^2 since $k_z > 0$ for downward propagating wave packet—i.e., Ray1W) behave along the ray near the cyclone.[6] The analysis will show the important role played by the strong positive ς (its gradients)

[6] A similar analysis was done on how topographic Rossby waves (TRW) are refracted by the mean shear in Oey and Lee (2002). As a side-note, under some fairly general conditions, there is a remarkable equivalence between the interpretation of TRW and internal waves rays (Oey, 2008).

on stalling. Take the dot product of **k** with the ray equation for **k** (equation 4.2b), and use equation (4.1):

$$d(k_h^2)/dt \approx -\mathbf{k_h}\bullet\nabla\varsigma + (k_h^2/k_3)(\partial\varsigma/\partial z) \qquad (4.4a)$$

$$d(k_3^2)/dt \approx -k_3\,((\partial\varsigma/\partial z) + k_h^2/(fk_z^2)\,\partial N^2/\partial z + 2(\mathbf{k_h}\times\nabla B)|_z/f) \qquad (4.4b)$$

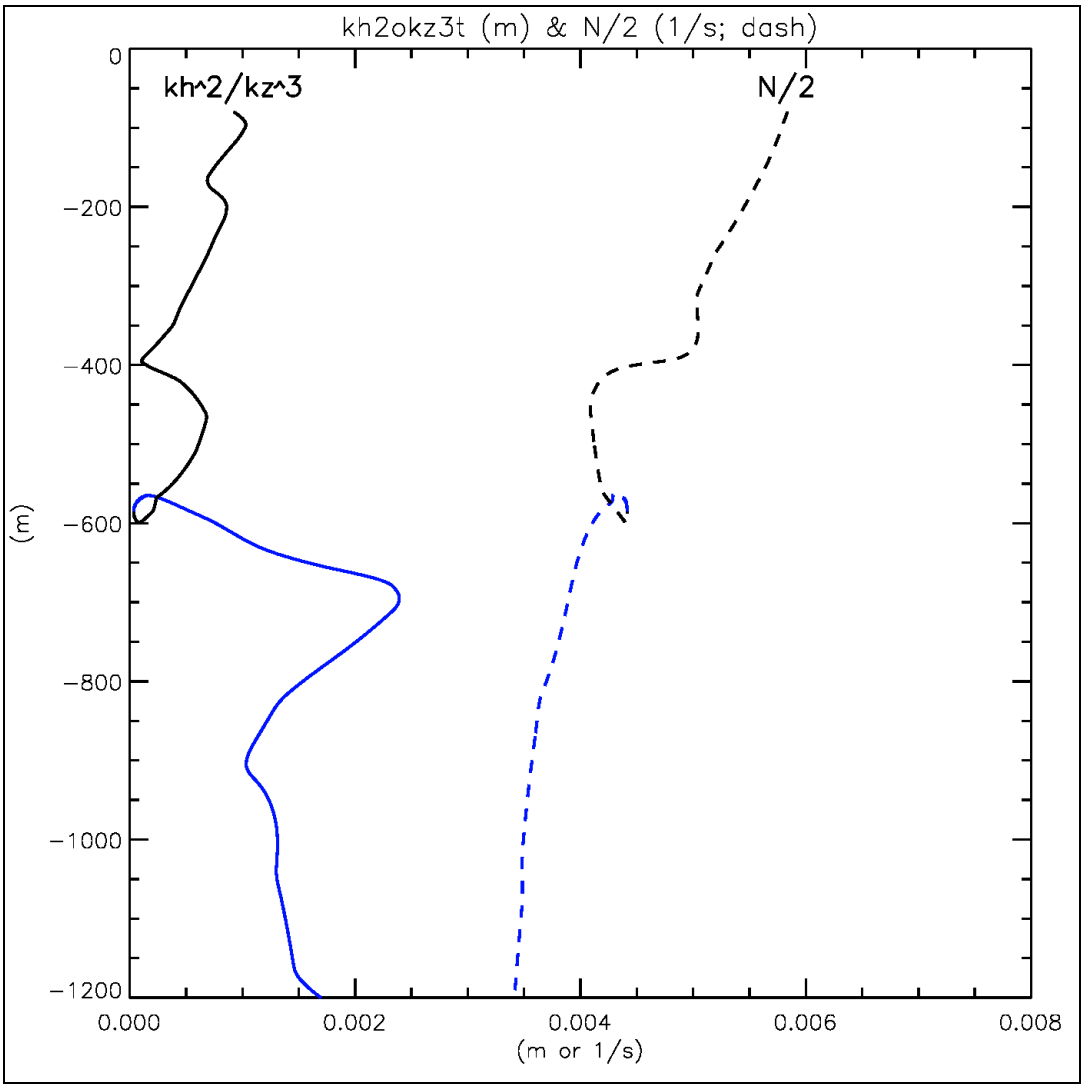

Figure 4.12. Two factors, kh^2/kz^3 and N (the factor 1/2 is included for plot convenience) that constitute the first (dominant) term C_{gz1} on the RHS of equation (4.3c) for the vertical component of the near-inertial wave group velocity, plotted along Ray#1W (c.f. Figure 4.11). The curves have been (arbitrarily) color-coded to indicate an upper (roughly above z ≈ –600 m; black) and lower (blue) trajectories.

Here, several small terms involving ∇N^2, w, u_{zz} and v_{zz} are dropped, and $B = g\rho/\rho_o$. We also let shears $v_x \approx -u_y \approx \varsigma/2$, a convenient (for symmetry) but inconsequential assumption. Approaching the subsurface cyclone from northwest and surface, we have (k_1, k_2, k_3) = (>0, <0, >0); the vector (k_1, k_2) makes an angle a little less than 45° clockwise from the x-axis, so that

since $\nabla\varsigma$ points eastward towards the cyclone, we have $\mathbf{k_h}\bullet\nabla\varsigma > 0$ (Figure 4.13). Approaching the cyclone from above, the vorticity increases (more positive; this too has been verified from the circulation model simulation) so that $\partial\varsigma/\partial z < 0$. Therefore k_h^2 tends to zero from equation (4.4a). This is confirmed in Figure 4.14 which shows that k_h decreases. Moreover, the figure also shows that k_3 increases near the cyclone. From equation (4.4b), the last two terms $\partial N^2/\partial z$ and $(\mathbf{k_h}\times\nabla B)|_{\mathbf{z}}/f$ are both positive (∇B points eastward towards the cyclone's center) so they cannot account for the increase in k_3. Thus only the first term on the RHS of equation (4.4b) with $\partial\varsigma/\partial z < 0$ is principally responsible for the increase in k_3.

Wang (1991; based on Mooers, 1975) found that anomalously-low-frequency ($\omega < f_{eff}$) waves from the cold side of a front can be trapped vertically at subsurface where isopycnals become flat[7]. We find that some rays are indeed anomalously-low-frequency. However, vertical trapping alone cannot explain why the ray stalls. Figure 4.10a shows that the ray at $z \approx -600$ m comes very near the center of the cyclone (defined as the location where ς/f is a maximum $\approx +0.4$), but does not cross it. This behavior is seen in Figure 4.10b which displays the ς/f as a surface towards which the ray propagates from above. In addition to being blocked from below, the ray bends northward being blocked also by the ς/f-ridge formed by the strong cyclonic meander. This is consistent with the above discussion on equation (4.4); since k_h^2 and k_3^2 are nonnegative, equation (4.4) puts a strong constraint on the allowable space to which ray paths may traverse. As seen in Figures 4.9c and 4.10a and b, the Ray1W cannot penetrate below the cyclone, nor to the east of the cyclone where the strong positive ς-ridge is present. Thus near-inertial motions are trapped inside the cyclone until, after about 7-day stalling, ray#1W is able to escape, and radiates horizontally and rapidly downward away from the mooring (Figure 4.9c).

A similar "stalling" occurs for ray#1E (Figure 4.9c). However, after radiating away from the ridge (cyclone), since this ray is sub-inertial, it stalls a second time at $z \approx -950$ m. Ray#1E is also strongly influenced by the LC. It follows and remains in the near-surface anticyclone of the LC for a relatively long time (5~6 days) before propagating downward towards the mooring at $z = -600$ m. Though not shown here, other rays (by varying the initial wavenumbers) originating on the western or cold (eastern or warm) side of the LC behave similarly as ray#1W (1E). Similar results are also obtained for rays through $z = -650$ m (instead of -600 m); but rays below $z = -650$ m are very different as they do not originate from the surface. In summary, then, the observed NIW-intensification near these depths at the LSU mooring may be explained by an accumulation of energy caused by trapping of NIW's by a subsurface cyclone, whose high $\varsigma/f > 1$ moreover prevents energetic NIW's from reaching mooring depths directly below. In vertical, the cyclone acts like an NIW-umbrella with its top at the mooring's depths at $z \approx -600$ m to -650 m, and explains why the observed NIW's attenuate at depths of 1000 m and deeper. The different arrival times of energetic NIW's at the mooring – super-inertial followed by sub-inertial (Figure 4.9a) – is caused by the strong influence of the LC on the latter waves as they are forced to loop around the anticyclone before escaping to deeper levels.

[7] The phase C_{p3} and group C_{g3} velocities are generally of opposite sign. For a.l.f waves, there is a narrow range, $1 > s/|\alpha| > 1-s^2/N^2$, for which C_{p3} and C_{g3} have the same sign (Mooers, 1975; Wang, 1991), where $\alpha = k_1/k_3$ and s is the isopycnal slope; $C_{g3} \sim O(s^2) << 1$. This range disappears under Kunze's (1985) approximation.

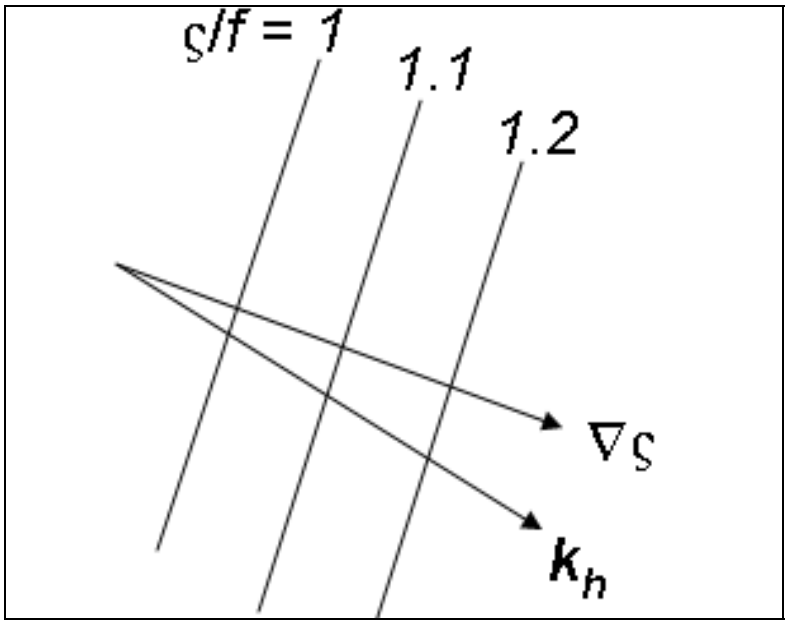

Figure 4.13. A schematic sketch of the ς/f-field near the cyclone and the horizontal direction of the wavenumber vector of ray#1W.

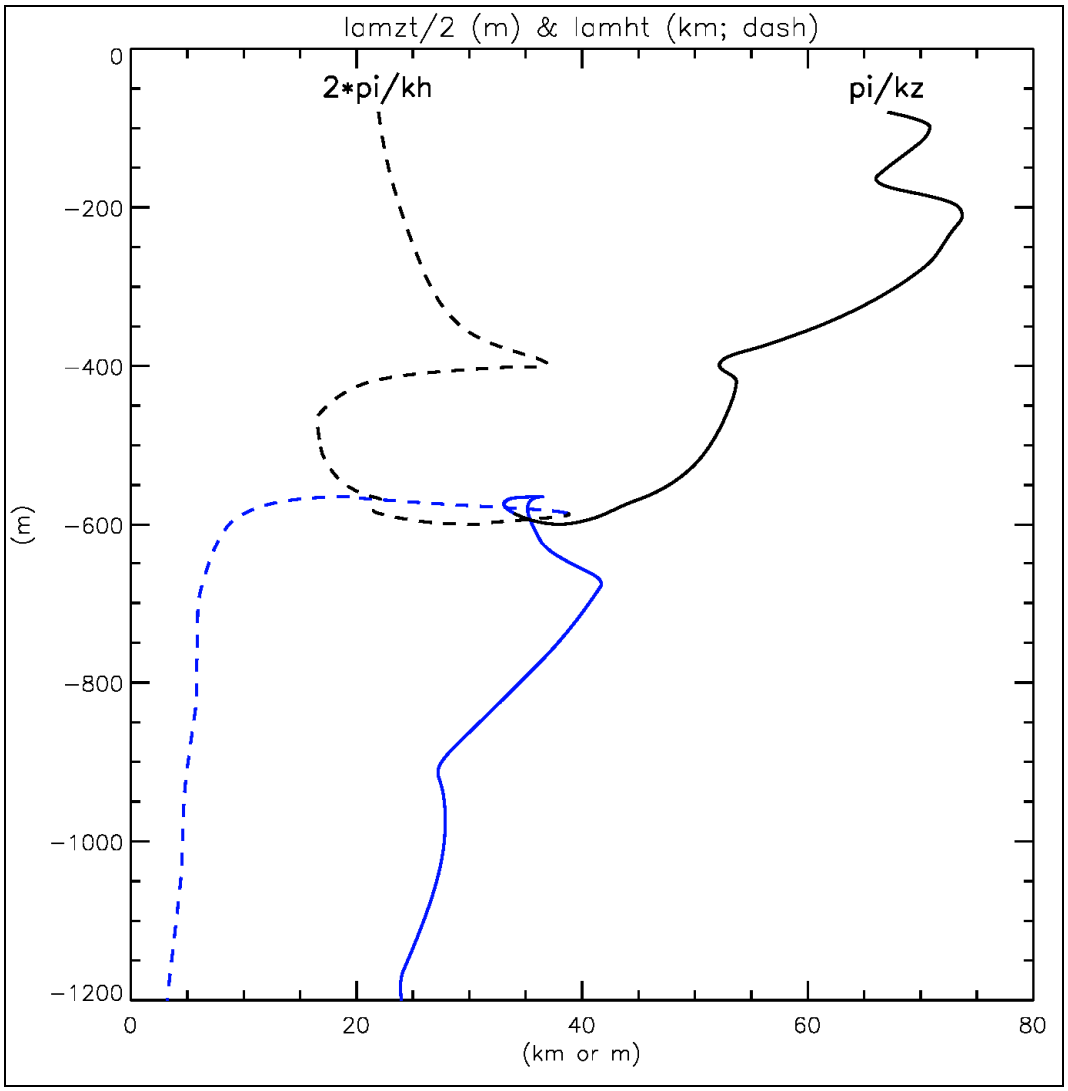

Figure 4.14. Plots showing the behaviors of the horizontal and vertical wavelengths of near-inertial wave ray#1W.

Other rays in Figure 4.9c illustrate different aspects of NIW spreading. Ray#2 begins near the surface between the LC and Eddy Vortex. It is "sucked" into Eddy Vortex (where f_{eff} is less), into the "chimney" seen in the ring (Figure 4.8). Ray#3 begins at the western side of the LC but within it, and displays a round-the-LC progression as it is being sucked anticyclonically downward to the eastern side, in rough agreement with the numerical simulation (e.g., Figure 4.8). There is no trapping in these two cases. Finally, ray#4 begins inside the LC in a region of strongly negative ς/f (≈ -0.4 at $z = -100$ m). This ray stalls at $z \approx -900$ m where in fact ς/f reaches a local maximum (≈ -0.1) and the ray's intrinsic frequency $\approx f_{eff} \approx 0.93$ f. However, the (PE) model ς/f is complicated: ς/f decreases (more negative, not shown) below $z \approx -900$ m. The combination of this and a strong downwelling velocity field, $w \approx -50$ m/day, allows ray#4 to penetrate deeper under the LC.

4.5. DISCUSSION AND CONCLUSIONS

As mentioned above, the model cyclone was spun up through an instability process (Oey, 2008). The ray-stalling mechanism, which depends on the existence of the cyclone, could therefore be coincidental. However, there is indirect evidence that a cyclone was present. Firstly, Eddy Vortex had separated or was in the process of separating from the LC during Katrina (Figure 4.8); shedding is often accompanied by the development of deep cyclones (e.g., Oey, 2008). Secondly, observed velocities at the mooring show 'open-fan' structure during the period when trapping occurred (Figure 4.10c); the open-fan is indicative (but not proof) of a cyclone passing the mooring. Finally, during the open-fan period the temperature decreases and then rises, a characteristic that is also consistent with the passage of a cyclone.

Summarizing, measurements after Hurricane Katrina indicate energetic NIW's intensified at $z \approx -600$ m, with amplitudes ≈ 0.3 m s^{-1}. The first waves that arrive at the mooring are super-inertial and originate from location to the west and north of the LC. Sub-inertial NIW's on the other hand originate from near the LC's center, and spiral anticyclonically and downward following the LC, arriving 1-2 days later. Both types of waves stall at approximately the above-mentioned subsurface level. Trapping is explained by waves entering a region where an intense subsurface frontal cyclone ($\varsigma/f \approx +0.4$) sat astride the mooring.

As pointed out by Kunze (1985; also Lueck and Osborn 1986, and Kunze et al. 1995), trapping of NIW's can lead to critical layers and mixing. Recent observational and modeling studies in the Gulf of Mexico suggest that subsurface cyclones are ubiquitous features of deep-ocean eddy field (e.g., Oey, 2008). Thus, in addition to anticyclones, the proposed mechanism of wave-stalling in subsurface cyclones can potentially contribute to deep mixing.

CHAPTER 5. STORM-INDUCED, NEAR-INERTIAL RESPONSES DURING THE 2005 ATLANTIC HURRICANE SEASON IN THE GULF OF MEXICO

Synopsis

We extend the model simulation and analyses (Chapter 4) of near-inertial responses at the LSU mooring in the Loop Current, as well as at other ADCP moorings in the northern Gulf of Mexico to the entire 2005 Atlantic hurricane season. We then compare the responses due to Rita with those due to Katrina.

Summary of the Main Results

Measurements at a mooring near the Loop Current in the Gulf of Mexico, Jun-Nov, 2005, show energetic subsurface ($z <\approx -200$ m) near-inertial waves (NIW), produced by the active hurricane activities during that period. The Empirical Mode Decomposition analysis gives a time-dependent frequency (ω) which visually correlates with the background vorticity (ς), roughly in agreements with the theoretical expectation that sub-inertial ($\omega < f$ = Coriolis frequency) NIW's tend to be produced in regions of anticyclonic vorticity ($\varsigma < 0$) and super-inertial NIW's in cyclonic-vorticity regions. Rings and Loop Current are therefore particularly efficient conduits through which near-inertial waves can propagate to deep depths and their strong currents can distribute the near-inertial energy through large horizontal distances. After Hurricanes Katrina and Rita crossed over Eddy Vortex (a warm ring), for example, the inertial currents penetrated to $z <\approx -1000$ m, and were spread around the ring and to the left side of the storm tracks for hundreds of kilometers. Such simulated phenomena are supported also by other ADCP measurements over the northern Gulf slope.

5.1. INTRODUCTION

Vertical profiles of currents, temperatures and salinities were measured with ADCP's (Acoustic Doppler Current Profilers) and Anderaa's at (87^{o}W, 25.5^{o}N) during the 2005 Atlantic hurricane season, from June through November, 2005. The instrument not only recorded ocean responses to four intense hurricanes: Dennis, Katrina, Rita and Wilma, it was also located in an ocean environment actively influenced by the Loop Current, the dominant feature of the circulation in the eastern Gulf of Mexico and the formation region of the Florida Current-Gulf Stream system (Figure 5.1). (The reader is referred to the recent collection of papers contained in Sturges and Lugo-Fernandez (2005), and references therein, for a glimpse of the current state of knowledge of the circulation in the Gulf of Mexico.) To the best of our knowledge, this is to-date the only long-term mooring deployed in close proximity of the Loop, and the 2005 measurements provide a rare chance to examine hurricane-induced near-inertial currents in an actively evolving mesoscale eddy field.

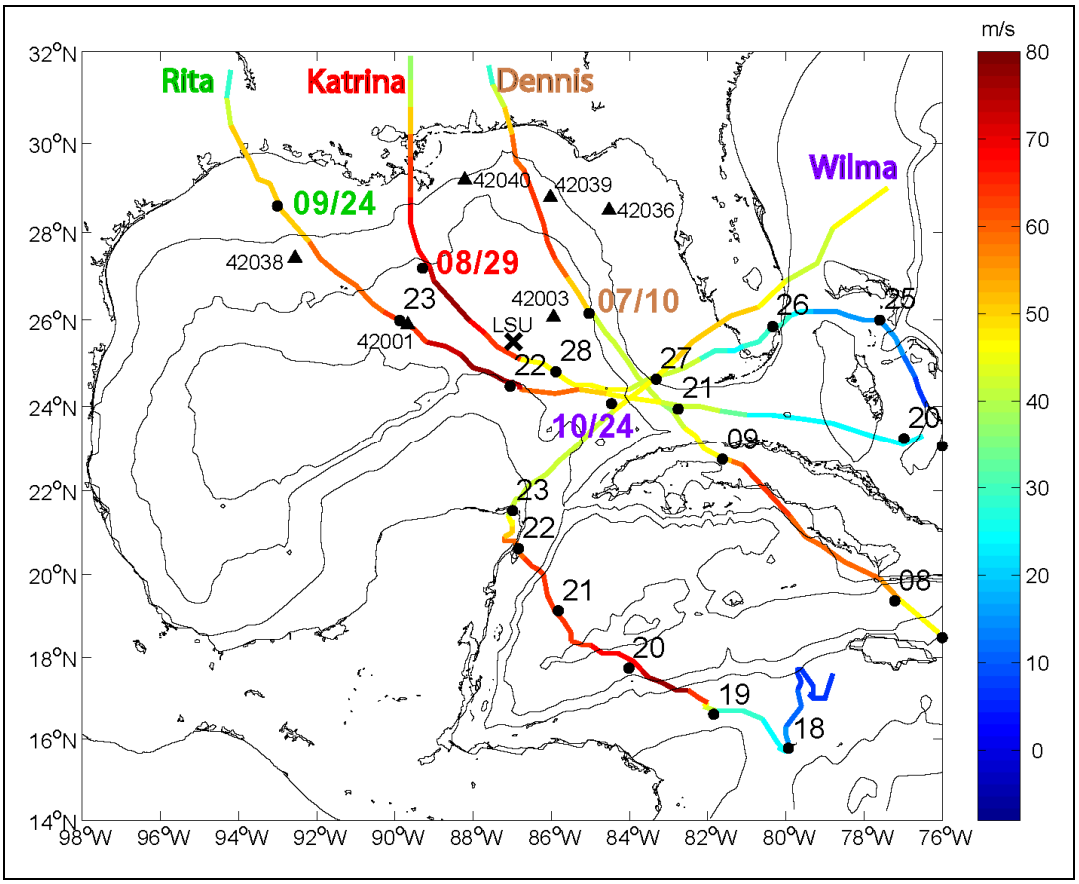

Figure 5.1. Tracks and intensities (colored is maximum sustained wind speed) of the four major hurricanes that blew past the northern Gulf of Mexico during the 2005 Atlantic hurricane season. Black dots indicate daily positions Contours are 200, 2,000, and 3,500 m.

5.2. RESULTS

We use the same model simulation and data analyses as those discussed in Chapter 4, so the methodologies will not be repeated here. As discussed in Chapter 4, background vorticity and its gradients (caused for example by mesoscale features such as the Loop Current, rings and cyclones) play an important role in affecting the propagation (spreading and/or focusing) of near-inertial wave (NIW) energy. As described in that chapter (see also Chapter 1), we estimate this background field from a model simulation that is assimilated with satellite sea-surface-height anomaly (SSHA) data. Figure 5.2 shows the surface vorticity fields (at z = 0 m) just before each of the four indicated hurricanes passed over the LSU mooring. The background fields are significantly different in each case. The change can be seen at the LSU mooring, for example. The mooring is outside the Loop during Hurricane Dennis, just within the Loop's western portion during Katrina, just outside the Loop's eastern edge during Rita, and inside the Loop again during Wilma. The corresponding vorticity and SSH (at the mooring) are shown in the lower panel of Figure 5.3. The upper panel of Figure 5.3 shows the time-depth contours of near-inertial wave energy obtained from FFT at the mooring. This gives a general idea of how energy was generated at the surface and how this penetrated deep into the subsurface. (A more exact analysis using the Hilbert spectra (Chapter 4) will be given below.) The forcing was particularly

strong for Hurricanes Katrina and Rita because of the proximity of the storms to the mooring, and also because the mooring was located to the right of the storms' paths (Chapter 2, section 2.3a; Chang and Anthes, 1978; Price, 1981; also Figure 3.1). There is a distinct difference between the two however. For Katrina, intense energy penetrated deep into depths of about 700m while for Rita the response is more diffused and weaker. For Katrina, the background (surface) ς/f is negative which is conducive to deep energy penetration. For Rita, ς/f is positive, and the surface NIW energy is more prone to horizontal spreading away from the mooring.

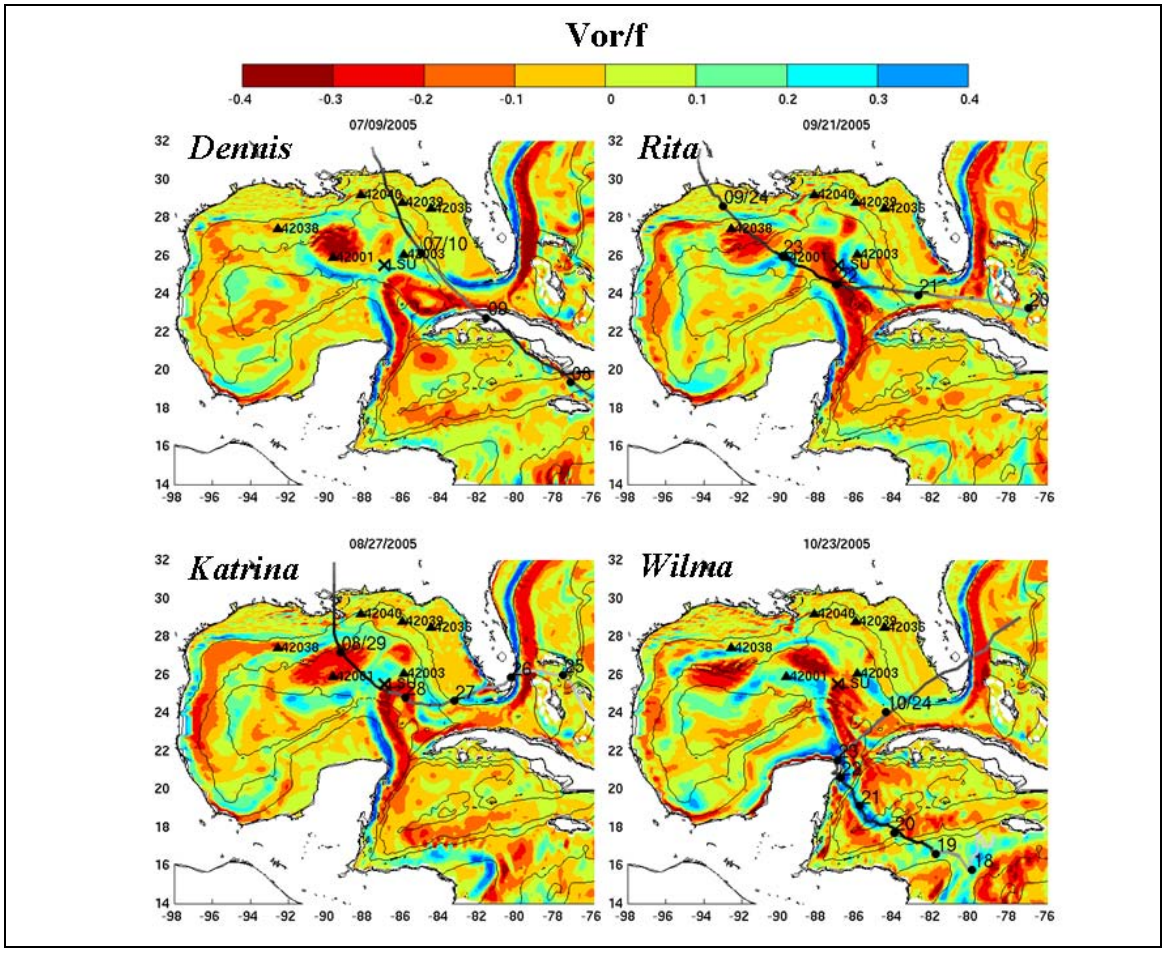

Figure 5.2. Maps of surface ς/f (negative red and positive blue) at times just before the four indicated hurricanes passed the LSU measurement site (indicated by "×"): on July 9 (Dennis), August 27 (Katrina), September 21 (Rita) and October 23 (Wilma). Thick white lines are zero-contours of SSH showing outlines of the Loop Current at the respective dates. Hurricane tracks are shown as gray-scale line: dark indicating most intense wind speed ≈ 70-80 m/s, and light gray weak speeds ≈ 10-20 m/s. Dark contours indicate the 200, 2000 and 3500 m isobaths.

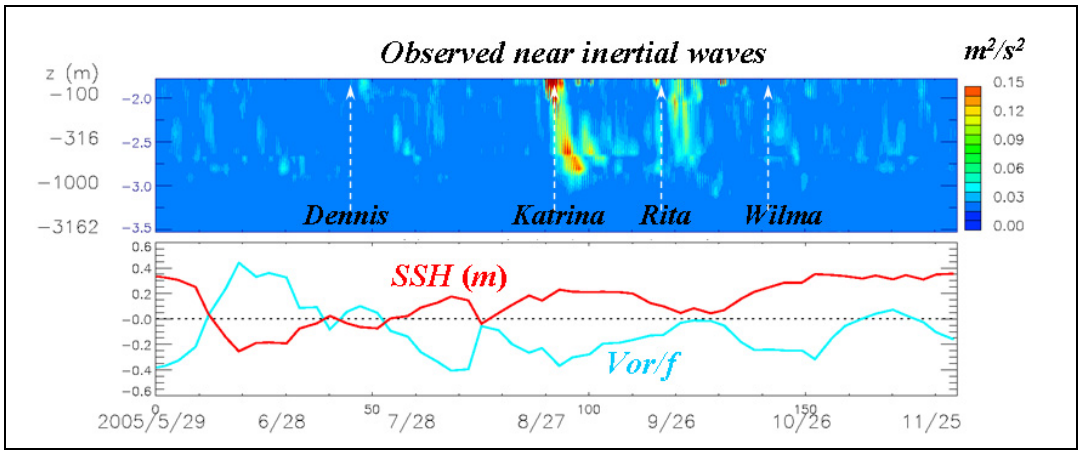

Figure 5.3. Upper panel: time-depth (in log10 scale) contours of near-inertial-wave energy at the LSU mooring (see Figure 5.1 for location). Lower panel: time-series of SSH and ς/f at the mooring.

Instead of the FFT, a more precise analysis of NIW energy as a function of both time and frequency was conducted using the Empirical Decomposition Method of Huang et al. (1998) as used also in Chapter 4. The corresponding Hilbert spectra for the second and third intrinsic modal functions is shown in Figure 5.4—the top panel is for the entire observational period from May through September, at z = –640m, while the bottom panel is more detail for the period August 25 through October 04 that includes only Hurricanes Katrina and Rita, at z = –640m. In both panels, we plot also the wind power (black line; defined in Chapter 4) P_w defined as $\log_{10}((|\mathbf{u_a}|/5)^3)/4$ (the factor 5 m/s and 1/4 are for plot convenience) computed from hourly data at NDBC buoy 42003 (25.74 °N, 85.73 °W; approximately 120km due east of the LSU mooring); only positive P_w is plotted, i.e., for $|\mathbf{u_a}|>5$ m/s. Additionally, the 5day-averaged ς/f (white line) is also plotted but in the upper panel only. The color shows energy E (red indicates high > 2×10^{-2} m^2s^{-2}) as a function of time and ω/f, where ω is frequency and the inertial frequency f ≈ 6.28×10^{-5} s^{-1} at the mooring location. At a particular date (time), one can "read off" the intensity of the near-inertial motion as well as its frequency. Periods of high P_w and large E roughly coincide particularly for Hurricanes Katrina, Rita and Wilma. There is also some visual correlation between ω (of high E) and ς during the second half of the period (i.e., after Katrina), such that lower ω < f occur during times of negative ς/f (Katrina and Wilma), and ω ≈ f when ς/f ≈ 0 (Rita and during November), roughly in agreement with the theory mentioned previously in Chapter 4. The NIW response at z = –640 m for Katrina (Figure 5.4 lower panel) was previously discussed in Chapter 4, and for Rita, the dominant energy is clearly super-inertial.

If the Gulf were void of mesoscale features, i.e., only vertically stratified, and if boundaries and continental slopes are ignored, then the storm-forced NIW's would concentrate predominantly in the upper layers (~100 m) and the most intense energy would be confined in the vicinity of the storm tracks. The Loop Current and eddies change this situation completely. Firstly, the anticyclonic vorticity in the Loop and warm rings tend to focus the NIW energy in them. Secondly, the strong advective speeds in the Loop and rings can efficiently spread NIW energy around them. Finally, deep vertical penetration of NIW can occur in these anticyclonic-vorticity regions. The first (focusing) was previously discussed in Chapter 4, and it and the second phenomenon (spreading) are also illustrated for Katrina in Figure 5.5. The top panel shows maximum NIW energy in nearsurface 200 m, the second panel the maximum energy from

200 m to 1000 m below the surface, both at September 1 at 03:00 GMT, and the third panel is the same as the second but at September 3 at 12:00 GMT. The focusing and deep vertical penetration phenomena are seen in all three panels, while spreading of NIW energy around the eastern portion of Eddy Vortex is seen from panels 2 and 3.

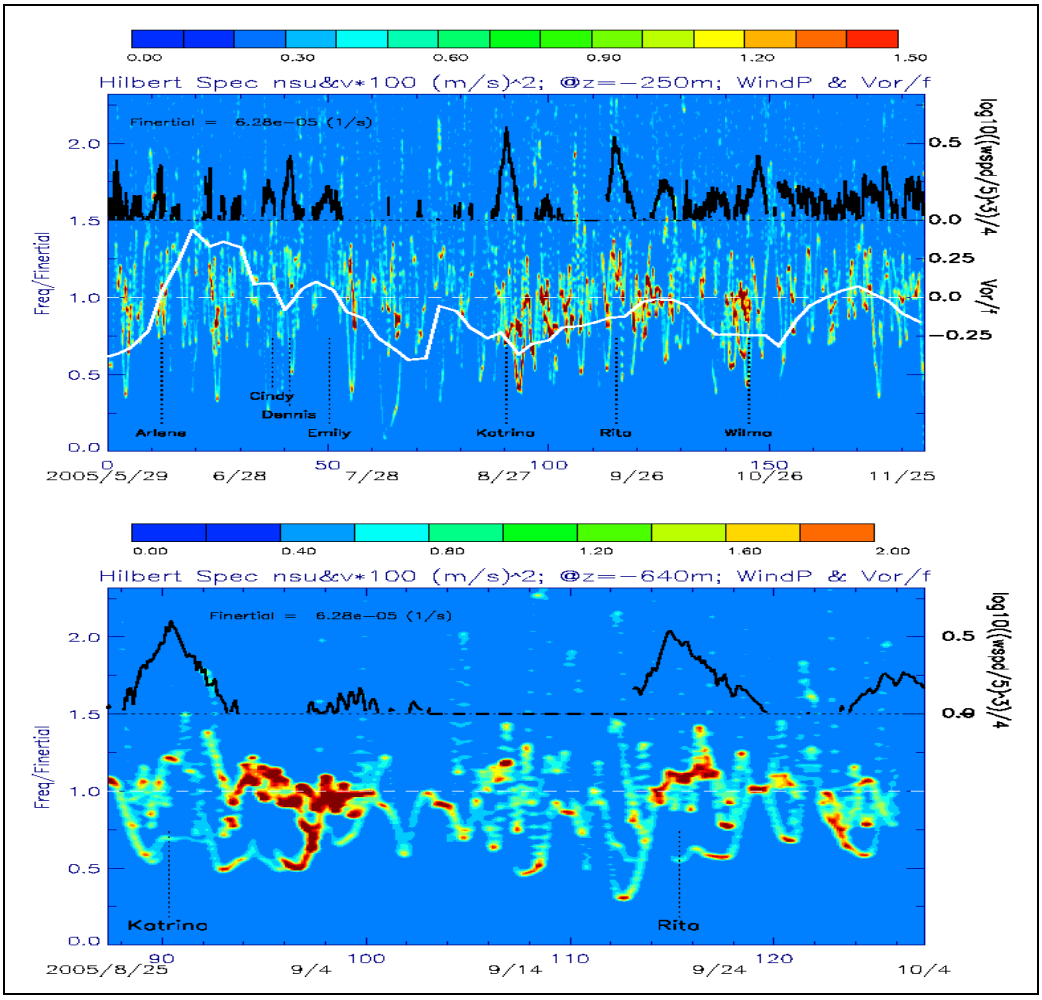

Figure 5.4. Hilbert energy spectra (color) of the second and third intrinsic modal functions (IMF's; see text) of the observed currents (see Figure 1 for location) at z = –250 m (upper) and z = –640 m focusing on the Katrina and Rita periods (lower panel) as a function of time and frequency ω (non-dimensionalized by the inertial frequency f = 6.28×10^{-5} s^{-1}). Also plotted are wind power (black line) Pw defined as log10((|ua|/5)3)/4 computed from NDBC buoy 42003 (25.74 °N, 85.73 °W), and model 5 day-averaged ς/f at z = –200 m (white line; upper panel only). Dates of hurricanes are marked.

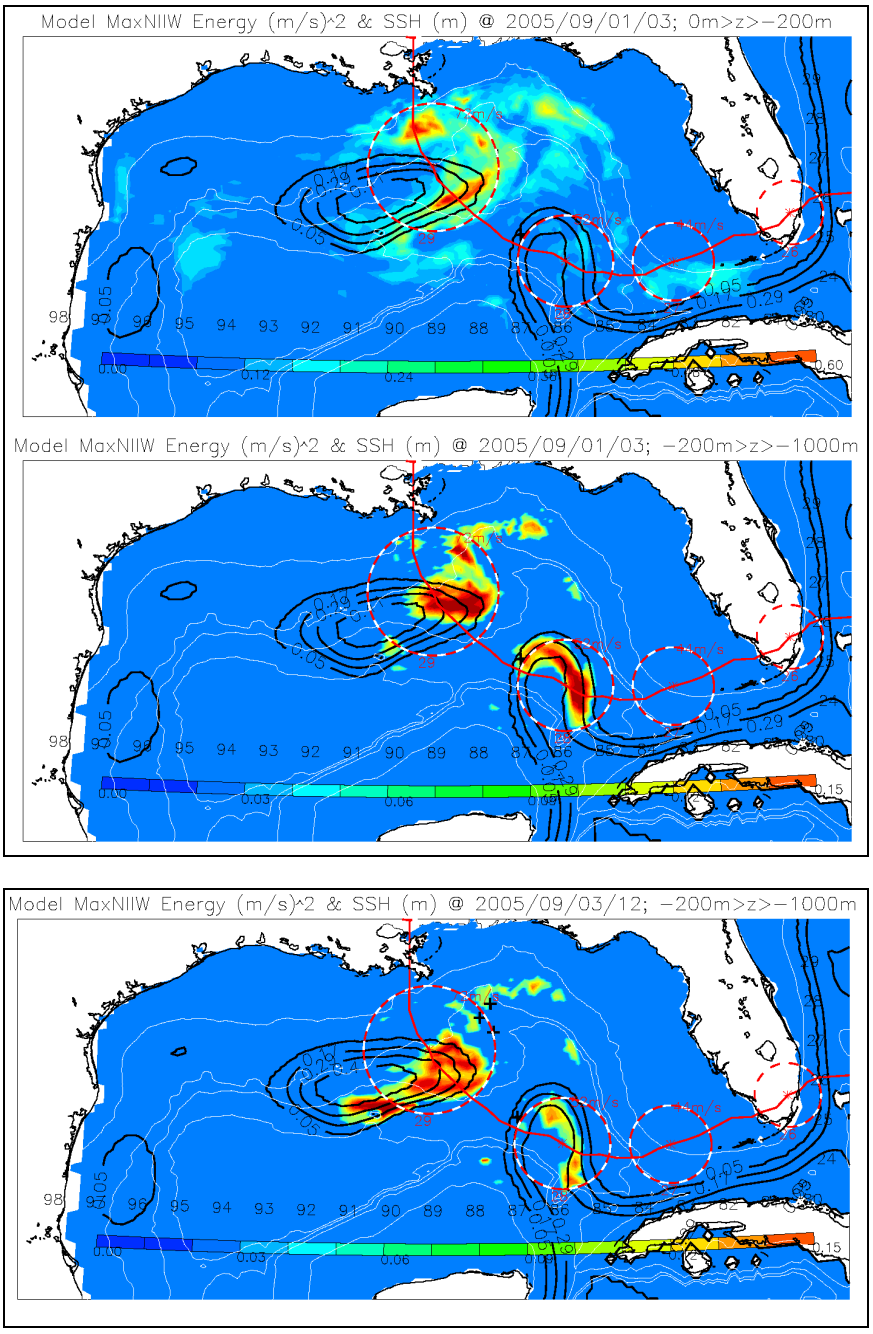

Figure 5.5. Maps of maximum inertial energy (m^2s^{-2}) in the depth range $0 > z > -200$ m (upper panel) and $-200 > z > -1000$ m (middle panel) after Hurricane Katrina on September 1, 2005, at 03:00 GMT and also on September 3 at 12:00 GMT (bottom panel). The hurricane's track is shown in red and marked daily at the center of an "intensity circle" whose radius is proportional to the maximum sustained wind speed on that day. Dark contours are SSH (m) indicating the positions of the Loop and the ring. White contours indicate the 200, 2000, 3000 and 3500 m isobaths. The LSU mooring is marked with a "+."

The importance of mesoscale features in affecting the distribution of NIW's is illustrated in Figure 5.6. Figure 5.6a shows the simulation with initially level isopycnals (i.e., no Loop, nor eddies), and the same Katrina wind forcing (as in the realistic run) is used. The date is September 05, some 8 days after the storm, but the intense NIW energies remained to the right of the storm as would be expected for such an idealized simulation. On the contrary, the run with realistic Loop and Eddy Vortex, Figure 5.6b, shows a much different NIW energy field in which the near-surface energy is all but dispersed by (September 05) and it is concentrated in the deep layers around the eastern side of Eddy Vortex as well as the Loop. The predicted energy-spreading on the eastern side of the ring is actually confirmed by the ADCP measurement at NDBC station 42872 as shown in the inset in Figure 5.6b. Figure 5.7 similarly compares the case without (5.7a) and with (5.7b) the Loop and eddy Vortex for Hurricane Rita case. In this case, NIW energy focusing and deep penetration are clearly seen in Eddy Vortex and a newly shed (small) Loop Current eddy (Figure 5.7b).

5.3. CONCLUSION

Summarizing, the observed near-inertial currents at a mooring in the vicinity of the Loop Current in the Gulf of Mexico during the 2005 hurricane season (1) display clockwise rotations and downward group propagation; (2) are primarily storm-induced; and (3) have time-dependent frequencies which near the surface ($z \approx -250$ m) are approximately in phase with ς, so that sub-inertial (super-inertial) motions tend to be produced when the background flow at the mooring has a negative (positive) ς. These are consistent with known properties of NIW's and their generation. By conducting experiments with and without Loop Current and rings, it is shown that the Loop and rings play an important role in focusing the NIW energies within them, in spreading them around them (because of the strong advection) and by allowing them to penetrate deep into the subsurface. Given that the Gulf of Mexico is virtually closed below a depth of about 1000m, these NIW-pathways in maybe particularly pertinent to the exchanges of upper and lower layer masses in the Gulf.

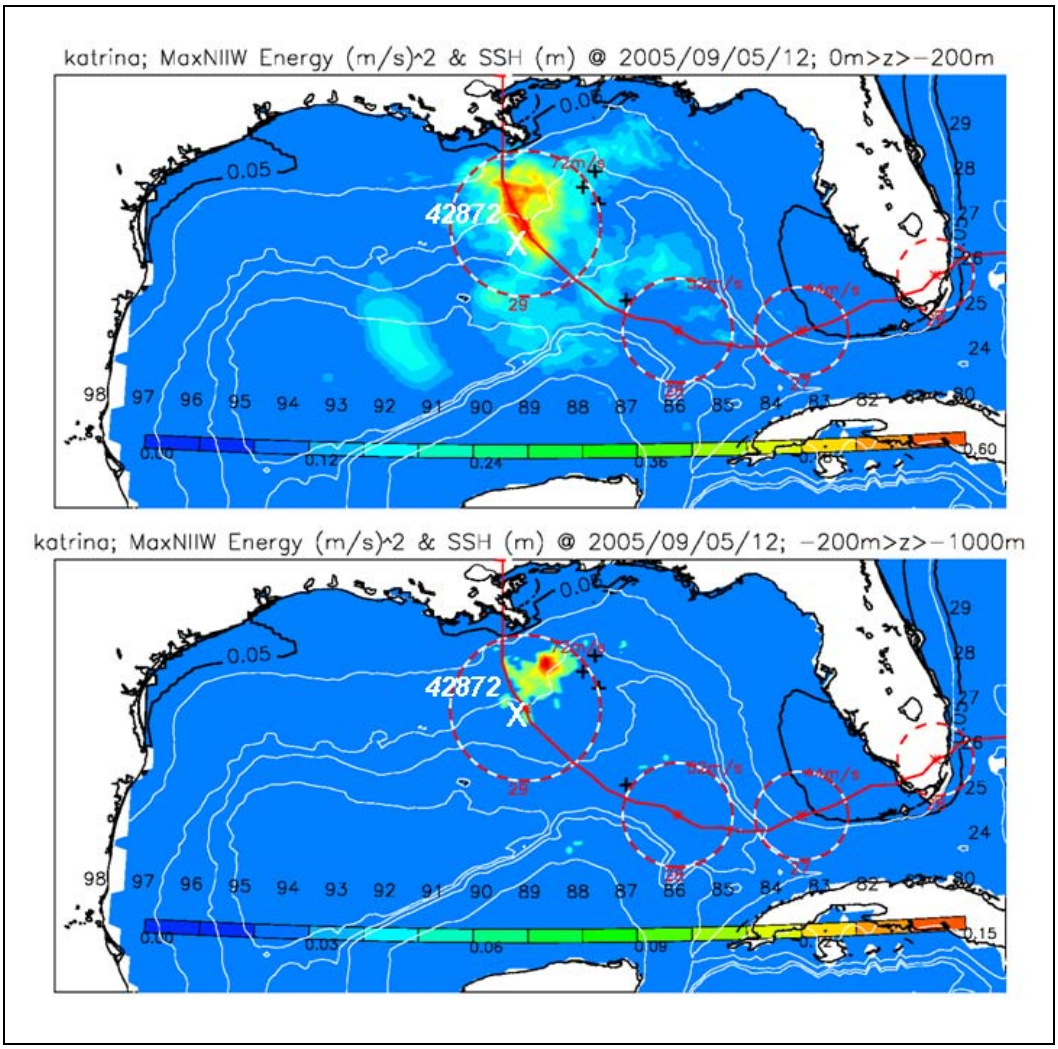

Figure 5.6a. Maps of maximum inertial energy (m^2 s^{-2}) in the depth range 0 > z >–200 m (upper panel) and –200 > z >–1000 m (middle panel) after Hurricane Katrina on September 5, 2005, at 12:00 GMT. The hurricane's track is shown in red and marked daily at the center of an "intensity circle" whose radius is proportional to the maximum sustained wind speed on that day. White contours indicate the 200, 2000, 3000 and 3500 m isobaths. The LSU mooring is marked with a "+." This model simulation has neither Loop Current nor rings.

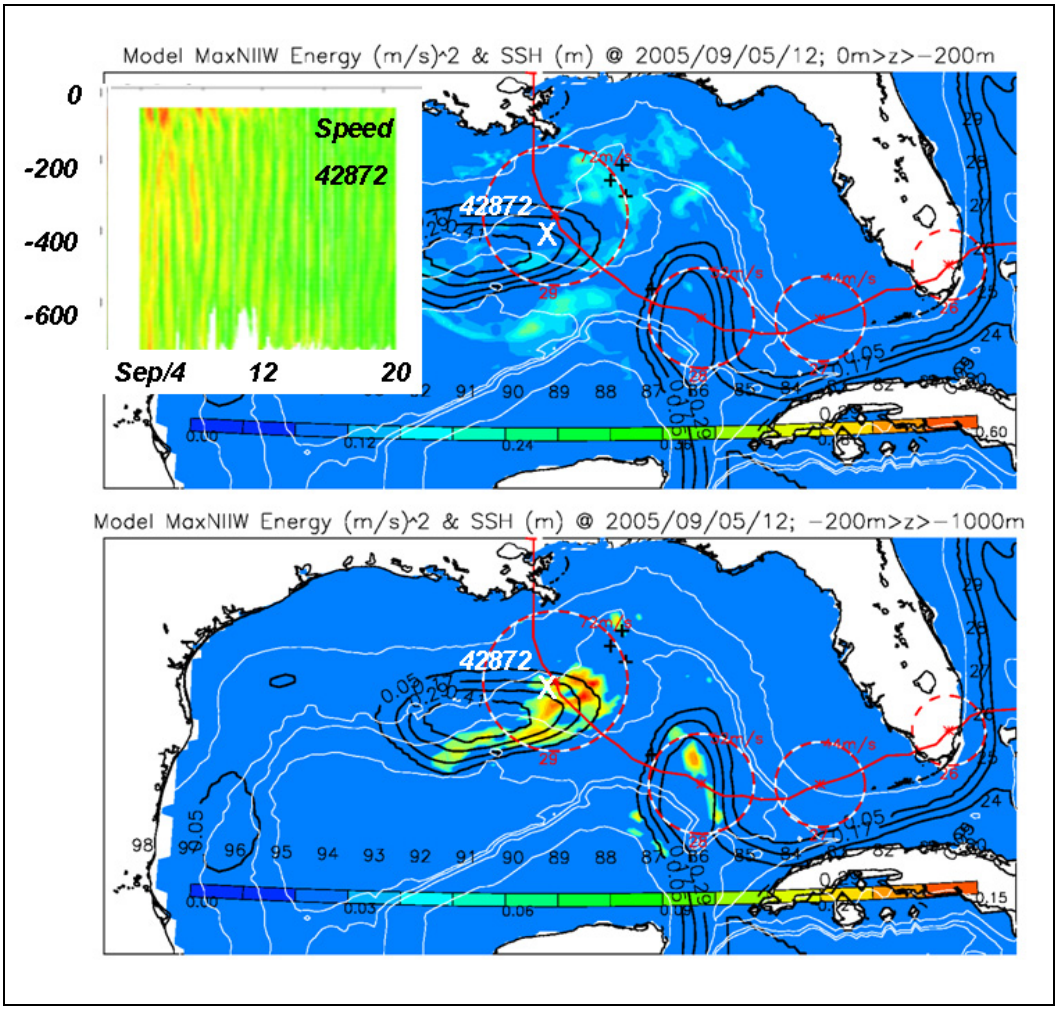

Figure 5.6b. Maps of maximum inertial energy ($m^2 s^{-2}$) in the depth range 0 > z >–200 m (upper panel) and –200 > z >–1000 m (middle panel) after Hurricane Katrina on September 5, 2005, at 12:00 GMT. The hurricane's track is shown in red and marked daily at the center of an "intensity circle" whose radius is proportional to the maximum sustained wind speed on that day. Dark contours are SSH (m) indicating the positions of the Loop and the ring. White contours indicate the 200, 2000, 3000 and 3500 m isobaths. The LSU mooring is marked with a "+." Inset shows time-depth contours of the speed (red = 1m/s; green=0 m/s) measured at NDBC42872 shown. This shows near-inertial waves propagating downward days after the passage of Hurricane Katrina.

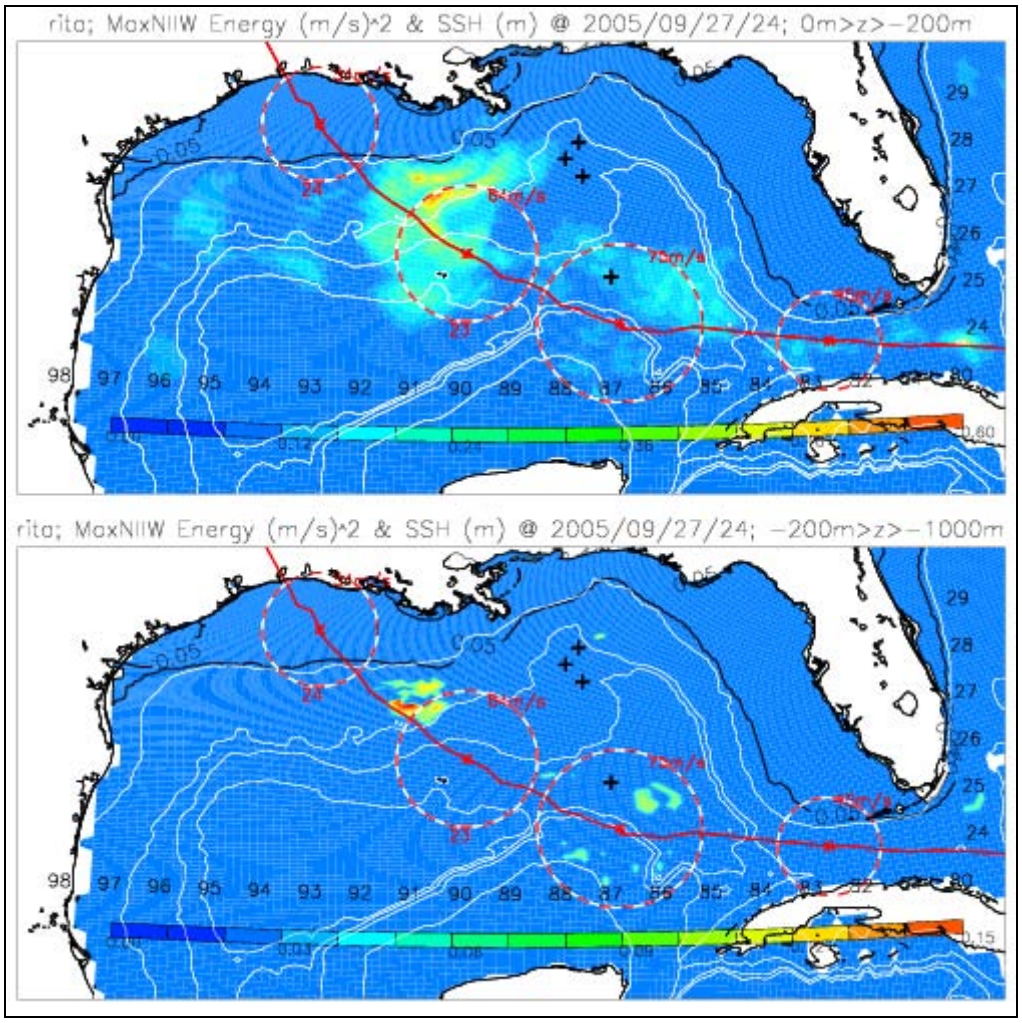

Figure 5.7a. Maps of maximum inertial energy (m^2 s^{-2}) in the depth range 0 > z >–200 m (upper panel) and –200 > z >–1000 m (middle panel) after Hurricane Katrina on September 28, 2005, at 12:00 GMT. The hurricane's track is shown in red and marked daily at the center of an "intensity circle" whose radius is proportional to the maximum sustained wind speed on that day. White contours indicate the 200, 2000, 3000 and 3500 m isobaths. The LSU mooring is marked with a "+."

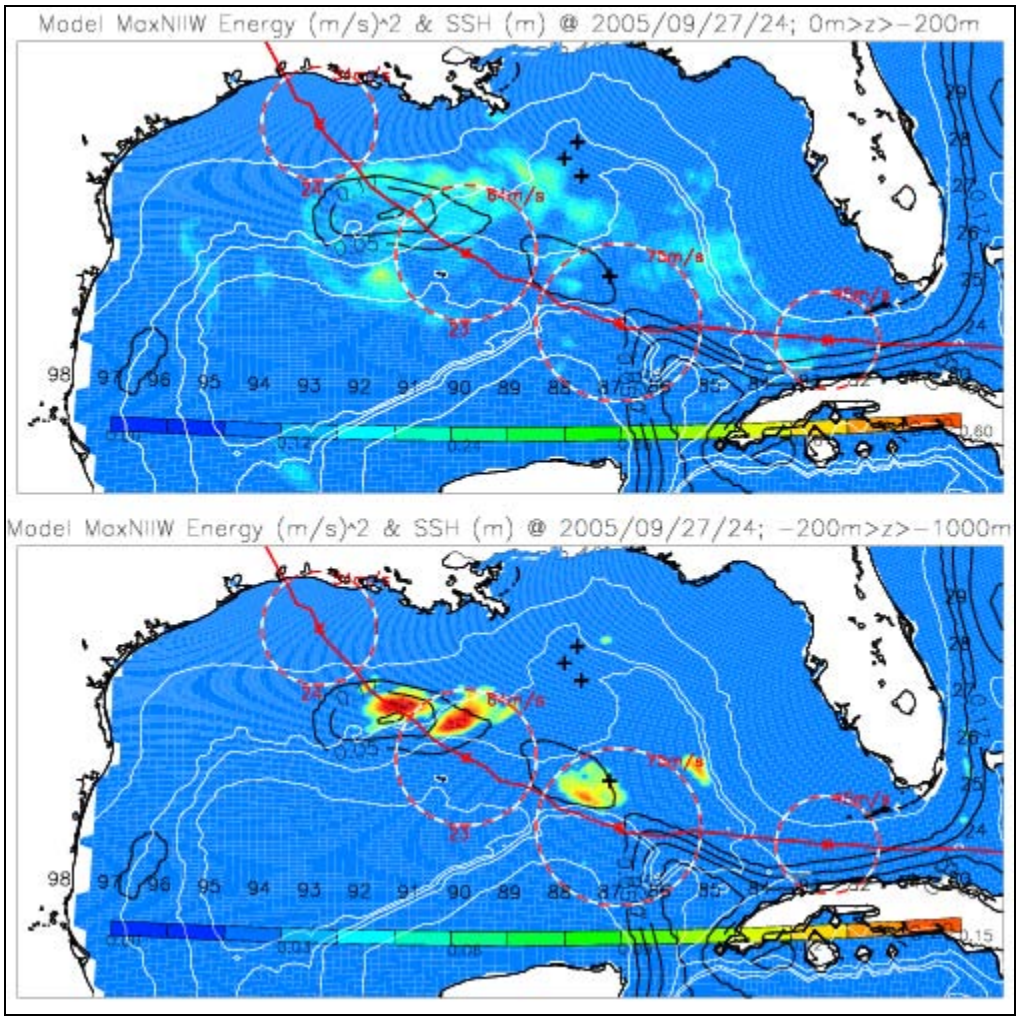

Figure 5.7b. Maps of maximum inertial energy (m^2 s^{-2}) in the depth range 0 > z >–200 m (upper panel) and –200 > z >–1000 m (middle panel) after Hurricane Katrina on September 28, 2005, at 00:00 GMT. The hurricane's track is shown in red and marked daily at the center of an "intensity circle" whose radius is proportional to the maximum sustained wind speed on that day. Dark contours are SSH (m) indicating the positions of the Loop and the ring. White contours indicate the 200, 2000, 3000 and 3500 m isobaths. The LSU mooring is marked with a "+."

CHAPTER 6. OCEAN RESPONSES TO HURRICANE WILMA, PART 1: LOOP CURRENT WARMING[8]

Synopsis

Hurricane Wilma presented a unique scenario in which a powerful storm interacted with a powerful ocean current flowing through a channel (the Yucatan). In this part 1, we describe a curious warming of the Loop through this interaction.

Summary of the Main Results

Hurricanes mix and cool the upper ocean, as shown here in observations and modeling of the Caribbean Sea and the Gulf of Mexico during the passage of Hurricane Wilma. Curiously, the upper ocean around the Loop Current warmed prior to Wilma's entrance into the Gulf. The major cause was increased volume and heat transports through the Yucatan Channel produced by storm-induced convergences in the northwestern Caribbean Sea. Such oceanic variability may have important impacts on hurricane predictions.

6.1 INTRODUCTION

Wilma (October 16~26, 2005) is the most powerful Atlantic hurricane on record. The storm's minimum surface pressure was 882 mb and its maximum surface wind speeds $|\mathbf{u}_a|$ was 78 m s^{-1} (http://www.nhc.noaa.gov/; Figure 6.1). The storm formed southwest of Jamaica near a warm eddy with high ocean heat content (OHC (Leipper and Volgenau, 1972); Figure 6.1). It strengthened on October 18 at 15Z ($|\mathbf{u}_a| \approx 34$ m s^{-1}), and became a category-5 hurricane on October 19 at 09Z as it moved west/northwestward over a high OHC region in the Cayman Sea. Wilma weakened as it made landfall on October 22 at 06Z at Cozumel Island and Yucatan peninsula, but $|\mathbf{u}_a|$ was still > 60 m s^{-1}. It weakened further ($|\mathbf{u}_a| \approx 45$ m s^{-1}) while it moved slowly overland, and strengthened some 24~30 hours later as it passed over the warm Loop Current ($|\mathbf{u}_a| \approx 56$ m s^{-1} on October 24) on its way to Florida.

Wilma is one of the few major hurricanes to directly hit the Yucatan Channel (http://www.nhc.noaa.gov/pastall.shtml),[9] and is also the only such hurricane to have remained in the northwestern Cayman Sea (west of 79°W) and the Yucatan Channel for a long 7-day period. While the storm was in the Caribbean Sea, its progression speed U was 2.5~3 m s^{-1}, and U > C (where C is the first-mode oceanic baroclinic wave speed, ≈ 2.5 m s^{-1} (Chelton et al. 1998)). Such a storm (U > C) produces lee waves with large vertical isopycnal movements (> 50 m; vertical velocity $w \approx \pm 10^{-3}$ m s^{-1}) in the ocean and no disturbances ahead (Geisler, 1970). The combined action of upwelling and mixing is effective in cooling the upper ocean near the storm's eye especially for a slowly-moving storm (Price, 1981). Mixing alters the OHC that in turn can modify the storm. On the other hand, less is known about the effects of a hurricane on the powerful Loop Current, where strong horizontal advection may defy interpretations based on vertical motions alone. (See Oey et al. (2005a) for a review of the Loop Current and general circulation in the Gulf of Mexico).

[8] This chapter is based on Oey et al. 2006.

[9] Hurricanes Emily (11-21/July 2005) came near the Yucatan Channel; other hurricanes are Ivan in 2004, Isidore and Lili both in 2002, Allen in 1980, Isbell in 1964, Carla in 1961, and Florence in 1953.

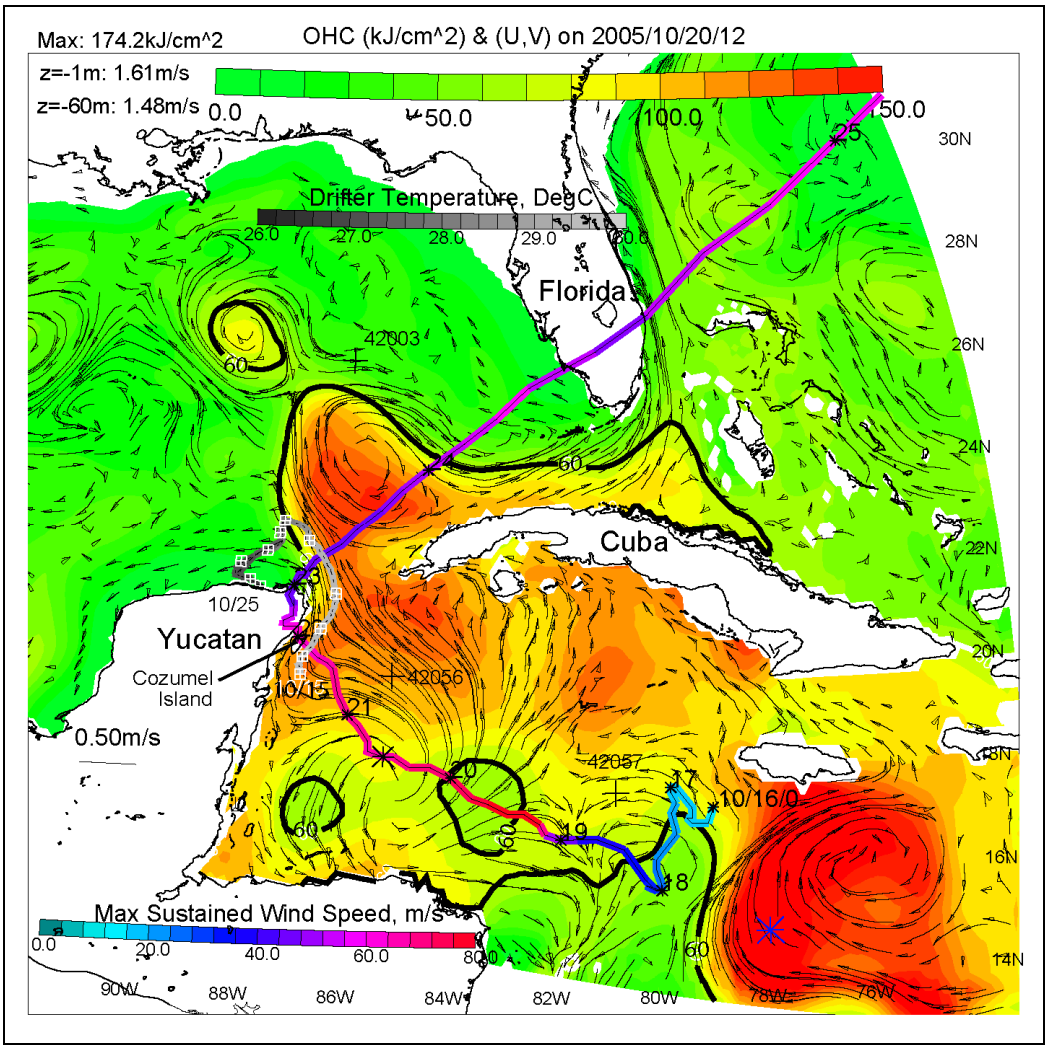

Figure 6.1. A color image of the forecast OHC on October 20 at 12:00 GMT, 2005 (color-scale across top) during Hurricane Wilma. Maximum OHC (blue asterisk south of Jamaica) is printed on the top-left corner of the page. Thick-black contour indicates OHC=60 kJ/cm^2. Forecast currents at z = –1 m are shown as black trajectories (with arrows) launched from every other four grid points. Maximum speeds (which occurred in Yucatan Channel) at z = –1 m and –60 m are also printed. Wilma's path is shown colored with its maximum sustained wind speeds (color-scale at bottom-left). Numbers at the small asterisks indicate days in October and the large asterisk the position of the storm corresponding to this forecast date. Off the Yucatan coast, the path of an observed drifter shaded with temperature (scale across "Florida") are marked daily with a crossed-square, from October 15 to October 25. Positions of the three NDBC stations are marked with plus signs.

6.2. METHODOLOGY

To analyze the upper-ocean changes caused by Wilma, we use data from the National Data Buoy Center (NDBC; http://www.ndbc.noaa.gov/), including SST (at z = –1 m) and meteorological observations (Figure 6.1 shows buoy locations). We also use results of an ocean

forecast (the "control" run) for the Caribbean Sea and the Gulf of Mexico (e.g., Oey et al. 2005b). Though we estimate large surface heat losses (peak ≈ 1300 J $m^{-2}s^{-1}$ at 42056, and 800 J $m^{-2}s^{-1}$ at 42057; c.f. Hurricane Opal (Shay et al. 2000)), these have small effects in decreasing the temperatures of the upper ocean, which is cooled more by mixing (Price, 1981).

The forecast is initialized with a nowcast ocean field (Loop Current and eddies) that has already been assimilated with satellite data up to October 16, 2005, after which the model is run through Nov/06, 2005 without data assimilation. Oey et al. (2005a and b) provide details of the model and the data assimilation scheme. Besides the 'control' run, other auxiliary runs are also conducted using different wind and initial density fields as will be pointed out below. The original forecast used Global Forecast System winds (Caplan et al. 1997), but the model was rerun for this study using also the high-resolution analyzed winds from http://www.aoml.noaa.gov/hrd/. This rerun is still referred to as "forecast" to emphasize that it is free from satellite data assimilation. Wind stresses were computed using a bulk formula. We use a drag coefficient (C_d) that curve-fits data for low-to-moderate winds (Large and Pond, 1981) with data for high wind speeds (Powell et al. 2003):

$$\begin{aligned} C_d \times 10^3 &= 1.2, && W \le 11 \text{ m s}^{-1}; \\ &= 0.49 + 0.065\, W, && 11 < W \le 19 \text{ m s}^{-1}; \\ &= 1.364 + 0.0234\, W - 0.00023158\, W^2, && 19 < W \le 100 \text{ m s}^{-1}, \end{aligned} \qquad (6.1)$$

where W is the wind speed. Surface heat and evaporative fluxes were set to zero, so that changes in the model ocean temperatures are due to its internal dynamics.

6.3. RESULTS

To account for wind mixing on the OHC of an evolving ocean, a non-dimensional parameter Φ is used, where Φ is obtained by estimating the energy required to mix water in an upper layer of depth Z_{26} with the cooler water in a subsurface layer of depth h, and comparing this energy to power dissipation by the wind:

$$\Phi = \left(\frac{1}{2} g h Z_{26} \Delta\rho\right) / \left(\gamma \int_0^{\tau} \rho_a C_d W^3 dt\right). \qquad (6.2)$$

Here, Z_{26} is taken as the depth of the 26 °C isotherm, Δρ is the initial density difference between the two layers (≈ 1~2 kg m^{-3} from the model), γ is the efficiency of work done by the wind, τ is a wind time scale, ρ_a is air density, t is time and g is acceleration due to gravity.

Figures 6.2b and 6.2c show observed and forecast sea-surface temperatures (SST's; at z = –1 m) and $\log_{10}$ of $\Phi \approx g(Z_{26})^2/\alpha W^3$, where we have set $h \approx Z_{26}$ in (2) and α is then a time scale proportional to the duration of the wind forcing (Turner, 1973). For convenience, we assume that both α (= 1 s) and Z_{26} (= 100 m) are constant. The SST should decrease with Φ if the dominant cooling is due to stirring by the hurricane. Figure 6.2 shows minimum SST's on October 19-20 at 42057 and on October 21-22 at 42056 following minima in Φ, with lags of about 1~2 days. The decrease in SST at 42057 (Figure 6.2c) began on October 17, a short time after Wilma formed. With the chosen parameters, Φ ≈ 2 appears to be an approximate critical value below which wind mixing is sufficiently strong to cool the upper ocean. The large drop on October 19-20 was caused by the sudden intensification of Wilma, even though the storm was

moving farther west. The model forecasted the large drop in SST but lost its predictability beyond October 26.

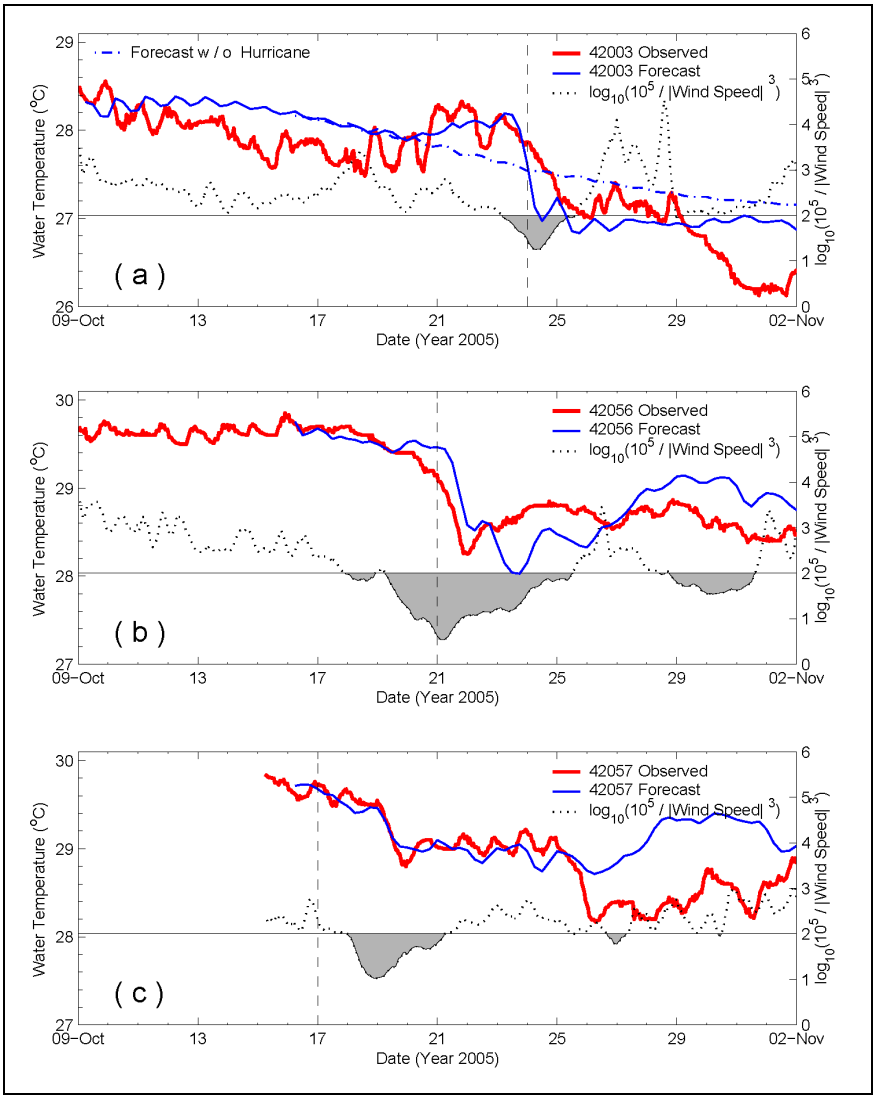

Figure 6.2. Observed (red solid) and forecast (blue solid) SST (at z = –1 m) at NDBC stations (a) 42003, (b) 42056 and (c) 42057 during Hurricane Wilma. The dotted curve in each panel is (log10 of) the inverse wind power dissipation (see text); shaded are values ≤ 2. The dash-dot curve in panel (a) is SST for auxiliary model run A1 in which Wilma is turned off. The vertical dashed line in each panel indicates time when Wilma is closest to the respective station.

The SST at 42056 (Figure 6.2b) decreased on October 18~19 while Wilma's center was still some 400~600 km to the east; the decrease in SST follows a decrease in $\Phi \leq 2$. A careful examination of satellite sea-surface height anomaly (SSHA; from AVISO (www.aviso.oceanobs.com)) data indicated no cold eddies nearby, so the cooling was most likely caused by mixing. By October 21 when the storm center was nearest to 42056, the SST had

already dropped by 0.5 °C, and SST decreased by another 0.9 °C through October 22. It is common for SST to decrease prior to the arrival of a hurricane, but that usually occurs within hours and in close proximity (100~200 km) of the storm's center (Price, 1981; Shay et al. 2000). In the case of Wilma, the slowness of the storm combines with its intensity and large size to produce winds that mixed and cooled the upper ocean hundreds of kilometers ahead of the storm's center. The forecast SST shows a similar (but less dramatic) "remote" effect; it also shows the large decrease when the storm center passes. The model looses its predictability at 42056 beyond about October 30.

Cooling ahead of the storm also exists in the Loop Current especially in its core. However, strong advection around the Loop complicates the picture. Buoy 42003 is located in close proximity of the Loop. The Φ in Figure 6.2a suggests that wind mixing at 42003 played a minor role (Φ > 2) prior to Wilma's arrival on October 23~24. The observed SST first decreased to a minimum on October 19~20; it then increased by about 0.4 °C from October 20 through October 23 before dropping sharply (–0.8 °C) on October 23~25 as Wilma passed south of the site. This final sharp drop is caused partly by wind-mixing (the Φ drops below 2), and partly by advection of cooler shelf/slope waters as Wilma moved towards Florida (not shown). The sharp drop agrees well with along-track data on October 24 at 15:00 GMT from satellite ENVISAT (www.aoml.noaa.gov/phod/dataphod), which flew almost exactly over 42003 on that date and recorded a minimum SSHA ≈ –0.3 m. The initial decrease to the minimum SST on October 19 (Figure 6.2a) seems to be part of the natural (i.e., unrelated to Wilma) variability of the Loop Current, since the SST for the auxiliary run A1 (without Wilma) shows a similar decrease. However, the subsequent ~3-day (October 20~23) warming is unique for 42003. No such SST-rise was observed at 42056 and 42057 (Figures 2b,c), nor have similar phenomena been observed previously. The forecast (Figure 6.2a) shows a similar SST-variation of the rise of SST on October 20~23 and the subsequent sharp drop. In contrast, the SST decreases monotonically with time in the auxiliary run.

The 3-day SST-rise prior to Wilma's entrance into the Gulf could have been induced by passage of an isolated warm feature. While this could not be ruled out (objective-analysis SSH (OASSH (AVISO)) maps based on altimetry data did not show such a feature), the model suggests an alternative explanation. Temperatures at other locations around the perimeter of the (model) Loop show a similar rise, suggesting a more wide-spread process that links Wilma to the Loop Current by way of heat and volume transports through the Yucatan Channel. Figure 6.3 shows increased (model) volume and heat fluxes through the Yucatan Channel from October 18 to October 22~23. The increased fluxes are due to northwestward convergent flows produced while the storm is in the Caribbean Sea. Subsequent variation (after October 23) consists of damped near-inertial oscillations in which the volume fluxes asymptote to pre-Wilma values, and the upper-150m heat flux indicates influx of cooled (i.e., negative heat flux) Caribbean Sea waters (previously observed at 42056, Figure 6.2b) into the Gulf. Excess (i.e., control minus auxiliary run A1) of total transport (blue curves) averaged over October 19~23 is 2 Sv, and the excess transport in the surface 150 m (red) is ≈ 5 Sv, indicating a large baroclinic response with opposite transport below 150m (green). The fluxes peak on October 22~23 when currents in the western Yucatan Channel become very strong (≈ 2.3 m s^{-1}) forced by strong northward wind in the channel as Wilma stalled over the northern Yucatan Peninsula. In contrast, pre-storm current speeds are weaker, about 1.5 m s^{-1} as inferred from the model and also from an observed drifter (from www.aoml.noaa.gov/phod/ dataphod; Figure 6.1). In Figure 6.4 we plot the SST

difference (at z = –1 m), control minus auxiliary run A1, on October 22 at 12:00 GMT.[10] This shows warming (red) around the edge of the Loop where currents are strong and cooling (blue) in the Caribbean Sea to the right of Wilma's path (c.f. Figure 6.2b). The asymmetry is striking. The warming is in part caused by localized wind-induced convergences especially at fronts, but a large part is by excess influx of warmer waters from the Caribbean.[11] Based on the excess heat influx (the October 18-23 average is 1.2×10^{7} °C m^3 s^{-1} (or 5×10^{13} W), Figure 6.3) heat balance in an adiabatic stream-tube around the Loop Current (75 km wide × 150 m deep × 400 km long) from October 18 to 23 is computed; this yields an average increase of 1 °C in agreement with Figure 6.4. The Yucatan-Loop Current system plays an important role in distributing the heat far north into the Gulf (around the Loop); in their absence, warming occurs only near the channel.[12]

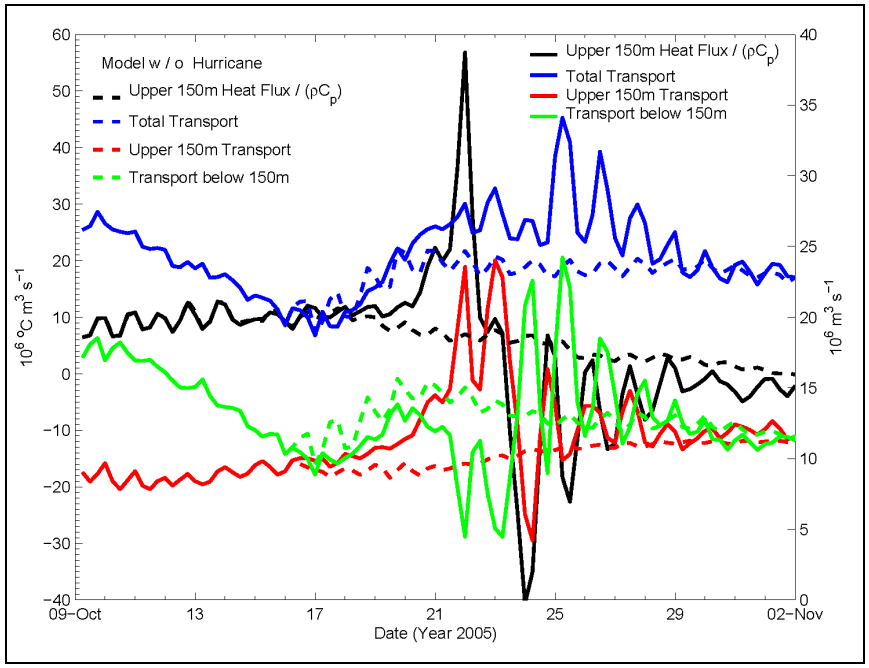

Figure 6.3. Model volume (right-side scale) and heat transports through the Yucatan Channel during Wilma. Solid (dashed) curves are for model with (without) Wilma. The upper 150-m heat flux transport is defined as $\rho_o C_p \iint v(T-26)dxdz$, where v is the velocity normal to the transect, T is temperature, and vertical integration is from z = –150 m to the surface.

[10] Subtracting the A1-solution minimizes contributions from background variability that is not related to Wilma. However, the general warming in the Loop and cooling in the Caribbean in Figure 6.4 remain if the initial condition is subtracted instead.

[11] To isolate localized advection by wind, a case that uses Wilma's wind field at the northern tip of Yucatan (on *October 23*) was run. We found *SST*-rise ≈ *0.3 °C* in the Loop, or about *20%* of the total shown in Figure 6.4.

[12] This is shown by forcing Wilma onto an initially quiescent ocean with level isopycnals. The surface then cannot show warming because there are no horizontal thermal gradients (and no surface heat flux), but there is subsurface warming of about *0.5 °C* at *z = –50m*, caused by flow convergence, just north of the channel.

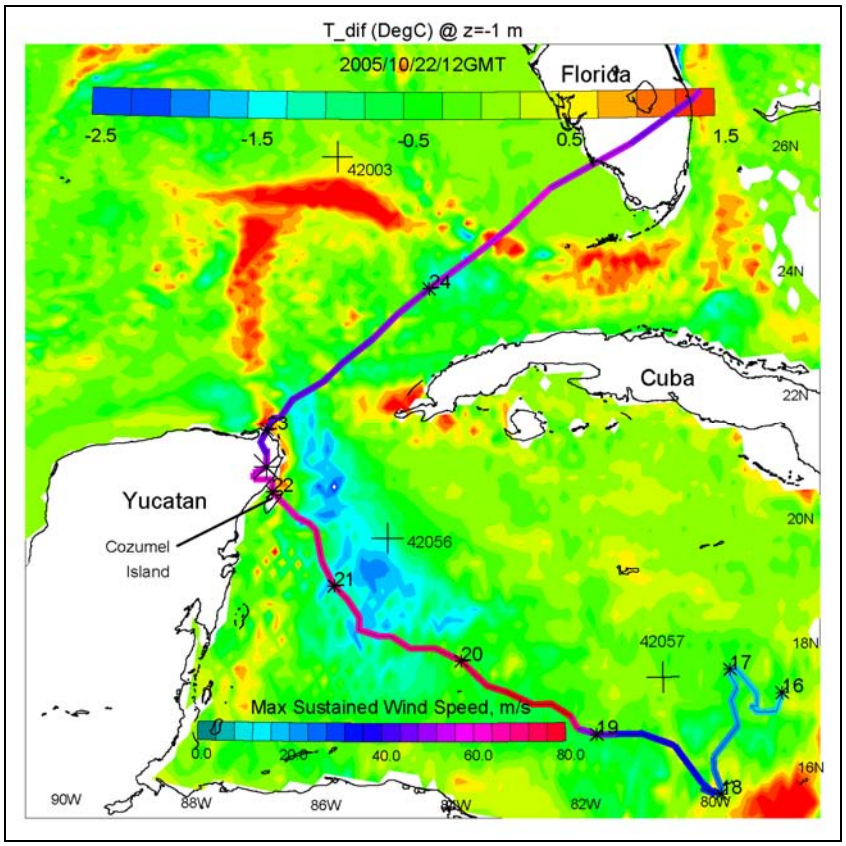

Figure 6.4. Color image of the temperature difference (°C; color-scale across top), control minus auxiliary run A1, on October 22 at 12:00 GMT and at z = –1 m, showing the effect of Hurricane Wilma winds in warming the Loop Current especially around the edge of the Loop. Maximum SST-rise in the Loop was 2.18°C, minimum SST-drop off Cozumel is –2.85°C. Hurricane Wilma's path and NDBC stations are also shown, same as in Figure 6.1.

6.4. DISCUSSION

We have computed geostrophic transports through the Yucatan Channel based on satellite altimetry data (OASSH; not shown). Prior to Wilma's entrance into the Gulf, the data shows an increased transport that is consistent with the model forecast shown in Figure 6.3, and the OASSH averaged over the Loop also increased. These data provide a tentative support of the warming episode observed at buoy 42003. Also, the model shows large subsurface (i.e., $z < -150$ m) transport into the Gulf days after Wilma has passed (Figure 6.3 green curve). Subsurface influx encourages Loop Current extension (Hurlburt and Thompson, 1980), and both model and OASSH maps show a more extended Loop following Wilma. The extension may be a response to the increased transport (Ezer et al. 2003), or (and) to the production of higher potential vorticity (Oey, 2004) by the intense cyclone that developed in the western portion of the Yucatan Channel when Wilma entered the Gulf.

6.5. CONCLUSION

Summarizing, cooling was observed at a buoy hundreds of kilometers from, and days ahead of Hurricane Wilma in the northwestern Caribbean Sea. A buoy in the northern edge of the Loop Current recorded SST-rise a few days prior to Wilma's entrance into the Gulf. The model study indicates that the rise was part of an overall warming around the Loop due in part to an increased influx of warm water into the Gulf of Mexico while Wilma was in the Caribbean Sea. Hurricane intensity is sensitive to slight changes in SST (Emanuel, 2005b). Results presented here suggest that hurricane predictions may benefit from prognostic ocean forecasts that have realistic representations of strong flows such as the Loop Current (and eddies).

CHAPTER 7. OCEAN RESPONSES TO HURRICANE WILMA, PART 2: COMPARISONS WITH SATELLITE DATA AND GENERAL INFERENCES OF INTERACTION WITH THE LOOP CURRENT[13]

Synopsis

In this part 2, we continue the analyses of ocean responses caused by Hurricane Wilma. Comparison with satellite data is made, the roles of transport through the Yucatan Channel are analyzed.

Summary of the Main Results

Hurricanes produce mixing and flow divergences (and convergences) that alter the upper-ocean heat content (OHC), which in turn affects the storm. Ocean observations under a hurricane are rare, making it difficult to validate forecast models. Past research have mainly focused on OHC-changes by vertical mixing and tacitly assumed that horizontal transports are slowly-varying. Moreover, effects of coastal boundaries on ocean responses to hurricanes are generally omitted. This work uses satellite data to detect and verify forecast isopycnal motions under Hurricane Wilma (October 16-26, 2005) in the Caribbean Sea and the Gulf of Mexico. The model is then used to show that Wilma-induced convergences in northwestern Caribbean Sea produce increased Yucatan-Channel transport into the Gulf ahead of the storm, and the Yucatan-Loop Current front diverts most of this heat around the Loop. This response is distinct from that of an ocean without the Loop, for which warming is widespread north of the channel. These intricate ocean responses can impact hurricane predictions.

7.1. INTRODUCTION

Because of its capacity to store, transport and release heat, the ocean is vital to a more complete understanding of the genesis and evolution of intense tropical storms (hurricanes in the Atlantic and typhoons in the Pacific). An excellent account of the subject is given in Emanuel (2005a). Over the North Atlantic Ocean, the so called "African easterly waves" which are generated by an instability of the African easterly jet are now believed to serve as the "seedling" circulations for a large proportion of tropical cyclones there (Burpee, 1972). Nearly 85% of the intense hurricanes (Saffir-Simpson Scale Categories 4 and 5) have their origins as easterly waves (Landsea, 1993). Amongst the various necessary conditions for the development of tropical cyclones (e.g., Emanuel, 2005a), an important one is the existence of warm ocean surface (warmer than approximately 26 °C throughout a sufficient depth ≈ 50~100 m) that provides the fuel for the heat engine of the storm.

The 2005 Atlantic hurricane season with three Category-5 hurricanes (Katrina, Rita and Wilma; see Figure 7.1a and http://www.nhc.noaa.gov/pastall.shtml) in the Caribbean Sea and the Gulf of Mexico underscored an important fact: as populations boom in coastal regions, and as the earth embraces a warmer climate with higher sea-surface temperatures (SST) over the tropical oceans, the next decade may see increasingly more intense storms that pose greater risks than ever before (Emanuel, 2005b); the year 2005 was in fact the warmest on record and

[13] This chapter is based on Oey et al. 2007.

unprecedented in the Atlantic in terms of tropical cyclone activity (Shein, 2006). The importance of the upper ocean in hurricane development and intensification was recognized by Leipper and Volgenau (1972) who introduced a quantity called the Ocean Heat Content (OHC):

$$OHC = \rho_o C_p \int_{Z_{26}}^{\eta} (T - 26) dz \,, \quad T \geq 26°C, \tag{7.1}$$

where Z_{26} (>0) is depth of the 26 °C isotherm, η = sea-surface height (SSH) , ρ_o density of sea water and C_p the specific heat of water. SST's in excess of 26°C are necessary for tropical cyclogenesis (Palmen, 1948; DeMaria and Kaplan, 1994). Regions where OHC > 60~90 kJ/cm^2 have been empirically found to be conducive to storm intensification, and OHC is now used as one of several parameters in hurricane prediction schemes (DeMaria et al. 2005).

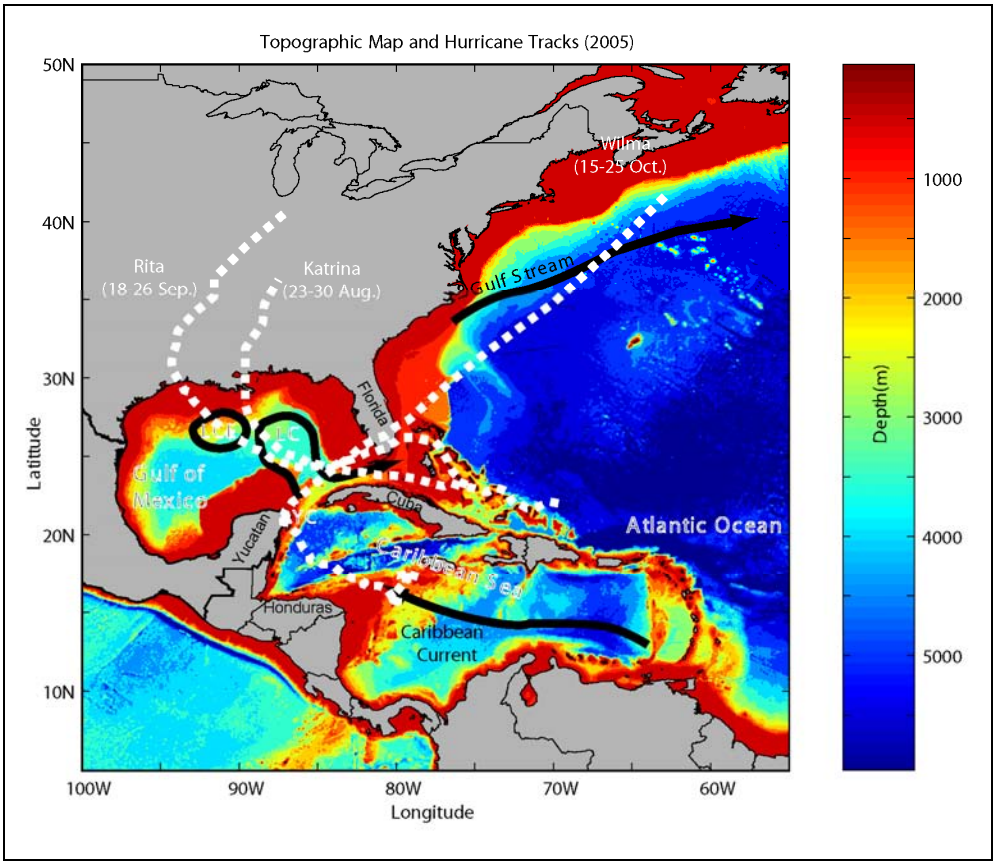

Figure 7.1a. Topographic map of the western North Atlantic (excluding the Pacific Ocean in the south-west corner, this is the area covered by our ocean forecast model, see text for details). The major ocean currents are indicated by heavy black arrows. The tracks of the three strongest hurricanes in 2005 are indicated in dashed white lines; all three reached a Category 5 status during their lifespan (Katrina and Rita in the Gulf of Mexico and Wilma in the Caribbean Sea). Acronyms are LC: Loop Current, LCE: Loop Current eddy, and YC: Yucatan Channel.

The OHC clearly depends on ocean dynamics. For example, lower OHC is generally associated with (vertical) mixing and upwelling that bring cooler water to the near-surface, i.e.,

both Z_{26} and T decrease (Price, 1981; Bender and Ginis, 2000; Shay et al. 2000). The progression speeds, U, of most hurricanes are such that U/C > 1, and usually U/C >> 1, where C is the first-mode baroclinic wave speed (≈ 2.5 m/s in the Caribbean Sea and the Gulf of Mexico (Chelton et al. 1998)). Such a storm (U > C) produces lee waves with large vertical isopycnal movements (> 50 m; vertical velocity $w \approx \pm 10^{-3}$ m s^{-1}) in the ocean and storm-induced upwelling and downwelling are confined to the immediate neighborhood of the hurricane eye and behind it (Geisler, 1970; Price, 1981; Gill, 1982; Greatbatch, 1983). Coupled with mixing, the local SST variations under the eye (diameters 10~100 km),[14] even a modest ±1°C, can mean the difference between a storm that rapidly intensifies and one that quickly decays (Cione and Uhlhorn, 2003; Emanuel, 2005a). Yet, the SST cooling patterns under the eye often go undetected since it is the most difficult region of the hurricane to accurately and routinely observe, and hence also to validate models. The first goal of this paper is to use satellite observations to detect isopycnal movements under the eye and in the wake of a hurricane (Wilma), and to verify an ocean forecast.

In the Caribbean Sea and Gulf of Mexico where powerful flows such as the Caribbean-Yucatan Current, the Loop Current and eddies (with diameters as large as 400km) exist, the OHC also depends on advection. (Please refer to Oey et al. (2005a) for a review of these currents). We have found (Oey et al. 2006), for example, that during Hurricane Wilma (October 16-25, 2005), the SST at a buoy around the Loop Current slowly increased (+0.4°C) a few days before the storm arrived, then decreased (–1°C) precipitously when the storm passed by. Oey et al. (2006) suggested that the sudden SST-drop could be explained by mixing and offshore advection of cooler shelf water by the storm, and that the pre-storm SST-rise was due to an increased influx of warm Caribbean Sea water into the Gulf, forced by hurricane-induced Ekman convergent flows that fed the Yucatan-Loop Current system.[15] The Yucatan-Loop Current system plays a central role in this warming process, which redistributes heat ahead of the storm, and which clearly has implications for hurricane predictions. The second goal of this paper is to further illustrate the warming process through numerical experiments.

Section 2 describes satellite data and the forecast model, section 3 compares satellite observations with forecast upwelling/downwelling cells, and section 4 presents model experiments that isolate the roles of Yucatan-Loop Current front on upper ocean heat distributions. This paper focuses on Hurricane Wilma (Table 7.1; Figure 7.1b), and detailed analyses on Hurricanes Katrina and Rita will be reported separately. Section 5 concludes the paper, and discusses future roles of ocean forecasts in improving hurricane predictions.

[14] Hurricane Wilma at its peak on *2005/October 19 at 12*:00 GMT had an eye's diameter that shrank to only *4~5 km*, a record (http://www.nhc.noaa.gov/pastall.shtml).

[15] Large and powerful hurricanes produce winds that mix and cool upper-ocean waters ahead of the storm, as Oey et al. (2006) also found for buoy measurements in the northwest Caribbean Sea during Hurricane Wilma.

Table 7.1.

Hurricane Wilma: Notable Status

Day/:00 GMT in October 2005	LON	LAT	Min Pressure (mb)	Max Wind Speed (m/s)	Saffir-Simpson Category	Comments
16/12Z	-79.4	17.1	1003	16	Tropical Depression	Genesis
18/15Z	-80.6	16.5	977	34	1	Hurricane
19/12Z	-82.8	17.2	882	78	5	Most Intense
22/06Z	-87.2	20.8	935	60	4	Yucatan Landfall
23/06Z	-86.8	21.8	962	45	2	To Gulf of Mexico
24/03Z	-83.7	24.4	958	51	3	Over Loop Current
24/09Z	-82.4	25.5	950	56	3	Prior to Landfall at Florida

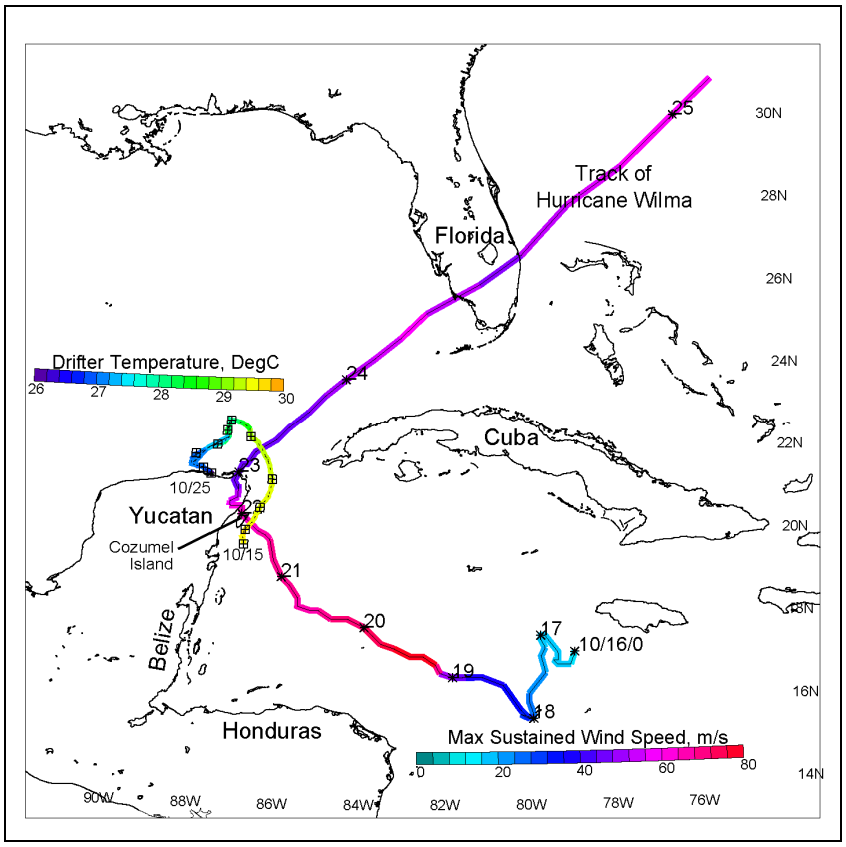

Figure 7.1b. Track of Hurricane Wilma colored with the storm's maximum sustained wind speed, and marked daily from October 16 at 0:00 GMT through October 25. Around the Yucatan peninsula, the track of a drifter colored by the sea-surface temperature that it measured is marked (crossed squares) daily beginning from October 15 through October 25.

7.2. METHODOLOGY

We use SSH anomaly (SSHA), objectively analyzed SSHA (OASSHA) and SST (OASST) from NOAA (www.aoml.noaa.gov/phod/dataphod), AVISO (www.aviso. oceanobs.com), and US-GODAE (www.usgodae.org) sites. Data before and after Wilma and on three pairs of tracks in close proximity are used to estimate changes (Figure 7.2). We used OASSHA maps to estimate errors due to the different positions of the paired tracks and found that these errors are small, so that the changes are dominated by the storm. We calculated differences, δSSHA = post-storm minus pre-storm SSHA, for each pair and interpolated the values onto a regular latitude grid. Using differences eliminates ambiguity associated with the unknown mean especially when comparing with the forecast response. In most cases, though, the storm-induced responses are so strong that using the actual SSHA yields very similar results. To verify some of the SST results, we have also used NDBC buoy data (http://www.ndbc.noaa.gov/; locations in Figure 7.3).

We use the Princeton Regional Ocean Forecast System (PROFS; http://www.aos.princeton.edu/WWWPUBLIC/PROFS/) to forecast ocean states in the Caribbean Sea and the Gulf of Mexico during Wilma (Figure 7.1). PROFS is based on the Princeton Ocean Model (POM; Mellor, 2004) and has been tested against observations as well as used for process studies (Oey et al. 2005a and b, where a list of recent publications is also given). The forecast, from October 16 through Nov/06, 2005, was initialized from a nowcast field that has already been assimilated with satellites' SSHA data up to October 16, 2005.[16] The nowcast positions of Loop Current and eddies compare well with AVISO. The original (real-time) forecast used Global Forecast System winds (Caplan et al. 1997), but was rerun for this study using the analyzed winds from the Hurricane Research Division (http://www.aoml.noaa.gov/hrd/) of the National Hurricane Center (NHC).[17] An animation of the wind field can be found at the PROFS web site (above). We will still refer to this rerun as "forecast" ("control experiment") to emphasize that it is free from satellite data assimilation. To calculate wind stresses, we use a bulk formula with a high wind-speed limited drag coefficient that curve-fits data for low-to-moderate winds (Large and Pond, 1981) and data for high wind speeds (Powell et al. 2003):

$$\begin{aligned} C_d \times 10^3 &= 1.2, && |\mathbf{u_a}| \le 11 \text{ m s}^{-1}; \\ &= 0.49 + 0.065\,|\mathbf{u_a}|, && 11 < |\mathbf{u_a}| \le 19 \text{ m s}^{-1}; \\ &= 1.364 + 0.0234\,|\mathbf{u_a}| - 0.00023158\,|\mathbf{u_a}|^2, && 19 < |\mathbf{u_a}| \le 100 \text{ m s}^{-1} \end{aligned} \qquad (2)$$

where $|\mathbf{u_a}|$ is the wind speed.[18] According to this formula, C_d is constant at low winds, is linearly increasing for moderate winds, reaches a broad maximum for hurricane-force winds, $|\mathbf{u_a}| \approx$ 30~50 m s^{-1}, and then decreases slightly for extreme winds. Donelan et al. (2004) suggest that the C_d-leveling at high wind may be caused by flow separation from steep waves. Moon et al. (2004) found that C_d decreases for younger waves that predominate in hurricane-forced wave fields. Bye and Jenkins (2006) attribute the broad C_d-maximum to the effect of spray, which flattens the sea surface by transferring energy to longer wavelengths.

[16] The nowcast was actually the continuation of a model run that has been assimilated with *SSHA* since *1992*.

[17] The timing and intensity for Wilma from all major forecast models were inaccurate especially when the storm was in the Caribbean Sea.

[18] This same formula was used in Oey et al. (2006), except that the coefficient for $|\boldsymbol{u_a}|^2$ was erroneously rounded off to *0.0002* at press.

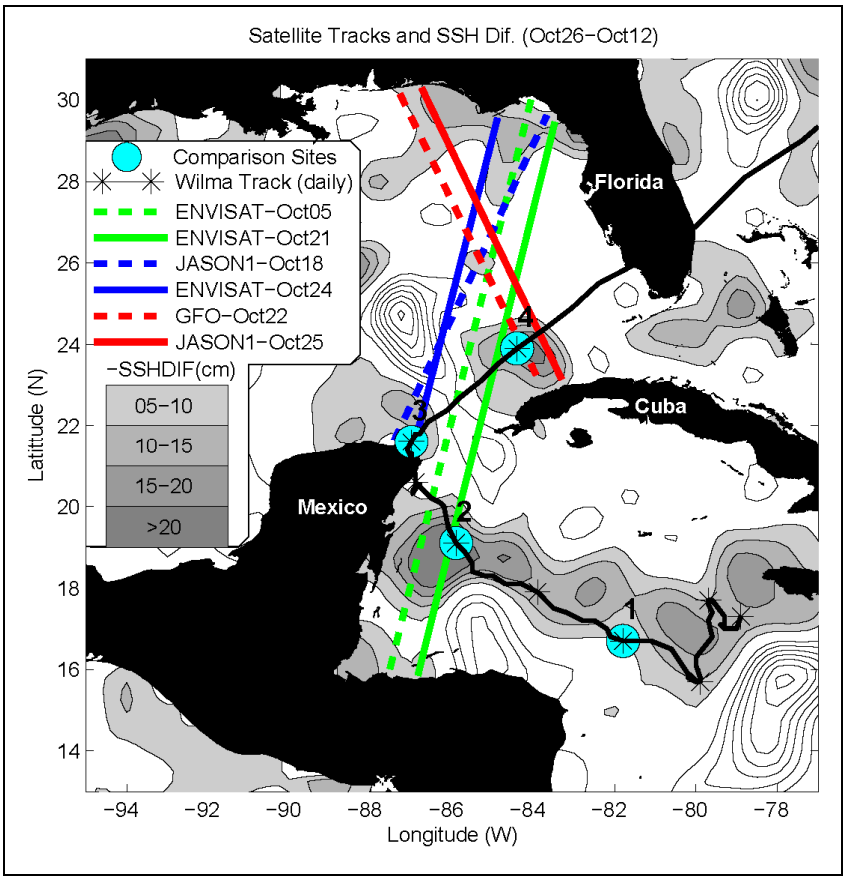

Figure 7.2. Contours of difference OASSHA (October 26 minus October 12; contour interval = 5 cm, zero contours omitted). Shaded are negative indicating regions of cooling; the inset chart shows contour values. Tracks for the indicated satellites and dates (see inset) are shown; colors indicate pairs of tracks from which differences, δSSHA, of along-track SSHA are shown in Figure 7.3. The path of Hurricane Wilma is shown marked daily beginning from October 16, 2005. Positions of the four sites labeled “1” through “4” at which observed and modeled SST and SSHA are compared (Figure 7.4) are also shown.

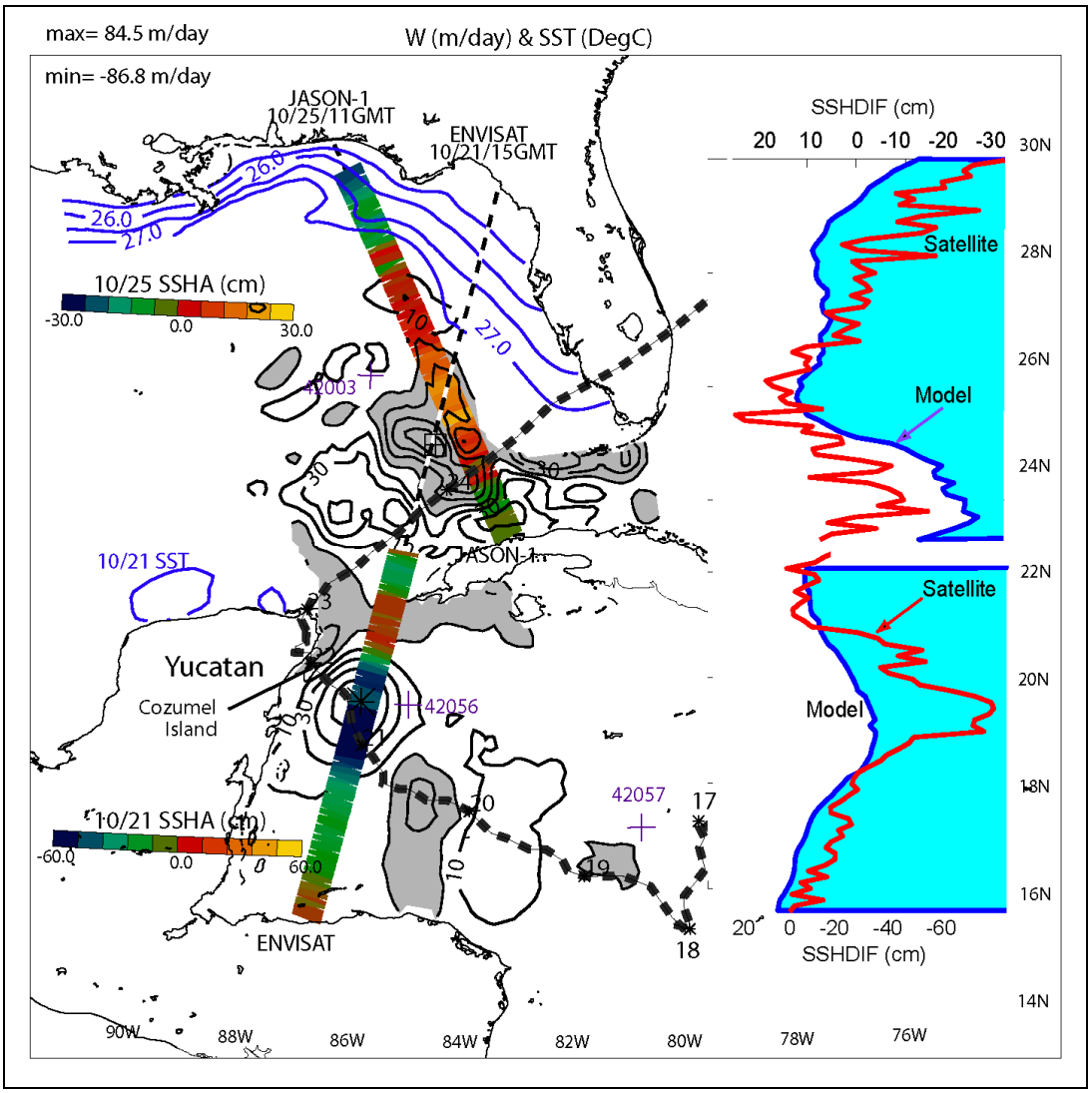

Figure 7.3a. Forecast vertical velocity w (black contours, interval = 10 m/day, negative shaded and zero-contour omitted) and SST (blue contours, interval = 0.5 °C). Contours south (north) of 22.5°N are for October 21 at 15:00 GMT (October 25 at 11:00 GMT) when Wilma was in the Caribbean Sea (has moved off east Florida). Maximum (minimum) w is indicated by a large asterisk (crossed-square) and values are shown on top-left corner of plot. Superimposed is ENVISAT satellite track (south of 22.5°N on October 21 at 15:00 GMT) colored with δSSHA = (post-storm minus pre-storm SSHA; color-bar shown left of track). A similar track north of 22.5°N is for the JASON-1 satellite on October 25 at 11:00 GMT (color-bar shown left of track). Wilma's path is shown; numbers on the path indicate days in October 2005. The insets on the right compare forecast and satellite δSSHA's along the tracks.

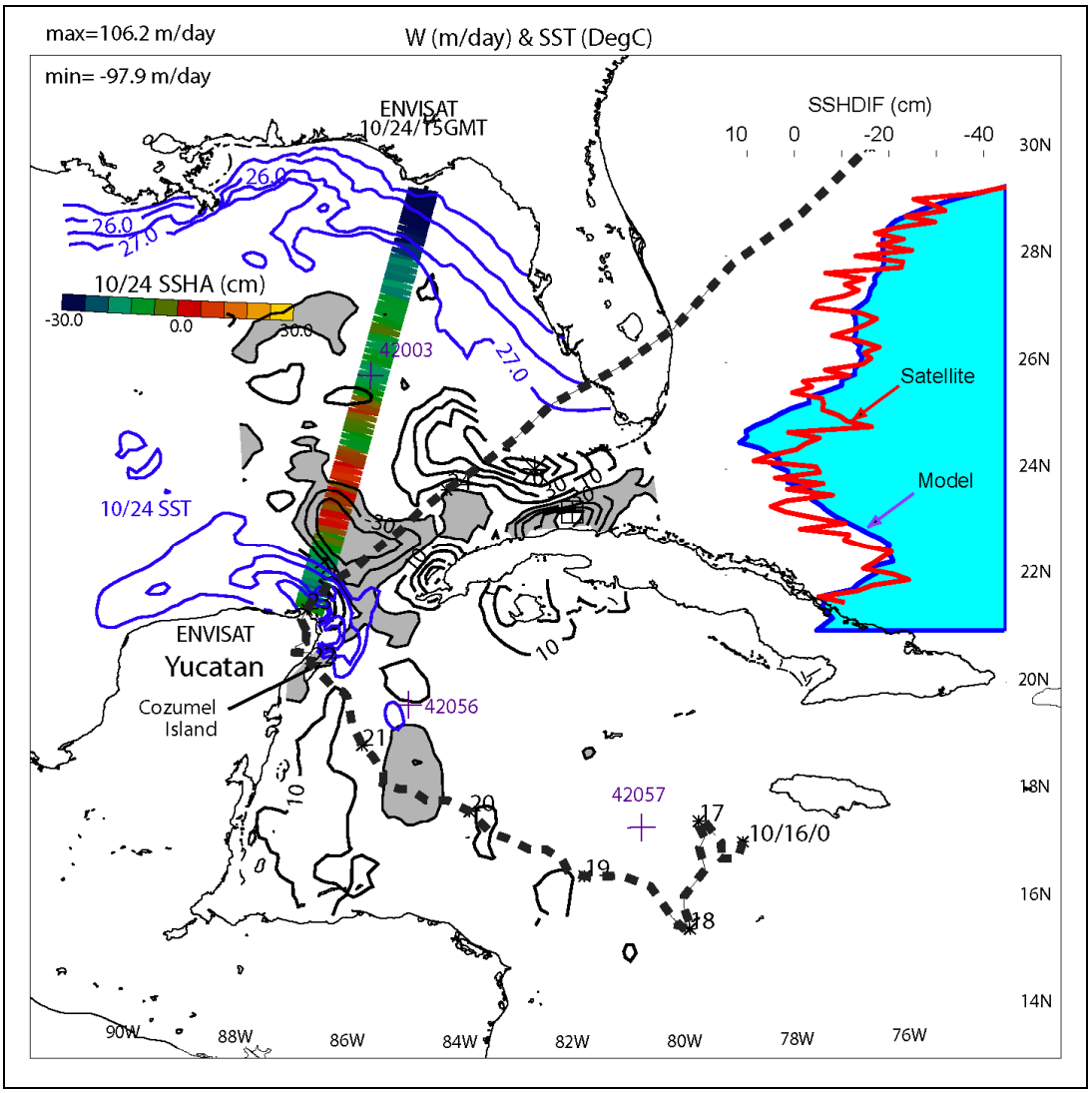

Figure 7.3b. Forecast vertical velocity w (black contours, interval = 10 m/day, negative shaded and zero-contour omitted) and SST (blue contours, interval = 0.5 °C). Maximum (minimum) w is indicated by a large asterisk (crossed-square) and values are shown on top-left corner of plot. Superimposed is ENVISAT satellite track on October 24 at 15:00 GMT colored with δSSHA = (post-storm minus pre-storm SSHA; color-bar shown left of track). Wilma's path is shown; numbers on the path indicate days in October 2005. The inset on the right compares forecast and observed δSSHA's along the track.

Surface heat and evaporative fluxes are set to zero so that the SST variations are due to model's internal dynamics; Price (1981) found that surface cooling by these fluxes is small compared to cooling by mixing. Bender and Ginis (2000) also used POM for the ocean component of the GFDL coupled model. The main difference is that they initialized using climatology for a spin-up time of O (months). Their initial ocean field therefore never reached an equilibrium state; it did not have a developed Loop Current, eddy-shedding and rings (Hurlburt and Thompson, 1980; Oey, 1996).

The model horizontal grid-size is variable and averages about 10 km in the Loop Current and northwestern Caribbean Sea. There are 25 sigma layers with 10 of them in the top 250 m for

local water depth ≈ 2500 m. The Mellor and Yamada's (1982) turbulence closure scheme modified by Craig and Banner (1994) to effect wave-enhanced turbulence near the surface is used. To account for mixing in stable stratification (e.g., internal waves; MacKinnon and Gregg, 2003), Mellor's (2001) modification of a Ridchardson-number-dependent dissipation is introduced.

7.3. SATELLITE OBSERVATIONS AND FORECAST

Except for special field programs (e.g., Price, 1981), survey of the upper ocean during a hurricane is not only costly but may also be impractical. One can use OASSH before a hurricane and assume that the ocean changes slowly (Shay et al. 2000). However, an active (time-varying) upper ocean is clearly essential in hurricane predictions (Bender and Ginis, 2000). Along-track altimeter data offers near-instantaneous and high resolution (≈ 5km) SSHA during a hurricane; it has been used in other oceanographic applications in which rapid observations of the sea-surface are required (e.g., in Tsunami detection, Geist et al. 2006). However, overlap of satellite tracks and the hurricane path is infrequent. An alternative is to use models. Here we validate forecast's upwelling and downwelling cells under Hurricane Wilma by comparing the forecast positions and timings of these cells and the corresponding SSHA's against along-track satellite data.

With a minimum surface pressure of 882 mb and maximum sustained wind speed of around 78 m/s (Table 7.1; Figure 7.1b), Hurricane Wilma was on record the most powerful Atlantic hurricane. The storm formed southwest of Jamaica near a warm eddy with high OHC; it strengthened on October 18 at 15Z ($|\mathbf{u_a}| \approx 34$ m s^{-1}) and became a category-5 hurricane on October 19 at 09Z as it moved west/northwestward into the Cayman Sea. Wilma weakened as it made landfall on October 22 at 06Z at Cozumel Island and Yucatan peninsula, but $|\mathbf{u_a}|$ was still > 60 m s^{-1}. It weakened further ($|\mathbf{u_a}| \approx 45$ m s^{-1}) while it moved slowly overland, and strengthened some 24~30 hours later ($|\mathbf{u_a}| \approx 51$~56 m s^{-1} on October 24) as it passed over the warm Loop Current and made landfall at Florida.

Wilma is one of the few major hurricanes to directly hit the Yucatan Channel (http://www.nhc.noaa.gov/pastall.shtml), and is also the only such hurricane to have remained in the northwestern Cayman Sea (west of 79^{o}W) and the Yucatan Channel for a long 7-day period. In the Caribbean Sea, Wilma traveled west/northwestward at U ≈ 2.5~3 m/s, so the averaged U/C ≈ 1.1. The storm was fast enough to produce lee waves, yet sufficiently slow that the combined action of upwelling and mixing was effective in cooling the near-surface waters (Price, 1981). Theory (Gill, 1982) gives a dominant (lee) wavelength $\lambda_F = (2\pi U/f)(1-(C/U)^2)^{1/2} \approx 160$ km, a frequency $\omega = f/(1-(C/U)^2)^{1/2} \approx 2f$ (period ≈ 1 day at 18^{o}N), and diminished trailing lee-wave amplitudes a fraction (≈ 0.2~0.3 for U/C ≈ 1.1) of the main disturbance immediately behind the storm.

Contours of OASSHA-difference (Figure 7.2), October 26 (post-storm) minus October 12 (pre-storm), show regions of negative SSH indicative of cooling along (and particularly to the right of) the storm in the Caribbean Sea. The rightward cooling bias has traditionally been attributed to the more intense mixing caused by stronger winds to the right of a moving hurricane (i.e., to the right of the storm, wind = hurricane wind + progression speed of the storm; e.g., Price, 1981, and more recently Sheng et al. 2006). This effect exists for Wilma, though it is weaker because the storm moves slowly in the Caribbean Sea. On the other hand, effects of flow convergence to the left of the storm due to the presence of the Honduran coast cannot be neglected (see below). Though the OASSHA maps in Figure 7.2 are highly smoothed as well as

aliased in time, one can still discern a pattern that shows wavelengths of 200~300 km with reduced trailing amplitudes. The wavelength is larger than but not inconsistent with the theoretical estimate. Wilma sped up in the Gulf of Mexico, U/C ≈ 2.3; theory gives $\lambda_F \approx 560$ km and $\omega \approx f$ (period ≈ 1.23 day at 24°N). However, while Figure 7.2 may contain storm-related signals in the Gulf, the presence of a strong Loop Current and continental shelves makes it difficult to interpret the results based solely on OASSHA maps.

Figure 7.3 shows the along-track δSSHA superimposed on forecast vertical velocity w-contours (chosen at z = −100 m near the base of the mixed layer, following Price (1981)). We also plot SST contours to show cooling over the northern Yucatan shelf during the 4-day period from October 21 (Figure 7.3a) to October 24 (Figure 7.3b). Low (high) δSSHA's colored as green-blue (red-yellow) generally coincide with upwelling (downwelling, shaded) cells. Prominent ones are (i) an upwelling cell southeast of Cozumel Island on October 21 at 15:00 GMT, a few hours after the storm center has passed: δSSHA ≈ −0.7 m and w ≈ 84 m/day (10^{-3} m/s; Figure 7.3a); (ii) a downwelling cell off southwestern Florida slope on October 25 at 11:00 GMT, more than 1 day after the storm: δSSHA ≈ 0.2m and w ≈ −87 m/day, and also for the same date a smaller upwelling cell north of Cuba where δSSHA ≈ −0.2m and w ≈ 50 m/day (Figure 7.3a); and (iii) on October 24 at 15:00 GMT (Figure 7.3b), an upwelling cell of cooled water off Yucatan where on the shelf δSST ≈ −1.5 °C (c.f. the SST's of Figures 7.3a and 7.3b) and δSSHA ≈ −0.15m, and also a downwelling cell further northeast with δSSHA ≈ 0.05m and w ≈ −50 m/day.[19] The 1.5 °C drop in SST on Yucatan shelf is in excellent agreement with the SST measured by a drifter released during Wilma (from the NOAA site www.aoml.noaa.gov/phod/dataphod), shown in Figure 7.1b. The drifter recorded an SST = 28.9 °C going northward in the Yucatan Channel on October 18 at 12:00 GMT, and an SST = 27.1 °C as it made a cyclonic turn onto the Yucatan shelf on October 23. Note that on the latter two dates (October 24 at 15:00 GMT & 25) shown in Figure 7.3, even though the storm has passed, strong ocean responses remain under the Loop Current. Figure 7.3 also compares model and satellite δSSHA's; these generally support the conclusions obtained from the w-plots in the ocean's interior. The agreements are better than expected considering the fast nature of the response involving rapidly propagating surface waves. Both observation and model also indicate low sea-levels along the northeastern Gulf Coast following Wilma's landfall at southern Florida on October 24 at 10:00 GMT. We do not know the source for the discrepancy between the intensities of observed and modeled minima off the Cozumel Island on October 21 at 15:00 GMT (Figure 7.3a). A closer examination of AVISO's OASSH maps before Wilma did show a small (diameter ≈ 100 km) cyclone east of Yucatan. The cyclone was not resolved by the model and may have accentuated the observed SSH-drop due to Wilma. The modeled −0.35m drop in this case actually agrees well with the smoothed OASSH map (see Figure 7.4 at site#2), and corresponds to an isopycnal uplift of about +60 m (not shown).

The w-contours in the Caribbean Sea (Figure 7.3a) show lee waves with amplitudes a fraction (≈ 1/3) of the main peak southeast of Cozumel Island and wavelengths ≈ 180~200 km consistent with the theoretical estimates and also with the OASSHA map of Figure 7.2. There is a discrepancy between the forecast oscillatory period of about 1.2 day (not shown) and the theoretical estimate of 1 day. However, the longer period may be caused by Doppler shift of the frequency by the westward currents u observed along the southern slope of the Cayman Sea

[19] The variations are clearly hurricane-induced. Much weaker vertical velocities (magnitudes ≈ *30 m/day* and less) are seen in sensitivity experiments we conducted with zero and weak winds.

(Fratantoni, 2001). The effective frequency = $(U+u)2\pi/\lambda_F$; substituting a period of 1.2 day gives $u \approx -0.4$ m/s, which agrees with the observed speeds of the westward currents in this region.

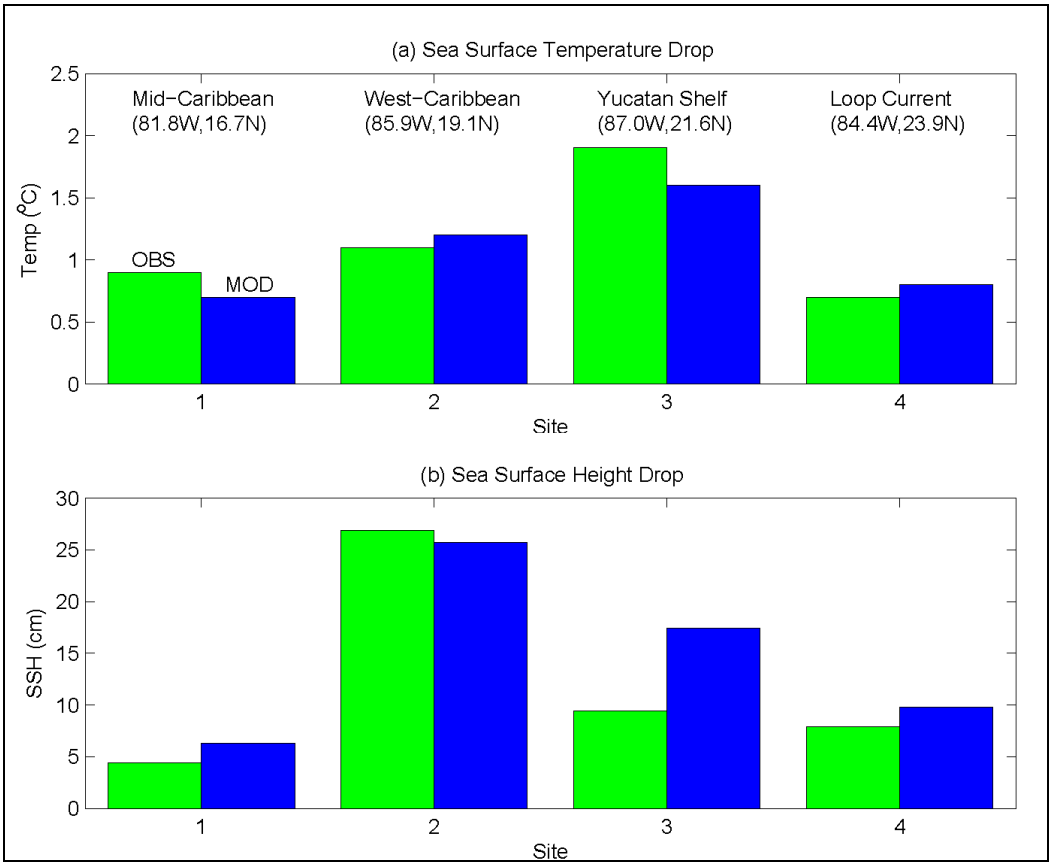

Figure 7.4. A comparison of observed (green) and forecast (blue) (a) SST and (b) SSHA drops (October 26 minus October 16) at the four sites shown in Figure 7.2.

Figure 7.4 compares model and observed drops in SST and SSHA at four locations along the storm's track as indicated in Figure 7.2. The largest drop in SSHA is at "site 2" indicating large upwelling (c.f. Figure 7.3) but because of deep mixed layer in the Caribbean Sea the corresponding SST drop is less than that over the Yucatan shelf ("site 3"). Similarly, smaller SST drops are seen at "site 1" (mid-Caribbean) and "site 4" (Loop Current). At "site 3" model and observed SST-drops compare well suggesting that (since model surface flux = 0) the predominant shelf cooling is due to upwelling from the upper slope, as seen also from the SST contours of Figure 7.3b and the drifter mentioned above. The 0.7~1.7 °C drop in SST's shown in Figure 7.4 reflects a general post-Wilma cooling in the Caribbean Sea and the eastern Gulf of Mexico, as we also confirm (not shown) from SST measurements at the three NDBC stations shown in Figure 7.2.

7.4. Loop Current and Hurricane-Induced Currents

The Yucatan-Loop Current is a western boundary current that flows along the eastern Yucatan coast into the Gulf; its speeds can exceed 2 m/s near the surface (please see the review and the extensive list of references in Oey et al. 2005a). Figures 7.5a and b show forecast

velocities from the control experiment at z = –1m superimposed on color OHC images on (a) October 20 at 12:00 GMT when Hurricane Wilma was in the Caribbean Sea and (b) October 23 at 6:00 GMT when the storm was about to leave Yucatan towards Florida. Figure 7.5a shows that the storm produces surface convergent flows against the northeast Yucatan coast. Note also flow convergence along the Honduran coast to the left of the storm, mentioned previously in conjunction with the rightward bias of the OASSHA-difference field of Figure 7.2. In Figure 7.5b, the wind has become directed along the Yucatan-Loop Current front. Convergence and down-front wind strengthen oceanic fronts (Wang, 1993; Thomas and Lee, 2005), and Figures 7.5a and b show large amount of near-surface currents into the Yucatan Channel.

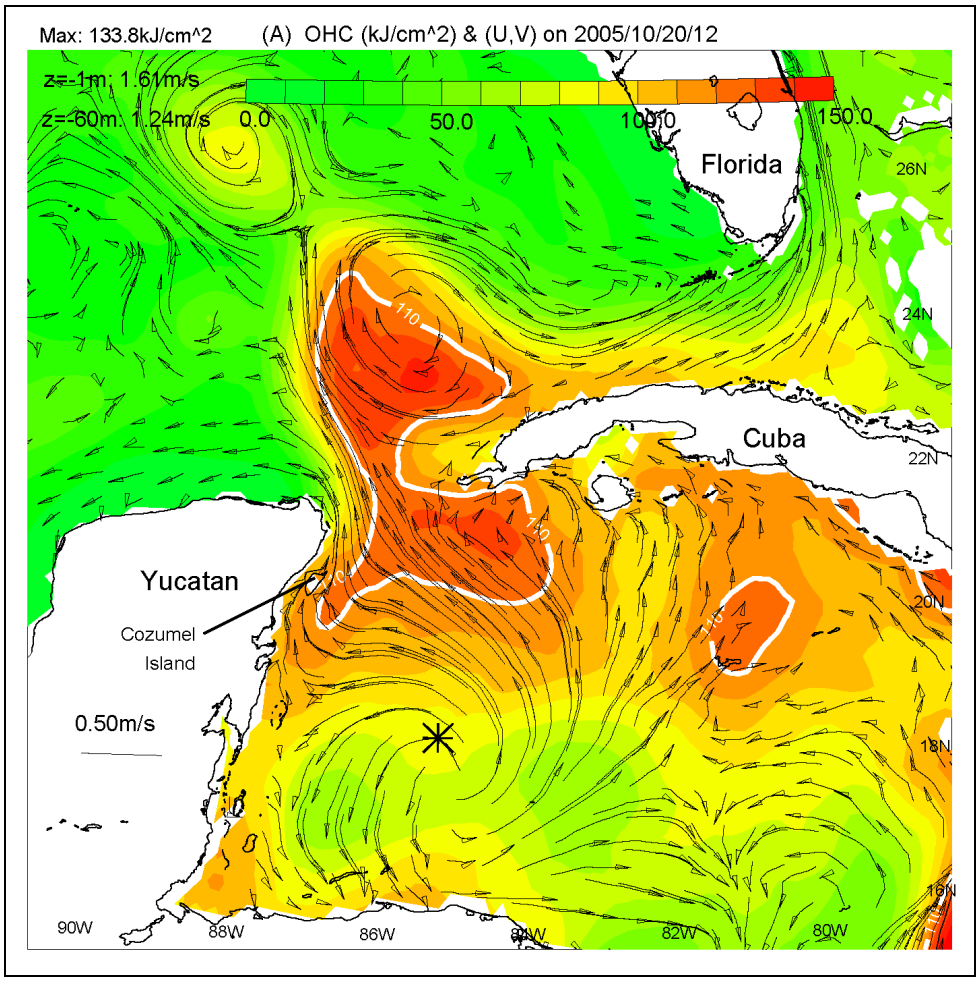

Figure 7.5a. Color image of the forecast OHC on October 20, 2005, at 12:00 GMT during Hurricane Wilma. Maximum OHC is printed on the top-left corner of the panel. Thick-white contour indicates OHC=110 kJ/cm^2. Forecast currents at z=–1 m are shown as black trajectories (with arrows) launched from every other four grid points. Maximum speeds (in Yucatan Channel) at z=–1 m and –60 m are also printed. The large asterisk indicates the position of Wilma at this forecast date.

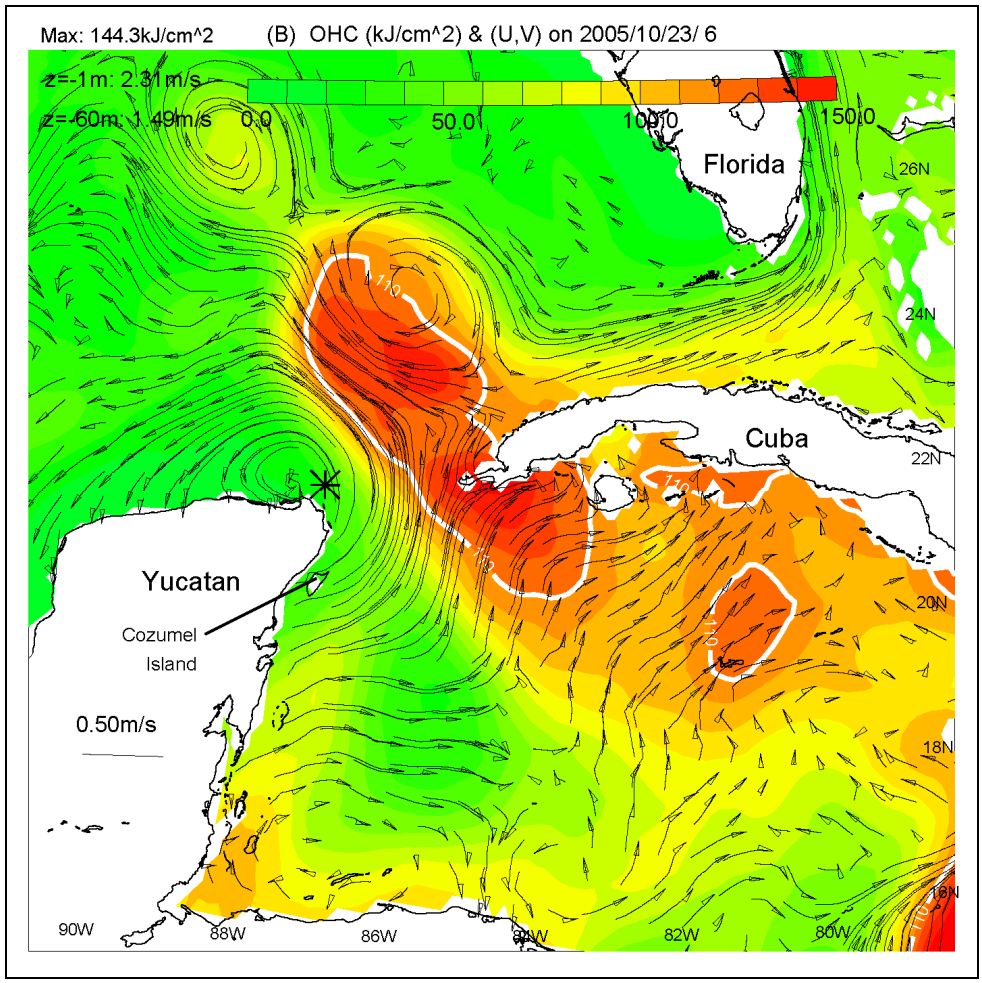

Figure 7.5b. Color image of the forecast OHC on October 23, 2005, at 6:00 GMT during Hurricane Wilma. Maximum OHC is printed on the top-left corner of the panel. Thick-white contour indicates OHC=110 kJ/cm^2. Forecast currents at z=–1 m are shown as black trajectories (with arrows) launched from every other four grid points. Maximum speeds (in Yucatan Channel) at z=–1m and –60m are also printed. The large asterisk indicates the position of Wilma at this forecast date.

Is the response fundamentally different if the Yucatan-Loop Current were absent? To address this, we conduct another experiment in which the model ocean is initially at rest with level isopycnals. We choose the vertical temperature and salinity (hence density) profiles to be area averages of the Caribbean Sea's climatology profiles used in the control experiment. The model is then forced by the same Wilma wind field used in the control experiment, and for the same period from October 16 through November 6, 2005. As a check, we repeated the same (level-isopycnal) experiment but without the wind, and confirmed that a trivial solution (zero velocities) was obtained.

Figures 7.5c and d show the OHC and surface velocities for the level-isopycnal experiment. In addition to cooling (indicated by decreased OHC) along the hurricane's path, the figures clearly show regions of increased OHC due to convergent (downwelling) flows onto coastlines: southern Cuba and also northeastern Yucatan (for Figure 7.5c). There are also increased flows

into the Yucatan Channel, but they are spread across the channel. By contrast, for the control experiment (Figures 7.5a and b), the surface flows tend to concentrate along the Yucatan-Loop Current front. Figure 7.6 compares near-surface, 150-m transports through the Yucatan Channel for the control and level-isopycnal experiments. Intensification of the western-boundary jet in the control experiment begins around October 20~21, while the level-isopycnal experiment shows broader increased flows that extend to the mid-channel. The broad flows result in a correspondingly broad increase in OHC north of the channel (compare Figures 7.5c and 5d). By contrast, Oey et al. (2006) show that, in the control experiment, the heat input through the channel is concentrated around the Loop, contributing to a temperature increase of about 1 °C.[20] The corresponding increase in OHC around the Loop is barely discernible in Figure 7.5. However, the increase is clearly seen by taking differences (in either temperature or OHC) between the experiment with wind (i.e., control or level-isopycnal) and a corresponding experiment without wind. Taking differences in this way minimizes contributions from background variability that is not related to Hurricane Wilma especially for the control experiment. However, we obtain very similar results by simply subtracting the initial conditions. Figure 7.7 shows the difference-temperatures at z = –50 m for (a) the control and (b) level-isopycnal experiments.[21] In (b) the warm water spreads into the Gulf, while in (a) it is concentrated along the Loop and has about three-time higher temperatures (1.5°C rise instead of 0.5°C).

[20] Another contribution, *20~30%*, is due to wind-induced convergence at the Loop Current front.

[21] We choose subsurface (e.g. $z = -50m$) for comparison because for the level-isopycnal experiment, since surface fluxes = *0* and initially there are no horizontal thermal gradients, warming can only occur below the surface, caused by flow convergences and advection by the storm.

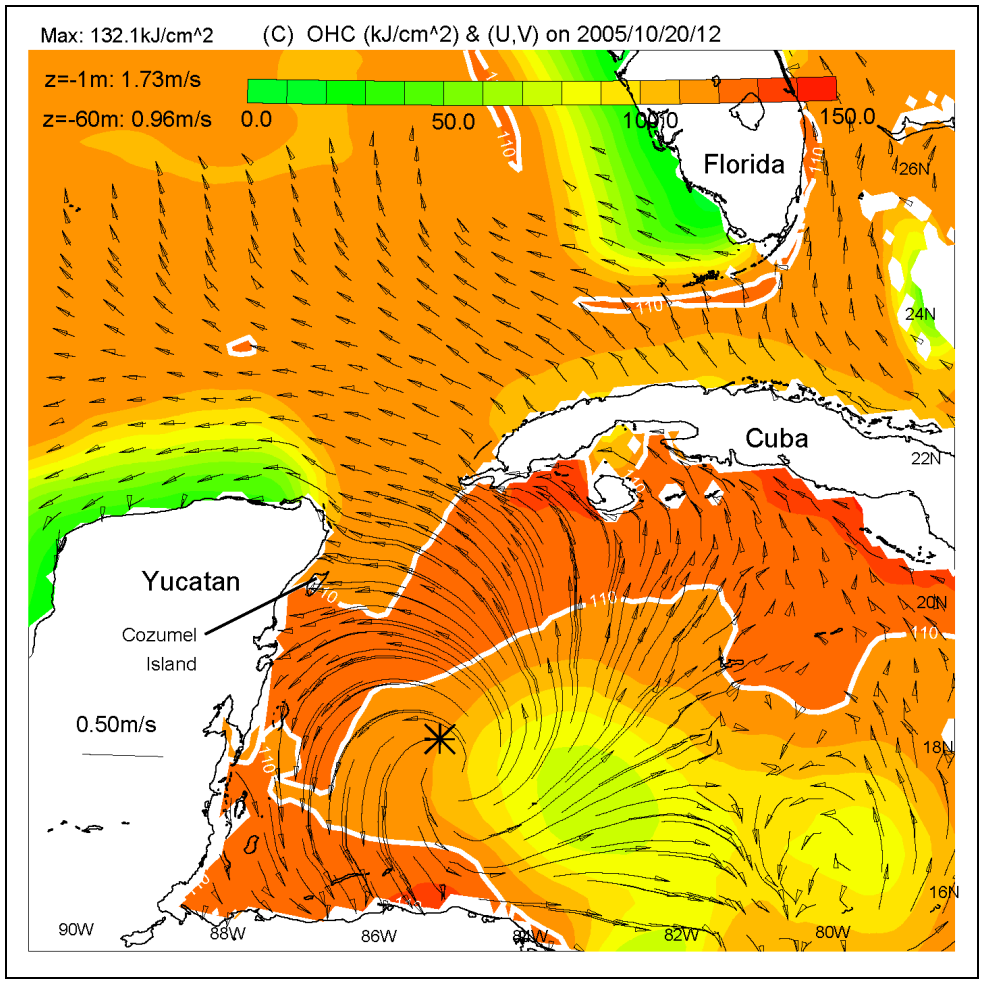

Figure 7.5c. Color image of the forecast OHC on October 20, 2005 at 12:00 GMT during Hurricane Wilma without the Yucatan-Loop Current frontal system. Maximum OHC is printed on the top-left corner of the panel. Thick-white contour indicates OHC=110 kJ/cm^2. Forecast currents at z=–1 m are shown as black trajectories (with arrows) launched from every other four grid points. Maximum speeds (in Yucatan Channel) at z=–1 m and –60 m are also printed. The large asterisk indicates the position of Wilma at this forecast date.

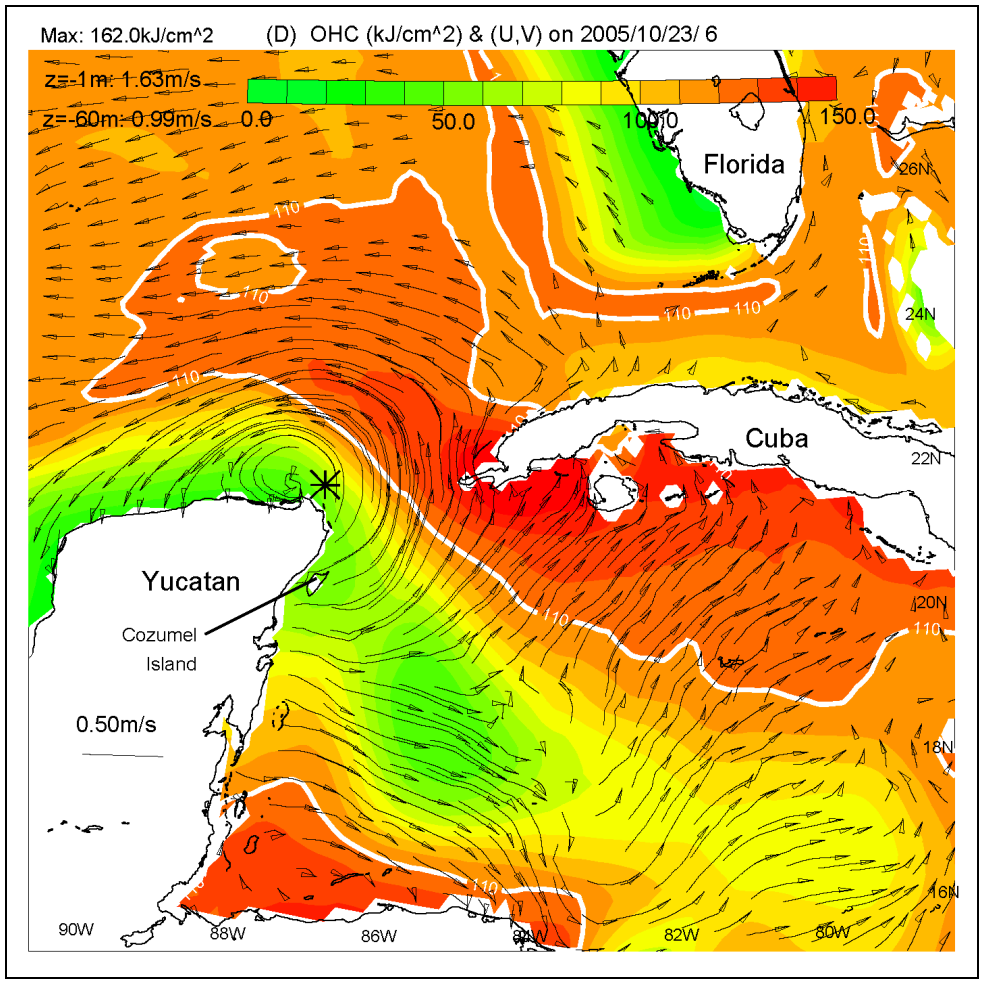

Figure 7.5d. Color image of the forecast OHC on October 23, 2005, at 6:00 GMT during Hurricane Wilma without the Yucatan-Loop Current frontal system. Maximum OHC is printed on the top-left corner of the panel. Thick-white contour indicates OHC=110 kJ/cm^2. Forecast currents at z = –1 m are shown as black trajectories (with arrows) launched from every other four grid points. Maximum speeds (in Yucatan Channel) at z=–1 m and –60 m are also printed. The large asterisk indicates the position of Wilma at this forecast date.

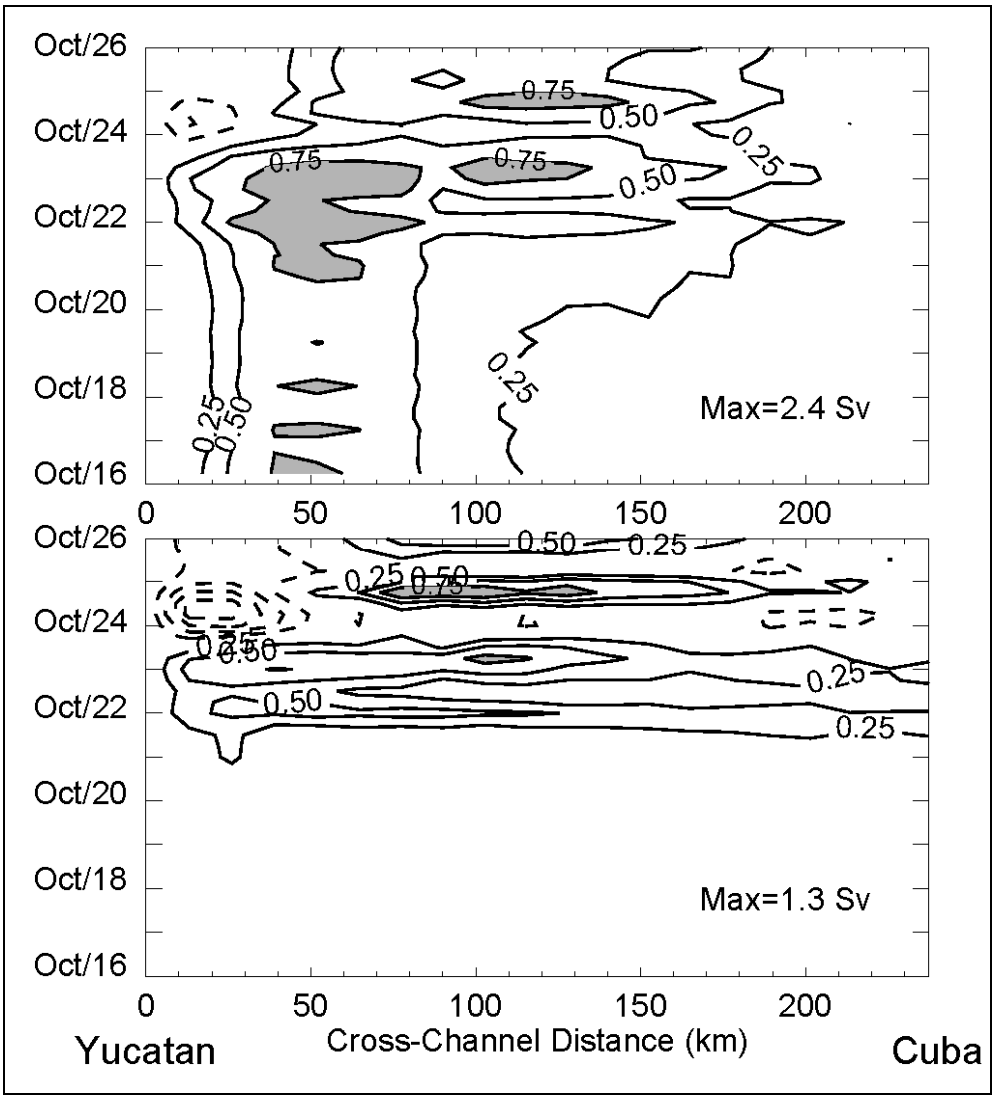

Figure 7.6. Transports through the Yucatan Channel in the near-surface 150 m of the model ocean for the control forecast experiment with Loop Current (upper panel) and for the experiment with no Loop Current (i.e., initially level isopycnals; lower panel). These are plotted as a function of cross-channel distance and time. Contours are in 1/4 of the maximum value in Sv (= 106 m/s^3) as indicated in each panel. Zero contour is omitted and shaded are where values > 3/4 of maximum.

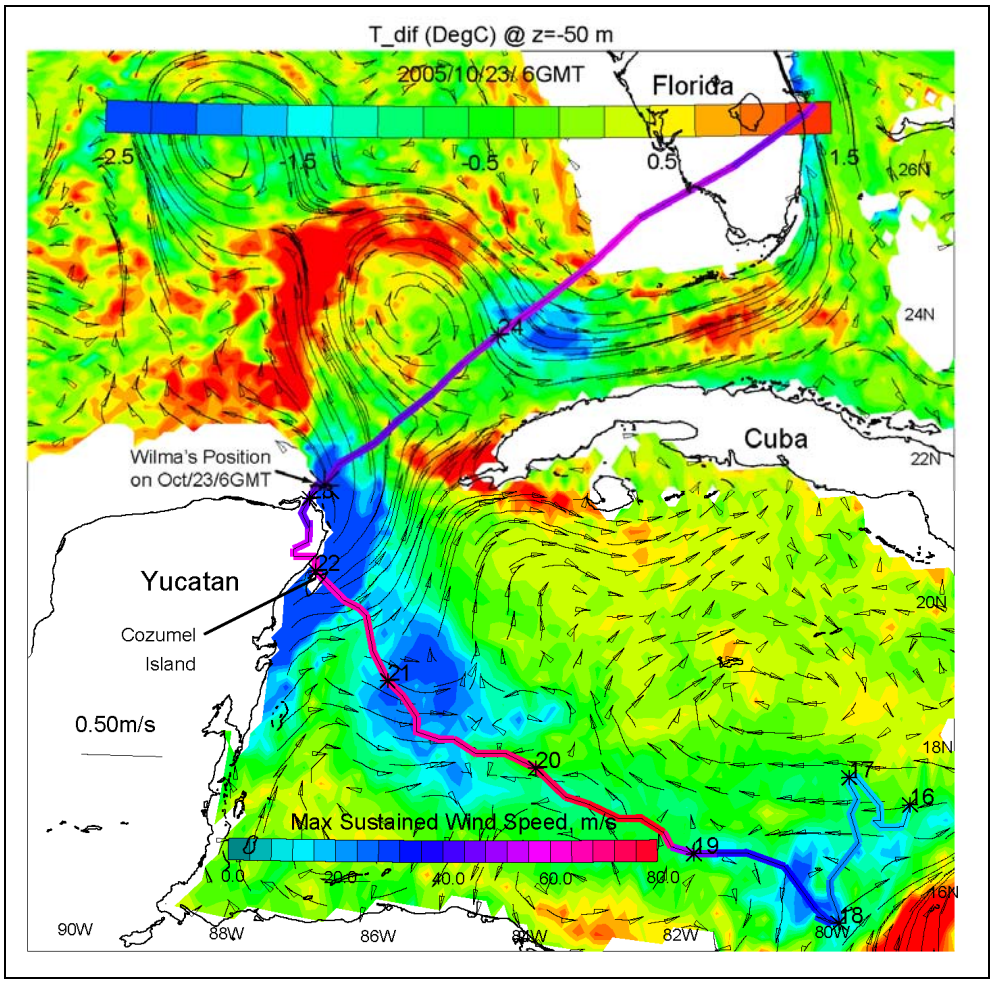

Figure 7.7a. Color image of the temperature-difference between experiments with and without Hurricane Wilma for the control experiment at z = –50 m on October 23 at 06:00 GMT. This shows Wilma-induced warming around the Loop Current, and cooling along Wilma's path in the Caribbean Sea. The path of Wilma is shown colored with its corresponding maximum sustained wind speeds (color-scale at bottom). Numbers next to small asterisks indicate days in October 2005, and Wilma's position on October 23 at 06:00 GMT is marked.

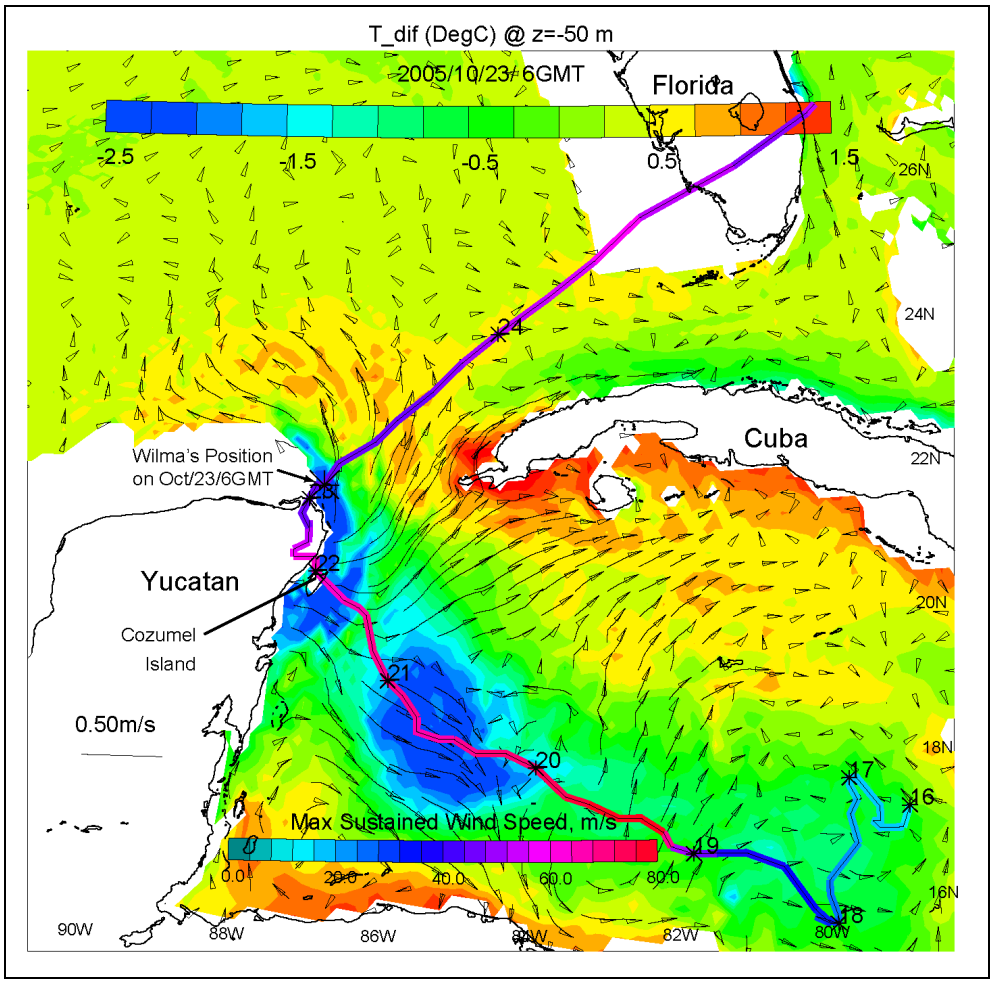

Figure 7.7b. Color image of the temperature-difference at z = –50 m on October 23 at 06:00 GMT between experiments with and without Hurricane Wilma for the initially-level isopycnal experiments. The path of Wilma is shown colored with its corresponding maximum sustained wind speeds (color-scale at bottom). Numbers next to small asterisks indicate days in October 2005, and Wilma's position on October 23 at 06:00 GMT is marked. In contrast to Figure 7.7a, this now shows the spread of warm water north of the Yucatan Channel from the Caribbean Sea into the Gulf of Mexico, though cooling along Wilma's path in the Caribbean Sea still exists.

Strong flows such as the Loop Current therefore impact the distribution of heat and cannot be neglected in hurricane predictions. In the case of Hurricane Wilma, the heat redistribution (by the Loop) may have had some practical significance. In the absence of the Loop the storm would have traversed over a larger area of high OHC on its way to Florida; in other words, Wilma would have traversed over the pool of warmer water that it forced through the channel into the Gulf (Figures 5c,d)! The Loop diverted this warm water "out of Wilma's way," so to speak. To further illustrate this finding, we average OHC (and other variables) over circles of radii 50km centered at the hurricane's track over its lifespan. This results in along-track and time (two-dimensional) arrays for each variable. The assumption is that, as far as the storm is concerned, the ocean surface directly under the eye is the most relevant (Emanuel, 2005a). Figure 7.8 plots

the OHC-difference (i.e., track values on October 16 are subtracted) contours for (a) the control experiment and (b) the initially-level isopycnal experiment. In general, cooling occurs when the storm comes near or after it has passed (i.e., solid contours are above the storm's track in the figure). Notable exceptions occurred in Figure 7.8a for the control experiment over the Yucatan shelf (along-track distance ≈ 1600 km; c.f. Figure 7.4a, site3) and also over the Loop Current's southern core just north of the Yucatan Channel (along-track distance ≈ 1900 km) where OHC-drop of as much as –30 kJ/cm^2 occurred a few days before the storm actually arrived. The cooling is caused by wind-induced vertical mixing and westward Ekman currents towards the Yucatan-Loop Current front. By contrast, despite a similar cooling in the absence of the Loop Current, Figure 7.8b actually shows a slight warming because of the presence of the pool of warmer water just north of the channel (Figures 5d and 7b).

7.5. CONCLUSION

We emphasize that the model isopycnal motions as indicated by the w-contours and SSHA's in Figure 7.3 are forecast results (i.e., not assimilated with satellite SSHA). We have shown, therefore, that along-track satellite altimeter data is useful for evaluating forecast skills of an ocean model during a hurricane. Assuming an accurate wind field, the generally good agreements between model and observation in terms of the timings and locations of upwelling and downwelling cells are encouraging, and suggest that hurricane-induced vertical motions are deterministic even in a complex mesoscale eddy field (e.g., Loop Current and eddies). We conclude that satellite along-track data offers a high-resolution dataset against which the ocean component of a hurricane forecast system can be routinely validated. The limiting factor is the availability of accurate forecast wind.

On the other hand, the presence of powerful ocean currents and coastal boundaries gives rise to intertwined hurricane-ocean interactions that in turn can modify the storm. In the case of Hurricane Wilma, we show that the Yucatan-Loop Current system diverted heat away from the storm's projected path, and may have helped tame the storm before it hit Florida.

Existing hurricane coupled models (e.g., Bender and Ginis, 2000) have simplified ocean-initialization schemes that do not accurately model the Loop Current and eddies. Statistical prediction systems (e.g., DeMaria et al. 2005) in part rely on smoothed OASSH maps and assume that the ocean is slowly-varying. The present study suggests that future hurricane predictions may benefit from more proactive ocean forecasts that are initialized by data assimilation (e.g., satellite data). An important facet of improved prediction is the inclusion of a more refined parameterization of wind-induced mixing process: effects of surface waves under strong winds in particular. For example, Oey et al. (2006) noted that the SST at NDBC 42056 (Figure 7.3) began to drop days before the arrival of Wilma; i.e., when the storm was near NDBC 42057. We attributed the cooling to the large size of the storm that produced current mixing from a distance. However, the cooling may also have been additionally induced by mixing due to swells that were generated when Wilma was at its peak intensity hundreds of kilometers to the east.

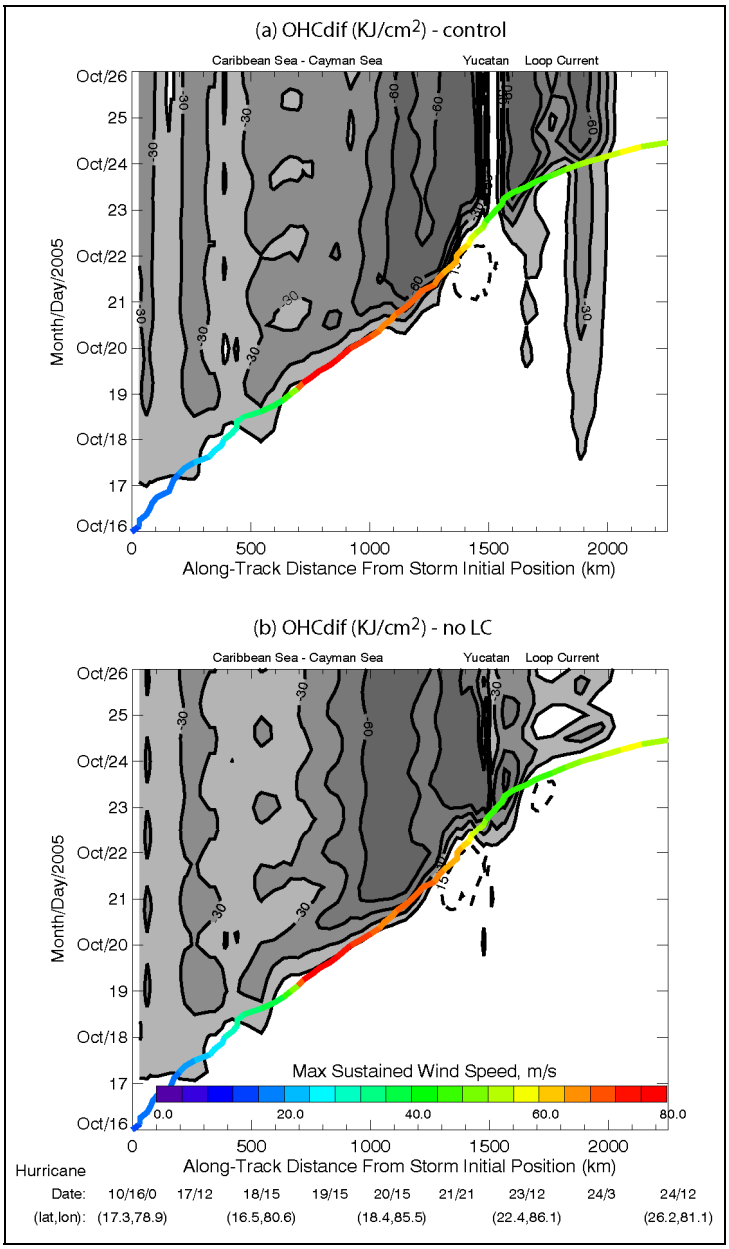

Figure 7.8. Along-hurricane-track and time contours of OHC-difference (i.e., the initial along-track values have been subtracted) in kJ/cm^2 for (a) the control experiment (with Loop Current) and (b) the initially-level isopycnal experiment (without Loop Current). Hurricane Wilma track (colored with its maximum sustained wind speed, scale shown) is also shown on this distance-time space, so that the slope is equal the inverse of the storm's progression speed. Negative contours (i.e., cooling) are solid and shaded, positive (i.e., warming) are dashes and the zero-contour is omitted. The white region above Wilma's track at Yucatan in "(a)" is land.

CHAPTER 8. CONCLUSIONS

This project has advanced our knowledge of hurricane-induced current and wave responses in the Gulf of Mexico by examining in details two cases of importance: Hurricanes Katrina and Rita. In addition, we have also examined the ocean responses due to Hurricane Wilma. A summary of our research has been given at the beginning of this report. In this concluding chapter, we summarize the practical implications of our work. We begin by listing the study's specific objectives as requested by MMS:

Specific objectives as requested by MMS are

1. Conduct a realistic simulation of responses of currents and waves to Hurricanes Katrina and Rita throughout the entire water column in the northern Gulf of Mexico;
2. Determine the length of time for which substantial ocean response to these hurricanes persisted, and
3. Determine the area or areas of greatest wave height and current speed.

That Objective 1 has been met is clear from the chapters of this report; in particular Chapters 2 (Katrina) and 3 (Rita). We have also examined the responses throughout the entire water column and have simulated responses to other major hurricanes for 2005 (Chapters 4 and 5). The particular case of Hurricane Wilma that gave rise to unique responses in the Loop Current is given in Chapters 6 and 7.

The length of time for which substantial ocean response to these hurricanes persisted (Objective 2) can also be assessed from the previous chapters. For wind-waves, the time-scale from generation, to peak and then decay is relatively short, about 2~3 days (e.g., see Figure 2.7 for Katrina; and Figure 3.9 for Rita). For currents, we concentrate on the inertial currents which contain most of the energy of hurricane-induced responses in the ocean. Near the surface, strong inertial currents can persist for a few days but the energy penetrates to great depths (~1000 m) and can persist for 10days or longer (e.g., see Figures 4.9, 5.4 and 5.6b). We find strong modification of these energy paths and lengths of time of persistent energies by Loop Current and rings.

For Objective 3, we have already given in Figures 2.6 (Katrina) and 3.8 (Rita) the swaths of maximum wave heights. The model wave heights exceed 25 m for Katrina and about 20 m for Rita. They are higher to the right of the storm than to the left as explained in Chapters 2 and 3. The great waves occurred just as the storms reached the continental slope and outer shelves; in the case of Katrina, this probably accounted for the severe damage to the oil platform Mars just south/southeast of the Mississippi delta.

Although information about the ocean currents is also contained in the various chapters, it is useful to re-plot them in the similar manner as the swaths of maximum wave heights. We show swaths of maximum near-inertial current speeds at z = 0 m (i.e., surface, Figure 8.1) and at z = –600 m (Figure 8.2) produced by Katrina and Rita. Consistent with the wind-waves, strongest inertial currents again occur to the right of the storms. Top speeds reach 3.8 m s^{-1} for Katrina and 2.8 m s^{-1} for Rita. Strong currents occur again just over the outer shelves and slope regions of the northern Gulf of Mexico, and also near the coast where great sea levels due to storm surges prevail (Figure 3.1).

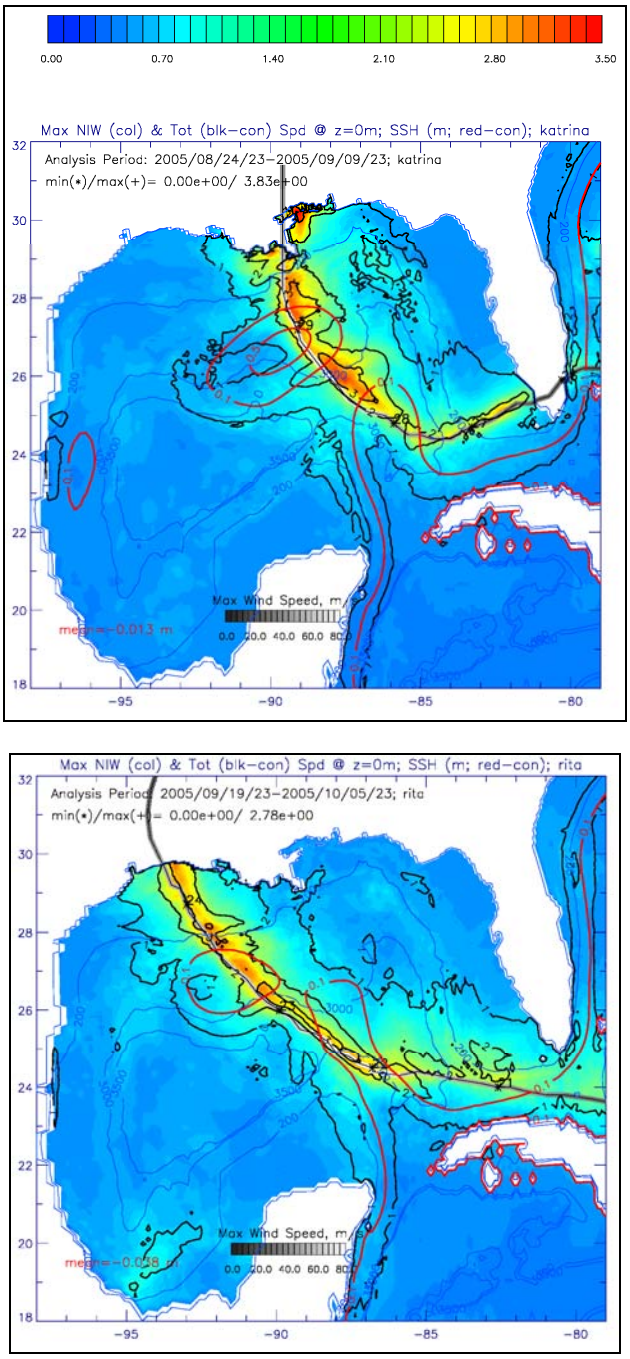

Figure 8.1. Swaths of maximum near-inertial current speeds (colors) at z = 0 m during Katrina (upper panel) and Rita (lower panel). Contours indicate total current speeds (black), sea-surface height = 0.1 m contour indicating the Loop Current and rings (red), isobaths (blue) and storm-tracks with wind speed (grey scale).

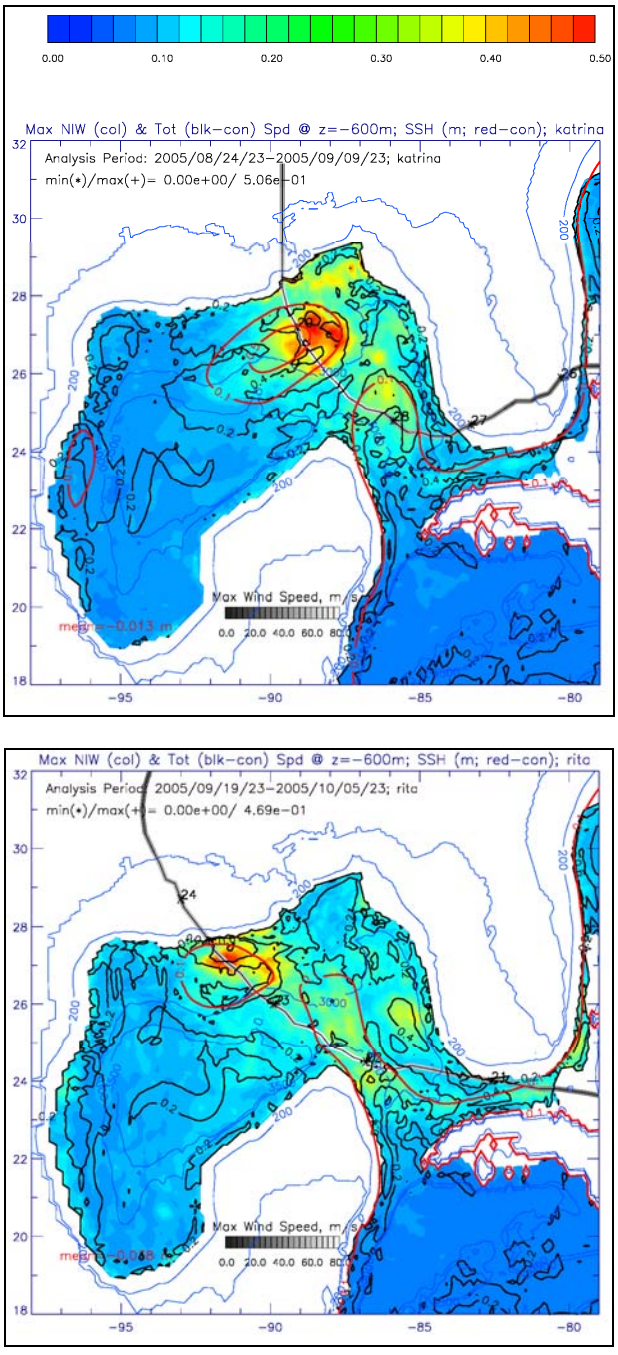

Figure 8.2. Swaths of maximum near-inertial current speeds (colors) at z = –600 m during Katrina (upper panel) and Rita (lower panel). Contours indicate total current speeds (black), sea-surface height = 0.1 m contour indicating the Loop Current and rings (red), isobaths (blue) and storm-tracks with wind speed (grey scale).

That inertial currents dominate the surface response can be seen from the black contours which show in Figure 8.1 the 1, 2 and 3 m s^{-1} total-current-speed contours. These generally coincide with amplitudes of inertial-currents, i.e., the bright-blue color background coincides with the 1 m s^{-1} total speed contour. In the case of Katrina, the surface inertial currents are stronger outside the Loop and ring than inside them (for examples between the Loop and ring and also north of the ring). The weaker currents inside the Loop and ring are consistent with the theoretical predictions (Chapters 4) that near-inertial energy tends to escape the surface and is chimneyed downward in these anticyclonic regions where the relative vorticity is negative (Figure 5.2). This is clearly seen from the inertial amplitude plots at z = –600 m in Figure 8.2, which shows a general concentration of near-inertial energy in the ring and the Loop Current. The weak surface inertial amplitudes inside the ring are particularly evident in Figure 8.1. In the case of Rita, the contrast between energy level inside and outside the Loop Current or ring is less, in part because the Loop and the ring had also weakened (Figure 3.1). Nonetheless, the inertial currents still peak north of the ring over the outer shelf of the Texas-Louisiana. As a consequence of the chimneying effect of the surface inertial energy to subsurface in regions with anticyclonic vorticity, a comparison of the near-surface inertial energy between Katrina and Rita shows an interesting contrast. Because the Loop Current and ring had weakened when Rita passed over the Gulf, the corresponding level of inertial energy at the surface is higher and more wide-spread. Finally, while regions and magnitudes of inertial and total currents very nearly coincide near the surface, such is not so for the subsurface currents (Figure 8.2). Here the inertial and total amplitudes coincide in certain regions, but in other regions they do not. The regions they coincide are in the Loop and ring. The conclusion is that in these regions, storm-induced inertial energy presumably contributes significantly to the sub-surface mixing, hence also to the dissipation (and weakening) of the Loop and rings. This mechanism may explain why the Loop Current and Eddy Vortex weakened after Katrina.

In summary, Objective 3 is addressed by Figures 2.6 (Katrina) and 3.8 (Rita) for the swaths of maximum wave heights, and Figures 8.1 and 8.2 for maximum inertial current speeds, both at the surface and also at subsurface. For both Katrina and Rita, the surface responses, i.e., waves and currents, were strongest to the right of the storm. For waves, that is because the wind is also stronger to the right of the storm's track. For currents, the ocean to the right experiences clockwise-rotating wind vector which reinforces the inertial currents which are also clockwise-rotating. Peak wave heights were about 25 m for Katrina and about 20 m for Rita, and they occurred just as the storms reached the continental slope and outer shelves of the northern Gulf of Mexico: south-southeast of the Mississippi delta in the case of Katrina, and due south of the Texas-Louisiana coast over a water depth of about 200-500 m in the case of Hurricane Rita. Surface current speeds of 2~4 m s^{-1} in the case of Katrina occurred at three places, between the Loop and the Eddy Vortex, south-southeast of the Mississippi delta where there was also peak wave height, and at the coast where Katrina made landfall near the border of Mississippi and Alabama. Surface speeds in the case of Rita are somewhat weaker 1~3 m s^{-1}; they too are strongest between the Loop and the ring, and also over the slope and outer shelf of Texas and Louisiana. At subsurface 600~1000 m deep, strong current amplitudes of about 0.5 m s^{-1} occur inside the Eddy Vortex as well as in the Loop Current.

CHAPTER 9. REFERENCES

Alves, J. H. G. M., Y. Y. Chao, and H. L. Tolman. 2005. The operational North Atlantic hurricane wind-wave forecasting system at NOAA/NCEP. NOAA/NWS/NCEP/MMAB Technical Note 244. 59 pp.

Anderson, D.L.T., J Sheinbaum, and K Haines. 1996. Data assimilation in ocean models. Rep. Prog. Phys. 59:1209-1266.

Bender, M.A. and I. Ginis. 2000. Real-case simulations of hurricane-ocean interaction using a high-resolution coupled model: Effects on hurricane intensity. Mon. Wea. Rev. 128:917-946.

Booij, N., R.C. Ris, and L.H. Holthuijsen. 1999. A third-generation wave model for coastal regions: 1. Model description and validation. J. Geophys. Res. 104:7649-7666.

Burpee, R. W. 1972. The origin and structure of easterly waves in the lower troposphere of North Africa. J. Atmos. Sci. 29:77-90.

Bye, J.A.T. and A.D. Jenkins. 2006. Drag coefficient reduction at very high wind speeds. J. Geophys. Res. 111, C03024, doi:10.1029/2005JC003114.

Caplan, P., J. Derber, W. Gemmill, S.-Y. Hong, H.-L. Pan, and D. Parrish. 1997. Changes to the NCEP operational medium-range forecast model analysis/forecast system. Wea. Forecasting 12:581-594.

Chang, S.W. and Anthes, R.A. 1978. Numerical simulations of the ocean's nonlinear baroclinic response to translating hurricanes. J. Phys. Oceanogr. 8:468-480.

Chelton, D.B., R.A. DeSzoeke, M.G. Schlax, K.E. Naggar, and N. Siwertz. 1998. Geographical variability of the first baroclinic Rossby radius of deformation. J. Phys. Oceanogr. 28:433-460.

Chu, P., Y. Qi, Y. Chen, P. Shi, and Q. Mao. 2004. South China Sea wind-wave characteristics. 1. Validation of Wavewatch-III using TOPEX/Poseidon data. J. Atm. Ocean. Tech. 21:1718-1733.

Cione, J.J. and E. Uhlhorn. 2003. Sea surface temperature variability in hurricanes: Implications with respect to intensity change. Mon. Wea. Rev. 131:1783-1796.

Cochrane, J.D. 1972. Separation of an anticyclone and subsequent developments in the Loop Current (1969). In: Capurro, L.R.A. and J.L. Reid, eds. Ocean Studies. Houston, TX: Gulf Publishing Co. Texas A & M Univ. 2:91-106.

Cooper, C., G.Z. Forristall, and T.M. Joyce. 1990. Velocity and hydrographic structure of two Gulf of Mexico warm-core rings. J. Geophys. Res. 95:1663-1679.

Craig, P.D. and M.L. Banner. 1994. Modeling wave-enhanced turbulence in the ocean surface layer. J. Phys. Oceanogr. 24:2546-2559.

DeMaria, M., and J. Kaplan. 1994. Sea surface temperature and the maximum intensity of Atlantic tropical cyclones. J. Climate 7:1324-1334.

DeMaria, M., M. Mainelli, L.K. Shay, J.A. Knaff, and J. Kaplan. 2005. further improvement to the statistical hurricane intensity prediction scheme (SHIPS). Wea. Forecast 20:531.

Donelan, M.A., B.K. Haus, N. Reul, W.J. Plant, M. Stiassnie, H.C. Graber, O.B. Brown, and E.S. Saltzma. 2004. On the limiting aerodynamic roughness of the ocean in very strong winds. Geophys. Res. Lett. 31, L18306, doi:10.1029, 2004GL019460.

Ducet, N., P.Y. Le Tron, and G. Reverdin. 2000. Global high-resolution mapping of ocean circulation from TOPEX/Poseidon and ERS-1 and -2. J. Geophys. Res. 105:19,477-19,498.

Elliott, B.A. 1982. Anti-cyclonic rings in the Gulf of Mexico. J. Phys. Oceanogr. 12:1292-1309.

Emanuel, K. 2005a. Increasing destructiveness of tropical cyclones over the past 30 years. Nature 436:686-688.

Emanuel, K.A. 2005b. Divine wind – the history and science of hurricanes. New York: Oxford Univ. Press. 285 pp.

Ehrendorfer, M., and J.J. Tribbia. 1997. Optimal prediction of forecast error covariances through singular vectors. J. Atmos. Sci. 54:286-313.

Ezer, T., and Mellor, G.L. 1994. Continuous assimilation of Geosat altimeter data into a three-dimensional primitive equation Gulf Stream model. J. Phys. Oceanogr. 24(4):832-847.

Ezer, T., L.-Y. Oey, H.-C. Lee, and W. Sturges. 2003. The variability of currents in the Yucatan Channel: Analysis of results from a numerical ocean model. J. Geophys. Res. 108(C1), 3012, doi:10.1029/2002JC001509.

Fan, S.J., L.-Y. Oey, and P. Hamilton. 2004. Assimilation of drifters and satellite data in a circulation model of the northeastern Gulf of Mexico. Cont. Shelf Res. 24(9):1001-1013.

Forristal, G.Z., K.J. Schaudt, and C.K. Cooper. 1992. Evolution and kinematics of a Loop Current eddy in the Gulf of Mexico during 1985. J. Geophys. Res. 97:2173-2184.

Fratantoni, D.M. 2001. North Atlantic surface circulation during the 1990's observed with satellite-tracked drifters. J. Geophys. Res. 106:22,067-22,093.

Geisler, J.E. 1970. Linear theory of the response of a two-layer ocean to a moving hurricane. Geophys. Fluid Dyn. 1:249-272.

Geist, E.L., V.V. Titov, and C.E. Synolakis. 2006. Tsunami: Wave of change. Scientific American 294:56-63.

Gill, A.E. 1982. Atmosphere-ocean dynamics. New York: Academic Press. 662 pp.

Greatbatch, R.J. 1983. On the response of the ocean to a moving storm: The nonlinear dynamics. J. Phys. Oceanogr. 13:357-367.

Hays, K. 2007. Shell's Mars suppresses pre-Katrina production levels. Houston Chronicle, January 22.

Hurlburt, H.E. and J.D. Thompson. 1980. A numerical study of Loop Current intrusions and eddy shedding. J. Phys. Oceanogr. 10:1611-1651.

Huang, N.E., Z. Shen, S. R. Long, M.C. Wu, H.H. Shih, Q. Zheng, N.-C. Yen, C.C. Tung, and H.H. Liu. 1998. The empirical mode decomposition and the Hilbert spectrum for nonlinear and non-stationary time series analysis. Proc. R. Soc. Lond. A., 454:903-995.

Johns, W.E., T.L. Townsend, D.M. Fratantoni, and W.D. Wilson. 2002. On the Atlantic inflow to the Caribbean Sea. Deep Sea Res. 49:211-243.

Kalnay, E. 2003. Atmospheric modeling, data assimilation and predictability. New York: Cambridge University Press. 341 pp.

Kamachi, M., Kuragano. S. Sugimoto, K. Yoshita, T Sakurai, T, Nakano, N. Usui, and F. Uboldi. 2004. Short-Range Prediction Experiments with Operational Data Assimilation System for the Kuroshio South of Japan. J. Oceanogr. Soc. Japan 60:269-282.

Knabb, R.D., J.R. Rhome, and D.P. Brown. 2005. Tropical cyclone report, Hurricane Katrina, 23-30 August 2005. Internet website: http://www.nhc.noaa.gov/pdf/TCR-AL122005_Katrina.pdf.

Kundu, P. 1976. An analysis of inertial oscillations observed near Oregon coast. J. Phys. Oceanogr. 6:879-893.

Kunze, E. 1985. Near-inertial wave propagation in geostrophic shear. J. Phys. Oceanogr. 15:544-565.

Kunze, E., R.W. Schmitt, and J.M. Toole. 1995. The energy balance in a warm-core ring's near-inertial critical layer. J. Phys. Oceanogr. 25:942-957.

Lai R.J and N. Huang. 2005. Investigation of vertical and horizontal momentum transfer in the Gulf of Mexico using empirical mode decomposition method. J. Phys. Oceanogr. 35:1383.

Landsea, C.W. 1993. A climatology of intense (or major) Atlantic hurricanes. Mon. Wea. Rev. 121:1703-1713.

Large, W.G. and S. Pond. 1981. Open ocean flux measurements in moderate to strong winds. J. Phys. Oceanogr. 11:324-336.

Leben, R.R. 2005. Altimeter-derived Loop Current metrics. In: Sturges, W. and A. Lugo-Fernandez, eds. Circulation in the Gulf of Mexico: Observations and models. Geophysical Monograph Series. Vol. 161. 360 pp.

Leith, C.E. 1974. Theoretical skill of Monte Carlo forecasts. Mon. Wea. Rev. 102:409-418.

Leipper, D.F., and D. Volgenau. 1972. Hurricane heat potential of the Gulf of Mexico. J. Phys. Oceanogr. 2:218-224.

Lin, X.-H., L.-Y. Oey, and D.-P. Wang. 2007. Altimetry and drifter data assimilations of Loop Current and eddies. J. Geophys. Res. 112, C05046, doi:10.1029/2006JC003779.

Lorenz, E.N. 1963. Deterministic non-periodic flow. J. Atmos. Sci. 20:130-141.

Lorenz, E.N. 1965. A study of the predictability of a 28-variable atmospheric model. Tellus 17:321-333.

Lorenz, E.N. 1993. The essence of chaos. Seattle: University of Washington Press. 240 pp.

Lueck, R. and T. Osborn. 1986. The dissipation of kinetic energy in a warm-core ring. J.Geophys.Res. 91: 803-818.

MacKinnon, J.A. and M.C. Gregg. 2003. Shear and baroclinic energy flux on the summer New England shelf. J. Phys. Ocenogr. 33:1462-1475.

Meid, R.P., C.Y. Shen, C.L. Trump, and G.L. Lindemann. 1986. Internal-inertial waves in a Sargasso Sea front. J. Phys. Oceanogr. 16:1751-1762.

Mellor, G.L. 2001. One-dimensional, ocean surface layer modeling: A problem and a solution. J. Phys. Ocenogr. 31:790-809.

Mellor, G.L. 2004. Users guide for a three-dimensional, primitive equation, numerical ocean model. Program in Atmospheric and Oceanic Sciences, Princeton University. 42 pp.

Mellor, G.L. and T. Yamada. 1982. Development of a turbulence closure model for geophysical fluid problems. Rev. Geophys. Space Phys. 20:851-875.

Mellor, G.L. and T. Ezer. 1991. A Gulf Stream model and an altimetry assimilation scheme. J. Geophys. Res. 96:8779-8795.

Mellor, G.L., M.A. Donelan, and L.-Y. Oey. 2008. A surface wave model for coupling with numerical ocean circulation models. J. Atmos. Oceanic Tech. 25:1785-1807.

Miyazawa, Y., S. Yamane, X. Guo, and T. Yamagata. 2005. Ensemble forecast of the Kuroshio meandering. J. Geophys. Res. 110, C10026, doi:10.1029/2004JC002426.

Moon, I-J., I. Ginnis, T. Hara, H.L. Tolman, C.W. Wright, and E.J. Walsh. 2003. Numerical simulation of sea surface directional wave spectra under hurricane wind forcing. J. Phys. Oceanogr. 33:1680-1706.

Moon, I.-J., I. Ginis, and T. Hara. 2004. Effect of surface waves on Charnock coefficient under tropical cyclones. Geophys. Res. Lett. 31, L20302, doi:10.1029/2004GL020988.

Mooers, C.N.K. 1975. Several effects of a bariclinic current on the cross-stream propagation of inertial-internal waves. Geophys. Fluid Dyn. 6:245-275.

Nowlin, W.D., Jr. 1972. Winter circulation pattern and property distributions. In: Capurro, L.R.A. and J.L. Reid, eds. Contributions on the Physical Oceanography of the Gulf of Mexico. Vol. II. New York: Gulf Publishing Co. Pp. 3-64.

Oey, L.-Y. 1995. Eddy- and wind-forced shelf circulation. J. Geophys. Res. 100:8621-8637.

Oey, L-Y. 1996. Simulation of mesoscale variability in the Gulf of Mexico. J. Phys. Oceanogr. 26:145-175.

Oey, L.-Y. 2004. Vorticity flux in the Yucatan Channel and Loop Current eddy shedding in the Gulf of Mexico. J. Geophys. Res. 109, C10004, doi:10.1029/2004JC002400.

Oey, L.-Y. 2008. Loop Current and deep eddies. J. Phys. Oceanogr. 38:1426-1449.

Oey, L.-Y. and P. Chen. 1992. A model simulation of circulation in the north-east Atlantic shelves and seas. J. Geophy. Res. 97:20,087-20,115.

Oey, L.-Y. and H.-C. Lee. 2002. Deep eddy energy and topographic Rossby waves in the Gulf of Mexico. JPO 32:3499-3527.

Oey, L.-Y., and H.-C. Zhang. 2004. A mechanism for the generation of subsurface cyclones and jets. Cont. Shelf Res. 24:2109-2131.

Oey, L.-Y., H.-C. Lee, and W.J. Schmitz, Jr. 2003a. Effects of winds and caribbean eddies on the frequency of loop current eddy shedding: A numerical model study. J. Geophys. Res. 108(C10), 3324, doi:10.1029, 2002JC001698.

Oey, L.-Y., P. Hamilton, and H.-C. Lee. 2003b. Modeling and data analyses of circulation processes in the Gulf of Mexico: Final Report. U.S. Dept. of the Interior, Minerals Management Service, Gulf of Mexico OCS Region, New Orleans, LA. OCS Study MMS 2003-074. 116 pp. Internet website: http://www.gomr.mms.gov/PI/PDFImages/ESPIS/2/3046.pdf.

Oey, L.-Y., T. Ezer, and T. Sturges. 2004. Modeled and observed empirical orthogonal functions of currents in the Yucatan Channel. J. Geophys. Res. 109, C08011, doi:10.1029, 2004JC002345.

Oey L.-Y., T. Ezer, and H.J. Lee. 2005a. Loop Current, rings and related circulation in the Gulf of Mexico: A review of numerical models and future challenges. In: Sturges, W. and A. Lugo-Fernandez, eds. Circulation in the Gulf of Mexico: Observations and models. Geophysical Monograph Series, Vol. 161. 360 pp.

Oey L.-Y., T. Ezer, G. Forristall, C. Cooper, S. DiMarco, and S. Fan. 2005b. An exercise in forecasting loop current and eddy frontal positions in the Gulf of Mexico. Geophys. Res. Lett. 32, L12611, doi:10.1029, 2005GL023253.

Oey L.-Y., T. Ezer, D.-P. Wang, S. Fan, and X.-Q. Yin. 2006. Loop Current warming by Hurricane Wilma, Geophys. Res. Lett. 33, L08613, doi:10.1029, 2006GL025873.

Oey, L.-Y., T. Ezer, D.-P. Wang, X.-Q. Yin, and S.-J. Fan. 2007. Hurricane-induced motions and interaction with ocean currents. Cont. Shelf Res. doi:10.1016/j.csr.2007.01.008.

Oke, P.R., J.S. Allen, R.N. Miller, G.D. Egbert, J.A. Austin, J.A. Barth, T.J. Boyd, P.M. Kosro, and M.D. Levine. 2002. A modeling study of the three-dimensional continental shelf circulation off Oregon. Part I: Model–data comparisons. J. Phys. Oceanogr. 32:1360–1382.

Paduan, J.D. and I. Shulman. 2004. HF radar data assimilation in the Monterey Bay area. J. Geophys. Res. Ocean 109, C07S09, doi:10.1029/2003JC001949.

Palmen, E. 1948. On the formation and structure of tropical cyclones. Geophysics 3:26-38.

Panchang, V.G. and D. Li. 2006. Large waves in the Gulf of Mexico caused by Hurricane Ivan. Bulletin American Met. Soc. 87:481-489.

Powell, M.D., P.J. Vickery, and T. Reinhold. 2003. Reduced drag coefficient for high wind speeds in tropical cyclones. Nature 422:279-283.

Price, J.F. 1981. Upper Ocean Response to a Hurricane. J. Phys. Oceanogr. 11:153-175.

Scharroo, R., W.H.F. Smith, and J.L. Lillibridge. 2005. Satellite altimetry and the intensification of Hurricane Katrina. EOS Trans. 86(40):366.

Shay, L.K., A.J. Mariano, S.D. Jacob, and E.H. Ryan. 1998. Mean and near-inertial ocean current response to Hurricane Gilbert. J. Phys. Oceanogr. 28:858-889.

Shay, L.K., G.J. Goni, and P.G. Black. 2000. Effects of a warm oceanic feature on Hurricane Opal. Mon. Wea. Rev. 128:1366-1383.

Shein, K.A., ed. 2006. State of the climate in 2005. Special supplement to the Bulletin of the American Meteorological Society. 87:6.

Sheinbaum, J., J. Candela, A. Badan, and J. Ochoa. 2002. Flow structure and transports in the Yucatan Channel. Geophys. Res. Let. 29(3), 1040, doi:10.1029/2001GL013990.

Sheng, J., X. Zhai, and R.J. Greatbatch. 2006. Numerical study of the storm-induced circulation on the Scotian Shelf during Hurricane Juan using a nested-grid ocean model. Prog. Oceanogr. 70, doi:10.1016/ *j*.pocean.2005.07.007, 233-254.

Sturges, W. and R. Leben. 2000. Frequency of ring separations from the Loop Current in the Gulf of Mexico: A revised estimate. J. Phys. Oceanogr. 30:1814-1818.

Sturges, W. and A. Lugo-Fernandez, eds. 2005. Circulation in the Gulf of Mexico: Observations and models. Geophysical Monograph Series, Vol. 161. 360 pp.

Thomas, L.N. and C.M. Lee. 2005. Intensification of oceanic fronts by down-front winds. J. Phys. Oceanogr. 35:1086-1102.

Tolman, H.L. 2002. Validation of WAVEWATCH III version 1.15 for a global domain. NOAA/NWS/NCEP/OMB Tech. Note 213. 33 pp.

Tolman, H.L. and D. Chalikov. 1996. Source terms in a third-generation wind wave model. J. Phys. Oceanogr. 26:2497-2518.

Toth, Z. and E. Kalnay. 1993. Ensemble forecasting at NMC: The generation of perturbations. Bull. Amer. Met. Soc. 74(12):2317-2330.

Toth, Z. and E. Kalnay. 1997. Ensemble forecasting at NCEP and the breeding method. Mon. Wea. Rev. 125:3297-3319.

Turner, J.S. 1973. Buoyancy effects in fluids. New York: Cambridge University Press. 367 pp.

Vukovich, F.M. 1995. An updated evaluation of the Loop Currents eddy-shedding frequency. J. Geophys. Res. 100:8655-8659.

Vukovich, F.M. and B. W. Crissman. 1986. Aspects of warm rings in the Gulf of Mexico. J. Geophys. Res. 91:2645-2660.

Wang, D.-P. 1991. Generation and propagation of inertial waves in the subtropical front. J. Mar. Res. 49:619-633.

Wang, D.-P. 1993. Model of frontogenesis: subduction and upwelling. J. Mar. Res. 51:497-513.

Wang, D.-P. and L.-Y. Oey. 2008. Hindcast of waves and currents in Hurricane Katrina. Bulletin of the American Meteorological Society. DOI:10.1175/BAMS-89-4-487.

Wang, D.-P., L.-Y. Oey, T. Ezer, and P. Hamilton. 2003. Nearsurface currents in DeSoto Canyon. J. Phys. Oceanogr. 33:313-326.

Xu, F., W. Perrie, B. Toulany, and P.C. Smith. 2007. Wind-generated waves in Hurricane Juan. Ocean Modeling 16:188-205.

Yang, S.-C., M. Cai, E. Kalnay, M. Rienecker, G. Yuan, and Z. Toth. 2006. ENSO bred vectors in coupled ocean-atmosphere general circulation models. J. Climate 19:1422-1436.

Yin, X.-Q. and L.-Y. Oey. 2007. Bred-ensemble ocean forecast of Loop Current and rings. Ocean Modelling, doi:10.1016/j.ocemod.2007.02.005.

APPENDIX 1.1. COMPLEX CORRELATION (CC)

The "CC" between two velocity time series $\mathbf{u_1} = (u_1, v_1)$ and $\mathbf{u_2} = (u_2, v_2)$, is defined as (Kundu, 1976):

$$CC = \langle w_1 w_2^* \rangle / (\langle w_1 w_1^* \rangle^{1/2} \langle w_2 w_2^* \rangle^{1/2}), \qquad \text{(A1)}$$

where $w_n = u_n + i\, v_n$, n=1,2, $i = (-1)^{1/2}$, the asterisk indicates the complex conjugate, and <.> denotes time averaging. Kundu (1976) was interested in the veering angle between $\mathbf{u_1}$ and $\mathbf{u_2}$ in the bottom Ekman layer and showed that the phase of CC, θ_{CC}, is the average veering angle (between the two vectors) weighted by the speeds of the instantaneous vectors. For the present case, CC measures how closely the model vector w_1 follows the observation vector w_2 in their indexed space, which can be the spatial dimension (e.g., in the vertical at a given time) or time (as in ADCP time series at a fixed depth. Clearly, θ_{CC} should be small for the two vectors to be 'close,' but |CC| should also be ≈ 1 (|CC| is < 1 from (A1)). By considering simple sinusoids, it can be shown that |CC| is small if $\mathbf{u_1}$ and $\mathbf{u_2}$ have disparate frequencies. For similar frequencies $|CC| \approx \cos(\phi)$, where ϕ is the (average) phase-shift between $\mathbf{u_1}$ and $\mathbf{u_2}$. On the other hand, θ_{CC} is independent of ϕ, so that it is possible for |CC| = 1 but $\theta_{CC} = 90^o$, and vice versa for |CC| = 0 but $\theta_{CC} = 0$. The behavior of CC is more complicated for general time series. The upshot is, for the model analysis to be any good, we require $|CC| \approx 1$ and $\theta_{CC} \approx 0$.

The Department of the Interior Mission

As the Nation's principal conservation agency, the Department of the Interior has responsibility for most of our nationally owned public lands and natural resources. This includes fostering sound use of our land and water resources; protecting our fish, wildlife, and biological diversity; preserving the environmental and cultural values of our national parks and historical places; and providing for the enjoyment of life through outdoor recreation. The Department assesses our energy and mineral resources and works to ensure that their development is in the best interests of all our people by encouraging stewardship and citizen participation in their care. The Department also has a major responsibility for American Indian reservation communities and for people who live in island territories under U.S. administration.

The Minerals Management Service Mission

As a bureau of the Department of the Interior, the Minerals Management Service's (MMS) primary responsibilities are to manage the mineral resources located on the Nation's Outer Continental Shelf (OCS), collect revenue from the Federal OCS and onshore Federal and Indian lands, and distribute those revenues.

Moreover, in working to meet its responsibilities, the **Offshore Minerals Management Program** administers the OCS competitive leasing program and oversees the safe and environmentally sound exploration and production of our Nation's offshore natural gas, oil and other mineral resources. The MMS **Minerals Revenue Management** meets its responsibilities by ensuring the efficient, timely and accurate collection and disbursement of revenue from mineral leasing and production due to Indian tribes and allottees, States and the U.S. Treasury.

The MMS strives to fulfill its responsibilities through the general guiding principles of: (1) being responsive to the public's concerns and interests by maintaining a dialogue with all potentially affected parties and (2) carrying out its programs with an emphasis on working to enhance the quality of life for all Americans by lending MMS assistance and expertise to economic development and environmental protection.